2014

Solid state NMR of carbon and catalyst materials with applications for biorenewable chemicals

Robert Lee Johnson
Iowa State University

Recommended Citation

Johnson, Robert Lee, "Solid state NMR of carbon and catalyst materials with applications for biorenewable chemicals" (2014). *Graduate Theses and Dissertations*. 14191.
https://lib.dr.iastate.edu/etd/14191

Solid state NMR of carbon and catalyst materials with applications for biorenewable chemicals

by

Robert L. Johnson

A dissertation submitted to the graduate faculty

in partial fulfillment of the requirements for the degree of

DOCTOR OF PHILOSOPHY

Major: Chemistry

Program of Study Committee:
Klaus Schmidt-Rohr, Co-Major Professor
Pat Thiel, Co-Major Professor
Brent Shanks
Marek Pruski
Keith Woo

Iowa State University
Ames, Iowa
2014

DEDICATION

To my father. Thank you for the lessons you taught me.

TABLE OF CONTENTS

CHAPTER 1. GENERAL INTRODUCTION

Background

As a consequence of the most recent petroleum shortages renewed interest has emerged to replace of fuels and chemicals produced from fossil fuel feedstocks with renewable plant based feedstocks. Even with high petroleum prices the economics of producing low value products such as biodiesel and cellulosic ethanol are still quite unfavorable and are inhibitory to establishment of a bio-based chemical industry. As an effort to limit the risk of having to compete with petroleum for low value products, one approach being explored is adapting the current starch-based ethanol industry to produce an array of mid- to high-value chemicals used as the building blocks for numerous processes in the chemical industry. The NSF engineering research center program has provided funding to create the Center for Biorenewable Chemicals (CBiRC) and develop technologies to realize this vision. CBiRC's approach to accomplish this utilizes biocatalysis with modified microorganisms to produce molecules close in structure to the desired product, which contain less functionality than carbohydrates and therefore are suitable for heterogeneous catalysis to complete the transformation to the desired molecule. The Center's leadership has recognized that an important technical obstacle is presented by poor stability of common catalyst and support materials when exposed to condensed phases, and in the presence of biogenic compounds required during fermentation.

Carbon materials have chemical properties well suited for heterogeneous catalysis in the condensed phase and account for 85% of my graduate research. First, one should note that the term "carbon materials" erroneously lumps a large number of materials into one category that have different functional groups, morphology, and porosity depending on the feedstock, synthesis environment, [1-5] and importantly the temperature used. Temperature has the most pronounced effect. Generally, if materials are produced above 600 °C, very little oxygen or nitrogen will remain and a non-polar surface will result. Considering the Center’s interest to transform “oxygen-rich” feedstocks in polar solvents, materials treated below 600 °C which retain some oxygen functionality are of particular interest. One hypothesis is that oxygen-containing functional groups will serve as sites to attach a catalytic site, more strongly physisorb reactant molecules, and improve metal dispersion. Carbon materials containing significant amounts of oxygen can be configured in a large number of possible combinations, and characterization methods commonly used do not provide meaningful information to rule out incorrect models. Additionally, understanding how the functionality of the carbon materials impacts the catalytic properties would be helpful to aid in catalyst improvement, and synthesis strategies.

Unfortunately, the majority of seminal work characterizing carbon materials has focused on materials treated at very high temperatures, which do not adequately represent carbon materials of interest to the Center. Nevertheless, there are numerous important conclusions about the carbonization and graphitization process that are still relevant for discussion of the chemical structures of moderate-temperature carbon materials. One of the earliest important distinctions of carbon materials is that between hard vs. soft (non-graphitizable vs. graphitizable) carbon made by Franklin, [4], which depends on the chemical nature of the precursor used. The essential conclusion is that if the precursor contains a significant fraction of heteroatoms, significant cross-linking will ensue that will preclude a transition through a liquid crystal phase, which is required for ordering of basic structural units (BSU) to produce crystalline graphite. For example, carbon materials produced from glucose are non-graphitizable, i.e. even treatment at 2000 °C does not produce sharp diffraction peaks similar as in graphite, and the material is a disordered array of graphene fragments. This has been described as a crumpled-paper, or sawdust morphology.

Commercially, activated carbon is used the most widely, taking advantage of the high surface area of these materials. This results from an "activation" following carbonization (usually of non-graphitizable feedstock) in which labile fragments are removed through oxidative treatments with elevated temperatures leading to a microporous structure (e.g. average pore < 10 A). Making "good" activated carbon is not based on a well-characterized structure–function relationship, and therefore often the methods to produce a particular activated carbon are closely held by the producing companies, and the effects of inorganic dopants are not well understood.

A great deal of literature related to utilization of ligno-cellulosic and other renewable materials has explored utilization of pyrolysis and gasification chars, and hydrothermal carbon, for a huge number of applications ranging from soil-quality enhancement to heterogeneous catalysis. Most commonly available characterization methods do not provide sufficient information to make accurate structural predictions, including vibrational spectroscopies, diffraction methods, chemical/destructive methods, and standard cross-polarized 1D spectra. Quantitative 1D NMR in-conjunction with dipolar dephasing experiments provides a great deal of information regarding the molecular structure of the BSU without isotopic enrichment. If ^{13}C isotopic enrichment is possible, solid state NMR can provide a nearly complete picture about the connectivities with two-dimensional ^{13}C-^{13}C correlation experiments, including DQ/SQ correlations [6], to develop much more realistic models for HTC and melanoidins.[7,8] Incorrect depictions of low temperature carbons materials are ubiquitous, showing aromatic clusters and oxygen-containing species incompatible with the elemental composition. Cartoons of moderate-temperature aromatic-rich materials are idealized to say the least, which presents an obstacle to studies to address how these differences influence material and catalytic properties.

Thesis Overview

This thesis describes the use of advanced multinuclear (^{13}C, ^{1}H, ^{29}Si) solid state NMR to study the structure of heterogeneous catalyst materials with the goal of improving synthesis strategies, and gaining a better understanding of mechanisms of deactivation. This research (excluding Appendix 1) was funded through the NSF Engineering Research Center for Biorenewable Chemicals (CBiRC). It is the result of collaborative work involving several universities within the Center, including the University of New Mexico (UNM), University of Wisconsin, Madison (UW-Madison), and the Chemical Engineering Department at Iowa State University. Numerous manuscripts have resulted from these collaborations. First-author manuscripts have been added as chapters, while manuscripts with co-authorship are included as Appendices.

Work with the B. Shanks group involved the characterization and synthesis of sulfonated carbon catalyst with improved hydrothermal stability. It started with the development of ^{13}C NMR approaches to determine an accurate molecular model of a suite of ^{13}C-enriched moderate-temperature carbon materials, and invention of a synthesis approach to capitalize on these findings. The resulting publications are included in Chapters 2-4, and Appendices 2-3. The Datye group from UNM had developed a composite catalyst system using carbon-coated metal-oxide surfaces as a means to improve hydrothermal stability of the silica support and reduce agglomeration of Pd nanoparticles. Understanding the chemical structure of the carbon overlayer was of interest and given the temperatures and ease of ^{13}C enrichment this was an ideal system for NMR investigation. Chapters 5 and Appendices 4-5 include a detailed description of the carbon overlayer on silica surfaces, and how the silica surface attenuates the pyrolysis process. Lastly, the Dumesic group at UW-Madison has been interested in reducing inhibition of supported Pd catalysts by biogenic impurities present in fermentation broth, and our contribution to this goal was to use ^{13}C NMR to study the fate of catalyst strongly poisoned by Met, as shown in Chapters 6, 7 and Appendix 6.

One problem that is central to this thesis is the challenge to accurately characterize aromatic-rich carbon materials. With ^{13}C enrichment, solid state NMR can provide the most detailed description of the molecular structure of materials rich in carbon. Nevertheless, without creative approaches such as spectral editing, ^{13}C-^{13}C 2D NMR spectra of aromatic-rich materials provide little meaningful information about intersegmental connectivities as a result of the strong diagonal ridge, which drowns out aromatic resonances in standard 2D spectra. Chapter 2 describes the approach that we have developed to extract information about the connectivities of the aromatic units, which was used to provide a basis to generate a molecular model that was validated by simulation of 1D spectra and comparison with experiment. This study has been published in *J. Mag. Res. 2013*. One carbon materials that has received a great deal of attention, and is of interest to the Center is hydrothermal carbon (HTC). This material contains a very high heteroatom content, and was previously believed to be composed primarily of furanic units. We tested this conclusion by implementing multi-dimensional HETCOR experiments to select specifically for phenolic carbons, and were able to show that one unusual peak could be attributed to a distinct ortho di-phenol structure. The manuscript describing this work can be found in Chapter 3 awaiting submission *J. Phys. Chem. C*. Based on the results shown in Appendices 2-3 (*Carbon 2014, Cat. Commun. 2014),* we invented a synthesis technique utilizing the Maillard reaction (between a reducing sugar and primary amine) with moderate pyrolysis at 250 ^{o}C to produce carbon materials with alkyl-linked sulfonic acid sites. NMR was critical to optimize and validate this synthesis. Using the same simple approach, a number of different starting materials incorporating different functional groups could be synthesized. (Chapter 4, *Chem. Mater.* 2014). A preliminary patent was filed in March 2013.

Work conducted at UNM by the Datye group showed that a thin layer of carbon originated from the pyrolysis of glucose led to a great improvement in hydrothermal stability of porous silica materials, and reduced Pd particle agglomeration. Given these exciting observations, very little was known about the carbon layer itself, and the mechanisms by which this layer was producing this result. Solid state NMR was then used to characterize this layer with a battery of experiments on a suite of different materials and show distinct and unexpected features which have interesting implications about the interactions of water with the carbon layer and the silica surface, the effect of surface heterogeneity on the formation of the carbon layer using pyrolysis of glucose, and suggest the carbon overlayer interacts through a network of strong hydrogen bonding with labile Si-OH rich regions leading to hydrothermal stability improvement (Chapter 5). Additionally we contributed 1D and 2D spectra and simulations to characterize the molecular structure of the carbon overlayer, as described in the Appendices (*Angew. Chem. 2012)* 4-5

Work with Tom Schwartz from the Dumesic group led to a detailed study of Pd catalyst poisoned with methionine (Met) and is the focus of Chapter 6 (awaiting submission to *Langmuir*). To study Met during the early stages of breakdown, it was vital to be capable of comparing spectra with accurate peak intensities for all ^{13}C bonding environments. The only reliable experiment to accomplish this is direct polarization (DP) NMR, which, however, requires long recycle delays to ensure complete relaxation. Although Met was ^{13}C enriched, there was only a very small amount of it inside the rotor, which made DP experiments with sufficient signal to noise very time consuming. A novel solution to acquire quantitative ^{13}C NMR spectra 30 times faster than by DP, using multiple ^{1}H–^{13}C cross-polarization, is presented in Chapter 7. (*J. Magn.*

Reson. 2014) Finally, a study with Tom Schwartz as lead author, *(Angew, Chem. 2014)* where NMR provided important evidence that the overcoat reduced retention of SCH_3 on the catalyst, is included as Appendix 6.

References

(1) Menéndez, J. A.; Phillips, J.; Xia, B.; Radovic, L. R. On the Modification and Characterization of Chemical Surface Properties of Activated Carbon: In the Search of Carbons with Stable Basic Properties. *Langmuir* **1996**, *12*, 4404.

(2) Titirici, M.-M.; Antonietti, M.; Baccile, N. Hydrothermal carbon from biomass: comparison of the local structure from poly- to monosaccharides and pentoses/hexoses. *Green Chem.* **2008**, *10*, 1204.

(3) Falco, C.; Perez Caballero, F.; Babonneau, F.; Gervais, C.; Laurent, G.; Titirici, M.-M.; Baccile, N. Hydrothermal Carbon from Biomass: Structural Differences between Hydrothermal and Pyrolyzed Carbons via 13C Solid State NMR. *Langmuir* **2011**, *27*, 14460.

(4) Harris, J. F. H. Rosalind Franklin's work on coal, carbon, and graphite. *Interdisiplinary Science Reviews* **2001**, *26*, 204.

(5) Rouzaud, J. N.; Oberlin, A. Structure, microtexture, and optical properties of anthracene and saccharose-based carbons. *Carbon* **1989**, *27*, 517.

(6) Baccile, N.; Laurent, G.; Babonneau, F.; Fayon, F.; Titirici, M.-M.; Antonietti, M. Structural Characterization of Hydrothermal Carbon Spheres by Advanced Solid-State MAS 13C NMR Investigations. *J. Phys. Chem. C* **2009**, *113*, 9644.

(7) Fang, X.; Schmidt-Rohr, K. Fate of the Amino Acid in Glucose−Glycine Melanoidins Investigated by Solid-State Nuclear Magnetic Resonance (NMR). *J. Agric. Food Chem.* **2009**, *57*, 10701.

(8) Fang, X.; Schmidt-Rohr, K. Alkyl and Other Major Structures in 13C-Labeled Glucose-Glycine Melanoidins Identified by Solid-State Nuclear Magnetic Resonance. *J. Agric. Food Chem.* **2010**, *59*, 481.

CHAPTER 2. SPECTRALLY EDITED 2D ^{13}C-^{13}C NMR SPECTRA WITHOUT DIAGONAL RIDGE FOR CHARACTERIZING ^{13}C-ENRICHED LOW-TEMPERATURE CARBON MATERIALS

Journal of Magnetic Resonance **234**, pp 112-124, 2013

Robert L. Johnson[a,c], Jason M. Anderson[b,c], Brent H. Shanks[b,c], Xiaowen Fang[a], Mei Hong[a], Klaus Schmidt-Rohr[a,c]*

[a] Department of Chemistry, Iowa State University, Ames, IA 50011

[b] Department of Chemical and Biological Engineering, Iowa State University, Ames, IA 50011

[c] Center for Biorenewable Chemicals (CBiRC), Iowa State University, Ames, IA 50011

*Corresponding author. Address: Chemistry Dept., Hach Hall, Ames IA, 50011.
srohr@iastate.edu

Keywords: Spectral editing; black carbon structure; char structure; melanoidin structure; furan rings; ketones; double-quantum NMR.

Abstract

Two robust combinations of spectral editing techniques with 2D ^{13}C-^{13}C NMR have been developed for characterizing the aromatic components of ^{13}C-enriched low-temperature carbon materials. One method (exchange with protonated and nonprotonated spectral editing, EXPANSE) selects cross peaks of protonated and nearby nonprotonated carbons, while the other technique, dipolar-dephased double-quantum/single-quantum (DQ/SQ) NMR, selects signals of bonded nonprotonated carbons. Both spectra are free of a diagonal ridge, which has many advantages: Cross peaks on the diagonal or of small intensity can be detected, and residual spinning sidebands or truncation artifacts associated with the diagonal ridge are avoided. In the DQ/SQ experiment, dipolar dephasing of the double-quantum coherence removes protonated-

carbon signals; this approach also eliminates the need for high-power proton decoupling. The initial magnetization is generated with minimal fluctuation by combining direct polarization, cross polarization, and equilibration by ^{13}C spin diffusion. The dipolar dephased DQ/SQ spectrum shows signals from all linkages between aromatic rings, including a distinctive peak from polycondensed aromatics. In EXPANSE NMR, signals of protonated carbons are selected in the first spectral dimension by short cross polarization combined with dipolar dephasing difference. This removes ambiguities of peak assignment to overlapping signals of nonprotonated and protonated aromatic carbons, e.g. near 125 ppm. Spin diffusion is enhanced by dipolar-assisted rotational resonance. Before detection, C-H dipolar dephasing by gated decoupling is applied, which selects signals of nonprotonated carbons. Thus, only cross peaks due to magnetization originating from protonated C and ending on nearby nonprotonated C are retained. Combined with the chemical shifts deduced from the cross-peak position, this double spectral editing defines the bonding environment of aromatic, COO, and C=O carbons, which is particularly useful for identifying furan and arene rings. The C=O carbons, whose chemical shifts vary strongly (between 212 and 165 ppm) and systematically depending on their two bonding partners, show particularly informative cross peaks, given that one bonding partner is defined by the other frequency coordinate of the cross peak. The new techniques and the information content of the resulting spectra are validated on sulfuric-acid treated low-temperature carbon materials and on products of the Maillard reaction. The crucial need for spectral editing for correct peak assignment is demonstrated in an example.

Introduction

Carbon materials produced from renewable feedstocks at moderate temperatures, including hydrothermal carbon [1] and chars [2], are attractive for a variety of applications, including as catalyst supports [3, 4], lithium-ion battery anodes [3, 5], absorbents to remove environmental contaminants such as metals [6], and for soil amendments and carbon sequestration [7, 8]. Carbon-rich materials produced by fires or pyrolysis, including oxidized char residues in soil [9], are generally of interest in environmental science [10, 11]. Other chemical transformations producing aromatic compounds at moderate temperatures are sugar caramelization [12] and the Maillard reaction between reducing sugars and amine compounds [13-15], which are relevant in food science. Furthermore, oxygen-containing carbon structures are of interest in the production of graphene from graphite oxide [16, 17].

Solid-state ^{13}C NMR is the best available method for characterizing the overall composition and local structure of such amorphous, carbon-rich materials that also contain oxygen in a variety of functional groups. [1, 8-11, 13-24] However, even by NMR the various aromatic structures are often difficult to identify. As seen in Fig. 1, the aromatic-carbon regions (100 – 155 ppm) of the ^{13}C NMR spectra of low-temperature carbon materials often exhibit strongly overlapping bands, which can be attributed to furans, phenols, other individual or fused six-membered arene rings, and possibly pyrroles.

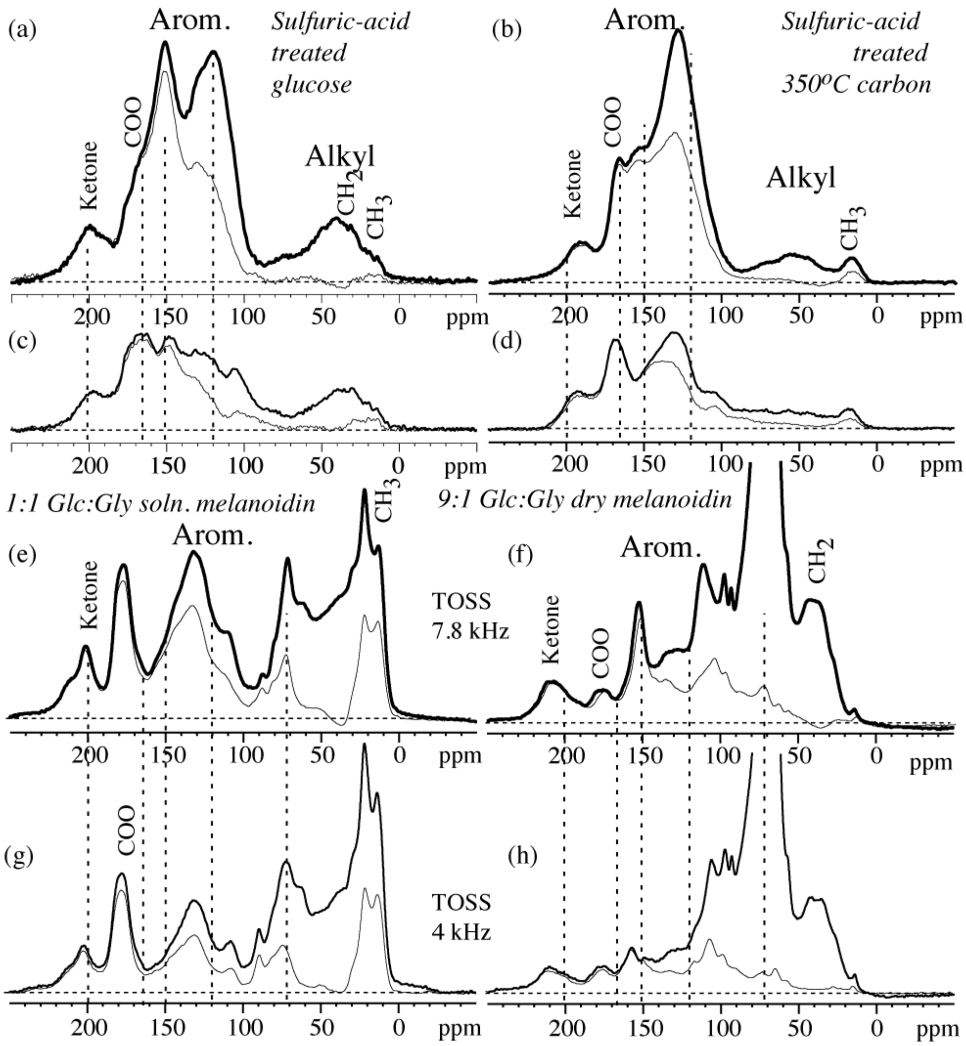

Figure 1. ^{13}C CP/TOSS NMR spectra (thick lines) and corresponding spectra after 40 μs of dipolar dephasing (thin lines) of (a, c) glucose after treatment with fuming sulfuric acid ("DirfumS"); (b, d) glucose pyrolyzed at 350°C and then treated with fuming sulfuric acid ("Pyr350fumS"); (e, g) 1:1 glucose:glycine melanoidin from Maillard reaction in solution ("Mel1:1"); (f, h) 9:1 glucose:glycine melanoidin from dry Maillard reaction ("Mel9:1"). All samples were made from uniformly (>99%) ^{13}C-enriched glucose. (a, b, e, f) were obtained at 7.8 kHz MAS, (c, d, g, h) at 4 kHz, where aromatic-carbon signals are reduced, revealing COO peaks near 165 ppm in (c) and (d). Vertical dashed lines at 200, 165, 150, and 120 ppm highlight the variations in ketone (C=O), COO, aromatic C-O, and aromatic CH, positions, respectively. The dashed lines at 72 ppm in (e-h) mark the OCH/NC$_q$ peak. In (f) and (h), the top of the high OCH peak near 70 ppm is not shown.

The main challenge in the spectral analysis of aromatic-carbon rich materials arises from ambiguities in the assignment of a signal at a certain ppm value to a specific type of carbon. For instance, a peak near 123 ppm can be due to C-H in six-membered aromatic rings (in particular when they are fused or heavily substituted) or arise from aromatic C two bonds from O, i.e. C=C-O in furan or phenol rings. Aromatic C-O resonating at 150 ppm can be due to furan or phenol rings, which are difficult to distinguish in one-dimensional NMR due to the similar local bonding structure of their aromatic carbons (highlighted by dashed outlines in Scheme 1). Signal at 162 ppm can be from C-O in a phenol or from COO bonded to a furan ring, and bands at 180 ppm may arise from COO bonded to alkyl C, or from C=O bonded to a furan ring (see below) [25]. Furthermore, in the presence of furans and/or phenols, the signals of nonpolar arenes (120-145 ppm) are often "sandwiched" between those of aromatic C-O (140-160 ppm) and C-C-O (100-130 ppm) and therefore difficult to resolve.

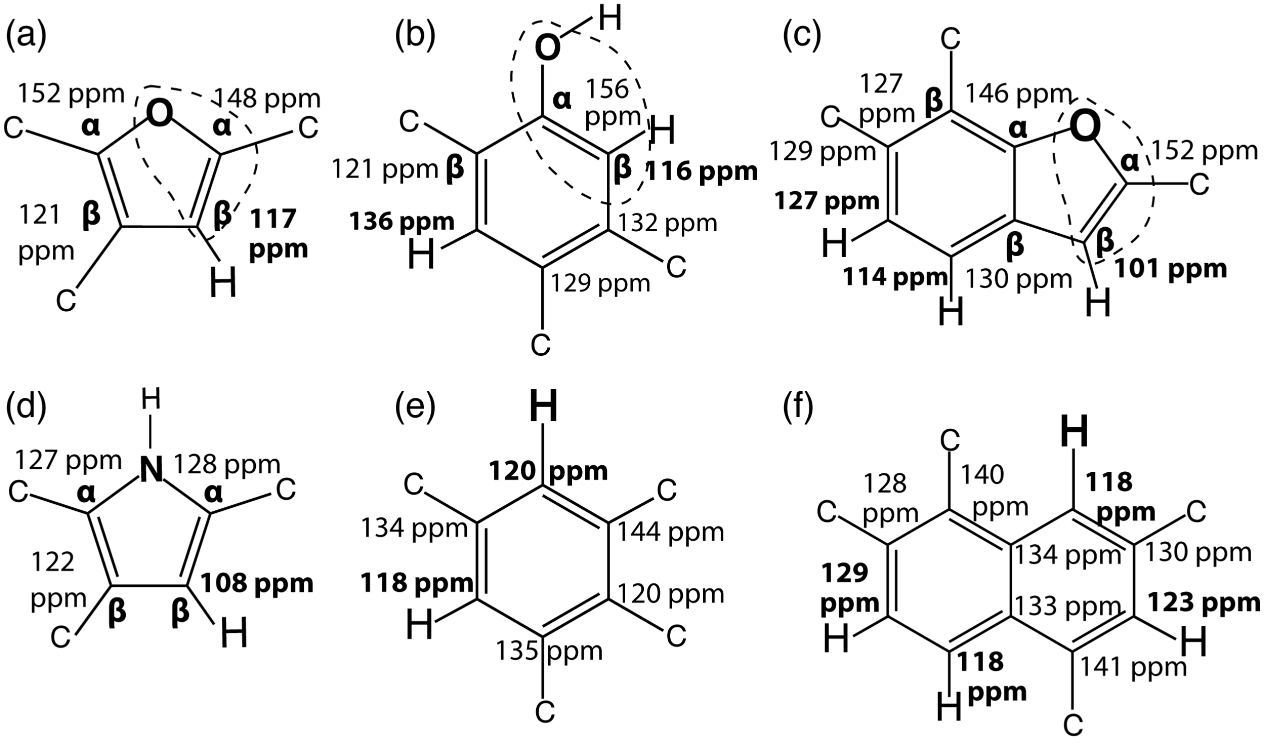

Scheme 1. Simple aromatic ring structures and typical chemical shifts, predicted by the empirical ACD/NMR program, with furan-ring, arene-ring, COO, and C=O substituents (shown here only as "C"; full structures are displayed in Scheme S1 in the Supplementary Material). Substituted (a) furan; (b) phenol; (c) benzofuran; (d) pyrrole; (e) benzene; (f) naphthalene.

Even two-dimensional ^{13}C-^{13}C NMR of ^{13}C-enriched materials, which identifies carbons in close proximity in terms of cross peaks at the carbons' frequency positions, often cannot resolve the ambiguities mentioned above. In particular, arene signals, which are observed typically near 130 ppm, are mostly overlapped by the dominant diagonal ridge in 2D exchange NMR spectra, see Fig. 2, or may remain sandwiched between furan peaks [24]. Figure 2 also indicates that cross peaks between sp^2- and sp^3-hybridized carbons may be impacted by spinning sidebands of the diagonal ridge.

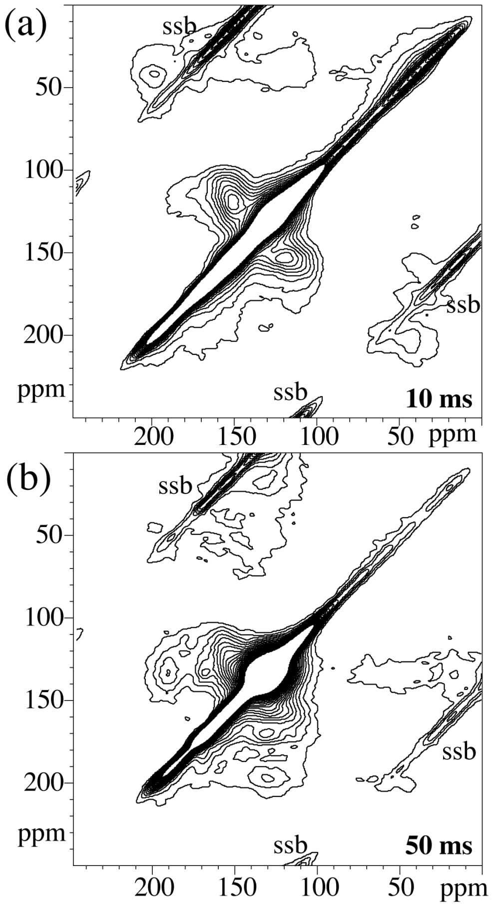

Figure 2. Contour plots of 'regular' 2D ^{13}C-^{13}C exchange NMR spectra of (a) ^{13}C glucose charred by fuming sulfuric acid (DirfumS material), with a spin-diffusion time of t_m =10 ms with DARR irradiation on ^1H, and of (b) Pyr350fumS, with t_m = 50 ms (the 10-ms spectrum was dominated by artifacts). The diagonal ridge in the aromatic region of each spectrum is above the highest contour line. "ssb": spinning sidebands of the diagonal ridge.

Here we show how these problems can be eliminated by two methods incorporating suitable spectral editing into ^{13}C-^{13}C correlation NMR. The first technique specifically correlates signals of protonated and nonprotonated carbons, the second method the peaks of two nonprotonated carbons. While the former can identify arenes convincingly, the latter is particularly suitable for characterizing the substituents of the various aromatic rings and the presence of clusters of fused aromatic rings. In both experiments, the positions of the observed cross peaks of ketone (C=O) carbons are very informative due to their systematic dependence on their two bonding partners. For instance, the chemical shifts for C=O with two ethyl vs. two furan substituents differ by more than 40 ppm. Different substitution patterns of furans (e.g. only on Cα, or on both Cα and Cβ, see Scheme 1) can be identified. Both experiments remove the overwhelming diagonal ridge and its associated spectral artifacts (see Fig. 2), thus enabling detection of cross peaks near and on the diagonal, as well as improving the dynamic range, which benefits detection of cross peaks of low intensity. We demonstrate both experiments on ^{13}C-enriched glucose carbonized by fuming sulfuric acid, 350°C glucose char treated with fuming sulfuric acid, and two melanoidins made from ^{13}C-enriched glucose and glycine [13, 14]. For one of the samples, we use the spectral editing to correct an erroneous structural assignment.

Dipolar-dephased DQ/SQ NMR. Figure 3 shows the pulse sequence for obtaining a 2D correlation spectrum with cross peaks only between signals of nonprotonated carbons, and without diagonal ridge. At the core it is a standard double-quantum (DQ)/single-quantum (SQ) pulse sequence in the tradition of the classical INADEQUATE experiment [26]. During the evolution period t_1, the two-spin double-quantum coherence evolves with the sum (ω_A+ω_B) of the frequencies, and during detection (t_2) the magnetization evolving with the individual frequencies ω_A and ω_B. The DQ coherence is generated and reconverted by the ^{13}C-^{13}C dipolar couplings recoupled by a suitable rotation-synchronized pulse sequence, such as SPC5 [27], for ca. 0.3 ms; it is selected by the standard phase cycling of the second block relative to the first [26]. To keep spinning sidebands from overlapping with centerbands in the DQ dimension, the experiment needs to be applied at a sufficiently high spinning frequency. In our magnet, at 0.1 kHz/ppm, 14 kHz corresponds to 140 ppm and is just fast enough to avoid significant overlap of the sidebands and centerbands. In the SQ dimension, sidebands at ν_r = 14 kHz do not interfere with the signals of interest, due to their favorable location in the spectral plane.

To select the signals of nonprotonated carbons, we need to dephase the double-quantum coherences involving protonated carbons, using recoupled dipolar dephasing by gated decoupling for about 68 μs [21]. A π-pulse must be applied at the center of the delay without decoupling to recouple the C-H dipolar interaction [21] and refocus the chemical shift evolution. However, this pulse interferes severely with the DQ reconversion [27]. It could be accounted for by a fairly complicated reversal of the SPC5 DQ excitation phase sequence, as pointed out in ref. [27]. A much simpler solution, however, is to add a compensating second π-pulse right at the end of DQ excitation, where it does not have any other significant effects.

It is important to note that dipolar dephasing *before* double-quantum excitation would not suppress the signals associated with CH carbons completely. Consider a $C_{A,nonprot}$- C_BH pair. Magnetization of $C_{A,nonprot}$ surviving the first dipolar dephasing would evolve into a $C_{A,nonprot}$ - C_BH double-quantum coherence oscillating with $(\omega_A+\omega_B)$; after reconversion, the $C_{A,nonprot}$ signal would survive the second dipolar dephasing and be detected at ω_A. As a result, a signal at $(\omega_A+\omega_B, \omega_A)$ with the protonated-carbon frequency ω_B would survive. Thus, dephasing of the double-quantum coherence itself is needed (and the dephasing before detection is really optional).

The SPC5 sequence is excellent for nonprotonated DQ NMR at 14 kHz MAS. The ^{13}C rf field of $\gamma B_1/(2\pi) = 5 \times 14$ kHz is about as strong as one can safely apply in our probe head. Being large compared to the range of chemical shifts (220 ppm or 22 kHz), it provides a broad excitation bandwidth. It also decouples the nonprotonated carbons from the protons, even without ^{1}H irradiation. In fact, we recorded the spectra without ^{1}H irradiation during SPC5, since the performance was better than with moderate-power ^{1}H irradiation.

The explicit selection of the signals of nonprotonated carbons removes the main technical difficulty of DQ/SQ NMR, which is the detection of the signals of aromatic CH carbons without significant attenuation. For protonated carbons, ^{1}H decoupling needs to be at least 2.5 times stronger than the ^{13}C irradiation during SPC5, which itself needs to be strong, about 70 kHz, for two reasons: It needs to be five times the spinning frequency of $\geq$14 kHz [27], and it needs to be much larger than the spread of ^{13}C frequencies (20 kHz for isotropic chemical shifts and up to 25 kHz for chemical shift anisotropy at 9.4 T). The required 2.5×70 kHz = 175 kHz ^{1}H radio-frequency field cannot be achieved in our 4-mm radio-frequency coil; in a smaller coil capable of generating 175 kHz without arcing, sensitivity would be seriously impaired. Detection of nonprotonated carbon signals in our edited spectra eliminates these serious difficulties and makes the experiment easy to perform.

Preparation of magnetization by combined DP and CP plus spin diffusion. At the beginning of the 2D experiment, magnetization of nonprotonated carbons must be produced efficiently and reproducibly. The standard method, cross polarization from ^{1}H, is not particularly efficient for nonprotonated ^{13}C at 14 kHz MAS and quite sensitive to fluctuations of radio-frequency power levels. We have used two simple approaches to mitigate these problems. Firstly, we combine standard 1-ms cross polarization from ^{1}H with direct polarization (DP) of ^{13}C to generate the ^{13}C magnetization at the start of the experiment[28] The 90^{o} pulse for direct polarization flips the ^{13}C magnetization onto the CP spin-lock field, to combine with the magnetization generated by CP. [28] Secondly, after CP a 90^{o} pulse flips the ^{13}C magnetization to the z-direction for ~ 100 ms of ^{13}C spin diffusion. This transfers magnetization from the protonated to the nonprotonated C, enhancing their magnetization and minimizing intensity fluctuations due to variations in CP efficiency for the nonprotonated carbons. [29-31] The "t_1 noise" along the vertical dimension in the spectrum that such fluctuations would produce was not observed in our data, which attests to the reproducible magnetization level at the start of the 2D pulse sequence achieved by combined DP and CP plus spin diffusion.

Shearing of the DQ/SQ spectrum. We shear the dipolar dephased DQ/SQ spectrum by 45^{o} along the ω_1 dimension in order to obtain a spectrum equivalent to a SQ-SQ exchange spectrum (but still without a diagonal ridge) [32]. This simplifies the comparison with exchange NMR spectra and provides symmetric cross peaks with respect to the diagonal, which can be a used as a criterion of spectral quality.

Specifically, the shearing displaces peaks from (ω_1, ω_2) to (ω_1–ω_2, ω_2). Thus, shearing of the signals of a ^{13}C spin pair with frequencies ω_A and ω_B originally at (ω_A+ω_B, ω_A) and (ω_A+ω_B, ω_B) moves them to (ω_A+ω_B- ω_A, ω_A) and (ω_A+ω_B- ω_B, ω_B), respectively. Thus, they appear at (ω_B, ω_A) and (ω_A, ω_B), just like the cross peaks in a 2D exchange spectrum.

Exchange with Protonated And Nonprotonated Spectral Editing (EXPANSE) NMR.

The second new pulse sequence, which probes the environment of protonated aromatic carbons in a simple two-dimensional experiment with favorable spectroscopic features, is shown in Fig. 4. It involves selection of only protonated-carbon signals before the evolution time, by combining short (72-μs) cross polarization with dipolar-dephasing difference (in two experiments, see below), and detection of nonprotonated carbons selected by dipolar dephasing. The complementary spectral editing removes the diagonal ridge (see below). 'Gamma averaging' [33] with the mixing time incremented in four steps of $t_r/4$ turned out to be crucial for suppressing sideband artifacts of the diagonal ridge of protonated carbons.

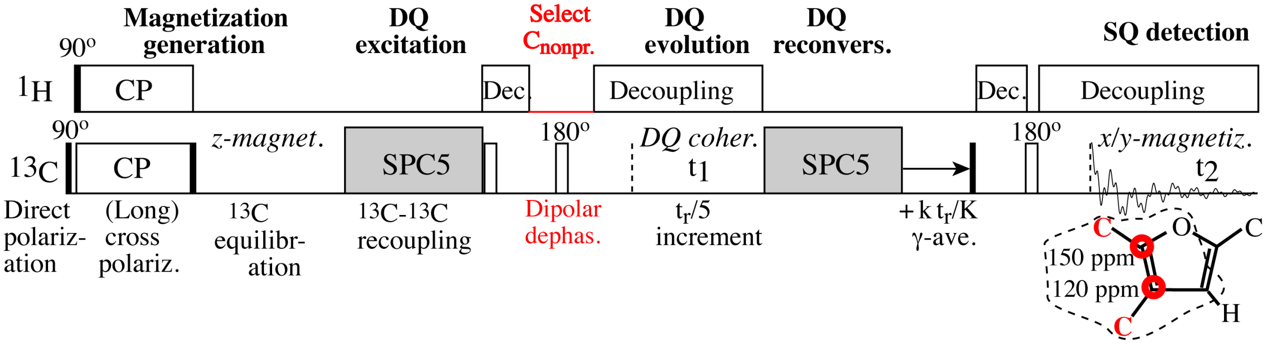

Figure 3. Pulse sequence for 2D ^{13}C-^{13}C correlation NMR of nonprotonated carbons, without diagonal ridge, by dipolar dephased DQ/SQ NMR. Filled narrow rectangles indicate 90° pulses, twice wider open rectangles 180° pulses. Combined direct and cross polarization (CP) is followed by transfer of z-magnetization from protonated to nonprotonated C. The SPC5 homonuclear recoupling sequence [27] (shown shaded) is applied in two blocks of 4 t_r = 0.286 ms duration each to generate and reconvert double-quantum coherence. In addition to the ^{13}C 180° pulse needed for C-H dephasing of the double-quantum coherence, a second 180° pulse is applied directly after the first SPC5 block, since an odd number of 180° pulses would interfere with reconversion by SPC5. A short period after the second SPC5 block, with only z-magnetization, is incremented in K = 4 steps of $t_r/4$ to decouple the rotor phases in the evolution and detection time ("γ-averaging") and avoid dispersive spinning sidebands. The pulse program can be found at http://www.public.iastate.edu/~nmrksr/.

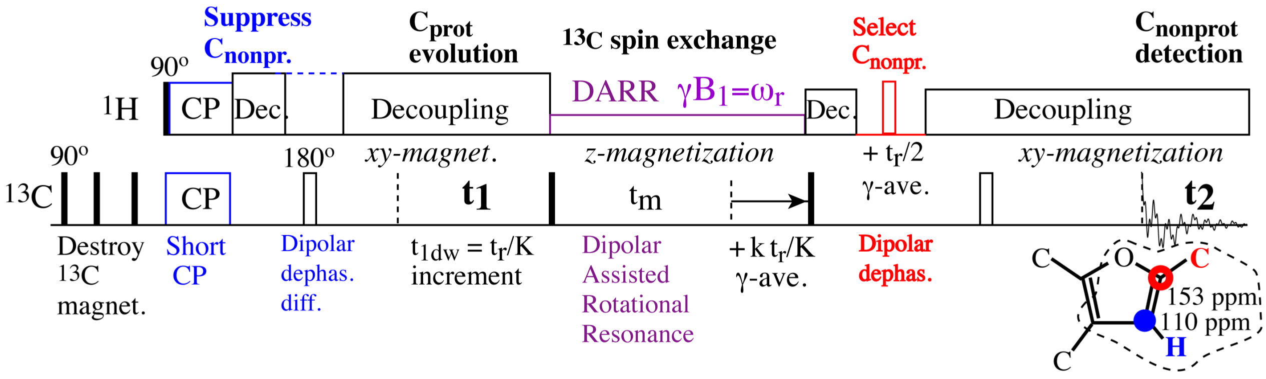

Figure 4. Pulse sequence for spectrally edited 2D ^{13}C-^{13}C correlation by exchange with protonated and nonprotonated spectral editing (EXPANSE) NMR, without diagonal ridge. After the ^{13}C magnetization has been destroyed by a series of 90° pulses, short cross polarization of 72 μs polarizes mostly the protonated carbons. Residual signals of nonprotonated C in the ω_1 dimension are removed by dipolar dephasing difference, i.e. by running a second experiment identical to the first, except for recoupled dipolar dephasing (2 x 16 μs of gated decoupling) before the evolution time, and subtracting this signal out (scaled up by ca. 1.3 to null the residual diagonal ridge). The evolution time is incremented in two steps of $t_r/2$, and the mixing time (at a given t_1) in two steps of $t_r/2$, to suppress sideband artifacts in ω_1 by "γ-averaging". During the mixing time, ^{1}H irradiation at $\gamma B_1 = \omega_r$ recouples the C-H dipolar couplings and thus speeds up ^{1}H-driven ^{13}C spin diffusion. Before detection, signals of immobile protonated carbons are suppressed by recoupled dipolar dephasing; the position of the gated decoupling delay is shifted by $t_r/2$ during signal averaging to remove first-order chemical-shift anisotropy sideband artifacts (γ-averaging).

In our 9.4-T magnetic field, the EXPANSE experiment is applied most conveniently at ≥14-kHz MAS. While a regular ^{13}C-^{13}C exchange NMR spectrum at 14 kHz would still contain spinning sidebands of the diagonal ridge (labeled "ssb" in Fig. 2) that overlap with real cross peaks, the removal of the diagonal ridge and its sidebands in EXPANSE NMR eliminates this problem. The evolution time is incremented in steps of $t_r/2$ or $t_r/4$, so that any higher-order spinning sideband artifacts in the ω_1 dimension coincide with the spectrum itself or with lower-order sidebands.

During the mixing time of about 10 ms, dipolar assisted rotary recoupling (DARR) is applied to recouple proton-driven ^{13}C spin diffusion [34]. The spectral editing ensures that the spin exchange rate should be quite similar for all signals observed: Since only magnetization of protonated carbons is observed in the cross peaks, it is certain that a C-H coupling is present that can be recoupled by DARR and produce the zero-quantum peak overlap that enables efficient spin diffusion [35].

The pulse sequence can also be implemented at slower spinning frequencies, e.g. 8 kHz, with sideband-suppression by TOSS (total suppression of sidebands) [36] before detection and TOSS and deTOSS (time-reversed TOSS) flanking the evolution period [37]. The dipolar dephasing can then be achieved simply by a delay of ~ 30 μs with decoupling gated off, without a π-pulse for recoupling. DARR should be applied even at these lower spinning frequencies since the low proton density of many carbon materials otherwise results in undesirably frequency-selective proton-driven spin diffusion.

Selection of CH_n signals by dipolar dephasing difference. A spectrum of only protonated carbons, in particular aromatic CH, can be obtained by short cross polarization and dipolar-dephasing difference spectroscopy [38, 39]. After 50 μs of CP, the signals of nonprotonated carbons will be small (~10% of their full intensity), but not negligible. They can be removed by recording and subtracting the spectrum obtained with the same parameters, except for additional dipolar dephasing after cross polarization. In this spectrum, the signals of nonprotonated C are retained at >90%, and correspondingly they will be reduced to <10% in the difference spectrum. The remaining intensity of the nonprotonated C is <1% (<10% of 10%) and therefore negligible.

In our 2D experiment, we implement this approach to achieve a CH_n-only spectrum in the first dimension. After short cross polarization, the dipolar dephasing difference can be obtained by recording two 2D spectra, one without the first dipolar dephasing period, the other with this dipolar dephasing, and taking their difference. To avoid artifacts from slow drifts in the experimental conditions, such as cross polarization, it is best to alternate between recording the time signal at a given value of the evolution time t_1 without and with the first dipolar dephasing period.

It should be noted that the dephasing time that produces vanishing C-H signal after short CP is significantly shorter than in “regular” experiments with direct polarization or long cross polarization. The C-H magnetization reaches zero after about 38 μs, instead of ~67 μs, without dipolar decoupling. This is primarily due to short cross polarization preferentially enhancing the magnetization of carbons with strong C-H couplings, which dephase fast. For instance, C-H bonds along the rotor axis are always at the magic angle with the B_0 field, and therefore cross polarize slowly. They also dephase slowly, so when they are taken out of the ensemble by short CP, the total dephasing will be faster. Secondly, due to the low ^{1}H density in the aromatic regions, H-H dipolar couplings are too weak to dampen out the oscillation of the dephasing curve. The dephasing of the observed nonprotonated-carbon signals is also faster. At the zero crossing of the CH carbons, the nonprotonated-carbon intensity is reduced by a factor of ~1.3. This scaling factor of the dipolar dephased spectrum, applied before the subtraction from the spectrum without dephasing, is fine-tuned to remove the residual diagonal ridge completely.

In order to avoid sideband artifacts arising from spatially asymmetric modulation of the magnetization by the dipolar dephasing before detection, we applied two-step γ-averaging to it. This involved shifting the position of the gated decoupling and the 180° recoupling pulse on ^{1}H by $t_r/2$ in the rotation period after the mixing time and adding the resulting signals. In order to avoid timing problems, the periods before and after the 180°-pulse for the Hahn echo before detection were each extended to $\tau = 2\ t_r$.

Identification of the specific bonding environment. In EXPANSE NMR, the CH and $C_{nonprot}$ spectral editing, combined with chemical-shift information in the two spectral dimensions, identifies the immediate bonding environment of the two coupled aromatic carbons unambiguously: One carbon, whose signal is shown in ω_1, is bonded to hydrogen and two aromatic carbons if it resonates below 137 ppm; if the ppm value is higher, the carbon must have bonds to H, O, and aromatic C. The other carbon, detected in ω_2, is not protonated and thus bonded to three carbons, or to two C and one O, if it resonates below or above 137 ppm, respectively.

Similarly, in the dipolar dephased DQ/SQ spectrum, a chemical shift above 142 ppm can be assigned to nonprotonated C-O, below 130 ppm to nonprotonated C-C-O (two bonds from O), and signals between 127 and 142 ppm signal to nonprotonated arene C. Thus, the first and most of the second shell of bonded carbons around the carbons observed can be uniquely identified in these spectrally edited 2D experiments.

Generally, any connection between aromatic rings gives a pair of signals in the dipolar-dephased DQ/SQ, since the two linked aromatic carbons cannot be protonated (the other two of their three bonding partners must be in their respective aromatic ring). This includes the signals of bridgehead carbons of fused aromatic rings, which will be prominent on the diagonal near 130 ppm.

Absence of the diagonal ridge. Both 2D techniques presented here provide spectra without the diagonal ridge typically observed in 2D exchange NMR. In DQ/SQ NMR, a diagonal ridge is always absent [26]. In EXPANSE NMR, the mutually exclusive spectral editing before evolution and before detection eliminates the diagonal ridge for aromatic carbons, since diagonal signals of protonated carbons are suppressed before detection and those of nonprotonated carbons before evolution; only magnetization that starts out on a protonated carbon and ends up on a nonprotonated one survives the double spectral editing. The diagonal ridge “survives”, with greatly reduced intensity, only for CH_3 groups, which combine features of CH groups (they contain protonated C) with those of nonprotonated carbons (their signal is not fully eliminated by dipolar dephasing, due to partial motional averaging of the C-H dipolar couplings by the rotational jumps around the C_3 axis).

The suppression of the diagonal ridge has various advantages. For instance, the associated sideband and cut-off artifacts are eliminated and as a result, the EXPANSE experiment can be performed with short spin-exchange time, to obtain cross peaks mostly for directly bonded carbons (one-bond couplings). Removal of the diagonal ridge also permits a reduction of the number of t_1 slices needed, with a resulting reduction in the measuring time required. Even more importantly, cross peaks near or even on the diagonal (from nonprotonated C resonating at the same frequency as the CH to which it is bonded) can be observed without overlap from the diagonal ridge.

Comparison of EXPANSE with DQ/SQ NMR. The absence of a trivial diagonal ridge is a favorable feature that EXPANSE shares with DQ/SQ NMR. Otherwise, the signals observed in the EXPANSE spectrum and in the dipolar-dephased DQ/SQ spectrum are fully complementary (except those involving CH_3 groups): In EXPANSE NMR, only CH_n-group signals are observed in ω_1, while all CH_n-signals are completely suppressed in dipolar-dephased DQ/SQ NMR.

While the DQ/SQ experiment can probe structure only on the scale of one or two bonds, proximities on the 1-nm scale can detected in EXPANSE NMR simply by extending the mixing time in the experiment. Furthermore, the EXPANSE spectrum can provide information that is not accessible by double-quantum NMR. Consider, for instance, two protonated–nonprotonated carbon pairs resonating at (ω_A and ω_B) and (ω_B and ω_A), i.e. with complete overlap of the signals, which makes it challenging to separate them. In the dipolar dephased DQ/SQ NMR spectrum, no signal would be observed for either pair, while in a double-quantum experiment with dipolar dephasing only before detection, this combination gives the same pair of signals at ($\omega_A+\omega_B$, ω_A) and ($\omega_A+\omega_B$, ω_B). In the EXPANSE spectrum, cross peaks at (ω_B, ω_A) and (ω_A, ω_B) identify the two pairs of carbons uniquely (while the combination of two nonprotonated or two protonated carbons resonating at ω_A and ω_B gives no signal).

Experimental Section

Materials.

Uniformly ^{13}C-enriched glucose and ^{15}N-enriched glycine were purchased from Cambridge Isotopes.

Pyrolyzed carbon preparation. One to two grams of uniformly ^{13}C-enriched glucose was loaded into a horizontal tube furnace purged with nitrogen gas (99.995% purity, purchased from Airgas) flowing at about 1 L/min for one hour prior to heating and heated to 350°C with a heating rate of 10°C/min and held at the temperature for 1 hour. To ensure uniform heat transfer and homogeneity, the materials were cooled and ground into a fine powder with a mortar and pestle. This material was then subjected to additional reaction for 9 hours using the same nitrogen flow rate and heating program.

Sulfonation of glucose and carbon materials by fuming sulfuric acid. Glucose also dehydrates in concentrated sulfuric acid to a char similar in appearance to pyrolytic carbons. In previous literature, this direct dehydration provided high sulfur incorporation [4].

Fuming sulfuric acid was prepared by addition of sulfur trioxide to neat sulfuric acid, immediately prior to the sulfonation reactions. Sulfonation was carried out by addition of either uniformly ^{13}C-enriched glucose (“DirfumS”) or the ^{13}C-enriched 350°C carbon (“Pyr350fumS”) into an Erlenmeyer flask with about 150 mL of 30% fuming sulfuric acid and heated to 150°C for 2 hours. The resulting black solid was then washed and filtered (4.5-5 µm Buchner funnel) with ~2-3 L of DI water until the solution was clear, colorless, and of neutral pH, and no sulfate ions were detected with barium chloride. The final material was dried overnight in an oven at 100 ºC. The C : H : O : S elemental compositions of the DirfumS and Pyr350fumS materials were 54 : 3 : 39: 3.5 and 61 : 3 : 32 : 3, respectively.

Melanoidin synthesis. The melanoidins were synthesized using standard procedures as described in ref.[13]. The first melanoidin was obtained by heating uniformly ^{13}C-enriched D-glucose and ^{15}N-labeled glycine in equimolar ratio in a sealed pH 8.5 buffer solution at 100°C for a week. The pH was maintained at 8.5 and the reaction continued for an additional five days. This solution-phase melanoidin is termed Mel1:1. A dry-reaction melanoidin (Mel9:1) was synthesized by dissolving glucose and glycine in 9:1 molar ratio in water and co-precipitation by freeze-drying. The precipitate was then heated in an oven at 125°C for 2 hours. Both materials were filtered, dialyzed and freeze-dried prior to the NMR experiments.

NMR parameters. The NMR experiments were performed on a Bruker Avance 400 spectrometer at a 100 MHz ^{13}C resonance frequency, using a 4-mm double-resonance probehead. The 2D spectra were measured at 14 kHz, where spinning sidebands are fairly small and have little overlap with centerbands. ^{13}C and ^{1}H 90^{o} pulse lengths were 4.2 µs, and the ^{1}H decoupling field strength was $\gamma B_1/(2\pi) = 70$ kHz. The recycle delay in most experiments presented was 0.8 – 1 s. One-dimensional 1-ms cross-polarization spectra were recorded at 7.8 kHz and 4 kHz with total suppression of spinning sidebands (TOSS) [36]. The regular two-dimensional DARR spin-exchange, the EXPANSE, and the dipolar-dephased DQ/SQ spectra were all recorded with a spinning frequency of ν_r = 14 kHz. The mixing time in the EXPANSE experiments was 10 ms, while the DQ excitation and reconversion in the DQ/SQ experiments consisted of two periods of SPC5 homonuclear recoupling of 4 t_r = 286 μs duration each. The evolution time was incremented by $t_r/2$ = 35.71 μs in EXPANSE and $t_r/4$ = 14.28 μs in DQ/SQ experiments, and reached a maximum of 0.9 ms and 1 ms, respectively. Other parameters of the new 2D experiments are given under “Technical Aspects”.

Chemical-shift calculations. The chemical shifts shown in Scheme 1 and Table 1 were calculated using the commercially available, empirically based ACD chemical-shift predictors. The complete molecules used to generate the chemical shifts given in Scheme 1 are shown in Scheme S1 in the Supplementary Material, and represent structures that are likely to be found in the materials studied given the functional groups and their connectivities determined in the 2D NMR spectra. Table 1 was produced by systematically varying the substituents bonded to ketones, including methyl, ethyl, arene, phenol, pyrrole Cα / Cβ, and furan Cα / Cβ. The complete set of simulated structures is shown in Scheme S2. The chemical shifts for the carboxylic acids were simulated for structures, shown in Scheme S3, that are found in our structural models of the sulfonated carbon materials. Additionally, experimental chemical shift values were looked up in the SDBS database for organic compounds [42], and were found to be in good agreement with the trends from the ACD chemical shift simulator.

Results

Sulfuric-acid carbonized glucose. Figures 5 and 6 show spectrally-edited 2D ^{13}C-^{13}C correlation spectra of two carbon materials produced by sulfuric-acid treatment, of ^{13}C-enriched glucose and of char produced from ^{13}C-glucose by pyrolysis at 350°C; the materials are termed DirfumS and Pyr350fumS, respectively. The spectral patterns show some similarities, in particular pronounced $C\alpha$–$C\beta$ cross peaks at (150 ppm, 120 ppm) with both types of spectral editing. These signals in the EXPANSE spectra must be assigned to $HC\beta$-$C\alpha_{nonp}$-O of furan or phenol, while those in the dipolar-dephased DQ/SQ spectra are from $C\alpha_{nonp}$-$C\beta_{nonp}$. Signals of O-$C\alpha_{nonp}$-$C\alpha_{nonp}$-O linkages around (148 ppm, 148 ppm) are less pronounced. This may be due to the fact that $C\beta_{nonp}$-$C\alpha_{nonp}$-O can occur both intra- and intermolecularly, while O-$C\alpha_{nonp}$-$C\alpha_{nonp}$-O can occur only between furan rings. A short, broad ridge in the EXPANSE spectrum ending at (109 ppm, 120 ppm) in Fig. 5 can be assigned to furan $HC\beta$–$C\beta_{nonp}$.

The EXPANSE spectra in Figs. 5 and 6 display a distinct ridge near (115 ppm, 180 ppm), which is assigned to two-bond $H\underline{C}\beta$-C-$\underline{C}$=O correlations, i.e. ketones linked to the furan rings. The same signal is also detected in the dipolar-dephased DQ/SQ spectrum, as is signal of furan-linked COO at ~162 ppm producing a pronounced shoulder around (125 ppm, 162 ppm) in the dipolar-dephased DQ/SQ spectrum. The COO peaks can also be verified in the one-dimensional slow-MAS TOSS spectra of Fig. 1, where the otherwise dominant aromatic signals have been greatly reduced. For the DirfumS sample, the EXPANSE spectrum also shows characteristic intensity near (150 ppm, 125 ppm). This intensity can be assigned with certainty to furan $HC\alpha$-$C\beta_{nonp}$, since aromatic C-H resonating at >145 ppm is impossible in arene rings, but normal for furan with a protonated α-carbon.

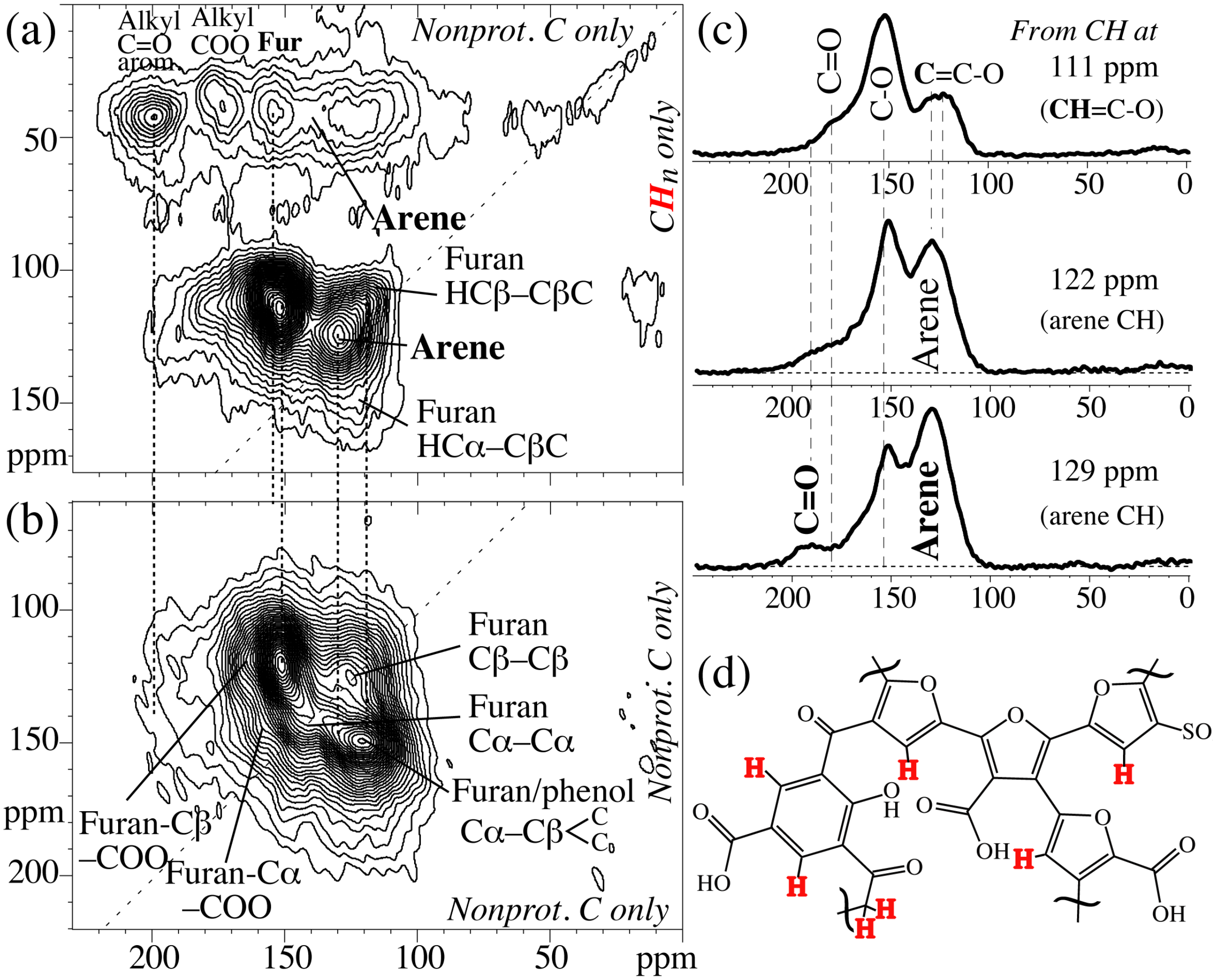

Figure 5. (a) EXPANSE spectrum with 10-ms spin-diffusion time, and (b) sheared dipolar-dephased DQ/SQ NMR spectrum of ^{13}C-labeled glucose carbonized by treatment with fuming sulfuric acid (DirfumS). The diagonal in the spectra (at $\omega_2 = \omega_1$) is indicated by a dashed line. Many of the cross peaks clearly seen in these spectra could not be observed in the corresponding unselective 2D spectrum of Fig. 2a. (c) Horizontal cross sections from the spectrum in (a) at CH chemical shifts of 111, 122, and 129 ppm. Note that the arene peak observed in the 122- and 129-ppm cross sections is completely obscured by the furan signals in the unselective spectra of Figs. 1a and 2a. (d) Partial structural model indicating some of the furan and arene rings and their connectivities deduced from the spectra in (a) and (b).

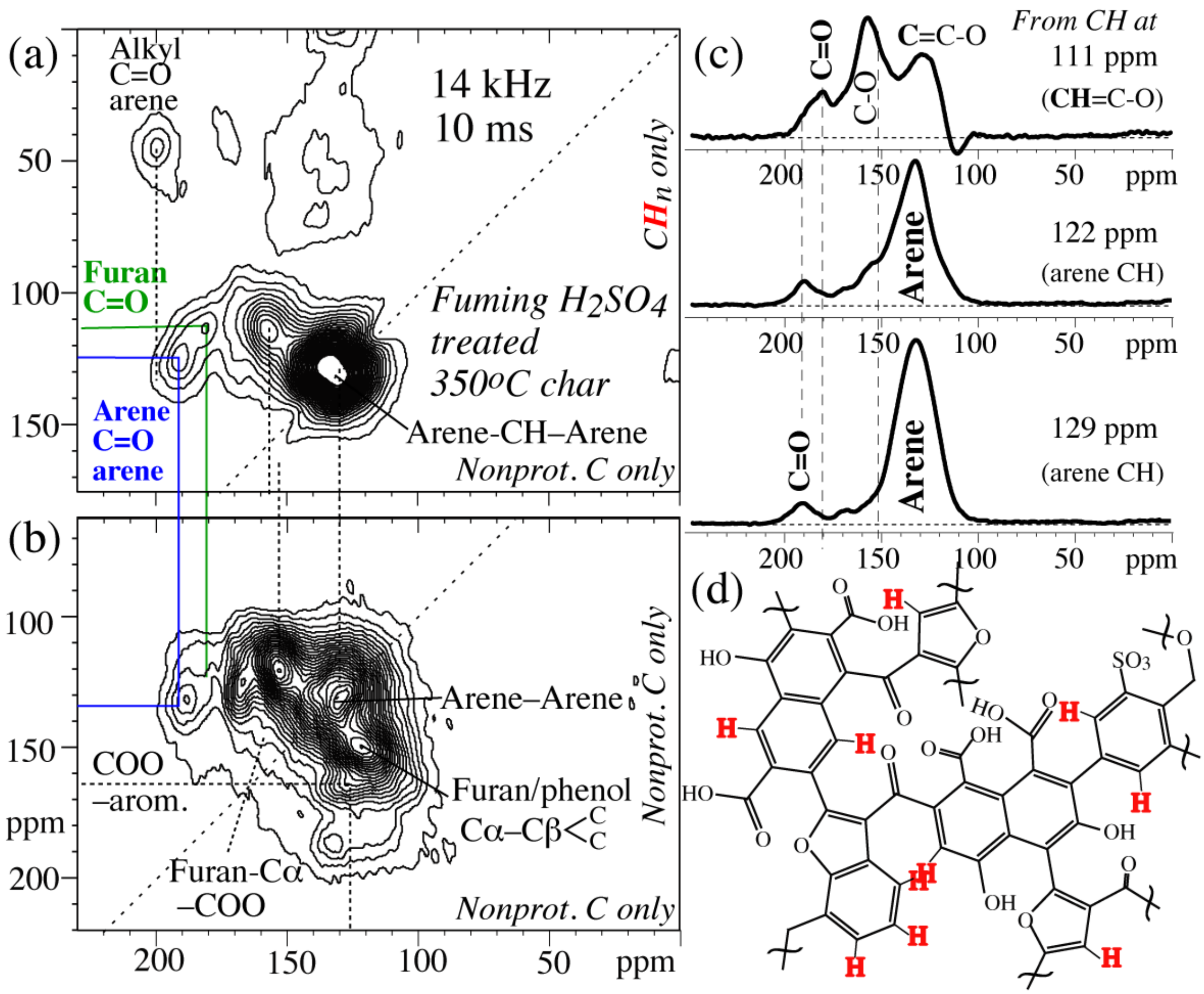

Figure 6. (a) EXPANSE (t_m = 10 ms) and (b) sheared dipolar-dephased DQ/SQ NMR spectra of ^{13}C-labeled glucose carbonized by pyrolysis at 350°C and treatment with fuming sulfuric acid (Pyr350fumS). In (b), note the absence of a strong peak near the diagonal at 130 ppm from pairs of nonprotonated arene carbons, which would be found in fused aromatic clusters (while the arene HC-C_{nonp} signal is prominent in a). (c) Horizontal cross sections from the spectrum in (a) at CH chemical shifts of 111, 122, and 129 ppm. (d) Partial structural model indicating some of the arene and furan rings and their connectivities deduced from the spectra in (a) and (b).

Both samples show characteristic arene peaks around (125 ppm, 130 ppm) in the EXPANSE spectrum. The relatively low chemical shift of 130 ppm of the nonprotonated arenes indicates substitution by COO, rather than alkyl or arene, which gives ~140-ppm chemical shifts. The expected cross peaks between COO resonating near 164 ppm and aromatic (arene and furan-

Cβ) carbons between 120 and 130 ppm are clearly observed in the dipolar dephased DQ/SQ spectra. It may also be due to fused rings such as benzofuran or naphthalene, see Scheme 1. Compared to Pyr350fumS, DirfumS shows a smaller arene carbon fraction.

The alkyl CH_n carbons (ω_1 = 30 – 60 ppm) in the EXPANSE spectrum of the DirfumS sample show various clear cross peaks. Ketone C=O bonded to alkyl CH_n is detected at 200 ppm; this low C=O chemical shift indicates linking of the ketone to an aromatic carbon. Furan Cα (155 ppm) and Cβ (115 – 125 ppm) bonded to alkyl CH_n is also prominent, while arene (140 ppm) bonded to alkyl CH_n is not abundant enough to produce a local maximum. Finally, COO (180 ppm) bonded to alkyl CH_n is also observed. Overall, comparison of the 2D spectra in Figs. 2 and 5/6 shows that EXPANSE and dipolar-dephased DQ/SQ spectra exhibit many cross peaks that are invisible in the unselective 2D spectra.

Melanoidins. Figures 7 and 8 show the EXPANSE and dipolar-dephased DQ/SQ spectra of two different melanoidins, one made in the solid state with moderate glycine concentration (9:1 glucose:glycine), the other in solution with a 1:1 glucose:glycine molar ratio. They exhibit cross peak patterns that are dramatically different from each other and from those of the sulfuric-acid treated glucose-based materials, both for the aromatic and alkyl regions.

The 9:1 solid-state melanoidin, Mel9:1, provides a clear example of a material with furan rings that are predominantly substituted or linked via Cα, mostly by alkyl groups: Cα at ~152 ppm is mostly not protonated and shows a pronounced cross peak with various alkyl carbons, see Fig. 7a. In the EXPANSE spectrum, the signal near (109 ppm, 120 ppm) from nonprotonated Cβ next to protonated Cβ is much weaker than in the sulfuric-acid treated carbon materials, confirming that most Cβ in this melanoidin are protonated and do not contribute much to the linkage of the furan rings.

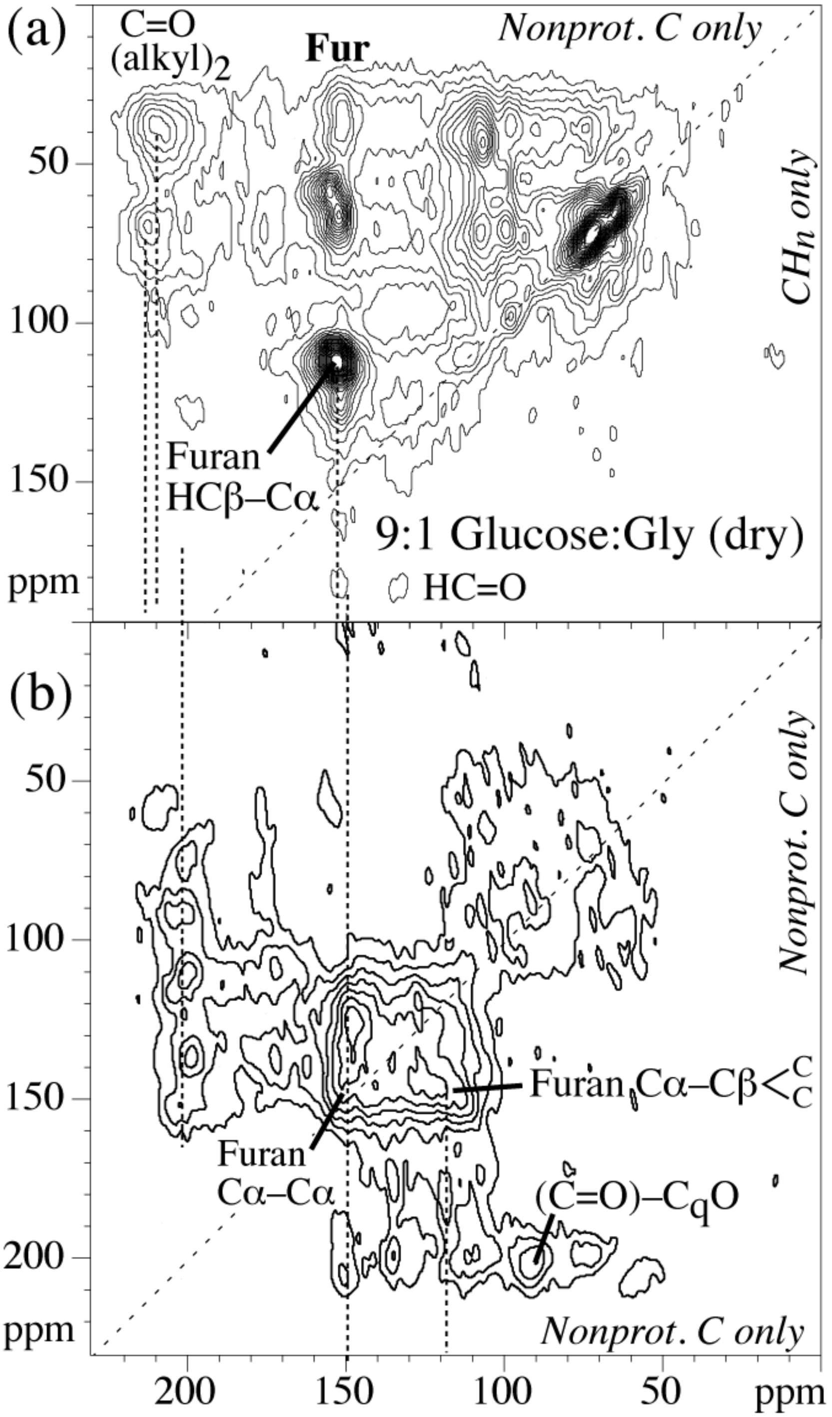

Figure 7. (a) EXPANSE (t_m = 10 ms) and (b) sheared dipolar-dephased DQ/SQ NMR spectrum of a high-molecular weight melanoidin made from glycine and ^{13}C-enriched glucose in 9:1 molar ratio at 125°C by dry reaction of coprecipitated powder (Mel9:1). Signals characteristic of furans (alkyl C bonded to aromatic C-O, labeled “Fur”) are clearly detected. The low spectral intensity in (b) can be attributed to the low abundance of directly bonded nonprotonated carbons in this material.

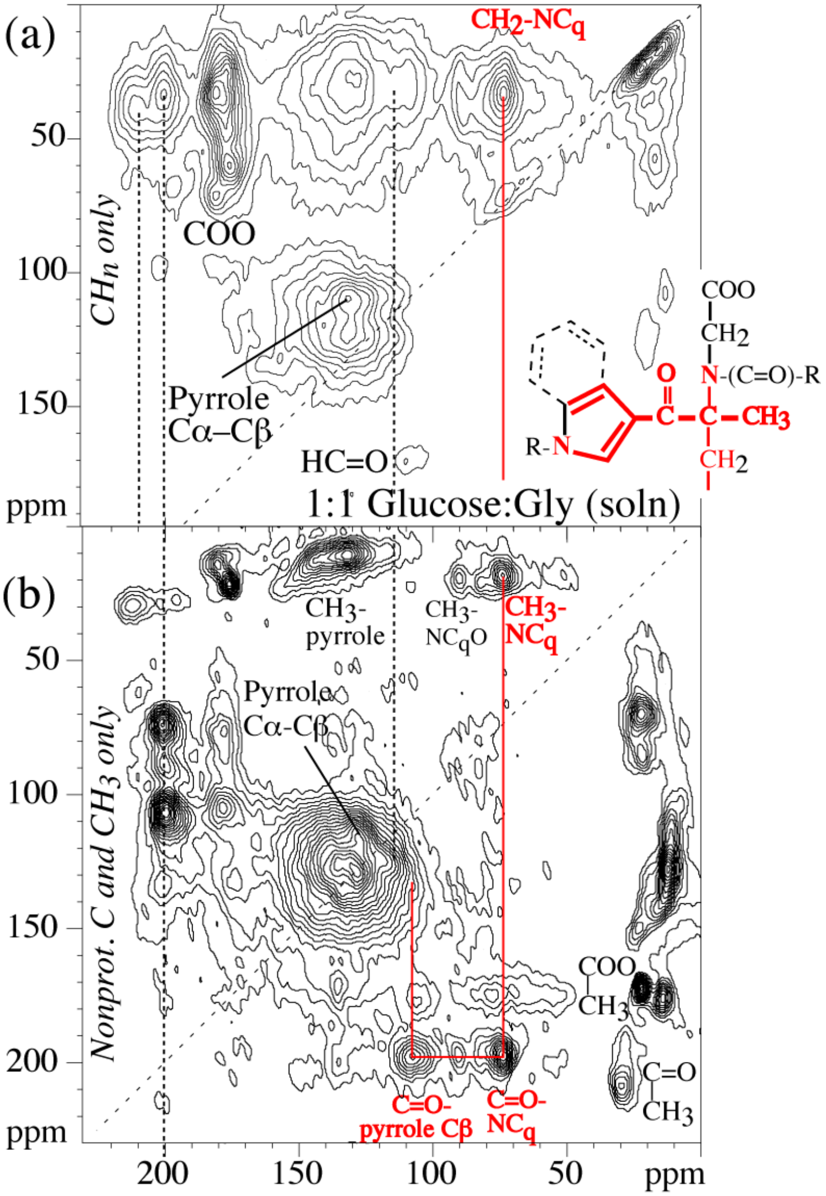

Figure 8. (a) EXPANSE (t_m = 10 ms) and (b) sheared dipolar-dephased DQ/SQ NMR spectrum of a high-molecular weight melanoidin made from glycine and ^{13}C-enriched glucose in 1:1 molar ratio in solution at 99^{o}C (Mel1:1). Sharp peaks from a sequence of carbons in a specific structural fragment (see proposed structure in (a) and in the Supplementary Material) are connected by a continuous red line.

The dipolar-dephased DQ/SQ spectrum, Fig. 7b, is of fairly low intensity since bonded nonprotonated carbons are relatively rare in this material: Its nonprotonated furan Cα is mostly bonded to protonated Cβ and to protonated alkyl C, while the nonprotonated C=O is mostly bonded to protonated alkyl C, and COO is rare (see Fig. 1f). Weak signals of furan Cα-Cα and, less clearly, Cβ-Cβ linkages are observed near the diagonal at 150 and 120 ppm, respectively, and nonprotonated Cα-Cβ cross peaks are also less pronounced than for the sulfuric-acid treated carbon materials. Arene signals, which were clearly identified in the EXPANSE spectra of the sulfuric-acid treated carbon materials, are of low intensity in this melanoidin.

Further, the series of cross peaks near 70 ppm in the EXPANSE spectrum shows that these signals are not from separate regions with incompletely pyrolyzed glucose, but are structurally integrated with the furan and C=O groups. The same can be said of the other alkyl segments, which also show a variety of cross peaks.

For the solution melanoidin, Mel1:1, the characteristic signals of Cα-substituted furan observed in the EXPANSE spectra of all the other materials are very weak. Instead, Fig. 8a shows a broad signal around (111 ppm, 135 ppm) that is indicative of Cα-substituted pyrroles. In the dipolar dephased DQ/SQ spectrum, Fig. 8b, a pronounced signal at (120 ppm, 130 ppm) can be assigned to pyrrole Cα-Cβ. Given that both carbons involved must be nonprotonated, this suggests significant substitution on both Cα and Cβ. By comparison, the (120 ppm, 120 ppm) near-diagonal ridge from Cβ-Cβ linkages is less pronounced. The 2D spectra show broad peaks near 123 ppm, which may be a superposition of arene and pyrrole signals. While the signal at (125 ppm, 132 ppm) is characteristic of arene rings in N-free carbon materials, in melanoidins and other N-rich systems imidazolium carbons are found to resonate in this range [13]. This ambiguity can be eliminated using $^{13}C\{^{15}N\}$ recoupled dipolar dephasing [13], see Fig. S1b, which indicates that N-containing aromatic rings are more common than arene rings.

In the dipolar dephased DQ/SQ spectrum of this melanoidin, Fig. 8b, the signals of various C=O/COO/NC=O carbons and CH_3 groups stand out (while the solution melanoidin showed hardly any CH_3 peaks). The former are mostly bonded to various alkyl CH_n, the latter to pyrrole Cα and Cβ, C=O (e.g. in acetyl or N-acetyl groups), and nonprotonated alkyl carbons. The CH_3 groups and some of the COO moieties are end groups, but the effect on connectivity is balanced by nonprotonated alkyl C (see dipolar dephased spectrum in Fig.1e, and region with $\omega_2 < 110$ ppm in Fig. 8a), which are bonded to two to four C and thus act as crosslink points. A specific structural fragment identified based on three relatively sharp cross peaks is discussed below.

Discussion

In the following, we will discuss the signals characteristic of various aromatic rings in our new spectrally edited 2D correlation spectra. We start with a discussion of the resonance positions of ketones, which we find to be excellent indicators of their bonding partners, such as arene, furan, or alkyl groups.

Bonding of ketones and COO. The edited ^{13}C-^{13}C correlation spectra reveal a variety of signals from ketones (C=O groups), whose two bonding partners can be identified from the cross peak frequencies. Their first bonding partner is specified directly by the alkyl or aromatic-carbon frequency of the cross peak, and then the second bonding partner can be identified based on the ketone chemical shift. Chemical shift databases show that ketones can resonate over a wide frequency range, between 212 and 165 ppm, depending on the bonding partners (see Scheme S2). The data compiled in Table 1 demonstrate that the ketone chemical shift is decreased most by bonding to furan Cα, then Cβ, and much less by bonding to arenes/phenols. The same trend is observed for COO groups (see Scheme S3 and the last row of Table 1), but the total shift range is smaller since COO groups have only a single bonding partner. On the basis of Table 1, COO and C=O signals, whose chemical shift ranges overlap near 180 ppm, can be correctly assigned when a cross peak specifies one bonding partner; some examples are given in the following.

Table 1: Chemical shifts (in ppm) of ketones R_1-(C=O)-R_2 for different substituents R_1 and R_2, as well as COOH (fixed R_2 = OH), from empirical chemical-shift predictions (ACD/NMR predictors); the chemical structures used are shown in Scheme S2 in the Supplementary Material. The average chemical shift change in ppm induced by each substituent (relative to ethyl) is also given. Secondary substituents (on R_1 and R_2) vary the C=O chemical shifts by approximately ± 5 ppm.

Substituent R_1 R_2	Ethyl	Methyl (-3)	Phenol (o-) (-3)	Arene (-9)	Pyrrole Cβ (-13)	Furan Cβ (-15)	Pyrrole Cα (-17)	Furan Cα (-20)
Ethyl	**212**	207	206	200	196	195	193	189
Methyl (-3)	**207**	**206**	203	198	193	192	189	185
Phenol (o-; -3)	**206**	**203**	**200**	201	193	195	188	186
Arene (-9)	**200**	**198**	**201**	**197**	190	188	185	182
Pyrrole β (-13)	**196**	**193**	**193**	**190**	**184**	183	180	178
Furan β (-15)	**195**	**192**	**195**	**188**	**183**	**176**	180	175
Pyrrole α (-17)	**193**	**189**	**188**	**185**	**180**	**180**	**174**	**174**
Furan α (-20)	**189**	**185**	**186**	**182**	**178**	**175**	**174**	**165**

R_2 = OH (-30) (i.e., COOH)	**181**	**178** acetic acid	**171**	**168**	**166**	**165**	**163**	**163**

The EXPANSE spectra of the melanoidins in Figs. 8 and 9 show signals of C=O at 210 ppm bonded to an alkyl C at 40 ppm; the high ppm value of the ketone requires another alkyl C as the second bonding partner, according to Table 1. Ketones resonating at 200 ppm and showing a cross peak to an alkyl C at 34 ppm in Fig. 8 must be bonded to an aromatic, and most likely arene, carbon (see Table 1); the corresponding cross peak at (200 ppm, 134 ppm) is indeed observed in the DQ/SQ spectrum.

The spectra of the sulfuric-acid treated materials exhibit ketone signals at < 200 ppm, as expected due to their predominantly aromatic structure. A cross peak near 180 ppm to any aromatic chemical shift (between 155 and 100 ppm) must be assigned to a C=O group, since COO bonded to aromatics resonates at < 169 ppm (Table 1). Pyr350fumS shows pronounced ridges ending at (125 ppm, 190 ppm) and (135 ppm, 190 ppm) in the EXPANSE and DQ/SQ spectra, respectively. Based on the 135-ppm chemical shift, which is very rare in furans, it must be assigned to C=O bonded to arene C. According to Table 1, the 190-ppm C=O frequency indicates that the other bonding partner must be an aromatic C, most likely a furan Cβ, which is consistent with the furan-rich sample composition. Consistently, the DQ/SQ spectrum shows intensity at (~120 ppm, 190 ppm).

Overall, the analysis presented here demonstrates that ketones can serve as excellent indicators of their environment, and can identify arenes in particular. This can be exploited even without isotopic enrichment, since the ketone peak positions can also be determined in one-dimensional spectra of ^{13}C in natural abundance.

Signals characteristic of arenes. The EXPANSE spectra of Pyr350fumS and DirfumS show several signals characteristic of arenes. The most telling are (i) the cross peak between CH at ~123 ppm and nonprotonated C at 131 ppm; and (ii) the cross peak between alkyl C (<90 ppm) and arene, specifically near 140 ppm, which is the resonance position of a nonprotonated arene carbon with a single bond to a substituent.

The C=O signals in the EXPANSE spectra also provide evidence of arenes (in the nitrogen-free materials). They show alkyl–C=O cross peaks at (40 ppm, 200 ppm). The C=O resonance frequency indicates that the other substituent of the C=O are most likely arenes, since Table 1 shows that C=O bonded to furan usually resonates at ≤ 195 ppm and alkyl-C=O-alkyl at ≥ 205 ppm. Confirming this analysis, the (40 ppm, 200 ppm) cross peak is seen particularly clearly in the sulfonated 350°C carbon, Fig. 6a, where arenes are known to be the major species. The spectrum of the DirfumS sample, Fig. 5a, also exhibits this cross peak, and no peak near (40 ppm, 190 ppm), indicating that ketones link alkyl groups mostly to arenes and not furans. The (40 ppm, 180 ppm) cross peak in the EXPANSE spectrum must be from C=O linking furan and another aromatic ring. It cannot be assigned to alkyl–C=O–furan, since Table 1 shows that the C=O chemical shift would be >185 ppm.

Cross peaks at (125 ppm, 190 ppm) in the EXPANSE and at (135 ppm, 190 ppm) in the DQ/SQ spectrum of the nitrogen-free materials, see Figs. 5 and 6, must be assigned to C=O bonded to an arene ring, based directly on the arene chemical shift in ω_1. With ω_2 = 190 ppm, according to Table 1 the second bonding partner is arene or furan Cβ; note that the peak in EXPANSE must be from a two-bond correlation, since aromatic CH cannot be directly bonded to C=O.

The dipolar-dephased DQ/SQ spectrum can provide some information about bonds *between* aromatic rings. A bond between two arene rings will result in signal near the diagonal around 140 ppm (while a Cα-Cα linkage of furans produces near-diagonal signal around 145 ppm). Generally, if two ring carbons of the same type are linked, the signals are close to the diagonal, where they would be impossible to observe in a simple spin-exchange spectrum without spectral editing.

Signals characteristic of fused aromatic rings. The abundant interior (bridgehead) carbons of graphene-like fused aromatic rings, which are not protonated and bonded to at least one, and often to three, similar nonprotonated bridgehead carbon, would produce a characteristic strong peak near (130 ppm, 130 ppm) in the dipolar-dephased DQ/SQ spectrum. Such a signal is not observed in any of the samples studied here. However, it dominates the spectrum of glucose pyrolyzed at 450°C (data not shown). Note that this peak on the spectral diagonal would be undetectable in a conventional 2D exchange spectrum due to the presence of the diagonal ridge and also due to strong overlap with the arene CH-$C_{nonprot}$ cross peak (seen prominently near the diagonal in the EXPANSE spectrum of Pyr350fumS, see Fig. 6a).

Signals characteristic of furans. The selective 2D correlation spectra contain several signals characteristic of furans and impossible or unlikely in phenols. The most telling signals are (i) the cross peaks between the aromatic C-O (~150 ppm) and alkyl C (<90 ppm); the corresponding linkage is impossible in a phenol, where the C-O carbon is always bonded to two aromatic C (see Scheme 1b). These furan signals can be seen very clearly in the EXPANSE spectra of DirfumS and Mel9:1, see Figs. 5a and 7a, and in the dipolar-dephased DQ/SQ spectra, Figs. 5b and 7b, for CH_3 groups (whose signals survive the dephasing due to motional averaging of the C-H dipolar coupling) in the same samples.

A second characteristic of furans is (ii) signal from two carbons bonded to one another that are each two bonds from oxygen, i.e. both resonate between 105 and 125 ppm. These occur automatically in every furan ring, namely the two Cβ carbons, while a very special arrangement of two phenols would be required to produce this constellation. If at least one of these Cβ carbons is not bonded to H (which is commonly only in DirfumS), signals from the Cβ pairs are observed near (111 ppm, 120 ppm) in the EXPANSE spectrum (if one Cβ is protonated), or at (120 ppm, 120 ppm) in the dipolar-dephased DQ/SQ spectrum (if both are not protonated), see Fig. 5.

Thirdly, C=O and COO groups bonded to furan Cα or Cβ show large shifts by ca. -10 to -15 ppm relative to those in phenols or other arenes, see Table 1. Thus, when bonded to furans, COO groups can resonate between 160 and 165 ppm, and C=O groups between 165 and 195 ppm. Indeed, Figs. 1c and 5b show indications of COO signals below 165 ppm. The signals observed near (112 ppm, 180 ppm) in the EXPANSE spectrum, particularly clearly in Figs. 6a and 6c, must be attributed to C=O bonded to furan (since C=O bonded to phenols has no signals in this range, see Table 1). We can also conclude that these C=O groups cannot be bonded to an alkyl carbon, since they would then resonate between 185 and 200 ppm (see Table 1). This is indeed correct, since this sample is almost free of alkyl components.

Signals characteristic of phenols. A cross peak of the Cγ carbons in a phenol, which would usually resonate between 130 and 140 ppm, with a Cβ resonance between 105 and 125 ppm, would be characteristic of phenol. Since every phenol has two β and two γ carbons, this signal should be quite pronounced if phenols were significantly present. Our spectra do not show prominent peaks of this kind, although some may be hidden by other, stronger signals.

Bonding of functional groups to phenol Cα is not possible, and C=O or COO groups bonded to phenol Cβ resonate at relatively "normal" chemical shifts of ~200 ppm or ~168 ppm, respectively. Since the substituted phenol Cβ and the C=O(O) carbons are both not bonded to H, their signal would be observed in the dipolar-dephased DQ/SQ spectrum at (120 ppm, 200 ppm) or (120 ppm, 168 ppm). Such signals are not seen prominently in our spectra.

Another characteristic of phenols is the arene O-H proton signal near 8 ppm, which is not dephased in MELODI-filtered ^{1}H-^{13}C correlation experiments [40] (not shown here). None of the samples studied here showed a pronounced phenol OH signal.

Identification of differently linked furans. The EXPANSE and dipolar-dephased DQ/SQ spectra can identify whether the furans are predominantly substituted on Cα, Cβ, or both, since they probe the protonation of these carbons. For instance, the signals at ω_1 = 111 ppm in the EXPANSE spectra of DirfumS and Mel9:1, see Figs. 5a and 7a, can both be attributed to Cβ-H in furan, but the different cross peak intensity near 120 ppm indicates a structural difference.

According to our experimental design, this 120-ppm band, which is strong for the DirfumS material, see Fig. 5c, must be due to a nonprotonated carbon. This rules out arene CH and leaves only nonprotonated aromatic C separated from oxygen or nitrogen by two bonds. Such a carbon will be found naturally as the second β-carbon in a furan ring next to the Cβ-H resonating near 111 ppm, which was selected in the ω_1 dimension by our experimental design, see Figure 4. This second β-carbon, being nonprotonated, must be bonded to another carbon outside the furan ring. In the spectrum of the Mel9:1 sample, Fig. 7a, the 120-ppm signal is not pronounced, which tells us that the β-carbons in these furan rings are mostly protonated and therefore do not show up in the ω_2 dimension of our EXPANSE spectrum. This matches the absence of a strong peak of nonprotonated Cα-Cβ pairs in the dipolar dephased DQ/SQ spectrum, as well as our previous observations [14] and the accepted picture that the furan rings in melanoidins are linked to other units mostly via their α-carbons. By contrast, spectral features such as the strong nonprotonated Cβ–Cα cross peak in Fig. 5b show that many of the β-carbons in the furan rings of sulfuric-acid treated glucose (DirfumS) are not bonded to H.

When Cα is bonded to H but Cβ is not, a cross peak will be observed at (145 ppm, 120 ppm) in the EXPANSE spectrum. A broad signal of this kind is indeed observed for the DirfumS sample, see Fig. 5a. An intermolecular Cβ-Cβ linkage will always give a signal near the diagonal around 120 ppm in the dipolar dephased DQ/SQ spectrum; intramolecular Cβ-Cβ cross peaks have been discussed above.

Nonprotonated O-Cα-Cβ. Peaks of nonprotonated O-Cα–Cβ pairs at (150 ppm, 120 ppm) dominate the dipolar-dephased DQ/SQ spectra of the sulfuric-acid treated carbon materials, Figs. 5b and 6b. Without the spectral editing, these signals would be trivial, since O-Cα is always bonded to Cβ, while the information that both carbons are not protonated reveals a valuable structural insight. In the spectra of the melanoidins, Figs. 7b and 8b, this signal is weak, confirming [14] that furan with nonprotonated Cβ is rare in these materials.

Structure of sulfuric-acid carbonized glucose and 350°C carbon. The cross peaks discussed provide fairly comprehensive structural pictures of DirfumS and Pyr350fumS; resulting simple structural models are shown in Figs. 5d and 6d, respectively. The DirfumS material consists mostly of a network of furan rings heavily substituted on both Cα and Cβ, by other furan rings or by COO and C=O groups. Alkyl segments and arene rings have also been detected unambiguously, but represent only relatively minor components in this material. The Pyr350fumS material consists of single and double aromatic rings, mostly arene but also some furan, again with direct and C=O linkages as well as COO substitution. Large clusters of fused aromatic rings are rare.

Characteristic structural fragment in solution melanoidin. In our previous studies [13, 14], the structure of the melanoidin from solution reaction appeared to be particularly complex and unsuitable for a detailed analysis. However, the dipolar dephased DQ/SQ spectrum in Fig. 8b shows a series of relatively sharp peaks (connected by red lines) that reveal a distinct structural fragment accounting for most of the ketones and a significant fraction of all carbons in this material. We start the analysis with the two peaks at 72 ppm. They are due to a nonprotonated alkyl carbon that is bonded to CH_3 (top cross peak at 15 ppm) and to C=O (bottom cross peak at 200 ppm). The remaining carbon substituent of the 72-ppm C is protonated and therefore observed in the EXPANSE spectrum in Fig. 8a, where it is seen to resonate at 32 ppm, which is quite characteristic of methylene groups [14]. The nonprotonated alkyl carbon is bonded to nitrogen (i.e. it is NC_q) as proved by previous $^{13}C\{^{15}N\}$ dipolar dephasing (see Fig. S1b) and consistent with the chemical shift (while OC_q would resonate at >80 ppm; such a signal is also observed, at lower intensity). Thus, we have identified all four bonding partners of the NC_q carbon: CH_3, C=O, CH_2, and N.

While the CH_3 groups cannot have a second carbon bonded, the 200-ppm C=O group must have one. That carbon resonates at 107 ppm, as evidenced by a sharp cross peak in Fig. 8b. We assign it to the β-carbon of a pyrrole or related heterocycle (most likely indole) based on several arguments: Spectral editing showed little nonprotonated alkyl carbon signal at 107 ppm (see Fig. S1d); in addition, the chemical shift of a ketone bonded to two alkyl carbons would be >205 ppm, not the observed 200 ppm (see Table 1). Furans, whose β-carbons could also resonate around 115 ppm, are not common in this material, as evidenced by the absence of their characteristic cross peaks at 150 and ~115 ppm in the spectra of Fig. 8. The low (107 ppm) chemical shift value suggests possibly a second heteroatom in the aromatic ring, or a fused arene ring forming an indole structure, which consistently results in a very low chemical shift of the β-carbon of interest here [25], similarly as for the corresponding carbon in benzofuran, see Scheme 1c. Overall, the seven carbons (CH_3, CH_2, NC_q, C=O, and three pyrrolic) clearly identified account for ca. 15% of the total in this melanoidin.

A similar set of cross peaks was observed in a solution glucose-glycine melanoidin (termed nitrogen-containing hydrothermal carbon) prepared at 180°C for 12 hours by Baccile et al. [15]. For ease of comparison with the (unselective) DQ/SQ spectrum in Figure 5 of ref.[15], Fig. S1e shows the dipolar dephased DQ/SQ spectrum of our sample in the format of ref.[15], without shearing. However, the corresponding peaks in ref. [15] were assigned to a quite different, O-CH_2-(C=O)-C(OH,R')-COO, structure, with "R' = H, OH" (see Fig. S1a). Thus, the 72-ppm signal was assigned to O-CH_2, not NC_q, and the 107-ppm signal to alkyl $C(OH)_2$, not to aromatic Cβ of pyrrole.

Our spectral editing conclusively shows that O-CH_2-(C=O)-C(OH,R')-COO is not the structural fragment in our sample, and the spectral evidence in ref.[15] supports this conclusion for their sample also. The lack of dipolar dephasing in our spectra shows that the signal at 72 ppm is not from an OCH_2 group, but from a nonprotonated carbon; the absence of this signal from the short-CP spectrum shown in ref.[15] indicates that this is also true for the sample in ref.[15]: CH_2 signal would be strong under those conditions, while nonprotonated C is not. $^{13}C\{^{15}N\}$ REDOR [14] further shows that this nonprotonated carbon is bonded to N (see Fig. S1b), which explains its chemical shift well.

The proposed identification of the other bonding partner of the C=O group is also doubtful based on further spectral editing. In ref.[15], its 107-ppm signal was assigned to an sp^3-hybridized $C(OH)_2$ carbon, but chemical-shift anisotropy filtering [41] of both 1D and DQ/SQ spectra, see Figs. S1c- S1f, suppresses this signal, which means that it must be sp^2-hybridized.

This example highlights that cross peak positions alone are not sufficient for correct structural analysis of complex organic materials, and spectral editing is needed for correct structure determination.

Conclusions

We have presented two complementary methods for obtaining spectrally edited 2D ^{13}C-^{13}C spectra of ^{13}C-enriched carbon materials. Both require only moderate radio-frequency power and give spectra free of a diagonal ridge and the spectral artifacts associated with it. The spectra provide specifically correlations between two nonprotonated carbons, or one nonprotonated C and one CH, which combined with the two chemical-shift coordinates of the cross peak define the local bonding environment. We have pointed out cross peaks, including several near the diagonal and others involving ketones, that are characteristic of arenes, clusters of fused aromatic rings, and furans. Different substitutions or linkages of furan rings can also be distinguished. Our revision of a published structure proposed for a solution melanoidin based on unselective DQ/SQ NMR demonstrates the importance of spectral editing for correct structure determination.

Acknowledgments

This work was supported by the Center for Biorenewable Chemicals (CBiRC) funded by NSF grant EEC-0813570.

References

(1) M.-M. Titirici, M. Antonietti, N. Baccile, Hydrothermal carbon from biomass: a comparison of the local structure from poly- to monosaccharides and pentoses/hexoses, Green Chem., 10 (2008) 1204-1212.

(2) M. Antonietti, K. Müllen, Carbon: The Sixth Element, Adv. Mater., 22 (2010) 787-787.

(3) B. Hu, K. Wang, L. Wu, S.-H. Yu, M. Antonietti, M.-M. Titirici, Engineering Carbon Materials from the Hydrothermal Carbonization Process of Biomass, Adv. Mater., 22 (2010) 813-828.

(4) V. Mirkhani, M. Moghadam, S. Tangestaninejad, I. Mohammadpoor-Baltork, M. Mahdavi, Preparation of an improved sulfonated carbon-based solid acid as a novel, efficient, and reusable catalyst for chemoselective synthesis of 2-oxazolines and bis-oxazolines, Monatsh Chem, 140 (2009) 1489-1494.

(5) L. Zhao, L.-Z. Fan, M.-Q. Zhou, H. Guan, S. Qiao, M. Antonietti, M.-M. Titirici, Nitrogen-Containing Hydrothermal Carbons with Superior Performance in Supercapacitors, Adv. Mat., 22 (2010) 5202-5206.

(6) M.-M. Titirici, M. Antonietti, Chemistry and materials options of sustainable carbon materials made by hydrothermal carbonization, Chem. Soc. Rev., 39 (2010) 103-116.

(7) D.A. Laird, The charcoal vision: A win-win-win scenario for simultaneously producing bioenergy, permanently sequestering carbon, while improving soil and water quality, Agronomy J., 100 (2008) 178-181.

(8) C.E. Brewer, K. Schmidt-Rohr, J.A. Satrio, R.C. Brown, Characterization of biochar from fast pyrolysis and gasification systems, Environ. Progress Sustain. Energy, 28 (2009) 386-396.

(9) J.-D. Mao, R.L. Johnson, J. Lehmann, D.C. Olk, E.G. Neves, M.L. Thompson, K. Schmidt-Rohr, , Abundant and Stable Char Residues in Soils: Implications for Soil Fertility and Carbon Sequestration, Environ. Sci. Technol., 46 (2012) 9571-9576.

(10) C.M. Preston, M.W.I. Schmidt, Black (pyrogenic) carbon: a synthesis of current knowledge and uncertainties with special consideration of boreal regions, Biogeosciences, 3 (2006) 397-420.

(11) K. Hammes, M.W.I. Schmidt, R. Smernik, L.A. Currie, W.P. Ball, T.H. Nguyen, P. Louchouran, S. Houel, O. Gustafsson, M. Elmquist, G. Cornellisen, J.O. Skjemstad, C.A. Masiello, J. Song, P.a. Peng, S. Mitra, J.C. Dunn, P.G. Hatcher, W.C. Hockaday, D.M. Smith, C. Hartkopf-Froder, A. Bohmer, B. Luer, B.J. Huebert, W. Amelung, S. Brodowski, L. Huang, W. Zhang, P.M. Gschwend, D.X. Flores-Cervantes, C. Largeau, J.-N. Rouzand, C. Rumpel, G. Guggenberger, K. Kaiser, A. Rodionov, F.J. Gonzalez-Perez, J.A. Gonzalez-Perez, J.M. De la Rosa, D.A.C. Manning, E. Lopez-Capel, L. Ding, Comparison of quantification methods to measure fire-derived (black/elemental) carbon in soils and sediments using reference materials from soil, water, sediment and the atmosphere, Glob. Biogeochem. Cyc., 21 (2007).

(12) A. Golon, N. Kuhnert, Unraveling the Chemical Composition of Caramel, J. of Ag. and Food Chem., 60 (2012) 3266-3274.

(13) X.-W. Fang, K. Schmidt-Rohr, The Fate of the Amino Acid in Glucose-Glycine Melanoidins Investigated by Solid-State NMR, J. Agric. Food Chem., 57 (2009) 10701-10711.

(14) X. Fang, K. Schmidt-Rohr, Alkyl and Other Major Structures in 13C-Labeled Glucose-Glycine Melanoidins Identified by Solid-State Nuclear Magnetic Resonance, J. Agric. Food Chem., 59 (2010) 481-490.

(15) N. Baccile, G. Laurent, C. Coelho, F. Babonneau, L. Zhao, M.-M. Titirici, Structural Insights on Nitrogen-Containing Hydrothermal Carbon Using Solid-State Magic Angle Spinning 13C and 15N Nuclear Magnetic Resonance, J. Phys. Chem. C, 115 (2011) 8976-8982.

(16) W. Cai, R.D. Piner, F.J. Stadermann, S. Park, M.A. Shaibat, Y. Ishii, D. Yang, A. Velamakanni, S.J. An, M. Stoller, J. An, D. Chen, R.S. Ruoff, Synthesis and Solid-State NMR Structural Characterization of 13C-Labeled Graphite Oxide, Science, 321 (2008) 1815-1817.

(17) W. Gao, L.B. Alemany, L. Ci, P.M. Ajayan, New insights into the structure and reduction of graphite oxide, Nature Chem., 1 (2009) 403-408.
(18) M.W.I. Schmidt, J.O. Skjemstad, E. Gehrt, I. Kögel-Knabner, Charred organic carbon in German chernozemic soils, Europ. J. Soil Sci., 50 (1999) 351-365.

(19) J.A. Baldock, R.J. Smernik, Chemical composition and bioavailability of thermally altered Pinus resinosa (Red pine) wood, Org. Geochem., 33 (2002) 1093-1109.

(20) M.S. Solum, J.M. Veranth, Y.-J. Jiang, A.M. Orendt, A.F. Sarofim, R.J. Pugmire, The Study of Anthracene Aerosols by Solid-State NMR and ESR, Energy & Fuels, 17 (2003) 738-743.

(21) J.-D. Mao, K. Schmidt-Rohr, Accurate Quantification of Aromaticity and Nonprotonated Aromatic Carbon Fraction in Natural Organic Matter by ^{13}C Solid State NMR, Environ. Sci. Technol., 38 (2004) 2680-2684.

(22) S.R. Kelemen, M. Afeworki, M.L. Gorbaty, M. Sansone, P.J. Kwiatek, C.C. Walters, H. Freund, M. Siskin, A.E. Bence, D.J. Curry, M. Solum, R.J. Pugmire, M. Vandenbroucke,

M. Leblond, F. Behar, Direct Characterization of Kerogen by X-ray and Solid-State 13C Nuclear Magnetic Resonance Methods, Energy & Fuels, 21 (2007) 1548-1561.

(23) K. Hammes, R.J. Smernik, J.O. Skjemstad, M.W.I. Schmidt, Characterisation and evaluation of reference materials for black carbon analysis using elemental composition, colour, BET surface area and 13C NMR spectroscopy, Applied Geochemistry, 23 (2008) 2113-2122.

(24) N. Baccile, G. Laurent, F. Babonneau, F. Fayon, M.-M. Titirici, M. Antonietti, Structural Characterization of Hydrothermal Carbon Spheres by Advanced Solid-State MAS 13C NMR Investigations, J. Phys. Chem. C, 113 (2009) 9644-9654.

(25) H.J. Reich, C-13 NMR Chemical Shifts (Wisconsin data base), http://www.chem.wisc.edu/areas/reich/Handouts/nmr-c13/cdata.htm, (2013).

(26) A. Bax, R. Freeman, S.P. Kempsell, Natural-abundance ^{13}C-^{13}C coupling observed via double-quantum coherence, J. Am. Chem. Soc., 102 (1980) 4849-4851.

(27) M. Hohwy, C.M. Rienstra, C.P. Jaroniec, R.G. Griffin, Fivefold symmetric homonuclear dipolar recoupling in rotating solids: Application to double quantum spectroscopy, J. Chem. Phys., 110 (1999) 7983-7992.

(28) J. Shu, P. Li, Q. Chen, S. Zhang, Quantitative Measurement of Polymer Compositions by NMR Spectroscopy:Targeting Polymers with Marked Difference in Phase Mobility, Macromolecules, 43 (2010) 8993-8996.

(29) G. Hou, F. Deng, S. Ding, R. Fu, J. Yang, C. Ye, Quantitative cross-polarization NMR spectroscopy in uniformly 13C-labeled solids, Chem. Phys. Lett., 421 (2006) 356-360.

(30) E. Katoh, K. Takegoshi, T. Terao, 13C Nuclear Overhauser Polarization−Magic-Angle Spinning Nuclear Magnetic Resonance Spectroscopy in Uniformly 13C-Labeled Solid Proteins, JACS, 126 (2004) 3653-3657.

(31) C.R. Morcombe, V. Gaponenko, R.A. Byrd, K.W. Zilm, Diluting Abundant Spins by Isotope Edited Radio Frequency Field Assisted Diffusion, JACS, 126 (2004) 7196-7197.

(32) K. Schmidt-Rohr, Complete Dipolar Decoupling of ^{13}C, and Its Use in Double-Quantum Solid-State NMR for Determining Polymer Conformations, J. Magn. Reson., 131 (1998) 209-217.

(33) E.R. deAzevedo, W.-G. Hu, T.J. Bonagamba, K. Schmidt-Rohr, Principles of Centerband-Only Detection of Exchange in Solid State NMR, and Extentions to Four-Time CODEX, J. Chem. Phys., 112 (2000) 8988-9001.

(34) K. Takegoshi, S. Nakamura, T. Terao, C13-H1 dipolar-assisted rotational resonance in magic-angle spinning NMR, Chem. Phys. Lett., 344 (2001) 631-637.

(35) B.H. Meier, Polarization Transfer and Spin Diffusion in Solid-State NMR, Adv. Magn. Opt. Reson., 18 (1994) 1-116.

(36) W.T. Dixon, Spinning-sideband-free and spinning-sideband-only NMR spectra of spinning samples, J. Chem. Phys., 77 (1982) 1800-1809.

(37) H. Geen, G. Bodenhausen, Pure absorption-mode chemical exchange NMR spectroscopy with suppression of spinning sidebands in a slowly rotating solid, J. Chem. Phys., 97 (1992) 2928-2937.

(38) S.T. Burns, X. Wu, K.W. Zilm, Improvement of Spectral Editing in Solids: A Sequence for Obtaining ^{13}CH + ^{13}CH2-Only ^{13}C Spectra, J. Magn. Reson., 143 (2000) 352-359.

(39) J.-D. Mao, L. Tremblay, J.-P. Gagné, S. Kohl, J. Rice, K. Schmidt-Rohr, Natural organic matter in the Saguenay Fjord and the St. Lawrence Estuary investigated by advanced solid-state NMR, Geochim. Cosmochim. Acta, 71 (2007) 5483-5499.

(40) X.L. Yao, K. Schmidt-Rohr, M. Hong, Medium- and Long-Distance ^{1}H-^{13}C Heteronuclear Correlation NMR in Solids, J. Magn. Reson., 149 (2001) 139-143.

(41) J.-D. Mao, K. Schmidt-Rohr, Separation of aromatic-carbon ^{13}C NMR signals from di-oxygenated alkyl bands by a chemical-shift-anisotropy filter, Solid State NMR, 26 (2004) 36-45.

(42) SDBS, NMR database, http://sdbs.riodb.aist.go.jp, accessed Nov. 2012.

CHAPTER 3. IMPROVED SOLID STATE NMR STRUCTURAL CHARACTERIZATION OF HYDROTHERMAL CARBON: PHENOLIC ARENE CORES, AND ORTHO-DIPHENOLS AS CENTRAL STRUCTURAL UNITS.

Robert Lee Johnson[1]*, Jason Anderson*[2]*, Brent Shanks*[2]*, Klaus Schmidt Rohr* [1]

Formatted for submission to *Journal of Physical Chemistry C*.

[1]Department of Chemistry Iowa State University, IA, USA

[2] Department of Chemical Engineering, Iowa State University, IA, USA

Keywords: EXPANSE, Spheres, DQ/SQ, MELODI.

Abstract

A new structural model of hydrothermal char is presented which shows these materials are comprised of arene, phenolic, and furanic structures and is supported using multidimensional ^{1}H-^{13}C and ^{13}C-^{13}C solid-state NMR experiments with spectral editing and multi-bond couplings. These findings improve previous models-based only on one-bond ^{13}C-^{13}C connectivities, which cannot distinguish clearly between the O-C=C structures in furans and phenols. In our model the cores of the observed hydrogen-poor aromatic structures are fused six-membered aromatic rings substituted by oxygen linked with furanic, and alkyl moieties. This model also assigns the ^{13}C NMR signal at 143 ppm to a distinct ortho-diphenol structure, proven to exist with a new 3D Hetcor experiment that is selective for OH-C correlation. Lastly, NMR was used to show that

functional groups are homogeneously distributed, providing strong evidence against the core-shell models previously proposed.

Introduction

Carbon materials, including hydrothermal carbon (HTC) produced from carbohydrate-rich feedstocks at moderate temperatures, have attracted a great deal of research attention since their rediscovery in the early 2000's. Research into these materials is a result of numerous desirable characteristics including: utilization of non-petroleum feedstocks, [1] the formation of uniform nanospheres,[2] which make these materials potentially useful for a broad range of applications ranging from environmental including carbon sequestration, [3] and soil engineering, [4] to functional materials for energy storage [5-7] and as heterogeneous catalyst. [1, 8-11] As of April 2014, a Google Scholar search using the term "hydrothermal carbon materials" produces 290,000 articles. One key difference between HTC (and low temperature chars) and conventional carbon [12, 13] materials is a much greater incorporation of oxygen containing functional groups. This feature results in the materials being hydrophilic, which is potentially advantageous for applications not well suited for hydrophobic carbon [14] Characterization of aromatic-rich functionalized carbon materials is not trivial, and commonly used techniques such as vibrational spectroscopies and diffraction methods provide limited useful information, as they are not quantitative and unable to resolve details about the nature of the aromatic connections and pendent functional groups. Understanding the dependence of properties on functionality requires the development of a realistic structural model.

Solid state NMR can provide both resolution and quantitation, but suffers from the low (1.1%) natural abundance of ^{13}C. With ^{13}C enrichment, solid state NMR can provide a great deal more information about the molecular connectivities and has been used previously to thoroughly investigate the carbon material's molecular structure. HTC produced from glucose has been shown to produce very materials with similar molecular structure as HTC produced from more commercially relevant materials such as lignocellulosic materials [15, 16] These experiments clearly show the materials produced at moderate temperatures (180 °C) are predominantly aromatic and suggest that >80% of this aromatic carbon is furanic [12, 13] This conclusion was contrary to previous publications depicting low temperature materials as large arene clusters decorated with phenol and carboxylate groups. One issue not fully resolved is the substantial signal at 120-140 ppm (typically arene) present in the quantitative DP spectra of glucose-derived HTC. [12, 13] ^{13}C chemical shifts of furanic aromatic rings have a characteristic pattern with two carbons resonating at 110-115 ppm and two other carbons at 140-155 ppm for C_β and C_α respectively. Solid-state NMR spectra of pyrolyzed poly-furfuryl alcohol are fully baseline resolved in the aromatic region between the C_α and C_β. [17] Sulfonated glucose (150 °C) was extensively studied with NMR and shown to have very high furan content. 1D DP spectra have a local minimum in the arene region, and the aromatic regionresembles [8] 1D CP spectra of HTC from fructose (135 °C) both of these materials have different features than HTC (180 °C) from glucose. [18] The first model published using NMR and ^{13}C enrichment attributed the arene content to a minor "graphene like" component. [12] More recently, a six-membered ring formed from fusion of 3 furanic rings has been proposed. [13]

DQ ^{13}C-^{13}C NMR provides valuable information about the connectivities by showing ^{13}C-^{13}C spin pairs without the presence of a diagonal ridge. Many assignments can be made unambiguously with this spectrum alone, but to discern furan structures from arene/phenol spectral editing is required. Recently, two complementary experiments were demonstrated to help solve this problem. One pulse sequence (EXPANSE) selects for CH_n in the w_1 dimension by applying a short CP and $C_{nonprot}$ in w_2 with dipolar dephasing through gated decoupling. A difference spectra is then produced to account for any spin diffusion that occurs to $C_{nonprotonaated}$ carbons. The complementary experiment (DQ/SQ) selects for non-protonated pairs of carbons by applying gated decoupling in both dimensions, using both EXPNASE and DQ/SQ spectra in a complementary fashion makes assignment of the aromatic region unambiguous. [8, 19, 20] Theseexperiments can provide information that is not accessible with double quantum NMR alone, which otherwise shares some advantages like the absence of a diagonal ridge and associated artifacts. Consider, for instance, nonprotonated C bonded to protonated C resonating at $\rceil_A$ and $\rceil_B$, respectively, overlapping completely with nonprotonated C bonded to protonated C resonating at $\rceil_B$ and $\rceil_A$, respectively. In the double-quantum experiment with dipolar dephasing before detection, this combination gives the same pair of signals at ($\rceil_A+\rceil_B$, $\rceil_A$) and ($\rceil_A+\rceil_B$, $\rceil_B$) as nonprotonated C bonded to nonprotonated C resonating at $\rceil_A$ and $\rceil_B$, respectively. In the CH-to-$C_{nonprot}$ exchange experiment, cross peaks at ($\rceil_B$, $\rceil_A$) and ($\rceil_A$, $\rceil_B$) identify the two pairs of carbons uniquely, while the combination of two nonprotonated (or two protonated carbons) resonating at $\rceil_A$ and $\rceil_B$ does not give any signal. Using the EXPANSE exchange-NMR method enables probing the structure beyond a single bond. For example, a protonated carbon resonating at 150 ppm correlating with a 115 ppm carbon must be from a furanic fragment as it is not possible to have a protonated phenolic carbon.

One distinct feature of the HTC (180 ^{o}C) is the large non-protonated intensity at 140 ppm, which is most prominent in HTC produced from hexoses monomers or polymers, including cellulose and starch. [12, 13, 15] This chemical shift is lower than that observed for typical non-protonated C_α in furans and phenols. A previous assignment for the 143 ppm peak was an unusual alkene-furan structure. [12] One possible alternative for this peak is the presence of an ortho di-phenol, Two carbons are ortho to a OH resulting in to a downward shift of 10 ppm. One approach to testing this hypothesis involves the use of NMR with spectral editing, but with the added ^{1}H dimension to include Hetcor experiments. Strong homonuclear (90 kHz) and heteronuclear ^{13}C (40 kHz) dipolar couplings can be leveraged to impose selection criteria in the ^{1}H dimension. Generation of a DQ coherence will retain magnetization only on ^{1}H pairs in close spatial proximity, and can be run as a DQ/SQ 2D, making both ^{1}H spin pair chemical shifts known. The ^{1}H-^{13}C dipolar couplings can be used to apply an additional selection criterion to the DQ ^{1}H ^{13}C Hetcor experiment. By applying the medium- and long-distance (MELODI) ^{1}H-^{13}C Hetcor sequence; selective dephasing of ^{1}H magnetization of CH and CH_2 groups is accomplished and traces as distance dependence REDOR curves. [21]

This study, we apply specialized NMR techniques to solve outstanding questions about the structure of HTC. We probe the arene/furanic components using EXPANSE/DQ/SQ 2D set, test the core shell model with long mixing 2D ^{13}C ^{13}C experiments, [12, 18, 22-24] and selectively probe phenol fragments using ^{1}H-^{13}C Hetcor experiments, including a new Hetcor ^{1}H ^{13}C 3D experiment DQ/SQ with MELODI H-C dephasing developed to select for di-phenols.

Experimental

Materials Preparation

In a stainless steel Parr reactor, glucose (5 g) was dissolved in deionized (DI) water (50 mL) and then nitrogen-flushed three times. The vessel was then pressurized to 500 psi and heated to 200 °C with a ramp rate of 10ºC min^{-1} and then held for ~18.5 hours. The resulting insoluble carbon material was filtered (4.5-5 μm Buchner funnel) and washed with DI water and dried overnight at 100 °C within an air atmosphere in an oven.

Material Characterization

Elemental analysis results for the carbon, hydrogen, nitrogen, and sulfur (CHNS) were acquired using a PE 2100 Series II combustion analyzer (Perkin Elmer Inc., Waltham, MA). Carbon materials were imaged with scanning electron microscopy (FEI Quanta-250 SEM).

NMR Methods

Quantitative 1D direct pulse (DP)

The ^{13}C NMR was performed at a resonance of 100 MHz on ^{13}C-enriched samples using a Bruker DSX400 spectrometer, magic angle spinning at 14 kHz, and high power ^{1}H decoupling. The 90° ^{13}C pulse-length was 4.5 μs. Quantitative ^{13}C spectra were measured using direct polarization (DP) magic-angle spinning (MAS) and a Hahn echo with high-power decoupling, with recycle delays of 30 s ($> 5\ T_1$), and spectra of nonprotonated carbons (and mobile segments) were obtained after recoupled ^{13}C-^{1}H dipolar dephasing. [25] Sufficiently strong ^{1}H decoupling at $\gamma B_1/\ 2\pi = 72$ kHz with the two-pulse phase-modulated (TPPM) scheme was applied during an acquisition time of 3 ms. Chemical shifts were referenced to neat TMS using the resonance of ^{13}C1-labeled glycine with a chemical shift of 176.46 ppm as a secondary reference.

Molecular modeling and spectra simulations

Simulated spectra were generated by drawing a proposed model into an ACD chemical shift prediction software to obtain the predicted chemical shift, and the protonation of carbons. This data was then entered into an in-house MatLab program to generate spectra for both full and dipolar dephased by application of a Gaussian broadening to each frequency. Given the identification of a distinct component of entrapped levulinic acid, the full spectra shown are the sum of a weighted average for levulinic acid and the carbon scaffold.

EXPNASE/DQ

EXPANSE and ^{13}C DQ/SQ with dipolar dephasing was used. (was described in detail previously. [19]) Mixing periods of 3 and 40 ms (DID WE USE DARR?) in the EXPANSE spectra, and 14 kHz MAS was used for both experiments. Gated decoupling was applied for 30 us in the center of the rotor period to dephase ^{13}C magnetization of groups CH, CH2.

^{1}H DQ ^{13}C 2D NMR

A pulse sequence diagram for the double quantum filtered ^{1}H ^{13}C Hector experiments is shown in Figure 1. Edited variations of this basic sequence begin with the generation of a ^{1}H-^{1}H DQ coherence by application of a 180° pulse at the center of the rotor period to interfere with MAS averaging of the ^{1}H ^{1}H homo-nuclear dipolar couplings. This magnetization can be use to transfer magnetization to ^{13}C with cross polarization. From this baseline we then applied selection criteria n the first variation, we applied a CP of only 30 us to select for CH groups, which is not sufficiently long for ^{1}H magnetization to transfer to carbon to directly bonded to protons. The second criteria introduced was the MELODI ^{1}H ^{13}C dephasing prior to CP to select for phenols and COO groups. We also used high power decoupling (70 kHz) during the evolution period to minimize T2 decay.

Suppress protons in immobile CH_n groups by ^{1}H dephasing of the double-quantum coherence; no ^{13}C decoupling during double-quantum excitation and reconversion also produces an additional $\langle\cos^2(\Phi_{CH}(t_r/2))\rangle$ dephasing (to ca. 0.4).

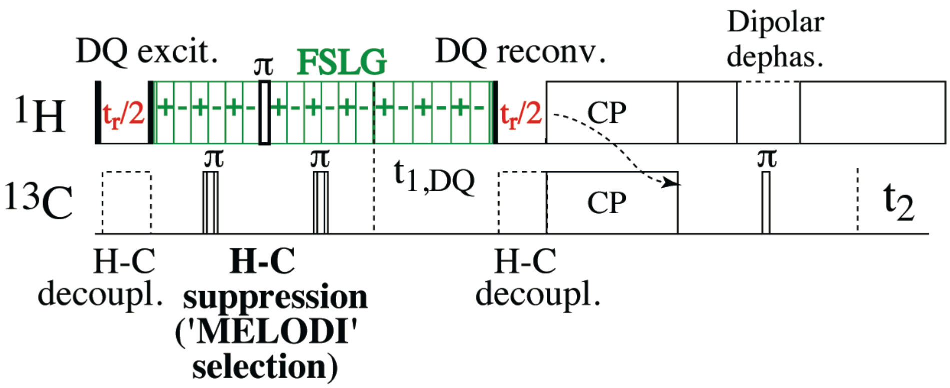

Figure 1. Selects OH signals with suppression of CH protons by ^{1}H ^{13}C recoupling MELODI scheme. This experiment is run with both in pairs that both select for CH and suppress them to compare the difference. CH groups are retained by applying decoupling during the DQ reconversion period.

^{1}H DQ ^{1}H SQ ^{13}C 3D NMR.

To unambiguously prove the presence of the diphenol structure, we applied a 3D experiment, the pulse sequence diagram of which is shown in Figure 2a. Shown in Figure 2b is a representative ^{13}C slice of the full 3D diagram shown in Figure 2c. This experiment gives the chemical shifts of carbons that are bonded to OH groups, with OH groups being in a close spatial proximity that is needed to generate the original DQ coherence. With the third dimension being incorporated, the identity of both protons in the DQ pair set is known, making the assignment of di-phenol unambiguous.

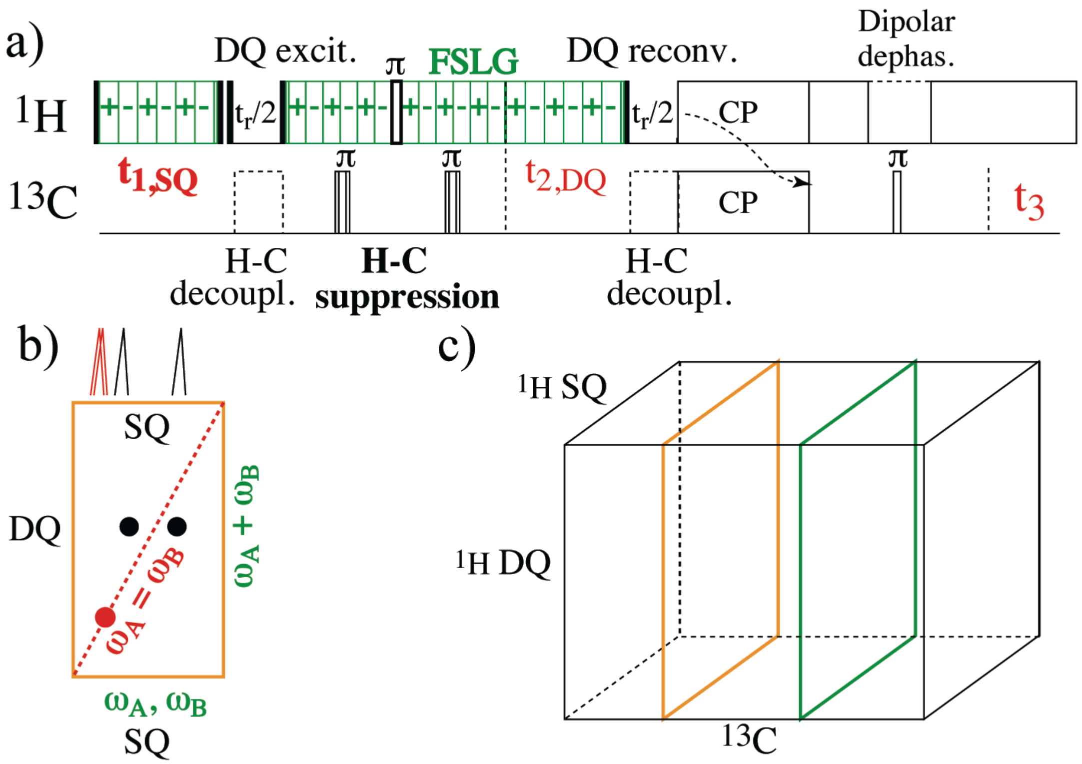

Figure 2. Shown in (a) is a pulse program diagram for the 3D ^{1}H ^{1}H DQ/SQ ^{13}C 3D experiment, in (b) is a representative ^{1}H DQ ^{1}H SQ 2D slice, and (c) is a depiction of the full 3D plot including the ^{13}C dimension.

1s spin diffusion ^{13}C-^{13}C 2D exchange

Standard 2D with 7.8 kHz MAS with TOSS with long mixing times to test material homogeneity. Long mixing periods (1 s) were applied and slices were extracted from different functional groups ranging from alkyl to ketone. If the interior is predominantly arene-like, we would expect slices from carbons in different environments to have distinct slices which reflect to which carbons the magnetization, at that particular frequency, are coupled.

Results/discussion

CHN elemental analysis of the HTC show a composition of 66%C, 4%H, 30%O (by difference), which are very similar to values reported by 62% +-4 C 4%H+-1 34%+-3 O. An

SEM image of the hydrochar are shown in Figure 3 and verify the material’s spherical morphology. The HTC in this study are 0.75 μM in diameter, which is consistent with previous studies.

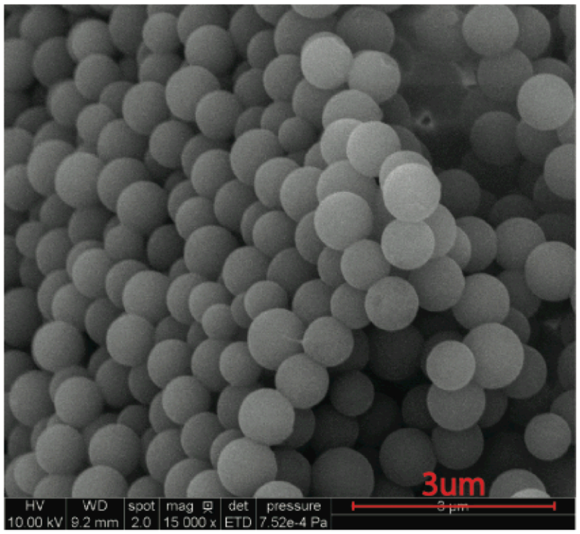

Figure 3. shows SEM images of hydrochar that consist of uniform spheres that have approximate diameters of 1um. If a sphere of this size were composed of differential core shell domains, it would contain regions that would be separated by hundreds of nanometers.

NMR I. EXPANSE, DQ/SQ, DP

DP spectra obtained from HTC, shown in Figure 4a, have very similar spectra as materials produced at 180 ºC in previous NMR studies. [12, 13] This provides strong evidence that the difference in synthesis temperatures between the two materials has a minimal effect on the molecular structure. Table 1 shows the integral values from these spectra for both the full and dipolar dephased spectra. The EXPANSE and DS/SQ spectra shown in Figure 4 (b,c) show strong signals characteristic of connections between furans, arenes, and alkyl carbons. These spectra support previous conclusions about the connectives of the furanic components. Figure 4d, shows simulated spectra from the molecular fragment shown in Figure 4e. Although, experiments in the following sections were critical to identify fragments to include in the model it is shown here for convienient visual comparison to the experimental spectra. (i.e. we did the modeling last, but we chose to show it here for easy comparison)

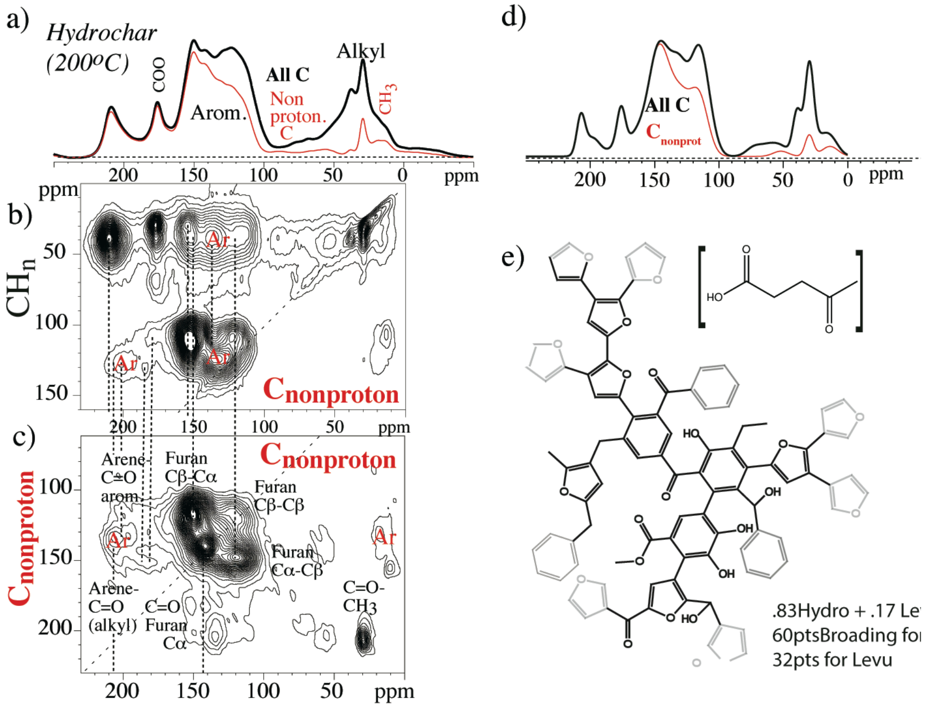

Figure 4. shows in (a) quantitative DP full (black) and dephased (red) spectra. Shown in (b,c) are EXPANSE and ^{13}C DQ/SQ spectra with dipolar dephasing in both dimensions. Simulated spectra are shown in (d) for molecular fragment (e). To handle the imbedded levulinic acid, this component was given a weighted average in the full simulated spectra. 0.17 was the weighting factor used produced the best match in intensity compared to the experimental spectra.

Table 1: Integration of DP spectra

229-188	188-165	165-138	138-123	123-89	89-62	62-16	16-0	SSB
.08	.07	.21	.14	.18	.04	.2	.03	.05
.07	.06	.18	.1	.1	.01	.05	.02	.03

To probe the bonding partners of furan and arene carbons, short and long mixing times were used and CH slices were extracted (Figure 5). This exchange experiment for CH is very useful for proving the presence of arene CH fragments, resonating between 120 and 130 ppm, bonded to non-protonated arene C not bonded to O, which resonates between 123 and 140 ppm. Figure 5a shows spectra arising from bonding a nonpolar arene CH (123 ppm) to non-protonated arene (131 ppm). In short mixing times, we see that bonding partners are predominantly other arene carbons. In addition, some ketone at around 200 ppm, indicating that an alkyl carbon is the bonding partner. In regular 2D exchange experiments, the cross peaks from these carbons are so close to the diagonal ridge that they cannot be convincingly identified.

Furans show protonated aromatic O-CH and aromatic O-CR bonded to alkyl R. The exchange experiment from CH can also show the O-C-**CH-CR**-C-O fragment quite characteristic of furans (with the same O shown twice in the linear formula). The two C_α carbons are so close in frequency that their exchange peak is usually not well resolved from the diagonal ridge. At short spin exchange times, the signals of the C-O and CR-C-O carbons bonded to the CH-C-O carbon resonating near 110 ppm have similar intensities, but due to the presence of the second C-O in the ring, its intensity increases at longer exchange times. Spin exchange from CH without suppression of CH, before detection, the 2:2 C-O and **C**-C-O intensity ratio characteristic of furan rings is indeed observed and is shown in Figure 4. For instance, a chemical shift of 110 ppm is not unusual for a protonated aromatic carbon (in a O-C=CH environment). However, a non-protonated aromatic carbon resonating at 110 ppm must be near two oxygens (in a O-C=CR-C-O environment). Or a peak at 123 ppm is not special, since nonprotonated **C**=C-OH resonate here. However, a protonated C at 123 ppm cannot be due to **C**=C-OH, and must be assigned to arenes.

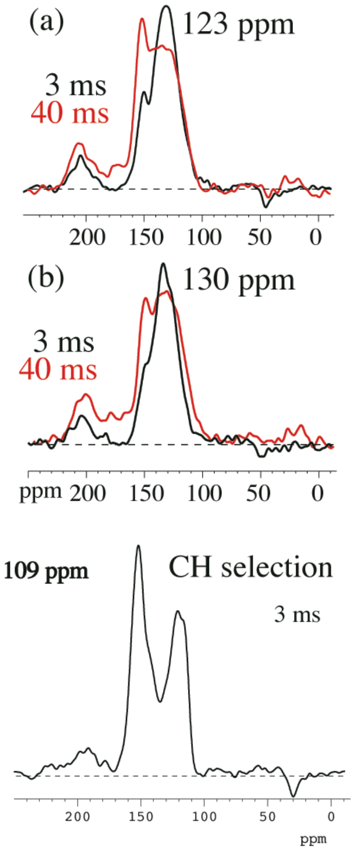

Figure 5. CH selected 2D exchange spectra with slices extracted from characteristic arene frequencies. After short mixing times, we see mostly cross talk with other arene carbons with the exception of ketones bonded to alkyl carbons. After 40 ms mixing period we see a dramatic increase in carbons resonating at 150 ppm, characteristic of phenols and furans.

NMR II. DQ ^{1}H filtered 2D

To further probe the phenol environment and test the degree of hydroxylation, we applied DQ ^{1}H ^{13}C Hector experiments. Using a DQ filter in the ^{1}H dimension selects for ^{1}H-^{1}H in close spatial proximity. Shown in Figures 6 (a,b) are 2D plots of double quantum hectore with short CP 6a, and H-C dephasing 6b. One sees that 6a displays the most intensity centered on the 112-125 ppm pak with ^{1}H at about 12-13 ppm, which is consistent with arene and furanic CH. Figure 6b (with MELODI ^{1}H-^{13}C dephasing), has most of the aromatic intensity centered around 140 ppm in the carbon dimension, and 14 ppm in the ^{1}H dimension, which is characteristic of ortho-diphenols. To verify observations from the 2D plot, slices were extracted from the ^{1}H dimension and are shown in Figures 6 (c,d). Shown in Figure 6d are the 143 ppm slices which indicate that the signal at 143 ppm is due to two non-protonated aromatic carbons bonded to O and two bonds from O; at least one of the oxygens is in an OH group. In addition to diphenols, another plausible structure is a Cb-hydroxylated furan (see SI). Our spectra do not support this type of structure, and is verified by the EXPANSE spectra in Figure 5b, showing an intensity minima between the 110 ppm CH and 130 ppm $C_{nonprot}$, as predicted by in Advanced Chemistry Devolopment (ACD) software.

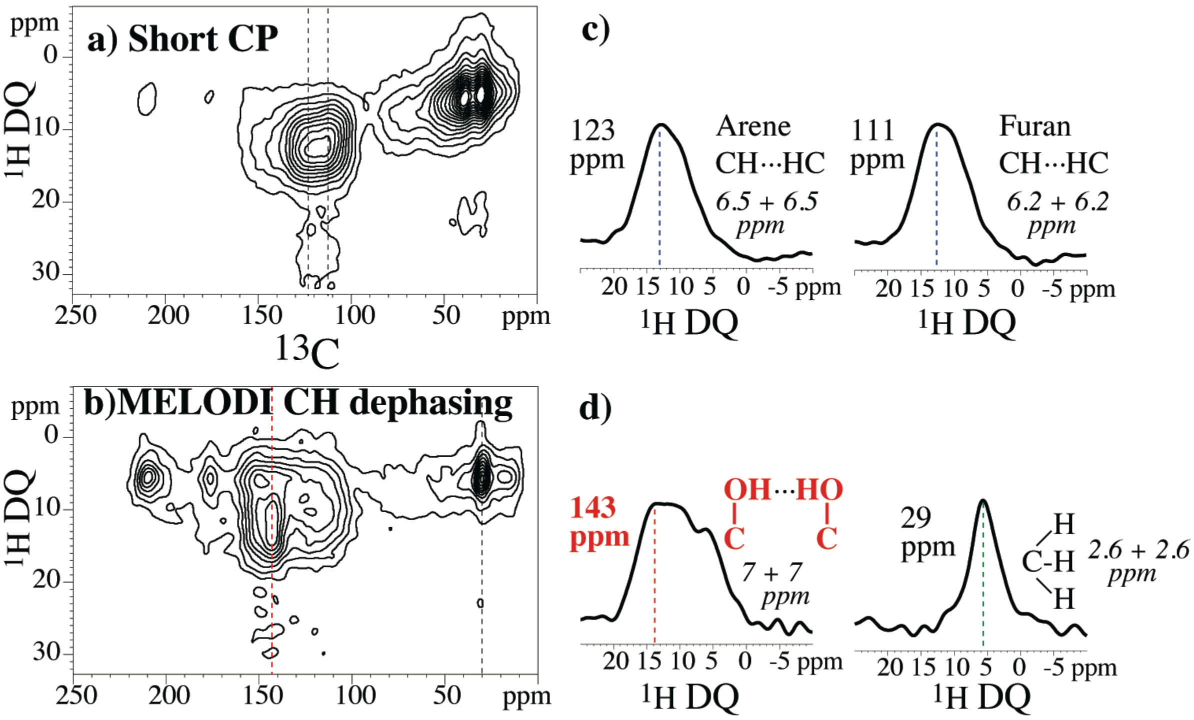

Figure 6. DQ 1H 13C 2D experiments with short CP for CH selection (a) with MELODI CH suppression (b). Slices extracted from 123 and 111 ppm are shown in c and in d are 143 and 29 ppm. Noteworthy is the evidence for a diphenol structure from the 143 ppm slice.

NMR III. ^{1}H DQ/SQ ^{13}C 3D

To prove the ortho-diphenol assignment to the 143 ppm intensity we used 3D DQ/SQ ^{1}H-^{1}H-^{13}C NMR. Shown in Figure 7c is the 143 ppm slice with application of MELODI C-H suppression. Given that the DQ dimension is the sum of the two ^{1}H spins which are paired, the assignment of the ^{1}H that correlate with 143 ppm carbons and both resonate at 7.2 ppm, phenolic ^{1}H. The DQ selection ensures they must be in close spatial proximity (otherwise no double quantum coherence can be generated). The ^{1}H-^{13}C dephasing ensures that these are not aromatic C-H but certainly OH protons. Their peak position is also distinct from that of aromatic protons. In this 3D spectrum, a signal will be observed only for non-protonated carbons which are in close proximity to pairs of ^{1}H not bonded to C ie OH. Shown in Figure 7a is the 3D slices from the short CP CH selected spectra, and in Figure 7b are the OH selected with slices from the143 ppm, and methyl peak for verification.

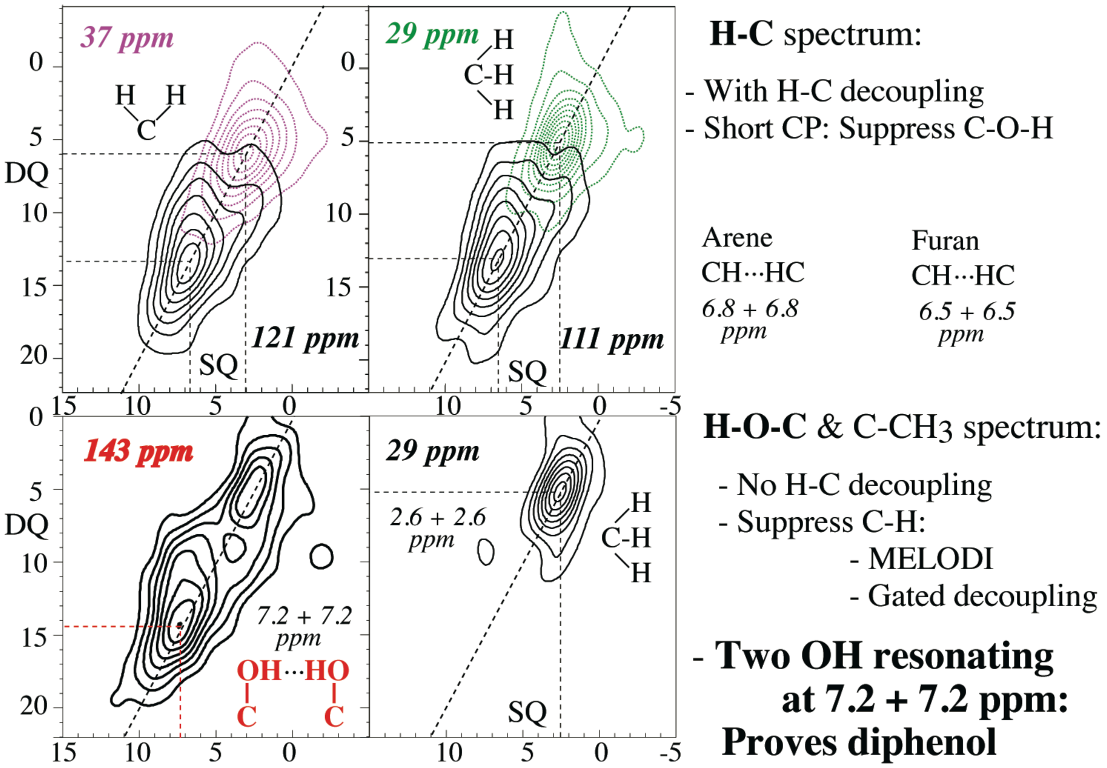

Figure 7. Shown in the top half are slices extracted from the CH selected and below are the CH suppressed spectra. In particular, the 143 ppm slices are informative.

NMR IV: NMR homogeneity test

To test if hydrochar is in fact composed of domains separated on the hundreds of nm scale, we ran a 2D exchange experiment with a long mixing time to see if magnetization that originated on one functional group equilibrated with other functional groups during that period. With a relatively long mixing time of 1 s, spin diffusion will spread and equilibrate magnetization over ten's of nanometers. The 2D plot (Figure 8a) for HTC and extracted slices (Figure 8b) from numerous functional groups. What is important is that all slices look the same, meaning that all functional groups in the material equilibrate with all other functional groups in the materials, therefore, are not spatially distant as would be the case with a core-shell structure with separation of at least 10's of nm.

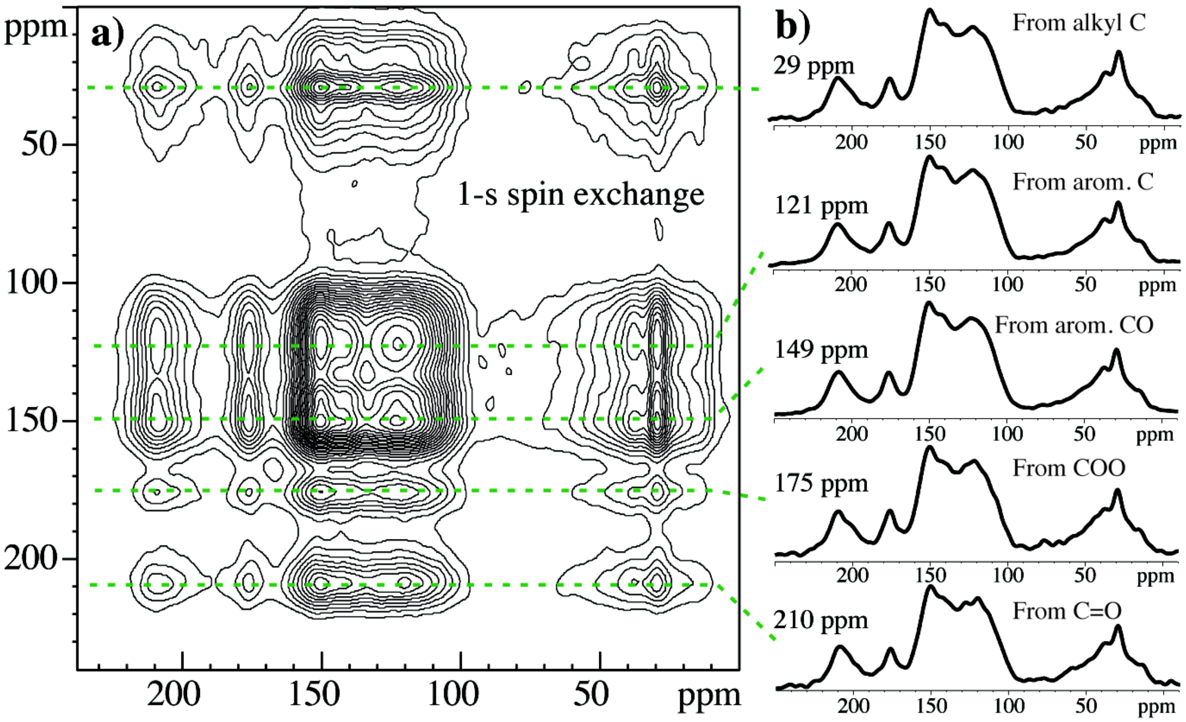

Figure 8. To test the hypothesis of distinct hydrophilic shells and hydrophobic domains in hydrochar slices from different groups were extracted and show that the 1D profile is identicle independent of the frequency which the slice originated. This is a strong indication that the materials are not composed of domains with different structural groups on the >2nm scale, as previously proposed.

Conclusions

We used a myriad of NMR experiments, which show that the HTC materials contain a significant fraction of arene carbons and are heavily hydroxylated in addition to furans previously identified. Additionally, we show that the 143 ppm resonance observed in 1D DP spectra originates from a distinct ortho di-phenol structure. Lastly, the core-shell model was tested using long spin exchange NMR and shows that this HTC carbon is homogeneous.

Acknowledgments

This work was supported by the Center for Biorenewable Chemicals (CBiRC) funded by NSF grant EEC-0813570.

References

(1) Hu, B., et al., *Engineering Carbon Materials from the Hydrothermal Carbonization Process of Biomass.* Adv. Mat, 2010. **22**(7): p. 813-828.

(2) Wang, Q., et al., *Monodispersed hard carbon spherules with uniform nanopores.* Carbon, 2001. **39**(14): p. 2211-2214.

(3) Titirici, M.-M., A. Thomas, and M. Antonietti, *Back in the black: hydrothermal carbonization of plant material as an efficient chemical process to treat the CO2 problem?* New J. Chem., 2007. **31**(6): p. 787-789.

(4) Libra, J.A., et al., *Hydrothermal carbonization of biomass residuals: a comparative review of the chemistry, processes and applications of wet and dry pyrolysis.* Biofuels, 2010. **2**(1): p. 71-106.

(5) Zhai, Y., et al., *Carbon Materials for Chemical Capacitive Energy Storage.* Adv. Mater., 2011. **23**(42): p. 4828-4850.

(6) Brun, N., et al., *Hydrothermal carbon-based nanostructured hollow spheres as electrode materials for high-power lithium-sulfur batteries.* Phys. Chem. Chem. Phys., 2013. **15**(16): p. 6080-6087.

(7) Demir Cakan, R., et al., *Hydrothermal carbon spheres containing silicon nanoparticles: synthesis and lithium storage performance.* Chem. Commun., 2008(32): p. 3759-3761.

(8) Anderson, J.M., et al., *Solid State NMR Study of Chemical Structure and Hydrothermal Deactivation of Moderate-Temperature Carbon Materials with Acidic SO3H Sites.* Carbon, 2014. **In Press (3-2014)**.

(9) Makowski, P., et al., *Selective partial hydrogenation of hydroxy aromatic derivatives with palladium nanoparticles supported on hydrophilic carbon.* Chem. Commun., 2008(8): p. 999-1001.

(10) Demir-Cakan, R., et al., *Hydrothermal synthesis of imidazole functionalized carbon spheres and their application in catalysis.* Catal. Today, 2010. **150**(1–2): p. 115-118.

(11) Tang, S., S. Vongehr, and X. Meng, *Carbon Spheres with Controllable Silver Nanoparticle Doping.* J. Phys.Chem. C, 2009. **114**(2): p. 977-982.

(12) Baccile, N., et al., *Structural Characterization of Hydrothermal Carbon Spheres by Advanced Solid-State MAS 13C NMR Investigations.* J. Phys. Chem. C, 2009. **113**(22): p. 9644-9654.

(13) Falco, C., et al., *Hydrothermal Carbon from Biomass: Structural Differences between Hydrothermal and Pyrolyzed Carbons via 13C Solid State NMR.* Langmuir, 2011. **27**(23): p. 14460-14471.

(14) Bulushev, D.A., et al., *Highly dispersed gold on activated carbon fibers for low-temperature CO oxidation.* Journal of Catalysis, 2004. **224**(1): p. 8-17.

(15) Titirici, M.-M., M. Antonietti, and N. Baccile, *Hydrothermal carbon from biomass: a comparison of the local structure from poly- to monosaccharides and pentoses/hexoses.* Green Chem., 2008. **10**(11): p. 1204-1212.

(16) Titirici, M.-M. and M. Antonietti, *Chemistry and materials options of sustainable carbon materials made by hydrothermal carbonization.* Chem. Soc. Rev, 2009. **39**: p. 103-16.

(17) Burket, C.L., et al., *Genesis of porosity in polyfurfuryl alcohol derived nanoporous carbon.* Carbon, 2006. **44**(14): p. 2957-2963.

(18) Yao, C., et al., *Hydrothermal Dehydration of Aqueous Fructose Solutions in a Closed System.* J. Phys. Chem. C, 2007. **111**(42): p. 15141-15145.

(19) Johnson, R.L., et al., *Spectrally edited 2D 13C13C NMR spectra without diagonal ridge for characterizing 13C-enriched low-temperature carbon materials.* J. Mag. Res., 2013. **234**(0): p. 112-124.

(20) Pham, H.N., et al., *Improved Hydrothermal Stability of Mesoporous Oxides for Reactions in the Aqueous Phase.* Angew. Chem. Int. Ed., 2012. **124**(52): p. 13340-13344.

(21) Yao, X.L., K. Schmidt-Rohr, and M. Hong, *Medium- and Long-Distance 1H–13C Heteronuclear Correlation NMR in Solids.* J. Mag. Res., 2001. **149**(1): p. 139-143.

(22) Sun, X. and Y. Li, *Colloidal Carbon Spheres and Their Core/Shell Structures with Noble-Metal Nanoparticles.* Angew. Chem. Int. Ed., 2004. **43**(5): p. 597-601.

(23) Shin, Y., et al., *Hydrothermal Syntheses of Colloidal Carbon Spheres from Cyclodextrins.* J. Phys. Chem. C, 2008. **112**(37): p. 14236-14240.

(24) Sevilla, M. and A.B. Fuertes, *Chemical and Structural Properties of Carbonaceous Products Obtained by Hydrothermal Carbonization of Saccharides.* Chem. Eur. J., 2009. **15**(16): p. 4195-4203.

(25) Mao, J.D. and K. Schmidt-Rohr, *Accurate Quantification of Aromaticity and Nonprotonated Aromatic Carbon Fraction in Natural Organic Matter by 13C Solid-State Nuclear Magnetic Resonance.* Environ. Sci. & Technol., 2004. **38**(9): p. 2680-2684.

CHAPTER 4. A SIMPLE ONE-STEP SYNTHESIS OF AROMATIC-RICH MATERIALS WITH HIGH CONCENTRATIONS OF HYDROTHERMALLY STABLE CATALYTIC SITES, VALIDATED BY NMR

Chemistry of Materials **26**, pp 5523-5532, 2014

Robert L. Johnson[a,c], Jason M. Anderson[b,c], Brent H. Shanks[b,c], Klaus Schmidt-Rohr[a,c]*

[a] Department of Chemistry, Iowa State University, Ames, IA 50011
[b] Department of Chemical and Biological Engineering, Iowa State University, Ames, IA 50011
[c] Center for Biorenewable Chemicals (CBiRC), Iowa State University, Ames, IA 50011
*Corresponding author: srohr@brandeis.edu. Current address: Department of Chemistry,
Brandeis University, Waltham MA 02453

Keywords: Functionalized carbon materials; solid acid catalysts; hydrothermal stability; solid-state NMR

Abstract

We report a facile one-step synthesis of aromatic-rich materials that contain high concentrations of Brønsted acidic or basic groups attached via alkyl linkers, which previous work has shown to be particularly hydrothermally stable. The method is based on the Maillard reaction and low-temperature (250°C) pyrolysis of glucose with primary amines linked to acidic sulfonic or phosphonic functionalities, or basic piperidine or pyridine groups. The resulting black, carbon-rich materials were characterized using one- and two-dimensional solid-state ^{13}C and ^{15}N NMR, supplemented by elemental analysis. Synthesis with ^{13}C-enriched glucose enabled a selective NMR characterization of the aromatic scaffold, which is composed mostly of interlinked pyrrole,

indole, and pyridine rings. The fraction of sp^2-hybridized C in the matrix is 72%, the aromaticity ~60% for the sulfonic-acid functionalized material made from glucose and taurine in 1:1 molar ratio, where sulfur exceeds 11 wt%. The alkyl linkers remained intact in the synthesis at 250°C, as proved by distinctive NMR signals of CH_2 groups bonded to heteroatoms. The incorporation of the amine-derived nitrogen into the aromatic matrix was characterized by ^{15}N, ^{15}N-^{13}C, and $^{13}C\{^{15}N\}$ NMR of a material made from ^{15}N-taurine with ^{13}C-enriched glucose. ^{15}N NMR shows that no significant unreacted alkyl amine groups remain in the material. Hydrothermal stability as well as catalytic activity of the materials for an esterification reaction was verified.

Introduction

Carbon materials containing acidic and/or basic functional groups are promising for numerous applications, including heterogeneous catalysis,[1-7] adsorbents,[8] polymer electrolyte fuel cells,[9] anodes in lithium ion batteries,[10,11] and capacitors.[12] Carbon materials with high nitrogen loading have been shown to be effective as supports for highly active and distributed Pd nanoparticles.[13] Moreover, carbon materials are better suited than metal oxides or silica for applications that require resistance to degradation in liquid phase, including acids, bases, and water under high temperature and pressures (hydrothermal conditions).[14] Uniformly functionalized carbon materials are also good precursors for nanocomposites.[1]

A few general approaches have been employed to produce functionalized carbon materials. More often, the carbon scaffold is produced in the first step, and then some type of grafting procedure is used to attach moieties to the scaffold. Incorporation of sulfonic-acid functionality is important for numerous applications, and a variety of carbon scaffolds including char,[15] graphene oxide,[16] reduced graphene oxide,[17] hydrolyzed lignin,[18] hydrothermal carbon,[19,20] and activated carbon[21,22] have been sulfonated with various methods. Most commonly, SO_x is introduced using SO_2,[23] fuming sulfuric acid,[24] SO_3,[22] or treatment in neat sulfuric acid at 150°C.[25] A similar methodology has been demonstrated to incorporate phosphonic acid groups.[26] Although shown effective, these methods are limited in the amounts of functional-group incorporation. In addition, the hydrothermal stability of sulfonic acid functional groups directly bonded to aromatic carbon atoms is insufficient.[27]

To improve hydrothermal stability, the functional group should be connected to the aromatic rings through an aliphatic linker.[27] However, introducing functional groups into a highly aromatic material through carbon-carbon bond formation is challenging due to the small number of reactive edge sites. Many proposed modification schemes [28-30] use oxidation or elevated temperature to introduce reactive sites, followed by a reaction that will transform the new sites into the desired functional group. Given the condensed aromatic nature of the scaffolds, few primary carbon atoms are going to be efficiently transformed with S_N2 type mechanisms, which makes this route rather inefficient. Many published papers proposing such reaction mechanisms provide sparse characterization of the materials formed, which makes the conclusions rather ambiguous, and sometimes the shown model is inconsistent with measured data from elemental or thermogravimetric analysis.[16,17,31,32] Attempts have been made to use azides to link moieties to mesoporous carbon, but no structural data confirm that these groups are in fact attached through a covalent bond.[33,34]

An alternative approach is co-pyrolysis of a mixture of reactants that undergo numerous reactions but yield a final product that contains the desired functional groups incorporated into an insoluble support or scaffold.[35,36] This approach is attractive but difficult to accomplish due to limited control over the various reactions occurring simultaneously, and few analytical techniques are available to characterize the influence of synthesis parameters on the final materials structure. While it has been shown that hydrothermal carbonization (180°C) of hydroxyethylsulfonic acid and furaldehyde will produce a solid sulfonated acid catalyst with high sulfur incorporation and activity,[36] no detailed information on the reaction mechanism or the final structure of the material was obtained,[36] and no stability data provided, which makes generalizing this reaction scheme to other starting materials difficult.

In this work, we demonstrate that the Maillard reaction [37,38] combined with moderate pyrolysis can be used to produce aromatic-rich materials with alkyl-linked functional groups. This reaction between reducing sugars and primary amines readily produces high-molecular-weight, aromatic-rich products.[38-41] Detailed NMR studies of the solids formed during the Maillard reaction of glucose and glycine have shown that much of the nitrogen originating from glycine is tightly incorporated, forming two bonds to carbons originating from glucose.[40] In particular, Strecker degradation of the amino compound is much less prevalent than previously suggested and >60% of the COO functional groups of glycine were found to be incorporated intact.[40] This suggests that reacting glucose with a functionalized primary amine could produce a aromatic-rich material with a large number of functional groups covalently attached to the aromatic-rich matrix through an alkyl linker. However, the conditions under which the materials were produced,[40] 100°C for 1 week in solution or 125°C in solid phase, were not optimized for high aromaticity.

Here, we show how the Maillard reaction under basic conditions, with all the amines deprotonated and thus acting as better nucleophiles, directly followed by moderate-temperature pyrolysis provides a versatile platform for one-step synthesis of functionalized highly aromatic, high-molecular weight materials from inexpensive feedstocks such as glucose and taurine or other functionalized ethyl amines (see Scheme 1). We exemplify the approach by describing the syntheses of four differently functionalized aromatic-rich materials, with N-ethyl sulfonic acid, phosphonic acid, pyridine, and piperidine functional groups.

The incorporation of the functional groups and the predominantly aromatic nature of the matrix are verified by elemental analysis, XPS, and multinuclear NMR. Solid-state NMR is the most reliable method for comprehensively determining the composition of low-temperature carbon materials.[20,38-46] Peak areas in vibrational spectra are not quantitative due to their dependence on transition dipole moments, which overrepresents signals of OH, C=O and other polar bonds in IR spectra, while NMR is inherently quantitative since the nuclear dipole moment is constant for any electronic configuration. Quantitative ^{13}C NMR [47,48] complemented by spectral editing provides not only the aromaticity, but also the fractions of protonated aromatic carbons, as well as C=O, COO, OCH, OCH_2, OCH_3, CH_2, CH, and CH_3 moieties.[49,50] For highly aromatic materials produced with ^{13}C-enrichment, two-dimensional solid state NMR combined with spectral editing can resolve overlapping signals from various types of aromatic rings and differently bonded C=O groups,[51] and determine their linkage patterns. Average molecular models can be generated based on quantitative one-dimensional and spectrally edited two-dimensional NMR spectra and verified with spectral modeling.[20,51] Use of reactants selectively labeled with ^{13}C and/or ^{15}N enables NMR to trace the chemical transformations of various parts of the molecules and monitor the extent of incorporation or fragmentation.[40,41]

In order to validate the predicted improved hydrothermal stability, the N-ethyl sulfonic acid material is subjected to multiple 24-h cycles of hydrothermal treatment at 160°C. The catalytic activity of the sulfonic-acid material toward the esterification of methanol and acetic acid is verified, and improvements by post-synthesis treatment are explored.

Experimental

Materials Synthesis

All materials without isotopic enrichment were obtained from Sigma-Aldrich and used directly as purchased. Glucose and each of the selected amines were co-precipitated from aqueous solution, freeze-dried, and pyrolyzed in a MTI 1200X tube furnace with a 1°C / minute heating ramp in flowing ultra-pure argon gas passed through a gettering furnace and reacted for 10 h at the final temperature (250^{o}C, 350^{o}C, or 550^{o}C). Sulfonic-acid and phosphonic acid groups were introduced by reacting glucose with taurine (‘GTaur’) or 2-aminoethyl phosphonic acid (‘GPhos’) and KOH in a 1:1:1 ratio. The reaction of glucose with 4-(2-aminoethyl) pyridine (‘GPyri’), and 4-(aminomethyl) piperidine did not require base since the primary amine was in the deprotonated form as received. Given the low boiling point of 4-(2-aminoethyl) pyridine, this reaction was carried out in two steps. In the first step, the sample was heated to 80°C and held there for 4 h, before heating to the final temperature. After samples had cooled to room temperature, they were removed from the reactor, ground with mortar and pestle, washed with e-pure water, and dried in a vacuum oven at 110 °C. Materials produced with sulfonic functional groups dispersed into a colloidal phase with exposure to water, and were washed with 0.5 M HCl in ethanol instead. To probe the fate of the different reactants, we purchased uniformly ^{13}C-enriched glucose from Cambridge Isotopes and taurine with either ^{13}C- or ^{15}N-enrichment to >95% from Isotec. Three different selective ^{13}C and ^{15}N-labeling combinations for the GTaur materials were prepared, as shown in Figure 1. Combining ^{15}N-labeled taurine and uniformly ^{13}C-labeled glucose, the structures of the N-C linkages can be determined with 1D and 2D ^{15}N-^{13}C NMR experiments.[40,41]

To test the hydrothermal stability of the GTaur material, a co-precipitate of glucose, taurine, and KOH in 4:1:1 molar ratio was pyrolyzed at 250^{o}C (4GTaur) and washed with 0.5 M

HCl. The resulting solid was milled using a cryo-mill in two 1-minute cycles at 10 rps with 1 minute between grinding. An acid wash with 5 M HCl stirring overnight at room temperature was followed by rinsing with copious amounts of E-pure water, and drying in a vacuum oven overnight (120 °C). The same treatment at 160°C under autogenous pressure for 24 hours as described previously[19,20] was used to test the hydrothermal stability of the sulfonic groups, which was assessed by CHNS analysis and catalytic testing.

Materials Characterization

Elemental and XPS analysis.

Elemental analyses of materials in terms of mass % of carbon, hydrogen, nitrogen, and sulfur (CHNS) were performed using a PE 2100 Series II combustion analyzer (Perkin Elmer Inc., Waltham, MA). The data of the GTaur materials, which were prepared with KOH, were corrected for the cation mass fraction estimated by mass balance analysis, which is confirmed by K:N molar ratios near unity (1.03 – 1.45). The chemical state of sulfur was analyzed using a Physical Electronics 550 Multitechnique XPS system employing a standard Al electron source. The samples were run at 10^{-9} Torr and mounted on double-sided tape. Charging was corrected for by adjusting the carbon peak to 284 eV.

Solid-state NMR

NMR spectra were measured using a Bruker Biospin DSX400 spectrometer at 100 MHz for ^{13}C and 40 MHz for ^{15}N with ^{1}H decoupling at 400 MHz, using magic-angle spinning (MAS) of 4-mm rotors in double- and triple-resonance probe heads.

Quantitative ^{13}C NMR.

Quantitative ^{13}C MAS spectra were obtained on labeled materials using direct polarization (DP) with 45 s recycle delays on ^{13}C-enriched materials, and using multiCP on unlabeled samples.[48] Given the low signal-to-noise ratio, and longer relaxation times, DP experiments on the unlabeled materials are time consuming. The multiCP sequence [48,52] solved this problem, showing excellent agreement with DP spectra for a wide variety of materials, including low to moderate temperature carbon materials.[48] Our multiCP/MAS experiments used five 1.1-ms 90-100% ramp CP periods and repolarization delays of 0.9 s under 14 kHz magic-angle spinning (MAS).[48] The DP/MAS experiments used a 4.3 μs ^{13}C 90° pulse length. Following a Hahn echo to refocus ^{13}C magnetization,[47] the signal was detected with ^{1}H decoupling of $|\gamma B_1| = 2\pi$ 65 kHz. Corresponding spectra of nonprotonated C and mobile segments (including CH_3) were obtained after 68 μs of recoupled ^{1}H-^{13}C dipolar dephasing before detection.[47]

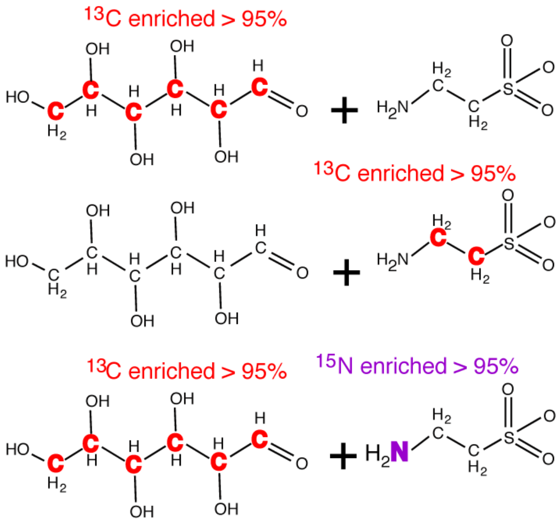

Figure 1. Three selective isotope enrichment combinations in the reactions of glucose and taurine. ^{13}C and ^{15}N are indicated by bold letters.

2D ^{15}N-^{13}C NMR.

In order to detect the connectivities between glucose-^{13}C and taurine-^{15}N on GTaur materials produced using the isotopic labeling indicated in Figure 1, the 2D ^{15}N-^{13}C heteronuclear single quantum (HSQC) pulse sequence [53] with REDOR [54] recoupling of 1.4 ms duration was applied in a ^{1}H-^{13}C-^{15}N triple-resonance probe, at a MAS frequency of 7 kHz with 4-pulse total suppression of spinning sidebands (TOSS) applied before detection. The same experiment was also performed with ^{1}H dipolar dephasing before detection, and with short cross polarization of 50 μs duration, to select nonprotonated- and protonated-carbon signals, respectively. The total experiment time was ~18 h per 2D spectrum.

MultiCP/MAS ^{15}N NMR.

Nearly quantitative ^{15}N MAS NMR spectra were obtained using multiCP with five ramp CP periods of 5.5-ms total duration and 0.9-s repolarization delays, at 7 kHz MAS, with a Hahn spin echo before detection. The ^{15}N 90° pulse length was 10 μs. The measuring time per spectrum was 8 h.

A selective multiCP/MAS spectrum of nonprotonated N was obtained by ^{1}H-^{15}N dipolar dephasing of 2 t_r duration before detection, with recoupling of the heteronuclear dipolar interactions by two ^{1}H 180° pulses.[40] Partial dephasing of the nonprotonated nitrogen was corrected for by multiplication with 1.3, the correction factor determined in a ^{15}N-tBOC proline model compound.

Combined ^{13}C{^{15}N} and ^{13}C{^{1}H } spectral editing.

Signals of C bonded to N, and their complement, peaks of C not bonded to N, were selected by ^{13}C{^{15}N} REDOR [54] of Nt_r = 1.4 ms duration.[40] Spectra recorded with (S) and without (S_0) 180° pulses on the ^{15}N channel contain signal mostly of C not bonded to N and the full reference signal S_0, respectively. The difference $\Delta S = S_0 - S$ derives selectively from C bonded to N, with <10% contributions of C separated from N by two bonds. A spectrum purely of C not bonded to N, without residual C-N signals, was obtained as $S' = S - 0.15\ \Delta S$. The experiments were performed at 7 kHz MAS with TOSS before detection.

Selection of CH_n signals was achieved by short (80 μs) cross polarization combined with 40-μs dipolar-dephasing difference, which in combination with $^{13}C\{^{15}N\}$ REDOR yielded selective spectra of NCH_n (ΔS) and of CH_n not bonded to N ($S - 0.15\ \Delta S$). Conversely, signals from nonprotonated carbons and mobile segments were selected by 40 μs of dipolar dephasing, and combined with $^{13}C\{^{15}N\}$ REDOR to give selective spectra of nonprotonated C bonded to N and of nonprotonated or mobile C not bonded to N.

Structural model.

A model of the average chemical structure of the sulfonated aromatic-rich material made from glucose and taurine was generated based on the quantitative 1D and spectrally edited 2D ^{13}C NMR spectra as well as elemental analysis (C, H, N, S, and then O by difference), which provide relative amounts of key structural fragments and atomic compositions and thus greatly constrain the possible structures. Integration of the one-dimensional ^{13}C NMR spectra directly provided quantitative amounts of major functional groups present, including ketones, carboxylic acids, protonated and nonprotonated aromatic C, O-alkyl and nonpolar alkyl C, see Table 1. Cross peaks in the spectrally edited two-dimensional NMR spectra were used to identify the predominant linkage patterns of the aromatic subunits and the ketones.

Catalytic activity

Catalyst performance was tested by ester formation of acetic acid and methanol, which is sensitive to the number of acidic sites and their pK_a value.[55] Reactions were run at 40°C in a 10-mL Alltech reactor loaded with 6 M methanol and 3 M acetic acid in dioxane (total volume 7 mL) and 10 mg of the sulfonated material. By running the reactions at low conversions (<5%), initial rates could be compared. Tests with a range of stir rates showed that no mass transfer effects occurred for stir rates >200 rpm. The products were analyzed using an Agilent 7890A gas chromatograph with a flame-ionization detector. The activity per mass of catalyst was compared, with units of mmol acetate formed min^{-1} (g $catalyst)^{-1}$.

Results

We report on four differently functionalized aromatic-rich materials, made by reaction of glucose with sulfonic-acid, phosphonic-acid, pyridine-, and piperidine-functionalized amines, at several different temperatures. Given the importance of sulfonated carbon materials as strong-acid catalysts and the availability of isotopically labeled starting materials, the most exhaustive NMR characterization was performed on the sulfonic-acid material ('GTaur'), made by reaction of glucose and taurine, $^{+}H_3N\text{-}CH_2\text{-}CH_2\text{-}SO_3^{-}$, a naturally occurring sulfonated amine, at 250°C. Also, in this material the sulfur content can be monitored easily by CHNS analysis and its oxidation state by XPS.

Temperature dependence of N and S incorporation

Figure 2 shows the CHNS data for the GTaur material as a function of synthesis temperature. The data demonstrate the desired high levels of S and N incorporation, in particular between 250°C and 350°C, and progressive carbonization with H and O loss. Assuming that oxygen accounts for the remaining mass not accounted in CHNS, one finds an S:O molar ratio of 1:6 at 250°C and 1:3 at 350°C. The high S content at 350°C may suggest that this is the optimum synthesis temperature, but the NMR analysis presented in the following reveals undesirable aromatization of the alkyl linkers at 350°C and above.

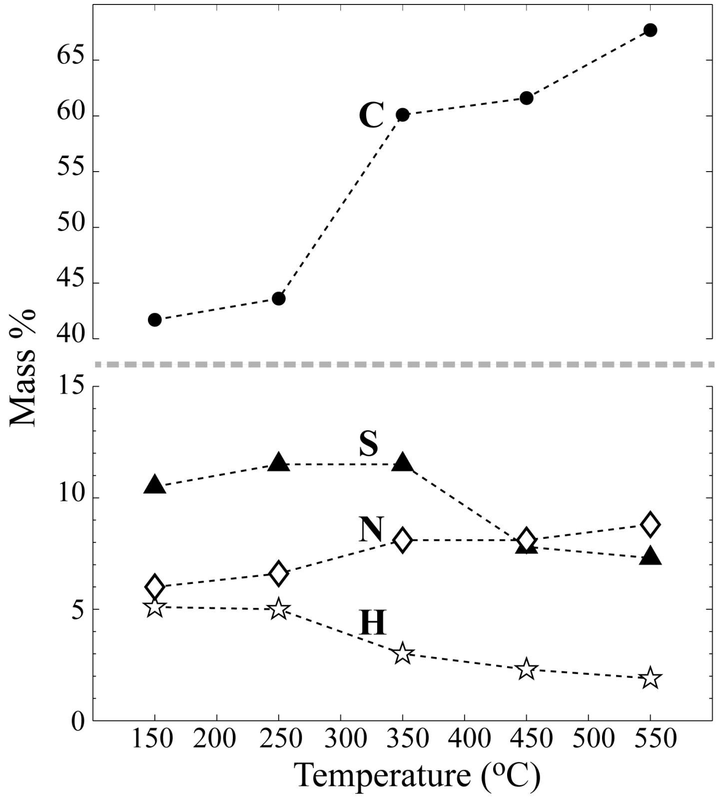

Figure 2. Mass % of C, N, S of GTaur (1:1 glucose:taurine) vs. synthesis temperature (held for 10 hours).

^{13}C NMR: Aromatic matrix and functional groups in glucose–taurine materials. The chemical structure of the GTaur material has been probed comprehensively by NMR. Shown in Figure 3a-c are quantitative ^{13}C NMR spectra for GTaur materials produced at 250°C without enrichment, $^{13}C_6$ glucose, and with $^{13}C_2$ taurine, respectively. The spectrum of ^{13}C in natural abundance shows the signals of carbons originating from both glucose and taurine, while the 90-fold isotopic enrichment of one component provides selective spectra of the carbons originating from that component. As expected, the spectrum of all carbons in (a) can be matched by a weighted superposition of the selective spectra of glucose- and taurine-derived carbons in (b) and (c), respectively.

The most prominent signal of the carbons derived from glucose, see Fig. 3b, is from aromatic rings, between 150 and 100 ppm. Unlike Maillard-reaction products generated at lower temperatures,[38,40,41] the present samples contain hardly any residual OCH or OCH_2 groups. CH_3 groups bonded to C resonating at < 28 ppm show two fairly strong peaks, at 23 and 12 ppm, which can be assigned to acetyl or N-acetyl and to pyrrole-bonded CH_3, respectively. These assignments have been confirmed by corresponding cross peaks in ^{13}C-^{13}C NMR, see Fig.S1.

The selective spectrum of C originating from taurine, see Fig. 3c, is particularly simple. It shows two prominent peaks, at 53 and 42 ppm, which account for ~60% of the total intensity and are close to the resonance positions of the CH_2 groups bonded to S and N, respectively, in taurine. This proves that a large fraction of taurine is incorporated with the N-CH_2-CH_2-SO_3 side group intact. This assignment is confirmed by CH_2 and CH spectral editing, see Fig. S2. The shoulder at <35 ppm is from CH_2 and CH_3 groups not bonded to heteroatoms, which must be regarded as degradation products. The only other significant signal observed is from aromatic carbons (27% of the total area after correction for glucose ^{13}C natural-abundance background). Even some of these aromatic carbons are bonded to -CH_2-SO_3 functional side groups. This is evidenced by cross peak of the aromatic carbons with alkyl C resonating at 53 ppm in the 2D ^{13}C-^{13}C NMR spectrum of the same sample shown in Fig. 3d. The C_{arom}-CH_2-SO_3 structure can be expected to be particularly hydrothermally stable [27] and contributes to the intensity of the large 53-ppm CH_2 peak in Figs.3a,c.

Generally, the ^{13}C-^{13}C cross peaks in the 2D spectrum of Fig. 3d show that many taurine molecules are incorporated into aromatic rings without breaking the ^{13}C-^{13}C bond. The observed aromatic chemical shifts between 130 and 150 ppm are consistent with bonding of the aromatic carbon to N in pyrrole or pyridine rings, which would again leave the S-C-C-N backbone bonds of taurine intact. The interaromatic cross peak at 128 ppm CH and 135-145 ppm C_{nonp} resonance positions can be tentatively assigned to CH=C_{nonp}-N- in pyridine rings, where loss of the SO_3 group seems likely, or to arene CH=C_{nonp}-SO_3.

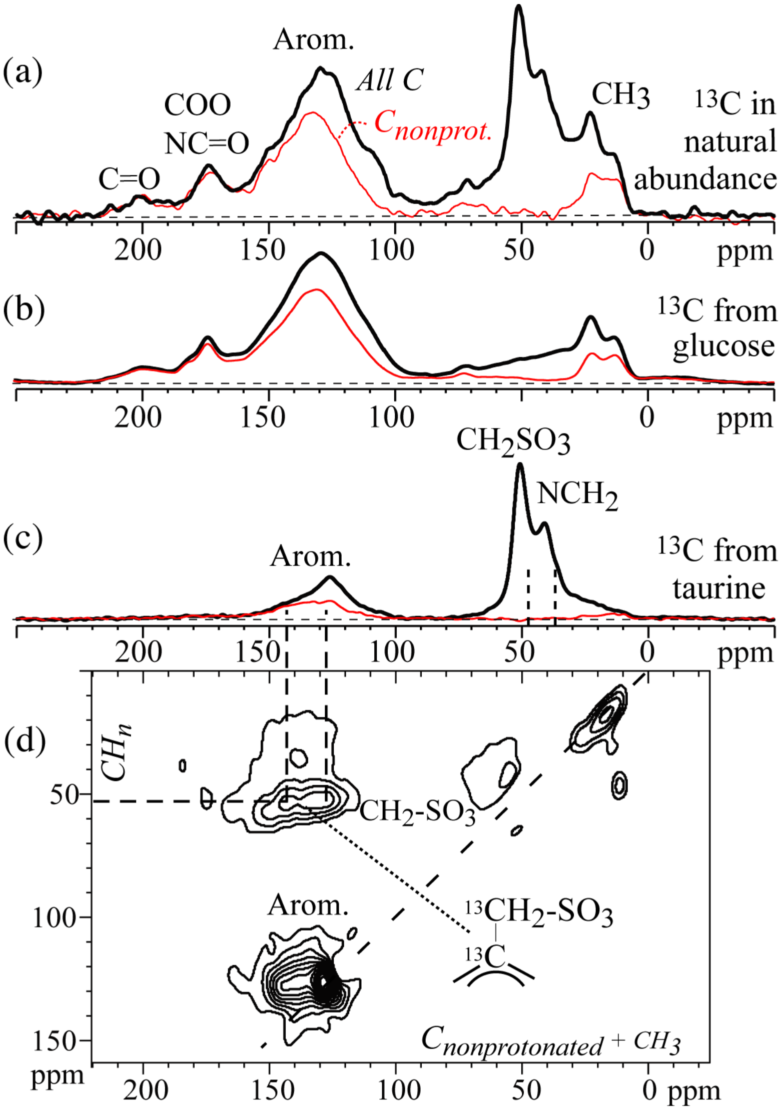

Figure 3. (a-c) Quantitative ^{13}C NMR spectra of sulfonic-acid functionalized aromatic-rich materials made by reaction of glucose with taurine (1:1) at 250°C. Corresponding spectra of nonprotonated C and mobile segments are shown as thin red lines. (a) MultiCP/MAS spectra of all carbons (^{13}C in natural abundance). (b) Direct-polarization spectra of glucose-derived carbons ($^{13}C_6$ glucose). (c) Direct polarization spectrum of taurine-derived carbons ($^{13}C_2$ taurine); the peak positions of crystalline taurine are indicated by vertical dashed lines. (d) ^{13}C-^{13}C EXPANSE NMR spectrum of the same sample as in (c), showing a cross peak between aromatic C and CH_2SO_3.

These data show that nearly 60% of the CH_2 groups originating from taurine are retained, resonating at chemical shifts characteristic of the sulfonic acid fragment and more than 72% of the glucose has been converted to sp^2-hybridized carbons. Results from XPS (see Fig. S3) and CHNS elemental analysis are consistent with the NMR findings, verifying that the sulfur is retained and remains predominantly in the desired C-SO_3H form.

Table 1: Peak areas (in %) from ^{13}C spectra of the GTaur material

Integration limits (ppm)	220-185	185-162	162-96	96-65	65-29	29-0
Assignment	C=O	COO	Arom.	OAlkyl	CH/CH_2	CH_3
No ^{13}C enrichment: **All C**	3%	6%	44%	5%	31%	12%
$C_{nonprot}$	3%	6%	27%	1%	1%	0%
>95% ^{13}C taurine: **All C**	1%	2%	28%	2%	58%	8%
$C_{nonprot}$	0%	1%	15%	0%	2%	0%
>95% ^{13}C glucose: **All C**	4%	8%	61%	4%	10%	13%
$C_{nonprot}$	3%	7%	40%	2%	1%	0%

^{15}N-based NMR: Nitrogen bonding in glucose–taurine materials.

The incorporation of the amine group of the bifunctional molecules into the glucose-derived matrix mostly provides the crucial covalent, hydrothermally stable attachment of the functional groups. The chemical environment of the nitrogen atoms after reaction can be determined by ^{15}N, ^{15}N-^{13}C, and $^{13}C\{^{15}N\}$ NMR of a material made by reacting ^{15}N-taurine and $^{13}C_6$-glucose at 250°C.

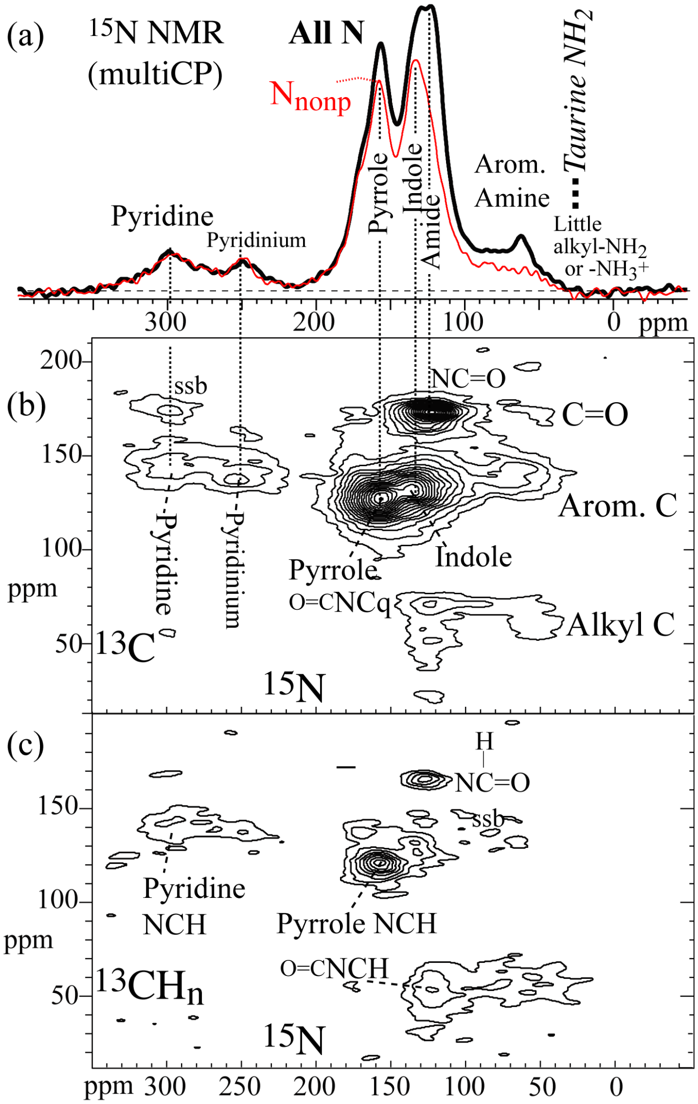

Figure 4. (a) MultiCP/MAS ^{15}N NMR spectra of a sulfonic-acid functionalized aromatic-rich material made from ^{13}C glucose and ^{15}N-enriched taurine (1:1 molar ratio) at 250°C, measured at 7-kHz MAS. Thick lines: Spectrum of all nitrogen. Thin line: Corresponding spectrum of nonprotonated N, obtained after 280 μs of recoupled dipolar dephasing and scaled up by a dephasing factor of 1.3 determined in a model compound, ^{15}N-tBOC proline. The frequency position of taurine NH$_2$ is indicated near the right end of the spectrum. (b, c) Two-dimensional ^{15}N-^{13}C NMR spectra of the same material as in (a), at 7-kHz MAS, enabling ^{15}N peak assignment. (b) Spectrum of all C bonded to N. (c) Spectrum of protonated C bonded to N, selected by short CP and dipolar-dephasing difference.

^{15}N NMR: Quantification of N environments, and tertiary N

The ^{15}N NMR spectrum shown in Fig. 4a provides an overview of the chemical environments into which nitrogen is incorporated. Most importantly, the ^{15}N spectrum exhibits no NH_2 signal near 40 ppm from unreacted taurine, or from taurine incorporated only via reaction of its sulfonate group. This proves that all taurine has been incorporated by reaction of the NH_2 group. The ^{15}N spectrum is dominated by signals of N in five-membered heterocycles and amides between 170 and 100 ppm, with smaller signals from pyridinic N near 300 ppm and aromatic amines between 50 and 90 ppm. Note that hardly any alkyl-NH_2 or alkyl-NH_3^+ groups, which would resonate at <50 ppm, are observed.

Unambiguous assignment of the ^{15}N peaks, in particular the signal at 133 ppm, is possible based on the ^{15}N-^{13}C spectra shown in Fig. 4b,c. Here, the most intense peaks in the ^{15}N spectrum, at 158 and 133 ppm, can be assigned to pyrrole and indole nitrogen, respectively, based on the cross peaks with aromatic C at 125 and 135 ppm, respectively. Among aromatic heterocycles, a ^{15}N chemical shift of 133 ppm is characteristic of indole (benzopyrrole).[56] The selective ^{15}N-correlation spectrum of protonated carbons in Fig. 4c shows that most of the N-C carbons of indole are not protonated; indeed, one of the two C-N carbons in indole is in the bridgehead to the 6-membered aromatic ring and cannot be protonated. The amide ^{15}N near 122 ppm has a cross peak with the amide C=O carbon near 175 ppm, as expected. Cross peaks to C resonating between 70 and 30 ppm show that some amide N is also bonded to alkyl C, both nonprotonated and protonated. A fairly small but distinctive signal of N(C-H)=O is seen in the spectrum of Fig. 4c near 165 in the ^{13}C dimension and can be assigned to a formamide moiety. For the aromatic amines with ^{15}N resonances between 50 and 90 ppm, cross peaks in the ^{15}N-^{13}C spectrum confirm bonding to aromatic C. Below, we show that these amines are mostly tertiary (bonded to three C atoms), so the alkyl carbon cross peaks also observed in this ^{15}N chemical shift range are from alkyl bonding partners.

Smaller peaks in the ^{15}N-^{13}C spectrum include signal at 250 ppm ^{15}N and 142 ppm ^{13}C. The chemical shift would match that of the second N (not bonded to H or C outside the ring) in an imidazole ring, or that of a pyridinium nitrogen bonded to three carbons. The latter assignment is more probable given the >135 ppm ^{13}C chemical shifts of these CH groups and the <130 ppm resonance position of CH in imidazole.[57] A broad secondary maximum seen near 300 ppm ^{15}N and 145 ppm ^{13}C can be attributed to pyridine-like N bonded to pyridinic CH and nonprotonated C. A cross peak between ^{15}N at 120 ppm and nonprotonated C at 70 ppm can be assigned to a structural fragment (indole-(C=O)-C(CH_3, CH_2)-NC=O) that has been observed prominently and identified by spectral editing in a glucose-glycine Maillard-reaction product made at lower temperature.[51]

The peak areas in the ^{15}N spectrum give 8% pyridine, 5% pyridinium, 35% pyrrole, 22% indole, 20% amide, and 10% aromatic amine. A spectrum of nonprotonated nitrogen (thin line in Figure 4a), selected by 280 μs of recoupled dipolar dephasing, allows determination of the number of carbons to which the nitrogen atoms are bonded. The limited dipolar dephasing shows that most N atoms are not bonded to hydrogen, which means that they must be bonded to three carbon atoms; one of these is usually the carbon already bonded to N in the precursor,[40,41] in this case CH_2 of taurine. This also applies to the aromatic amides resonating between 50 and 90 ppm, most of which must be tertiary since they are not protonated.

Integration of the peaks in the ^{15}N multiCP/MAS spectra of Fig. 4a shows that tertiary N, i.e. with the linkage to taurine C intact, accounts for more than half of all N. Of these, 23% are found in pyrrole, ca. 20% in indole rings, and 8% in tertiary amides and amines. In addition, we have documented 20% of pyrrole with protonated N as well as pyridine rings that have carbon-bonded -CH_2-SO_3 side groups. Thus, in total nearly 60% of the taurine molecules produce CH_2-SO_3 groups linked to aromatic rings. An additional 24% is incorporated into secondary amides and amines, where the linkage to -CH_2-SO_3 may also be intact.

Table 2. Integral values for ^{15}N multiCP/MAS spectra of GTaur 250 material.

Integral (ppm)	350-267	267-212	212-141	141-91	91-0
All ^{15}N	8%	5%	35%	42%	10%
$^{15}N_{nonprot}$	7%	4%	23%	24%	4%

Identification of glucose C bonded to N, and of arene signals

In order to identify and quantify glucose-derived C bonded to N and its complement, glucose-C not bonded to N, we recorded their signals selectively using $^{13}C\{^{15}N\}$ REDOR NMR applied to a material made from ^{13}C-enriched glucose and ^{15}N-enriched taurine. For additional deconvolution and structural information, this $^{13}C\{^{15}N\}$ dephasing was combined with $^{13}C\{^{1}H\}$ dipolar dephasing, and with short CP plus dipolar dephasing difference. This yields selective spectra of NCH_n, of nonprotonated C bonded to N, of CH_n not bonded to N, and of nonprotonated C not bonded to N, see Fig. 5. As in the ^{15}N and the unselective ^{13}C spectra, in the C-N spectra the signals from aromatic rings are the most pronounced, see Fig. 5a, confirming incorporation of the amine compound into the glucose-derived aromatic matrix.

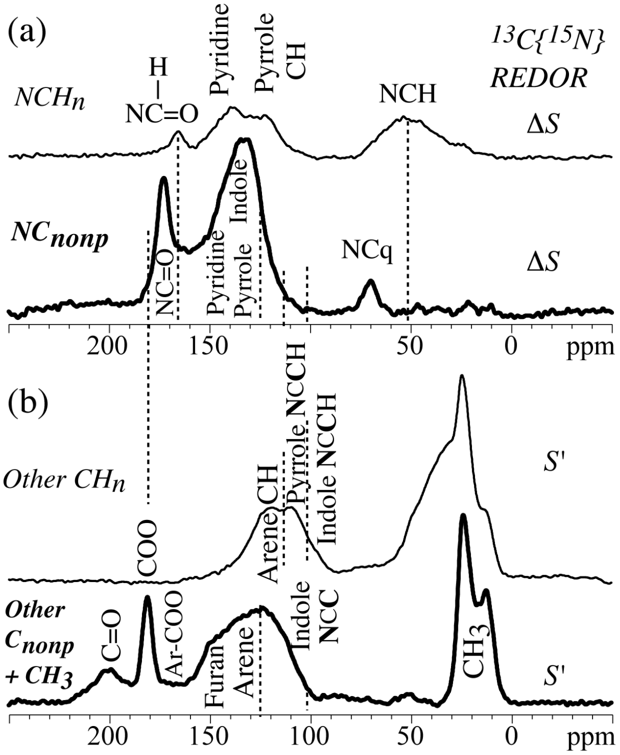

Figure 5. Selective ^{13}C NMR spectra of (a) C bonded to N and (b) C not bonded to N, obtained with spectral editing based on ^{13}C{^{15}N} and ^{13}C{^{1}H} dipolar couplings, in a carbon material made from $^{13}C_6$-glucose and ^{15}N-enriched taurine (1:1 molar ratio), at 7-kHz MAS. (a) Signals of C bonded to N. Top trace: NCH$_n$; bottom trace: Nonprotonated C bonded to N. (b) Signals of C not bonded to N. Top trace: CH$_n$ not bonded to N. Bottom trace: Nonprotonated C not bonded to N. Assignments based on spectral editing, the ^{15}N-^{13}C spectra of Fig. 4, and general ^{13}C chemical shift trends are indicated.

The four spectra in Fig. 5 are quite distinctive and resolve the broad aromatic band of the unselective ^{13}C spectrum in Fig. 3b into at least 4 peaks. In particular, this enables us to separate the strongly overlapping signals of NC in pyrroles in (a) from those of six-membered arene rings in (b). In indoles, carbon 3, which is separated from N by two bonds, has a characteristic downfield chemical shift near 100 ppm (protonated C) or near 110 ppm (nonprotonated C), according to chemical-shift databases. Not being bonded to N, this carbon should give signal in Fig. 5b. Indeed, aromatic CH intensity is clearly observed around 100 ppm, and C$_{nonp}$ signal near 110 ppm.

The sharp peak at 173 ppm is from amide C=O bonded to alkyl or arene carbons, as confirmed by cross peaks in ^{13}C-^{13}C correlation spectra (Fig. S1). Amide C=O bonded to pyrrole rings resonates between 160 and 170 ppm, and can explain the relatively high intensity in that range in Fig. 5a, bottom trace.

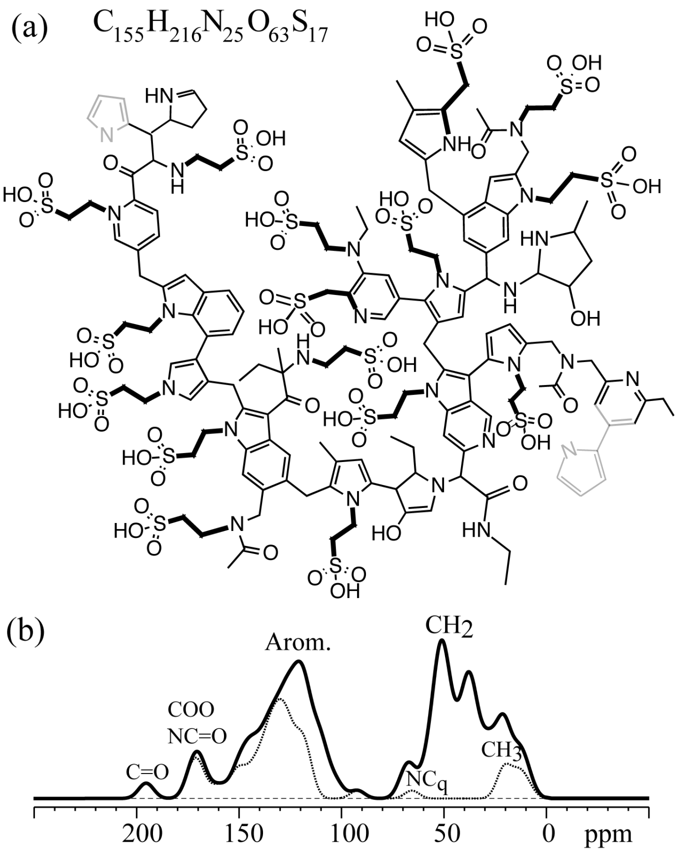

Figure 6. (a) Structural model of a representative “repeat unit” of 1:1 glucose–taurine material made at 250°C as deduced from NMR and elemental analysis. Intact taurine-derived units are highlighted in bold. Structures in gray belong to the next “repeat unit”. (b) Corresponding simulated ^{13}C NMR spectrum, to be compared with the experimental spectrum in Fig. 3a.

Structural model

Based on the structural information from ^{13}C and ^{15}N NMR as well as CHNS analysis, a structural model was developed, see Fig. 6a. Its details were optimized so that the corresponding quantitative ^{13}C NMR spectra, see Fig. 6b, matched those in Fig. 3a. The structure, which should be considered as a typical repeat unit, consists of a network of interconnected indole, pyrrole, and pyridinium rings abundantly substituted by alkyl-linked SO_3H groups.

Effects of pyrolysis temperature

The ^{13}C NMR spectrum of the material heated to 350°C, Fig. 7, lacks the signals from the alkyl segment originating from taurine. This shows that the ethyl sulfonate groups aromatize when heated to 350°C, and that solid-state NMR is an excellent method for determining the optimum pyrolysis temperature. Elemental analysis showed that sulfur is retained in high percentages even after reaction at 550°C (Fig. 2). However, XPS (see spectrum in Fig. S3) indicates that as the temperature is increased to 350°C and beyond, the sulfur is reduced to an SO_2, sulfone-type structure. This is also deduced from an O:S atomic ratio < 3, which does not provide enough oxygen for all sulfur to be in SO_3 groups. The sulfur must be attached to or incorporated into the aromatic scaffold, since NMR shows the loss of the alkyl linkers.

Our detailed characterization has focused on the material synthesized at 250°C , the highest temperature tested that keeps the sulfonic groups intact. The empirical formula derived from CHNS analysis for GTaur materials produced with NaOH or KOH was estimated to be $C_{7.5}H_{6.75}NSO_5Na$ and $C_{6.3}H_{9.2}NS_{0.67}O_4K$, respectively, assuming a fixed N:K ratio and estimating O by difference. This is to be compared to $C_8H_{13}NSO_9Na$ for the precipitate prior to reaction. The observed loss of O and H is an indication of dehydration. Interestingly, the GPyri material, $C_{28}H_{27}N_{4.7}O$, was dehydrated more extensively at temperatures as low as 250 °C. Table 3 shows that this material retains a high N content of 12.5% even after pyrolysis at 500°C.

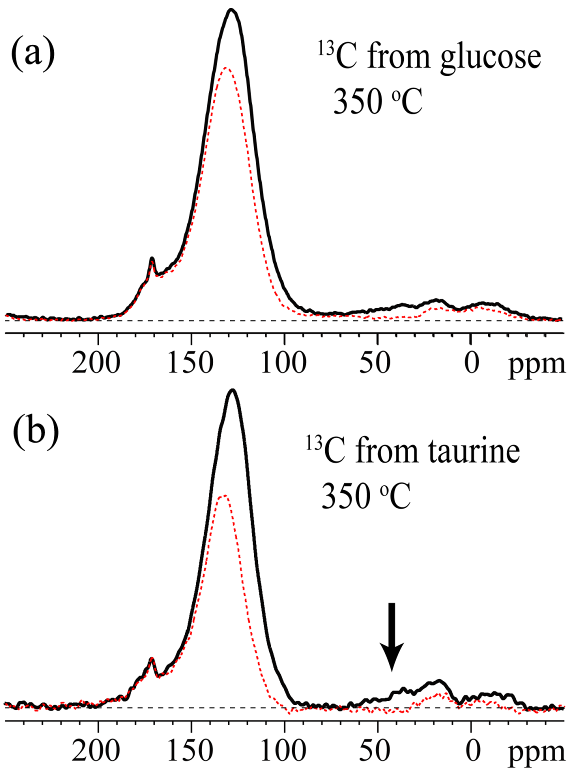

Figure 7. ^{13}C DP/MAS NMR spectra of sulfonic-acid functionalized polyaromatic materials made by reaction of glucose with taurine (1:1) at 350 °C. Corresponding spectra of nonprotonated C and mobile segments are shown as dashed red lines. Material made from (a) u^{13}C-glucose; (b) $^{13}C_2$-taurine. The arrow marks the position of the NCH_2-CH_2-SO_3 methylene signals observed in the material made at 250°C, which are negligible in the 350°C material.

Table 3. Elemental compositions (in wt%) of GPyri and GPip materials made at 250 °C, and the GPyri material pyrolyzed at 500°C.

	C%	H%	N%	Rem%
GPip	71	7.4	11.5	10
GPyri	75	6.6	14.8	3.6
GPyri500	76	2.4	12.5	9

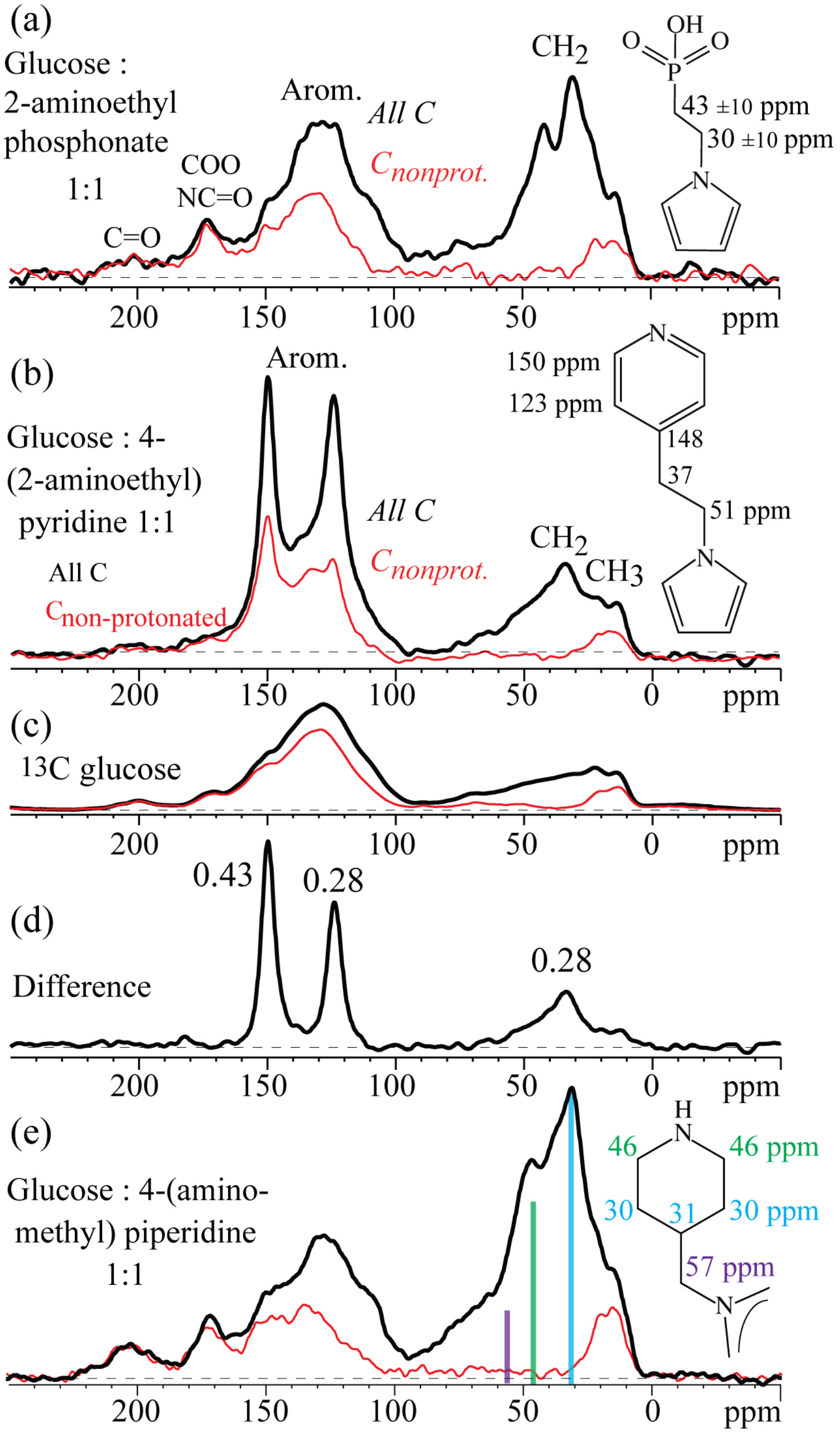

Figure 8. Quantitative multiCP/MAS ^{13}C NMR spectra of functionalized aromatic-rich materials made at 250°C by reaction of glucose with (a) 2-aminoethyl phosphonic acid, (b-d) 4-(2-aminoethyl) pyridine, and (e) 4-(aminomethyl) piperidine, all in 1:1 molar ratios. (c) $^{13}C_6$-glucose derived C in amino ethyl pyridine. (d) Difference between the suitably scaled spectra in (b) and (c), revealing the signals of the ethyl pyridine-derived carbons. Isotopic labeling was used only in (c). Expected sidegroup structures and chemical shifts are shown on the right in (a), (b, and (e).

Glucose–phosphonic-acid material

The spectrum of the phosphonic-acid material in Figure 8a generally shows the expected signals. The aromatic and CH_3 components closely resemble those of the sulfonic-acid material. The prominent CH_2 signals are shifted to the right by about 10 ppm, in agreement with predicted chemical-shift effects of SO_3 vs. PO_3.

Glucose-pyridine material

Figures 8b, c show ^{13}C NMR spectra of GPyri without ^{13}C enrichment and made with $^{13}C_6$ glucose, respectively. Figure 8b exhibits distinctive peaks at 150 and 123 ppm, the characteristic chemical shifts of pyridine, which are absent in the spectrum of the glucose-derived matrix, Fig. 8c. This shows that pyridine is preserved as a pendent group in the structure. The difference spectrum in Fig. 8d, obtained with a scaling factor that minimizes the residual C=O and CH_3 signals, shows the amino ethyl pyridine CH_2 peaks between 35 and 60 ppm with the expected intensity.

Elemental analysis (Table 3) confirms that this material reacts in a fashion similar to the other analogs, since it contains twice more nitrogen than the sulfonic- or phosphonic acid materials due to the N in the pyridine ring. The nitrogen content (15% at 250^{o}C and 12.5% at 500^{0}C) of GPyr is much higher than the values of 7.8%,[13] 6.7%,[12] or 4.1% [58] reported for other carbon- and nitrogen-rich materials and is promising for platinum immobilization and other applications.[13,12,58,59]

Unlike the SO_3 and PO_3 side groups, pyridine does not contain oxygen; thus, the oxygen content of the glucose-derived matrix can be estimated easily in the GPyri material. Elemental analysis shows little oxygen (<5% at 250°C), consistent with NMR, where only 5% C=O, NC=O or COO groups are detected. Our ^{15}N NMR with dipolar dephasing (Fig. 4a) has shown that the protons of the NH_2 group of the amine compound are mostly lost during the reaction; presumably, they combine with OH from glucose to form H_2O and thus facilitate the removal of oxygen from the aromatic-rich matrix.

Piperidine-functionalized material.

The ^{13}C NMR spectra in Fig. 8e show that the synthesis works similarly well with piperidine, another, more basic ($pK_a > 10$) nitrogen-containing ring system. Here, a shorter linker, CH_2, instead of $(CH_2)_2$, connects the functional group to the matrix. The dominant signals of the sp^3-hybridized carbons on the piperidine ring are consistent with the expected 3:2:1 ratio. Additionally, elemental analysis shows a high level of N incorporation, see Table 3.

Catalytic activity

Catalyst testing showed that the acid groups of GTaur and GPhos are active toward the esterification of methanol and acetic acid (Fig. 9). Although both activities are relatively low, they are substantially above the baseline conversion without catalyst present. GTaur is more active than the GPhos material, as expected based on the lower pK_a value of sulfonic relative to phosphonic acid.

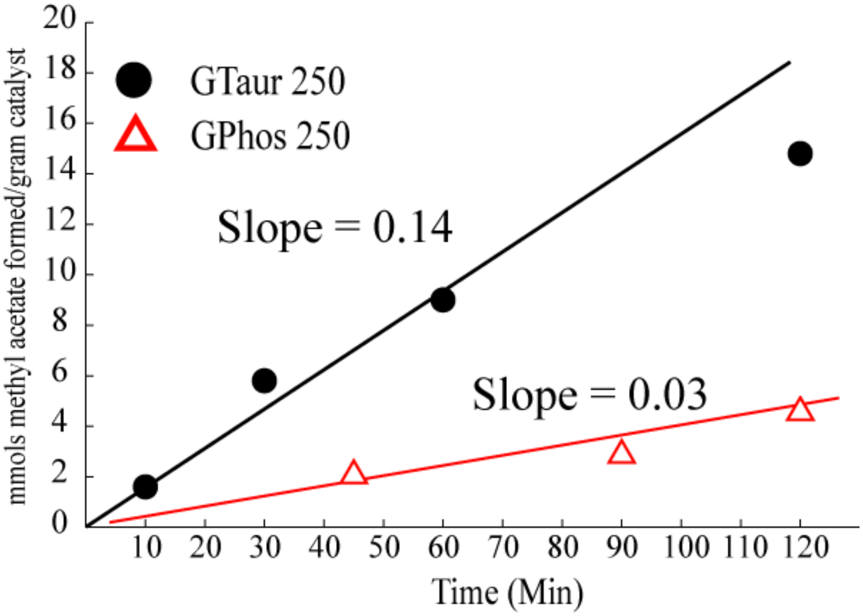

Figure 9. Verification of catalytic activity of the GTaur and GPhos materials, monitored via the esterification reaction of acetic acid and methanol. Reactions were run at 40°C in a 10-mL Alltech reactor loaded with 6 M methanol and 3 M acetic acid in dioxane, with 10 mg of the catalyst material. GTaur (black circles) has a substantially higher reaction rate (0.14 mmols/gram catalyst/min) than GPhos (0.03 mmols/gram catalyst/min), shown as red triangles.

Hydrothermal stability of 4GTaur catalyst

As emphasized in the Introduction, a primary goal of this research was to improve the hydrothermal stability of sulfonic-acid catalysts, in particular by reducing the leaching of sulfur, which is pronounced in aromatic materials with directly bonded SO_3H groups.[19,20] The mass% sulfur from CHNS analysis and the catalytic activity of 4Gtaur after repeated hydrothermal treatments are shown in Figure 10. The data in Figure 10(a) demonstrate that sulfur is retained to a far greater extent (> 65% of the initial sulfur after three hydrothermal cycles) than in sulfonated carbons produced via electrophilic aromatic substitution, which all retained less than 33% of the initial sulfur after the same treatment.[19,20] Reaction rates shown in Figure 10(b) are seen to increase as a result of the first hydrothermal treatment, followed by a gradual loss in activity, which after three hydrothermal cycles is again close to the initial rate. We speculate that the decrease in activity may reflect esterification of SO_3 groups [38] or formation of SO_3K from cations in the reaction mixture. The initial increase may be due to increased accessibility of sulfonate groups after washing-out of low-molar mass compounds during the hydrothermal treatment.

In order to improve the catalytic activity, post-synthesis treatments were applied to the 4GTaur material, including cryo-milling and acid washes; results are shown in Table 4. The catalytic activity of the material directly out of the reactor is below the detection limit, as expected, and reflects SO_3 being almost entirely in the SO_3K form. Increasing the acid concentration from 0.5 to 5 M leads to a three-fold increase in reaction rate, and cryo-milling in a further two-fold improvement.

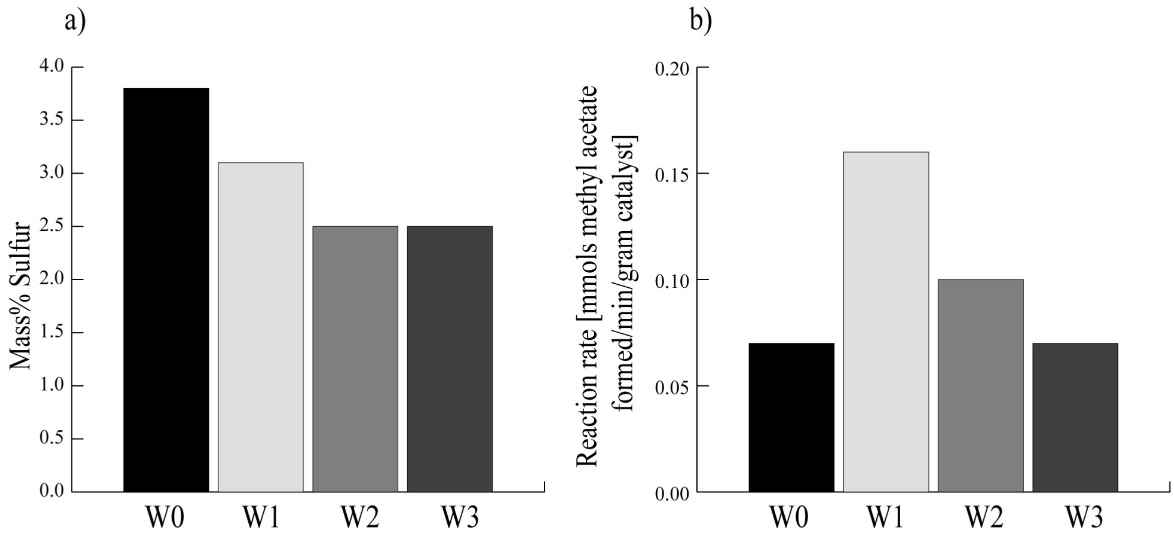

Figure 10. Hydrothermal stability testing of 4GTaur (4:1 glucose:taurine ratio). The plots show (a) sulfur retained and (b) catalytic activity after increasing numbers of 24-h hydrothermal treatments at 160°C. Reactions were run at 40°C in a 10-mL Alltech reactor loaded with 6 M methanol and 3 M acetic acid in dioxane, with 10 mg of the catalyst material.

Table 4. Effect of cryomilling and HCl treatment of 4GTaur on the initial catalytic rate of the esterification reaction of acetic acid and methanol.

Sample	Reaction rate [mmols methyl acetate formed/min/(g catalyst)]
4GTaur no milling, no acid wash	No reaction
4GTaur no milling, 0.5 M HCl	0.07
4GTaur no milling, 5 M HCl	0.20
4GTaur milled, 5 M HCl	0.37
4GTaur milled, 5 M HCl, acetone wash	0.41

Discussion

The NMR and CHNS characterization has confirmed the successful synthesis of highly acid- or base-functionalized aromatic-rich materials based on the Maillard reaction of glucose with functionalized primary amines, in combination with low-temperature pyrolysis. The glucose molecules produce an aromatic-rich matrix that strongly bonds to the nitrogen of the amine group, mostly through two covalent carbon-nitrogen bonds. The starting materials have very high concentrations of functional groups, and NMR has shown that about 2/3 of these are retained intact after the thermal treatment at 250°C. At this synthesis temperature, the functional group mostly remains connected to the nitrogen through the linker originally present in the amine molecule. They exhibit the expected relatively good hydrothermal stability. The catalytic activity of the sulfonic-acid materials was increased by suitable post-synthesis treatments. Given that the surface area of the materials studied here is low (< 1 m^2/g), the catalytic performance may be further enhanced by increasing the surface area. Investigations along these lines are in progress in our laboratory.

Synthesis without a stoichiometric amount of base led to poorer taurine incorporation, with the NMR spectra showing sharp peaks from unreacted taurine. This indicates that the use of NaOH to deprotonate the nitrogen was a successful approach for improving the reaction with the aldehyde on glucose and the uniformity of the material. The basic conditions and increased temperature have enhanced the aromaticity compared to corresponding traditional Maillard reaction products.[40,41]

All materials have similar aromatic-rich backbones resulting from carbon originating from glucose. The limited degree of aromatic condensation is similar as in other carbon materials made at moderate pyrolysis temperatures,[19,20,45] and the degree of sulfonation is higher.[19,20] The NMR analyses have highlighted the complex nature of carbon materials made by pyrolysis and similar processes at low temperature, which is difficult to elucidate with IR, Raman, or surface techniques. Structural cartoons with large fused aromatic clusters shown in some publications[16,17,31,32,36] are not realistic models of carbon materials produced at moderate temperatures.

Given the robust nature of the synthesis evident from the variously functionalized amines that react in an analogous manner, multi-functional catalysts containing both acidic and basic functional groups from this platform can be envisaged. One excellent example of the utility of heterogeneous catalysts with both acidic and basic residues is the dehydration of glucose to hydroxyl-methyl furfural, where a base-catalyzed isomerization to the ketose sugars is followed by acid-catalyzed dehydration.[60]

In addition to incorporation of numerous Brønsted acid sites, the materials synthesized here display various interesting properties that can be tuned by changing the pyrolysis temperature, pyrolysis environment, and ratio of glucose:taurine. We have demonstrated this principle producing an insoluble solid-acid catalyst (4GTaur) by increasing the ratio of glucose:taurine to 4:1. Materials produced with a 1:1 glucose:taurine ratio at 250°C form a colloid in water, but are insoluble in alcohols. This colloidal behavior in water makes it easy to disperse the material onto surfaces and template the formation of nanocomposites. The polyanionic nature of the GTaur materials was verified by running them in a 1% agarose gel against a DNA ladder, see Fig. S4. We observed a migration rate similar to that of a 5 kDa fragment of DNA. While the migration rate is a function of numerous factors including the charge:mass ratio, and morphology, this does indicate that the material is polyanionic, and composed of relatively high molecular weight fragments. This could potentially be useful for formation of nanocomposites and deposition onto surfaces, recently shown[61] to be an effective method to disperse Pd catalyst.

The aromatic materials produced have very high amounts of nitrogen incorporated into the aromatic matrix that are retained even at fairly high pyrolysis temperatures. Such nitrogen-rich carbon materials have desirable properties as Pt supports in fuel cell applications,[3,59,62] supercapacitors,[12] and dispersion of Pd catalyst.[13]

Conclusions

We have described a simple one-step procedure to produce highly functionalized aromatic-rich materials through the reaction of a functionalized molecule containing a primary amine with a reducing sugar. This procedure, which can be broadly generalized, results in an aromatic-rich scaffold where the functional group of the reactant is connected via a linker (often ethyl) that is attached to the matrix via nitrogen mostly with two bonds to matrix carbons. The structure has been characterized in detail by ^{13}C, ^{15}N, and ^{15}N-^{13}C NMR complemented by elemental analysis, which confirmed that the aromaticity and degree of aromatic condensation resembles that of other carbon materials made at moderate pyrolysis temperatures. NMR also showed that the alkyl linkers mostly remained intact at a synthesis temperature of 250°C, but were aromatized at 350°C. The sulfonic-acid functionalized material made from glucose and taurine at 250°C was shown to be catalytically active and has better hydrothermal stability than sulfonated carbons produced via electrophilic aromatic substitution.

The Maillard reaction synthesis platform introduced here has several desirable characteristics. It is versatile and can be used to produce aromatic-rich materials with a wide variety of different functional groups by simply changing the R-group of the primary amine. Large amounts of nitrogen can be incorporated into the aromatic matrix by using nitrogen-rich primary-amine reactants. Lastly, this approach is environmentally appealing given that glucose, one of the primary reactants, is a renewable material.

Acknowledgements

The authors would like to acknowledge NSF (award number EEC-0813570) for generously supporting this work, as part of the Center for Biorenewable Chemicals (CBiRC). Jim Anderegg graciously ran and expertly helped interpret the XPS results. Any opinions, findings, and conclusions, or recommendations expressed herein are those of the authors and do not necessarily reflect the views of the National Science Foundation.

References

(1) Zhi, L.; Hu, Y.-S.; Hamaoui, B. E.; Wang, X.; Lieberwirth, I.; Kolb, U.; Maier, J.; Müllen, K. *Adv. Mater.* **2008**, *20*, 1727.

(2) Janaun, J.; Ellis, N. *J. App. Sci.* **2010**, *10*, 2633.

(3) Vinayan, B. P.; Ramaprabhu, S. *Nanoscale* **2013**, *5*, 5109.

(4) Kiciński, W.; Szala, M.; Bystrzejewski, M. *Carbon* **2014**, *68*, 1.

(5) Stöhr, B.; Boehm, H. P.; Schlögl, R. *Carbon* **1991**, *29*, 707.

(6) Jagtap, S. R.; Raje, V. P.; Samant, S. D.; Bhanage, B. M. *J. Mol. Catal. A: Chem.* **2007**, *266*, 69.

(7) Jagtap, S. R.; Bhor, M. D.; Bhanage, B. M. *Catal. Commun.* **2008**, *9*, 1928.

(8) Feng, W.; Borguet, E.; Vidic, R. D. *Carbon* **2006**, *44*, 2998.

(9) Kuroki, S.; Nabae, Y.; Chokai, M.; Kakimoto, M.-a.; Miyata, S. *Carbon* **2012**, *50*, 153.

(10) Kim, Y. J.; Lee, H. J.; Lee, S. W.; Cho, B. W.; Park, C. R. *Carbon* **2005**, *43*, 163.

(11) Zhou, P.; Papanek, P.; Bindra, C.; Lee, R.; Fischer, J. E. *J. Power Sources* **1997**, *68*, 296.

(12) Zhao, L.; Fan, L.-Z.; Zhou, M.-Q.; Guan, H.; Qiao, S.; Antonietti, M.; Titirici, M.-M. *Adv. Mater.* **2010**, *22*, 5202.

(13) Li, Z.; Liu, J.; Xia, C.; Li, F. *ACS Catal.* **2013**, *3*, 2440.

(14) Pham, H. N.; Anderson, A. E.; Johnson, R. L.; Schmidt-Rohr, K.; Datye, A. K. *Ang. Chem. Int. Ed.* **2012**, *51*, 13163.

(15) Dehkhoda, A. M.; West, A. H.; Ellis, N. *Appl. Catal. A: Gen.* **2010**, *382*, 197.

(16) Sydlik, S. A.; Swager, T. M. *Adv. Funct. Mater.* **2013**, *23*, 1873.

(17) Tessonnier, J.-P.; Barteau, M. A. *Langmuir* **2012**, *28*, 6691.

(18) Yasuda, S.; Asano, K. *J. Wood Sci.* **2000**, *46*, 477.

(19) Kang, S.; Ye, J.; Zhang, Y.; Chang, J. *RSC Adv.* **2013**, *3*, 7360.

(20) Anderson, J. M.; Johnson, R. L.; Schmidt-Rohr, K.; Shanks, B. H. *Carbon* **2014**, *74*, 333.

(21) Onda, A.; Ochi, T.; Yanagisawa, K. *Topics in Cat.* **2009**, *52*, 801.

(22) Yantasee, W.; Lin, Y.; Alford, K. L.; Busche, B. J.; Fryxell, G. E.; Engelhard, M. H. *Sep. Sci. Technol.* **2004**, *39*, 3263.

(23) Macías-García, A.; Valenzuela-Calahorro, C.; Espinosa-Mansilla, A.; Bernalte-García, A.; Gómez-Serrano, V. *Carbon* **2004**, *42*, 1755.

(24) Kitano, M.; Arai, K.; Kodama, A.; Kousaka, T.; Nakajima, K.; Hayashi, S.; Hara, M. *Catal. Lett.* **2009**, *131*, 242.

(25) Liang, X.; Yang, J. *Catal. Lett.* **2009**, *132*, 460.

(26) Mayes, R. T.; Fulvio, P. F.; Ma, Z.; Dai, S. *Phys. Chem. Chem. Phys.* **2011**, *13*, 2492.

(27) Anderson, J. M.; Johnson, R. L.; Schmidt-Rohr, K.; Shanks, B. H. *Catal. Comm.* **2014**, *51*, 33.

(28) Su, D. S.; Perathoner, S.; Centi, G. *Chem. Rev.* **2013**, *113*, 5782.

(29) Chen, D.; Feng, H.; Li, J. *Chem. Rev.* **2012**, *112*, 6027.

(30) Balasubramanian, K.; Burghard, M. *Small* **2005**, *1*, 180.

(31) Okamura, M.; Takagaki, A.; Toda, M.; Kondo, J. N.; Domen, K.; Tatsumi, T.; Hara, M.; Hayashi, S. *Chem. Mater.* **2006**, *18*, 3039.

(32) Mirkhani, V.; Moghadam, M.; Tangestaninejad, S.; Mohammadpoor-Baltork, I.; Mahdavi, M. *Monatsh. Chem.* **2009**, *140*, 1489.

(33) Wang, X.; Liu, R.; Waje, M. M.; Chen, Z.; Yan, Y.; Bozhilov, K. N.; Feng, P. *Chem. Mater.* **2007**, *19*, 2395.
(34) Mo, X.; Lotero, E.; Lu, C.; Liu, Y.; Goodwin, J. *Catal. Lett.* **2008**, *123*, 1.
(35) M. Toda; A. Takagaki; M. Okamura; J. N. Kondo; S. Hayashi; K. Domen; Hara, M. *Nature* **2005**, *438*, 178.
(36) Liang, X.; Zeng, M.; Qi, C. *Carbon* **2010**, *48*, 1844.
(37) Mao, J. D.; Schmidt-Rohr, K. *J. Magn. Reson.* **2005**, *176*, 1.
(38) Fraile, J. M.; García-Bordejé, E.; Roldán, L. *J. Catalysis* **2012**, *289*, 73.
(39) Benzing-Purdie, L.; Ripmeester, J. A.; Preston, C. M. *J. Agric. Food Chem.* **1983**, *31*, 913.
(40) Fang, X.; Schmidt-Rohr, K. *J. Agric. Food Chem.* **2009**, *57*, 10701.
(41) Fang, X.; Schmidt-Rohr, K. *J. Agric. Food Chem.* **2010**, *59*, 481.
(42) Kelemen, S. R.; Afeworki, M.; Gorbaty, M. L.; Sansone, M.; Kwiatek, P. J.; Walters, C. C.; Freund, H.; Siskin, M.; Bence, A. E.; Curry, D. J.; Solum, M.; Pugmire, R. J.; Vandenbroucke, M.; Leblond, M.; Behar, F. *Energy & Fuels* **2007**, *21*, 1548.
(43) Cai, W.; Piner, R. D.; Stadermann, F. J.; Park, S.; Shaibat, M. A.; Ishii, Y.; Yang, D.; Velamakanni, A.; An, S. J.; Stoller, M.; An, J.; Chen, D.; Ruoff, R. S. *Science* **2008**, *321*, 1815.
(44) Brewer, C. E.; Schmidt-Rohr, K.; Satrio, J. A.; Brown, R. C. *Environ. Progress Sustain. Energy* **2009**, *28*, 386.
(45) Baccile, N.; Laurent, G.; Coelho, C.; Babonneau, F.; Zhao, L.; Titirici, M.-M. *J. Phys. Chem. C* **2011**, *115*, 8976.
(46) Mao, J.-D.; Johnson, R. L.; Lehmann, J.; Olk, D. C.; Neves, E. G.; Thompson, M. L.; Schmidt-Rohr, K. *Environ. Sci. Technol.* **2012**, *46*, 9571.
(47) Mao, J. D.; Schmidt-Rohr, K. *Environ. Sci. Technol.* **2004**, *38*, 2680.
(48) Johnson, R. L.; Schmidt-Rohr, K. *J. Magn. Reson.* **2014**, *239*, 44.
(49) Mao, J. D.; Holtman, K. M.; Scott, J. T.; Kadla, J. F.; Schmidt-Rohr, K. *J. Agric. Food Chem.* **2006**, *54*, 9677.
(50) Schmidt-Rohr, K.; Mao, J. D. *J. Am. Chem. Soc.* **2002**, *124*, 13938.
(51) Johnson, R. L.; Anderson, J. M.; Shanks, B. H.; Fang, X.; Hong, M.; Schmidt-Rohr, K. *J. Magn. Reson.* **2013**, *234*, 112.
(52) Tang, W.; Nevzorov, A. A. *J. Magn. Reson.* **2011**, *212*, 245.
(53) Bodenhausen, G.; Ruben, D. J. *Chem. Phys. Lett.* **1980**, *69*, 185.
(54) Gullion, T.; Schaefer, J. *J. Magn. Reson.* **1989**, *81*, 196.
(55) Miao, S.; Shanks, B. H. *Appl. Catal., A.* **2009**, *359*, 113.
(56) Thorn, K. A.; Cox, L. G. *Org. Geochem.* **2009**, *40*, 484.
(57) Li, S.; Hong, M. *J. Am. Chem. Soc.* **2011**, *133*, 1534.
(58) Zhao, Y.; Nakamura, R.; Kamiya, K.; Nakanishi, S.; Hashimoto, K. *Nat. Comm.* **2013**, *4*, 2390.
(59) Zhou, Y.; Neyerlin, K.; Olson, T. S.; Pylypenko, S.; Bult, J.; Dinh, H. N.; Gennett, T.; Shao, Z.; O'Hayre, R. *Energy Environ. Sci.* **2010**, *3*, 1437.
(60) Ohara, M.; Takagaki, A.; Nishimura, S.; Ebitani, K. *Appl. Catal. A, Gen.* **2010**, *383*, 149.
(61) Zhao, Y.; Jia, L.; Medrano, J. A.; Ross, J. R. H.; Lefferts, L. *ACS Cat.* **2013**, *3*, 2341.
(62) Lei, Z.; An, L.; Dang, L.; Zhao, M.; Shi, J.; Bai, S.; Cao, Y. *Microporous Mesoporous Mater.* **2009**, *119*, 30.

Supporting Information

A SIMPLE ONE-STEP SYNTHESIS OF AROMATIC-RICH MATERIALS WITH HIGH CONCENTRATIONS OF HYDROTHERMALLY STABLE CATALYTIC SITES, VALIDATED BY NMR

Robert L. Johnson, Jason M. Anderson, Brent H. Shanks, Klaus Schmidt-Rohr

Table S1. Spectral areas from the ^{13}C NMR spectrum of GNPIP 250

ppm	218-181	181-164	164-143	143-121	121-94	94-72	72-53	53-39	39-25	25-17	17-0
All C	4%	4%	7%	14%	10%	4%	9%	16%	19%	6%	5%
C_{nonp}	3%	3%	4%	6%	2%	0%	0	0	0	-	-

Spectrally edited 2D ^{13}C-^{13}C NMR. Two-dimensional (2D) NMR spectra to identify nonprotonated C near CH were measured by 2D exchange NMR after short (0.07 ms) cross-polarization and with dipolar dephasing before detection (exchange with protonated and nonprotonated spectral editing, EXPANSE NMR), at a magic-angle spinning frequency of $\nu_r = 14$ kHz, see Fig. S1a. Dipolar assisted rotary recoupling (DARR) was applied during the mixing time of 10 ms. Details of this combination of spectral editing with 2D ^{13}C-^{13}C NMR are described in ref.[51] 2D NMR correlation spectra showing selectively peaks from pairs of nonprotonated were obtained by dipolar dephasing of double-quantum coherence in a double-quantum/single-quantum (DQ/SQ) correlation experiment, with a total of 0.57 ms of SPC5 homonuclear dipolar recoupling,[51] see Fig. S1b. The initial magnetization was generated by a combination of cross polarization and direct polarization, followed by 100 ms of spin diffusion.[51] The DQ/SQ spectrum was sheared for direct comparison with the EXPANSE spectrum. [51]

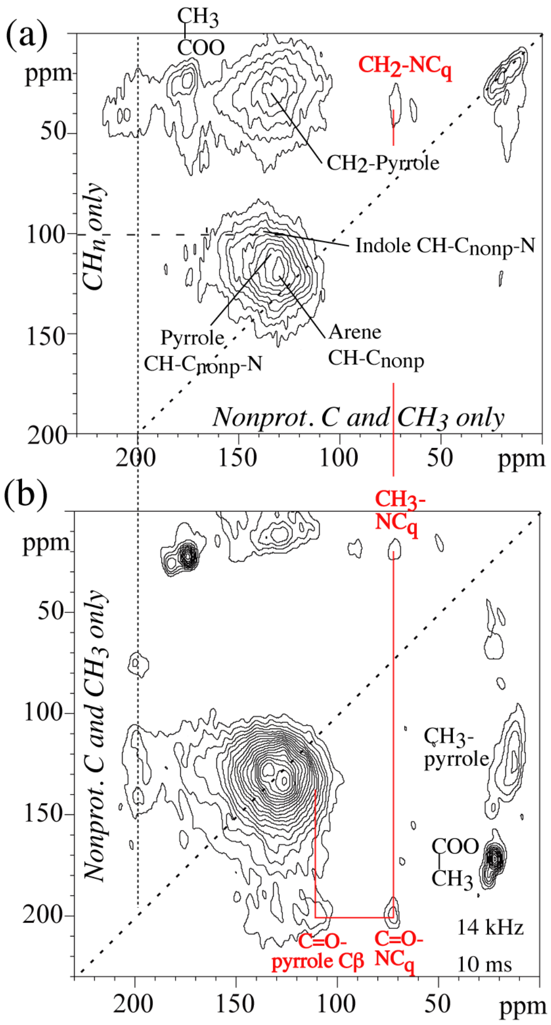

Figure S1. Spectrally edited ^{13}C-^{13}C NMR spectra of a sulfonic-acid functionalized aromatic-rich material made by reaction of ^{13}C$_6$-glucose with taurine (1:1) at 250°C. (a) EXPANSE NMR spectrum, correlating signals of protonated and nonprotonated C. (b) Dipolar dephased DQ/SQ correlation spectrum (sheared), correlating signals of bonded nonprotonated carbons and CH$_3$ groups. Signals of a structural fragment identified more prominently in lower-temperature melanoidins[51] have been highlighted in red.

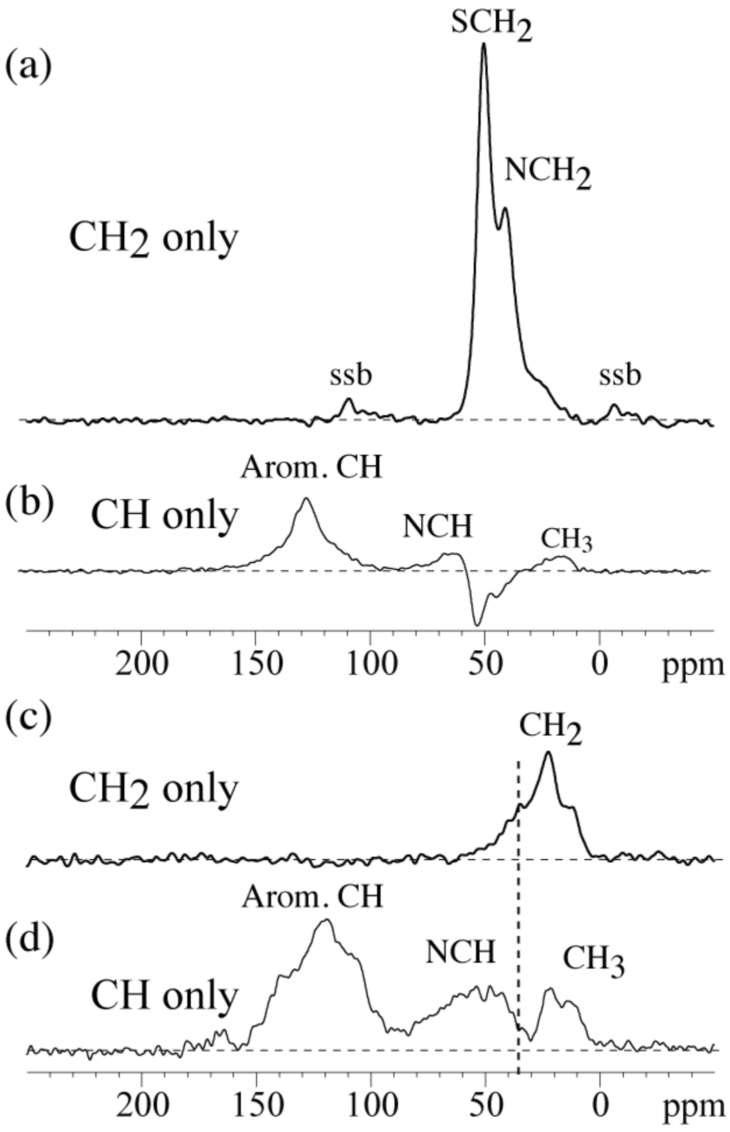

Figure S2. Spectrally edited ^{13}C NMR spectra of ^{13}C-labeled sulfonic-acid functionalized carbon-rich materials made by reaction of glucose with taurine (1:1) at 250°C. (a,b) Material produced using $^{13}C_2$-taurine, (c, d) material produced using $^{13}C_6$-glucose. (a,c) CH_2-only spectra, obtained by three-spin coherence selection. (b,d) CH-only spectra obtained by dipolar DEPT with residual CH_3 signals and negative bands from CH_2 groups of limited mobility. Spinning frequency: 5.787 kHz.

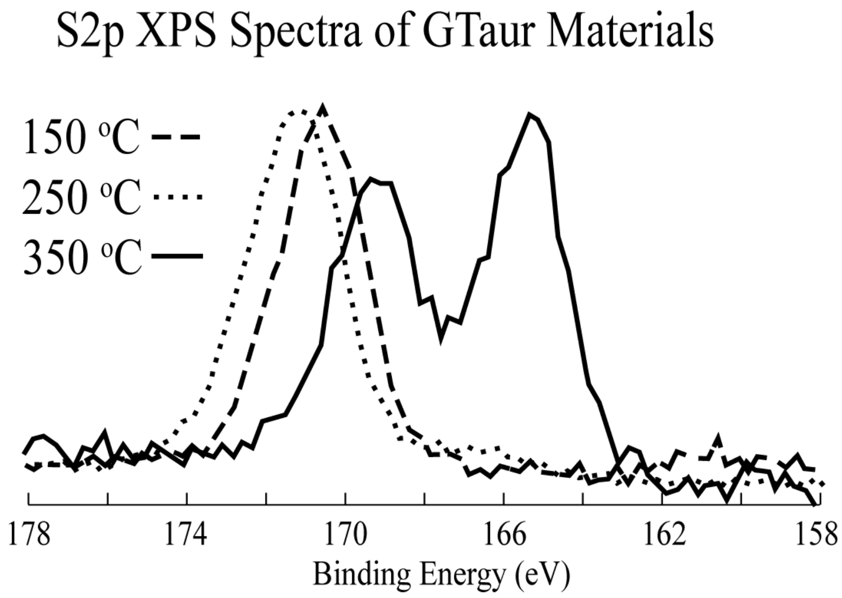

Figure S3. Sulfur 2p XPS spectra of GTaur materials prepared from 1:1 glucose:taurine at 150, 250, and 350°C.

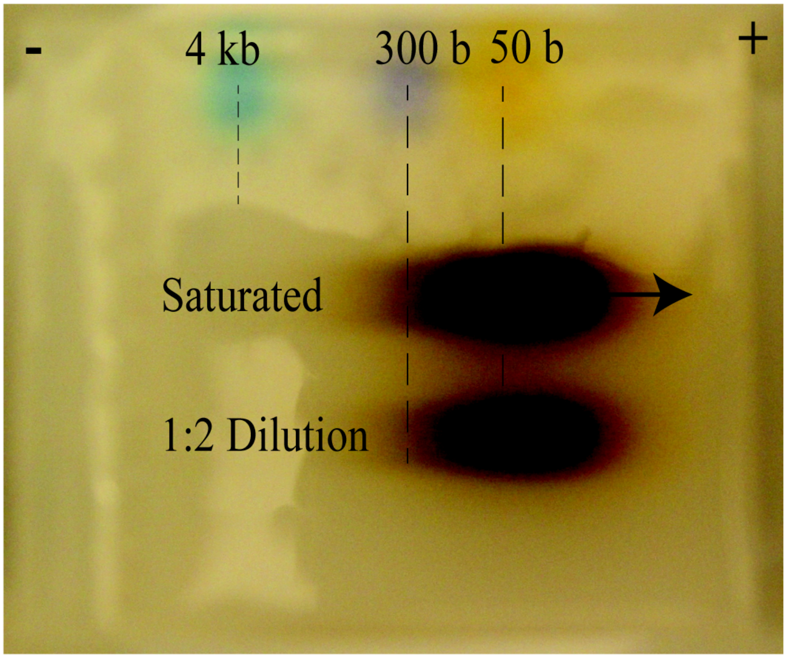

Figure S4. Electrophoresis of GTaur prepared from 1:1 glucose:taurine on a 1% agarose gel.

CHAPTER 5. SOLID-STATE ^{13}C NMR OF METHIONINE-POISONED PD/γ-Al_2O_3 CATALYSTS

Table Of Contents Graphic

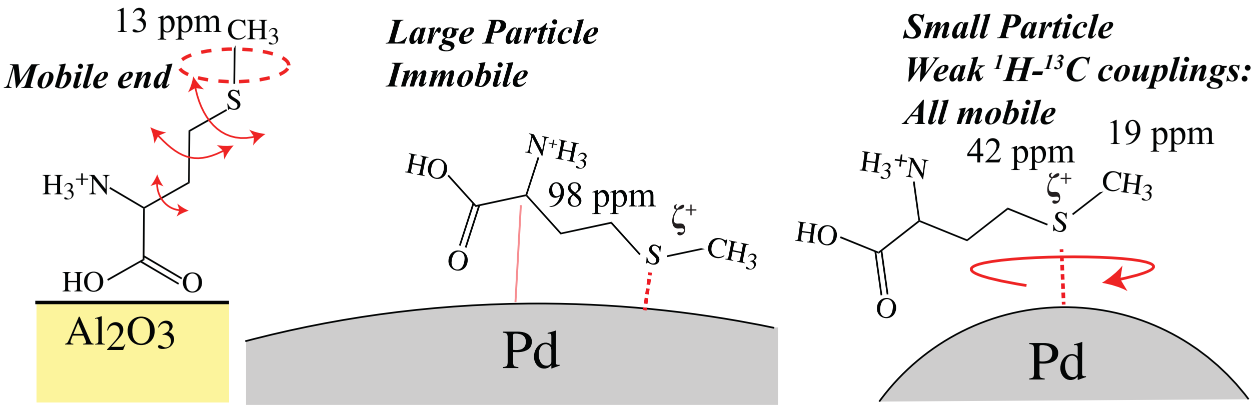

TOC. Different motional dynamics of methionine is observed on different surfaces using solid state NMR.

Robert L. Johnson[1], Thomas J. Schwartz[2], James A. Dumesic[2], Klaus Schmidt-Rohr*[,1,3]

[1]Department of Chemistry, Iowa State University, Ames, IA 50011

[2]Department of Chemical and Biological Engineering, University of Wisconsin, Madison, WI 53706

[3]Department of Chemistry, Brandeis University, Waltham, MA 02453

To be submitted to *Solid State NMR*

Abstract

The chemisorption and breakdown of methionine (Met) on Pd/γ-Al_2O_3 catalysts was investigated by solid-state NMR. ^{13}C-enriched Met impregnated onto Al_2O_3 or Pd/γ-Al_2O_3 gives NMR spectra with characteristic features of binding to Al_2O_3, to Pd nanoparticles, and oxidative or reductive breakdown of Met. The SCH_3 groups of Met showed characteristic changes in chemical shift on Al_2O_3 (13 ppm) vs. Pd (19 ppm), providing strong evidence for preferential binding to Pd, while the CH_2 and NCH groups generate small resonances assigned to distinct steady-state transition species from partial oxidation by Pd. Additionally, NMR shows that the SCH_3 groups of Met surface are mobile on Al_2O_3 but immobilized by binding to large Pd particles (ca. 10 nm); on small Pd particles (ca. 4 nm), the NCH groups undergo large-amplitude motions. In a reducing environment, Met breaks down by C-S bond cleavage followed by formation of several C_2-C_4 organic acids. The SCH_3 signal shifts to 23 ppm, which is likely the signature of the principal species responsible for strong catalyst inhibition. These experiments demonstrate that solid-state NMR of ^{13}C-enriched Met can be a sensitive probe to investigate catalyst surfaces and characterize catalyst inhibition both before reaction and postmortem.

Keywords: Postmortem catalyst characterization; multiCP/MAS; surface NMR;

Introduction

Utilization of biomass to produce mid- to high-value commodity chemicals currently obtained from petroleum is an important area of research. Efficient transformations of renewable feedstocks into platform chemicals directly by either biological or chemical catalysts are possible, but the number of available species is restricted either by low yields in biocatalysis or a limited number of chemical modifications in the case of chemical catalysis. One approach being explored, by the NSF ERC Center for BioRenewable Chemical (CBiRC) among others, is to use biological catalysts to produce functionalized platform molecules that further upgraded by heterogeneous catalysis.[1-3] One target molecule, sorbic acid, can be produced metabolically from sugars via triacetic acid lactone (TAL), followed by hydrogenation with a supported Pd catalyst. [4] However, sulfur-containing amino acids (i.e., methionine and cysteine) and vitamins present in the biologically synthesized TAL solutions are strong catalyst inhibitors, and catalytic activity substantially decreases in a matter of hours.

More generally, deactivation of reduced metal hydrogenation catalysts can result from several effects, including coke formation, particle agglomeration (sintering), leaching of the active phase, and decomposition of the support material. In addition to macroscopic breakdown on the catalyst, inhibition can be caused by strongly-bound reactive intermediates [5] such as CH_3 groups [6] or ethylidine species [7]. Lastly, contamination in the feedstock can irreversibly deactivate catalyst by adsorption of sulfur under reducing conditions, which has been shown for the dehydrogenation of cyclohexane,[8] hydrogenolysis of fatty esters,[9] and hydrogenation of butadiene [10].

Recently, we demonstrated that the poisoning of the supported Pd catalyst by methionine can be mitigated by application of a poly(vinyl alcohol) (PVA) overcoat to a bimetallic PdAu catalyst. [11] The NMR investigation of ^{13}C-enriched methionine in this system indicated that less carbon from Met was retained on the surface as a result of the PVA overcoat, which provided some explanation for the observed favorable effect. [11] In addition to detecting changes in the amount of Met retained on the catalyst, NMR can provide information about how Met interacts and reacts with the Pd catalyst. This is an interesting basic research question that may lead to a better understanding of catalyst deactivation and reactions on surfaces. Spectra from these initial NMR investigations showed interesting changes in the S-CH_3 chemical shift, presumably due to S interacting with the Pd surface. [11] Here, we further explore the $^{13}CH_3$ chemical shift as a sensitive probe for Pd catalysts. Spectra from materials shown previously [11] used uniform ^{13}C enrichment, with the methionine applied to the sample in a batch reactor. Due to the large background signal from adsorbed solvent, interpretation of the spectra and description of the binding and breakdown of Met was not straightforward. We avoid the background problem by studying samples prepared by impregnation of the catalyst with methionine followed by removal of the solvent. Another interesting observation during our initial investigation was slow oxidation of the carbon on the catalyst to carbonate, while the catalyst showed no appreciable activity toward reduction of carbon-carbon double bonds.

Characterizing catalysts post-mortem [12-14] can complement in-situ studies [12, 15, 16] to provide information that is useful for developing strategies that mitigate deactivation processes. NMR is a powerful tool to study small molecules inside mesopores [17] and on catalyst surfaces [18] as they interact with [19-21] and are transformed by these surfaces, since it can provide information not accessible with other techniques.[22] The chemical shift reflects the bonding environment around the ^{13}C nucleus and can monitor chemical transformations and modified interaction with surfaces.

Effects of unpaired electrons or conduction electrons in metallic species can, on the one hand, lead to very large changes in peak position and a general broadening of signals from directly metal-bonded carbon, e.g. in CO on transition metals. [23-25] On the other hand, several recent studies [26, 27] have shown that for carbon not directly bonded to the metal, e.g. separated by a heteroatom such as S [26] or physisorbed, [28-30] the change in peak position is more moderate, < 20 ppm, and can be useful to monitor adsorption. One recent example demonstrated that the chemical shift of formate on different metal nanoparticles correlated well with the calculated d-band center, formate decomposition rate, the metal work function, and the specific activity. [27] In metal oxide catalysts, ^{13}C NMR of acetone has been shown to be a viable means for measuring solid-acid strength.[31-34] NMR can provide a clear measure of both strong and weak molecular interactions with a surface (chemisorption and physisorption, respectively), [35-38] and additional information about molecular mobility and 3D molecular orientations [39] can be extracted using chemical shift anisotropy (CSA) measurements, CRAMPS, [40] and WISE. [41]

One advantage intrinsic to NMR is the quantitative relationship between the peak intensity and the number of spins in the corresponding chemical environment, and this information provides a critical parameter to trace how the molecule is affected by the surface. This approach has been used to characterize CO adsorption on an electrolyte material, [42] but it is not readily applicable with molecules containing several carbons. Until recently the only reliable method to obtain quantitative spectra was via direct polarization (DP) experiments with sufficiently long recycle delays to ensure uniform ^{13}C T_1 relaxation. [43] This is very time-consuming for molecules on surfaces, due to their weak signal even with ^{13}C enrichment. Cross-polarization (CP) from ^1H to ^{13}C is generally used, since it requires far less time to acquire (mainly due to fast ^1H spin-lattice relaxation compared to ^{13}C) but it is notoriously non-quantitative as a result of differential polarization rates for ^{13}C depending on the distance to the nearest ^1H. Thus far, the best compromise between quantitative spectra and acquisition time is provided by the recently published multiCP/MAS experiment, which shows excellent agreement with DP spectra for a range of complex organic materials. [44] The quantitative 1D spectra are complemented by spectrally edited 2D ^{13}C-^{13}C NMR spectra, [44] which identify bonding partners and multi-bond ^{13}C-^{13}C connectivities.

To improve the understanding of the mechanism by which Met deactivates Pd/γ-Al_2O_3, we have conducted NMR experiments on materials prepared with different Pd particles sizes and free of solvent background signals with an impregnation procedure. The results show which functional groups are immobilized by strong interactions with the surface, and the interaction with both the Pd nanoparticles and the Al_2O_3 support, and thus provide a detailed picture of the chemical species on the catalyst surface before and after treatment at reaction conditions, including.

Experimental

Sample Preparation.

Catalyst synthesis

Pd/γ-Al_2O_3 catalysts were prepared by incipient wetness impregnation of γ-Al_2O_3 (Strem, low-soda) with $Pd(NO_3)_2$ (prepared from Aldrich 10% $Pd(NO_3)_2$ solution in 10% HNO_3, 99.999%). The catalysts were subsequently dried at 383 K for 2 hours, calcined in flowing air at 673 K (Medical Grade, USP), reduced in flowing hydrogen (Industrial Grade), and passivated with 1% O_2 in Ar (Research Grade).

Catalyst characterization

CO uptake (99.99%) was measured using a Micromeritics ASAP 2020 following reduction in flowing hydrogen (UHP) at 373 K for 3 hours. Pd dispersion was determined using a stoichiometry of 0.67 CO per surface metal atom. Surface area, pore volume, and pore diameter were measured via nitrogen physisorption (UHP) using a Micromeritics ASAP 2020. Surface area was determined by the BET method, and pore volume and diameter via the BJH method using the desorption isotherm. These values have been reported previously.[11]

Methionine treatment

Materials were prepared using either $S^{13}CH_3$-labeled or uniformly ^{13}C-enriched methionine (Cambridge Isotope Laboratories, L-methionine Methyl-13C, 99% and L-methionine U-13C5, 97-99%) was added to samples by incipient wetness impregnation of the Pd/γ-Al_2O_3 catalysts using solutions in D_2O (Aldrich, 99.0 atom% D). Samples were subsequently dried under vacuum at 318 K for 2 hours. Samples were also prepared by treatment of Pd/γ-Al_2O_3 catalysts under simulated batch reaction conditions using butanol solutions saturated with ^{13}C-labeled methionine. This treatment was performed in a stainless steel autoclave (Parr Instruments) at 323 K pressurized with 34 bar of H_2 (Airgas, industrial grade) for 12 hours. Residual impurities in 1-butanol (Sigma-Aldrich, 99.5%) were removed by refluxing with $NaBH_4$ overnight under bubbling argon followed by distillation.[45] Samples treated in this way were recovered from solution by filtration, washed with Milli-Q grade water, and dried under vacuum at 318 K for 2 hours.

NMR.

MultiCP ^{13}C NMR

Quantitative spectra were obtained by applying a multiCP as described previously.[46] The spinning speed was 14 kHz, with 90° pulse lengths of 4.3 μs, and ^1H decoupling of 50-60 kHz. The delay for ^1H relaxation between 1.1-ms cross-polarization periods was 0.9 s, and 4 recycle loops with 2-s recycle delays were used. Nonprotonated and mobile fractions were identified by applying a period of gated decoupling of 68 μs to dephase magnetization of carbons with strong ^1H dipolar coupling, such as CH and immobile CH_2.

Two-dimensional ^{13}C-^{13}C Exchange NMR

2D ^{13}C-^{13}C exchange experiments were run under the same conditions as the multiCP experiments, with the addition of a DARR mixing period of 30 or 100 ms duration.

Chemical-Shift Anisotropy Filter

Three-pulse chemical-shift anisotropy (CSA) filtered spectra were measured to determine the nature of the 98 ppm chemical on the impregnated the 163 ppm and the relative mobility of the COO groups. [47]

Sulfur XPS:

The chemical state of sulfur of Met impregnated onto the catalyst surface was analyzed using a Physical Electronics 550 Multitechnique XPS system employing a standard Al electron source. The samples were run at 10^{-9} Torr and mounted on double-sided tape. Charging was corrected for by adjusting the carbon peak to 284 eV.

Results

Impregnated Met

Evidence of Met binding to Pd. Quantitative ^{13}C spectra of samples impregnated with uniformly ^{13}C-enriched Met are shown in Figure 1, and show numerous interesting features. Met impregnated on the γ-Al_2O_3 support without Pd has a resonance position that is shifted slightly, to 13 ppm, but the signal is not broadened much. The presence of Pd nanoparticles leads to CH_3 resonating at 19 ppm, which is outside the range typical for Met (95% of all SCH_3 resonances are found between 12.5 and 17 ppm from neat TMS). [48] It also results in substantial NCH and CH_2 peak broadening and shifts both resonances to higher frequency. Furthermore, unusual peaks are observed at 98 and 165 ppm, and peak areas in quantitative 1D spectra indicate that these signals are formed at the expense of CH_2 and NCH, which suggests oxidative changes of Pd-bound Met without breaking of sigma bonds.

Met dynamics and binding. The NMR spectra in Figure 1 after dipolar dephasing by ^1H (red lines) show that the particle size affects the dipolar dephasing of the CH_2 resonance, which is a good indicator of molecular mobility. The signals of the CH_2 groups in the presence of large Pd particles (ca. 10 nm diameter) are dephased efficiently, indicating strong ^1H-^{13}C dipolar couplings and no fast large-amplitude motions. By contrast, with small Pd particles (ca. 4 nm) the dipolar dephasing of all resonances is slower, which indicates that the molecule as a whole is undergoing large-amplitude molecular motions.

Assignment of additional peaks. The origin of the peaks at 98 and 165 ppm was probed using a 2D ^{13}C-^{13}C exchange experiment, where cross peaks reveal the frequencies of directly bonded carbons. The 2D spectra shown in Figure 2 show that signals at both 98 and 163 ppm have only weak cross peaks even with a 100-ms DARR exchange period. The 98-ppm peak does have undisputable cross peaks to carbons that resonate near 25 and 170 ppm. This chemical shift pattern can be explained by the structure shown in Figure 2c, where binding of Pd to the CN carbon results in a carbon predicted to resonate just below 100 ppm, and it is bound to a COO group as well as a CH_2 resonating near 25 ppm. The fairly intense 163-ppm peak shows no significant cross peak intensity, with the exception of a small shoulder near 35 ppm. Given the large signal at 163 ppm, a substantial cross peak should be visible if another ^{13}C was directly bonded. Therefore, although a small fraction of this intensity could be attributed to the proposed intermediate structure shown in Figure 2d, the majority should be assigned to carbonate, presumably due to oxidation of surface species after exposure of the catalyst to air.

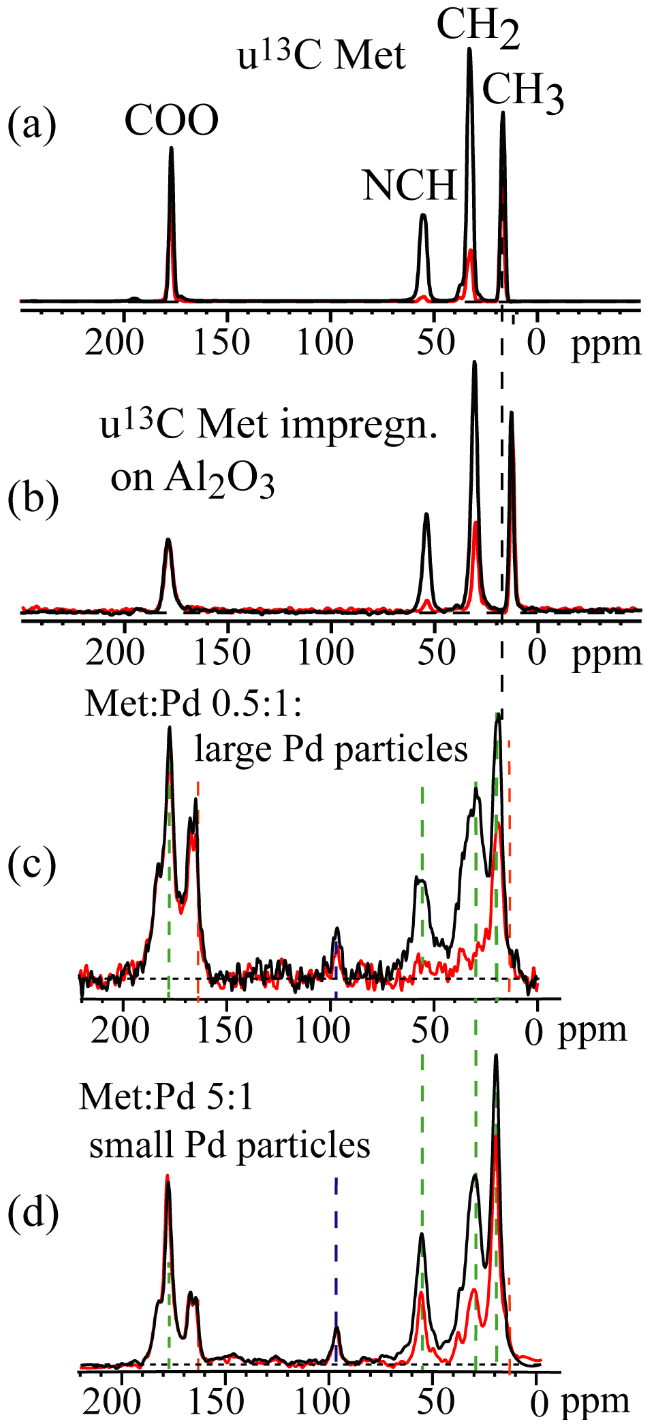

Figure 1. Quantitative multiCP ^{13}C NMR spectra of methionine on Pd/γ-Al_2O_3 catalysts. The Pd/Al_2O_3 was impregnated with u^{13}C-enriched (thin full lines). Corresponding spectra after dipolar dephasing, which retain signals of nonprotonated C and mobile segments, are also shown (thick full lines). (a) Neat Met. (b)Met on γ-Al_2O_3 support (c) Met on ~10-nm diameter Pd particles, Met:Pd$_{\mathrm{Suf}}$ = 0.5:1, where Pd$_{\mathrm{Surf}}$ is determined by CO chemisorption. (d) Met on ~4-nm diameter Pd particles, Met:Pd$_{\mathrm{Surf}}$ = 5:1.

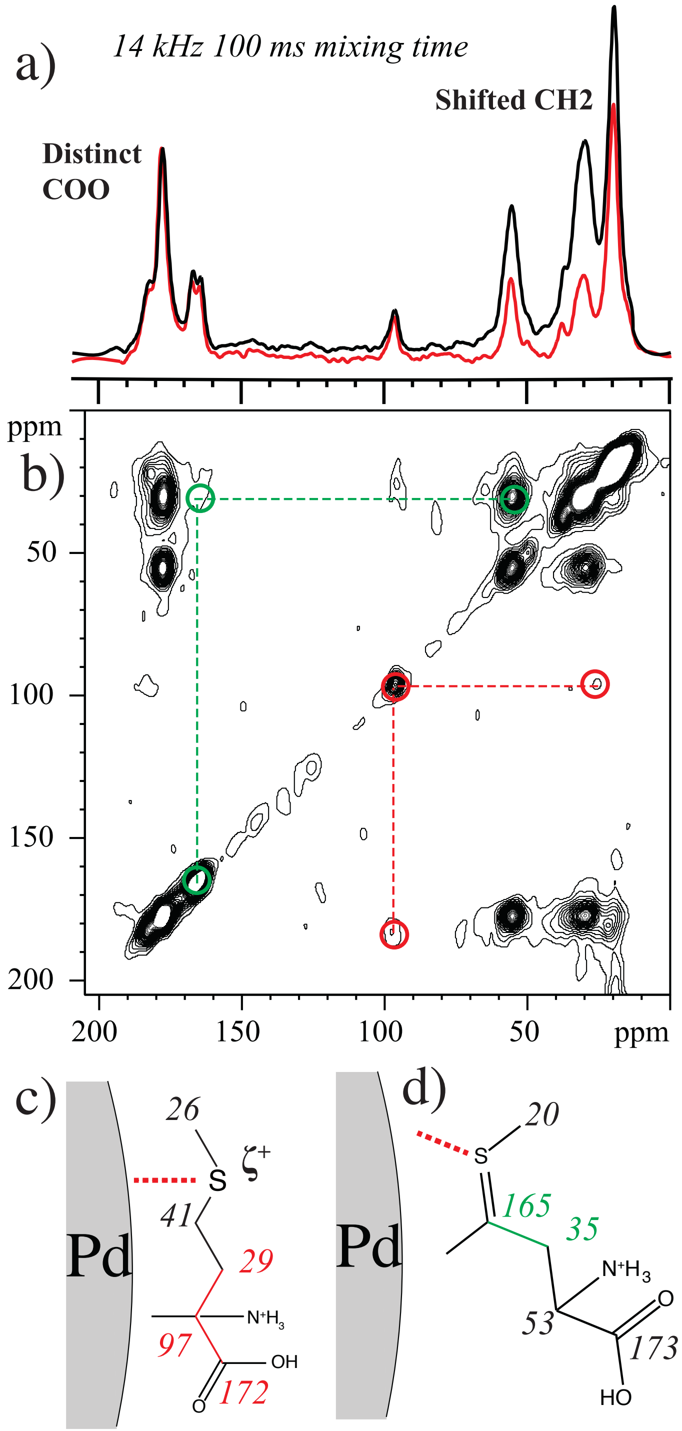

Figure 2. a) Quantitative multiCP 1D spectra, without and with dipolar dephasing. b) MultiCP 2D ^{13}C-^{13}C spectrum with a 100 ms DARR period for spin diffusion under 14 kHz MAS. c) Proposed structure to explain the presence of the 98 ppm peak, and d) proposed structure which would account for some 165 ppm intensity not from carbonate.

Impregnated Met breakdown on catalyst. To simulate reaction conditions but avoid background from solvent, catalyst samples were impregnated with Met and placed in a tube furnace under flowing hydrogen and heated to 40 °C. While exposed to air at room temperature, oxidation of Met and formation of carbonate was observed, but after even a short time under reaction conditions the carbonate peak is decreased (presumably lost as CO_2) and several CH_3 peaks are produced from Met by fragmentation at the CH_2–S bond, which leads to a mixture of different small acid species. Shown in Figures 3 are 1D and 2D spectra of the breakdown products from Met immediately following treatment at 40 °C in flowing hydrogen. A characteristic 8-ppm CH_3 signal appears, which 2D ^{13}C-^{13}C correlations NMR shows to be due to the 2-amino butyric acid, obtained by loss of SCH_3 and butyric acid from loss of both SCH_3, and NH_2. Interestingly after exposure to air, the 13-ppm peak from butyric acid is reduced significantly, while intensity has increased significantly at 21 ppm, indicating that acetic acid has re-formed and butyric acid has been cleaved upon exposure to air. Additionally, a significant amount of carbonate has re-formed, another indication of rapid oxidation by air even at ambient temperature.

Met break-down in batch and impregnated catalyst. To test if the impregnated materials break down in an analogous manner to those produced in the more realistic batch process, Figure 6 compares 1D and 2D DQ/SQ NMR spectra of breakdown products of Met on Pd prepared via the two methods. Unambiguous one-bond cross peaks can be used to identify the molecular structures. For instance, while an OOC to CH_2 cross peak in a ^{13}C-^{13}C spin exchange spectrum could be due to a two-bond transfer in OOC-CH(RNH_3)-CH_2 as in methionine or from a one-bond OOC-CH_2 correlation as in propionic acid, only the latter gives a distinctive OOC-CH_2 peak in the DQ/SQ spectrum. In addition, cross peaks near or even on the diagonal are detectable, since the DQ/SQ spectrum is free of a diagonal ridge. COO-CH_3 signal pairs are due to acetate; the high COO chemical shift value makes an ester unlikely. After treating the impregnated samples in H_2, a sharp peak at 8 ppm is observed.

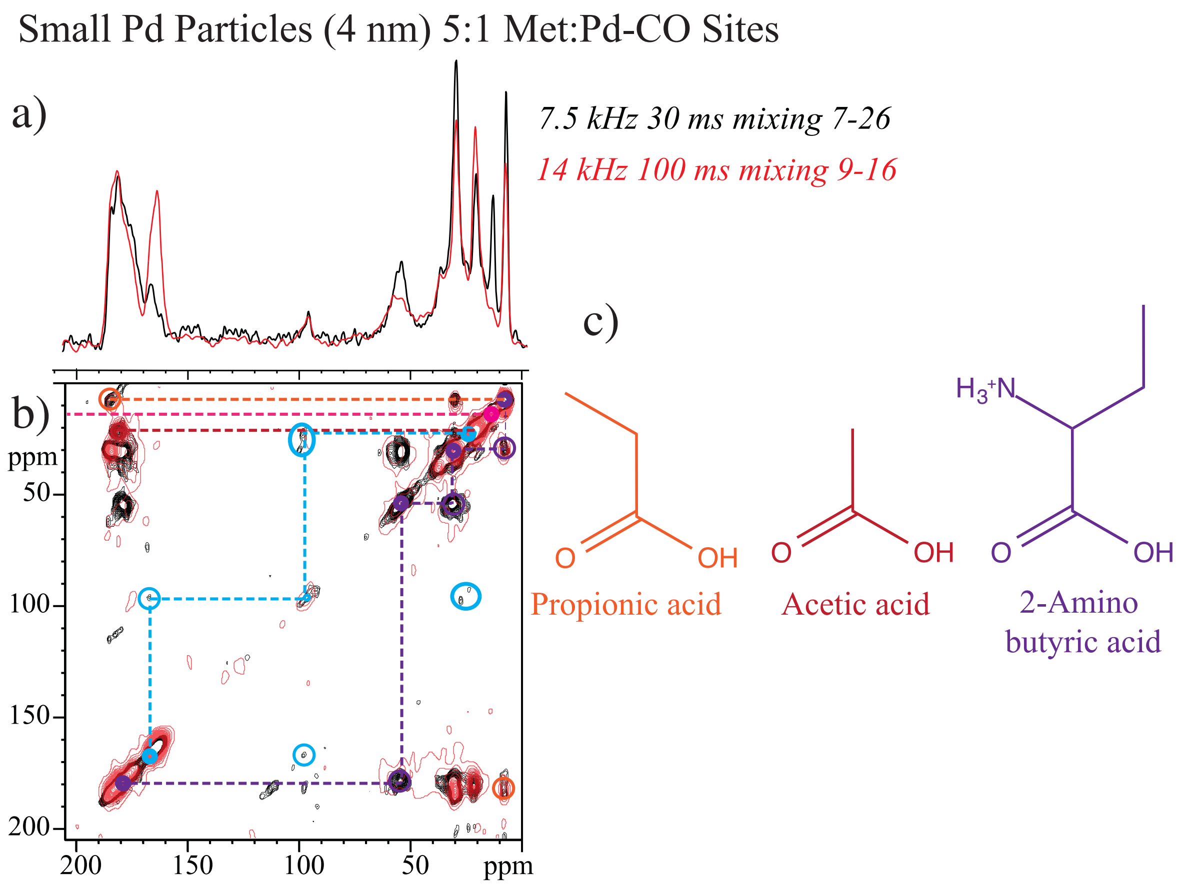

Figure 3. Effect of temperature-activated reaction on quantitative multiCP ^{13}C NMR spectra of methionine impregnated onto Pd/γ-Al_2O_3 catalysts. Shown in part a) are multiCP spectra of the material after reaction (black) and after storage at room temperature for 60 days (brown). 2D spectra for these two time points are shown superimposed in b) with key cross peaks highlighted in colors. Shown in c) are structures derived from Met after reaction in flowing H_2 at 40 °C.

The chemical shift is characteristic of a CH_3 in an ethyl group linked to a CH or sp^2-hybridized carbon. The 2D ^{13}C-^{13}C and DQ/SQ spectra show that this signal is from two different methionine fragments. After the batch reaction, the 8-ppm signal is from the methyl end group of 2-amino butyric acid, formed from γ-CH_2 of Met after loss of SCH_3. Cross sections at the 8-ppm CH_3 peak position show all the signals (CH_3, CH_2, NCH, and COO) of 2-amino butyric acid. By contrast, in the impregnated sample the signal is instead from propionic acid, with OOC-CH_2 one-bond and OOC-..-CH_3 two-bond cross peaks in the DQ/SQ and ^{13}C-^{13}C exchange spectra, respectively. Signals of glycine are also observed.

While for the most part, the products formed and chemical shifts seen are similar for the reacted Met in the impregnated vs. batch materials, there are some subtle differences. The impregnated samples have larger amounts of propionic acid than the batch materials. Possibly, the effects of the solvent and high pressure of the reaction system used to produce the batch materials have different effects on how easily the sulfur species is released from the Pd particle. In addition to fragmentation and breakdown of Met, we also see loss of carbon from the surface. The presence of an oxidation product of butanol (butyric acid) indicates that SCH_3 could be slowly oxidized after exposure to batch conditions, where it would likely be lost as a gas under flowing hydrogen.

With selective isotopic labeling of the SCH_3 carbon, other differences between the batch and reacted impregnated samples can be probed. The SCH_3 resonance in both samples is shifted to higher ppm values. It likely remains bound to Pd as a CH_3 still through the S, but in the batch preparation more than 30% is converted to COO (confirmed in Figure 7), and some may be lost as CO_2.

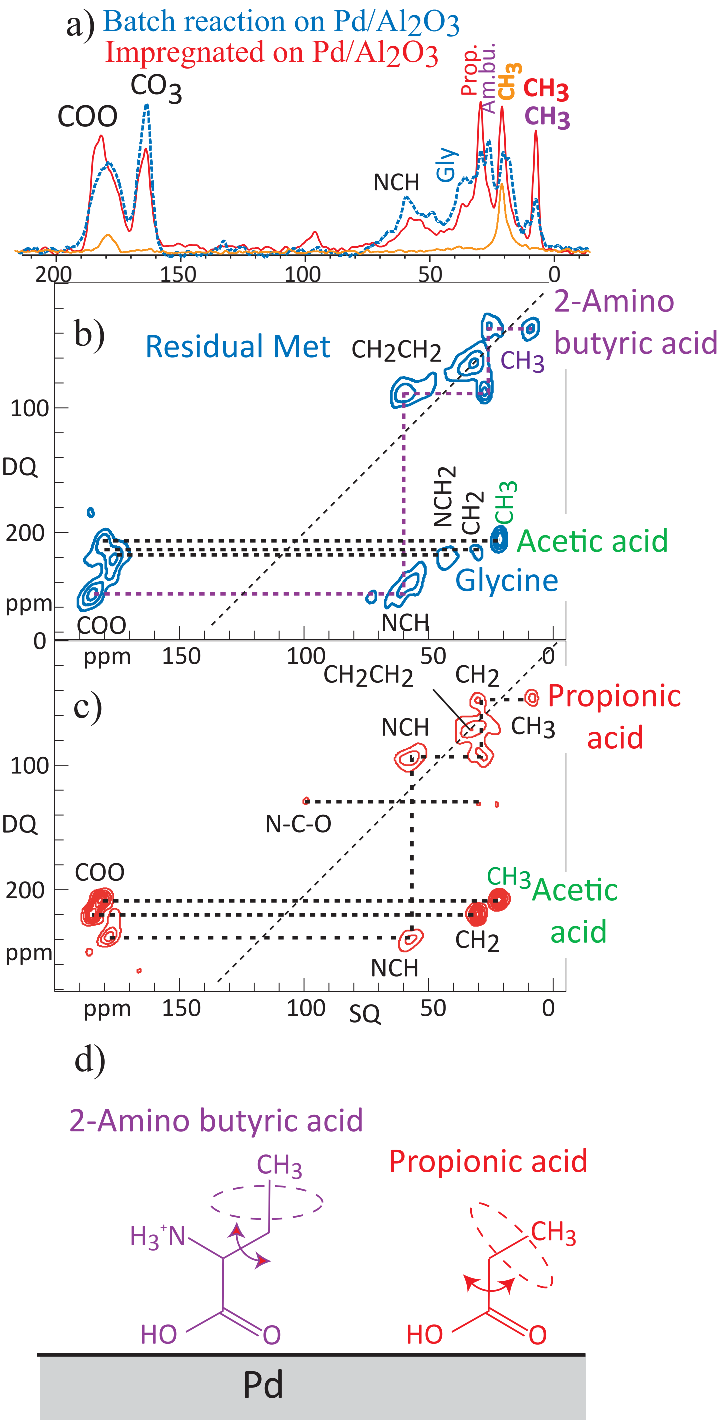

Figure 4. ^{13}C NMR characterization of methionine decomposition on Pd/γ-Al_2O_3. in batch and impregnated-sample reactions. (a) MultiCP spectra for batch u^{13}C Met (blue), SCH_3-labeled Met (yellow), and impregnated and reacted material after 60 days stored at room temp (red). (b) DQ/SQ 2D spectrum of the batch reacted material. c) Same as b) for the impregnated and reacted material. Information from dipolar dephased spectra indicates that the molecule binds to Pd on the COO end, and a model of this is shown in d).

The fate of SCH_3. A nearly perfect linear relationship between the number of Pd-CH_3 bonds and catalyst deactivation has shown that binding of CH_3 groups to Pd can inhibit hydrogenation reactions [5, 6] Therefore the fate of the SCH_3 group is interesting from the perspective of catalyst deactivation. Met impregnated onto the catalyst surface has some distinct changes in chemical shift, in particular of the SCH_3 resonance. Met SCH_3 on Al_2O_3 resonates at 13 ppm, in the neat, as-purchased crystalline Met at 16 ppm, and adsorbed on Pd resonates at 19 ppm. [11] When Met is reacted under batch conditions, the resonance is observed near 22 ppm; most likely, this is the signal of SCH_3 bonded to the metal. [11] The ~+6 ppm shift from the 13-ppm resonance of neat Met is comparable to values of ~+10 ppm for thiols on gold. This sensitivity of the SCH_3 chemical shift to the surface with which it interacts suggests that Met can be used as a probe for reduced metal surfaces. To test if the Pd sites could be saturated, a catalyst with low Pd loading (corresponding to 50:1 Met:Pd loading) was impregnated with Met. In the spectrum of this sample in Figure 4 (blue line), the majority of the intensity lines up exactly with Met on Al_2O_3 at 13 ppm (black trace) and only a small fraction resonates at the 19 ppm peak position observed for $S^{13}CH_3$-Met with high Pd loading (red, corresponding to 0.5:1 Met:Pd molar ratio).

Oxidation of sulfur. To complement the information from ^{13}C NMR, XPS was used to probe how sulfur was affected by impregnation and reaction. XPS spectra reflect the oxidation state of the atom, which should be affected if the interpretation of the changes in ^{13}C NMR spectra are correct.

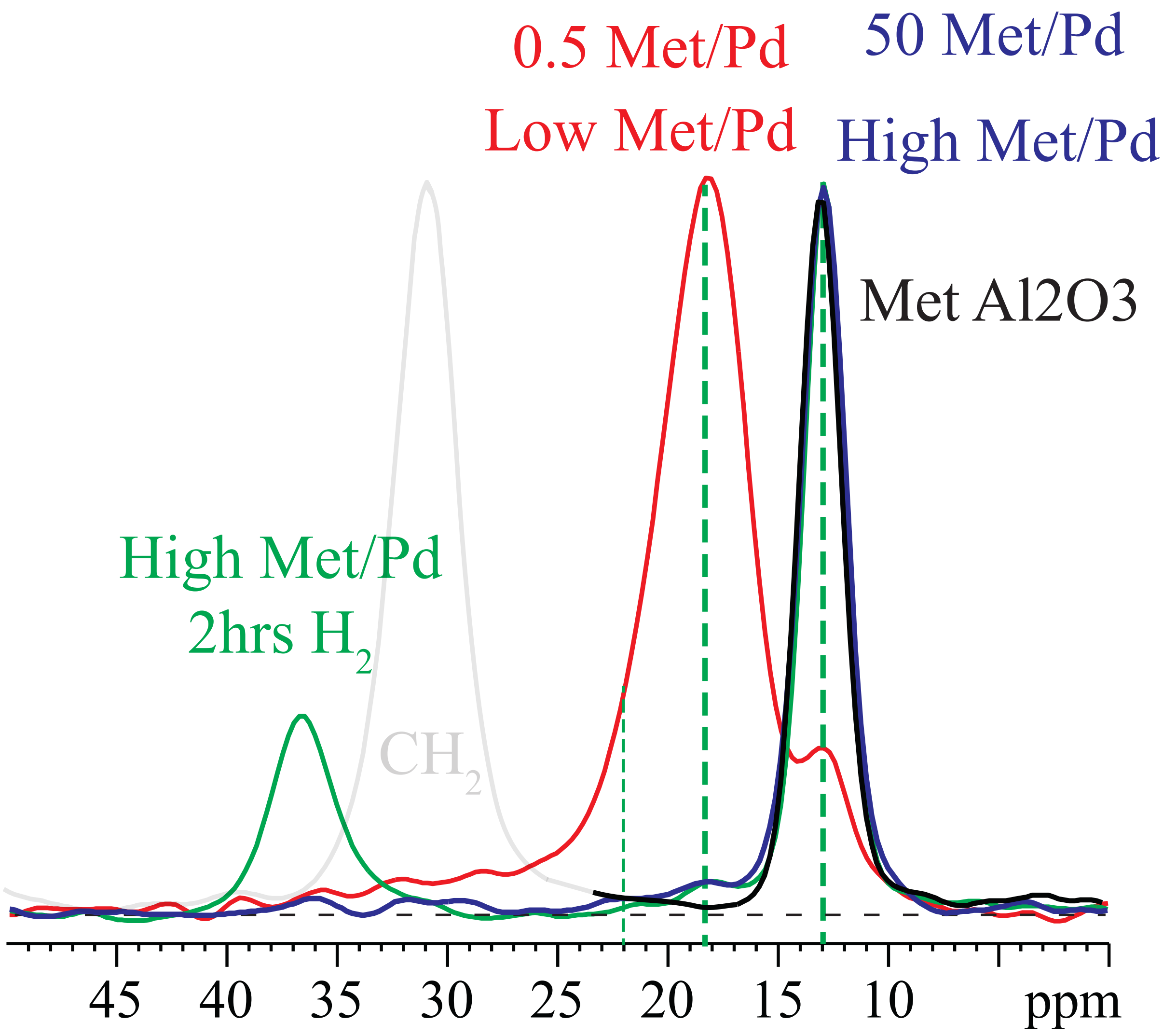

Figure 5: Comparison of $S^{13}CH_3$ chemical shifts with constant Met and different Pd loadings. Black: Met on Al_2O_3 without Pd. Red (maximum at 18 ppm): Sample with 100 times more Pd sites compared to that shown in blue (peak at 13 ppm).

The results observed from the S2p XPS spectra shown in Figure 5 are consistent with the conclusions from ^{13}C NMR. Sulfur in crystalline Met has a peak of 162.8 eV, and is shifted to 164 eV when impregnated onto the Pd catalyst, an indication of some loss in electron density. After the impregnated material is reacted in flowing H_2 at 40°C the sulfur peak shifts to 168.4 eV, consistent with oxidation of sulfur. Likely this results from the decomposition products of Met on the catalyst surface under reducing conditions, which are rapidly oxidized upon re-exposure to air. This implies that the C-S bond must have been cleaved during treatment in flowing hydrogen, consistent with the conclusions from the ^{13}C NMR experiments.

It has been observed that catalyst deactivation occurs even without Met [11] and a very large fraction of the carbon on the surface is derived from the solvent and reactant molecules, making XPS peaks of sulfur not distinguishable from noise. The presence of oxidation products from butanol, used as a solvent in both the batch reactions and the PVA overcoating procedure, is an indication that Pd is capable of oxidation at ambient conditions in the presence of air. Additionally, it is surprising that although Pd is deactivated for hydrogenation reactions by Met deposition, it still catalyzes the oxidation of Met and butanol, which continues to occur slowly at room temperature, resulting in the observed formation of carbonate. XPS shows that the sulfur of Met initially impregnated onto the Pd/γ-Al_2O_3 catalyst is in the reduced form. After reaction in H_2 for two hours, the sulfur appears oxidized. Interestingly, this oxidation does not induce a shift dramatic enough to correspond to full conversion to sulfate, and indeed the Pd appears slightly reduced. Taken together, this is evidence of Pd-S bond formation.

Formation of acac on Al_2O_3, from TAL. Interestingly, in spectra of batch samples with TAL in the reaction mixture on the Al_2O_3 surface (without Pd), see Fig. 7, we observe signals of unlabeled acetylacetonate (acac) bound to Al, presumably as a TAL breakdown product. Indeed, it has been reported that TAL readily decarboxylates to form acetylacetone. [49, 50] Spectra shown in Figure 6 show four alkyl peaks at < 45 ppm, one more than expected for methionine. They also display significant additional peaks at 98 and 190 ppm. The assignment of these peaks is helped by comparison with the spectrum of Met impregnated on Al_2O_3, which does not show the peak at 26 ppm. Further, the peaks at 190, 98, and 26 ppm do not display cross peaks in 2D NMR. This strongly suggests that these signals are from ^{13}C in natural abundance, which has mostly ^{12}C neighbors and therefore no detectable cross peaks.

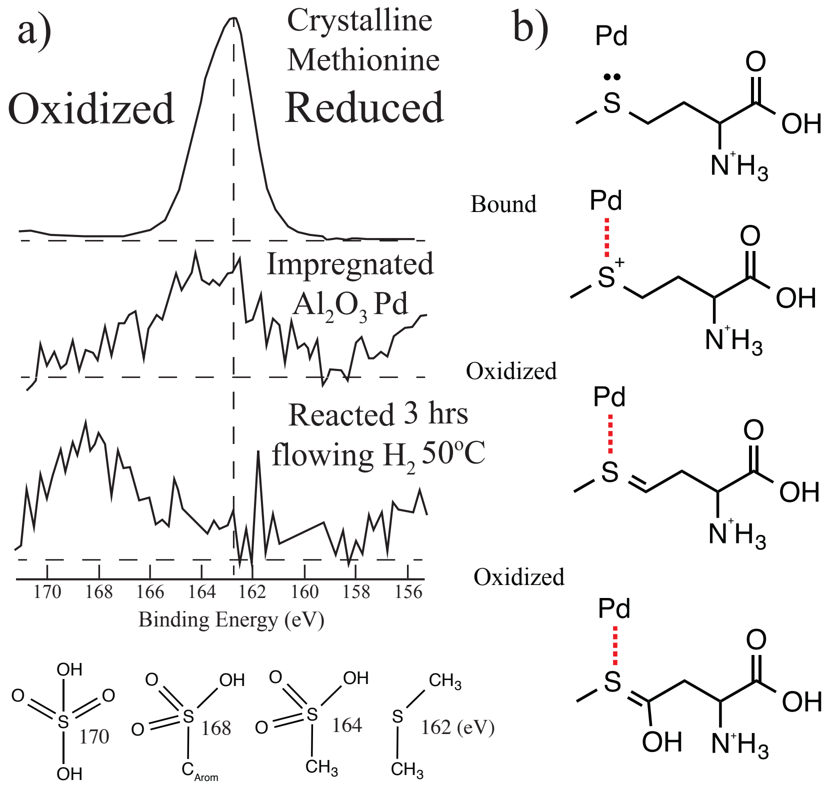

Figure 6. Comparison of S2p XPS peaks of Met-impregnated materials. Shown in a) is the XPS spectra of the impregnated material and neat Met before and after reaction in flowing H_2. b) Scheme proposed to explain this change.

The peak positions are in agreement with previous NMR studies of acac bound to Al_2O_3 (see inset in Figure 6 of ref. [51]): The 190-ppm chemical shift is indicative of a ketone or aldehyde; dipolar dephasing shows that the carbon is not protonated, which excludes an aldehyde. The signal at 98 ppm is associated with a large chemical-shift anisotropy that excludes an sp^3-hybridized carbon (see below).

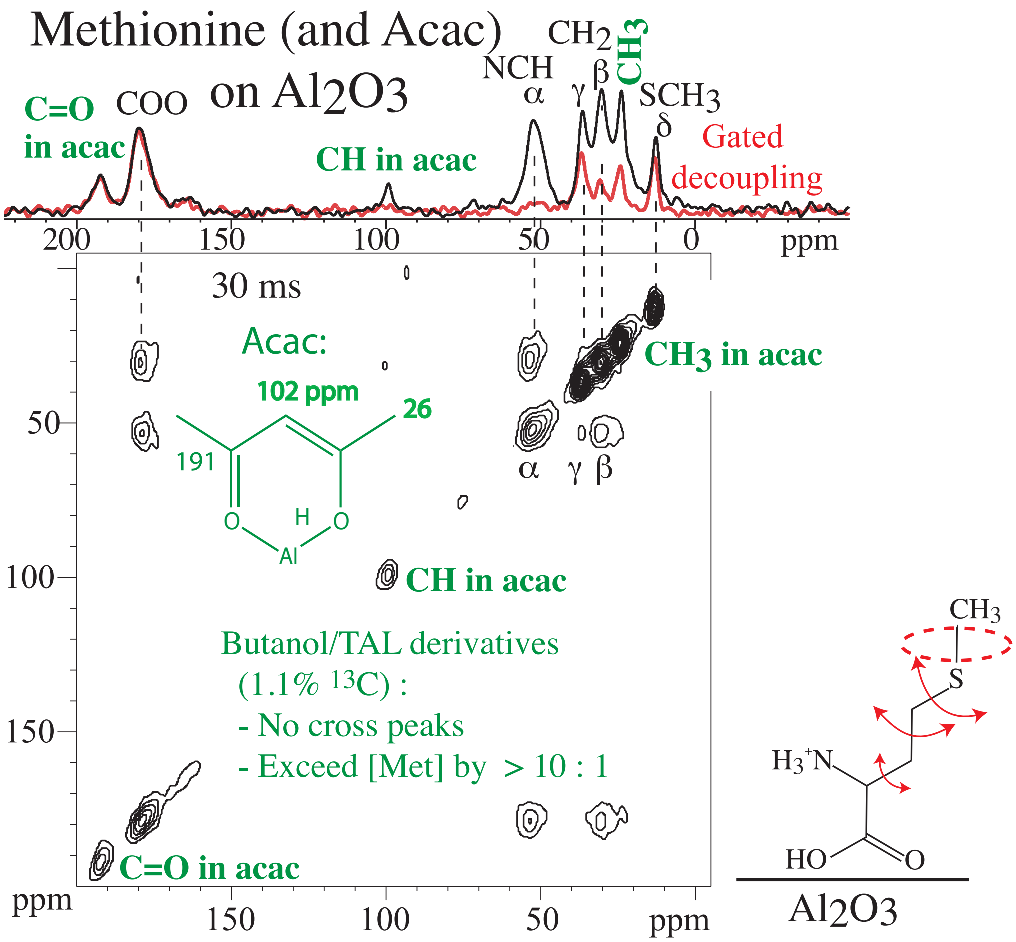

Figure 7. Quantitative multiCP ^{13}C NMR spectra of u^{13}C-enriched (thin full lines) or ^{13}CH$_3$-labeled (dashed lines) methionine on (a) Al$_2$O$_3$ and (b) Pd/γ-Al$_2$O$_3$ in a flow-through batch reactor. Corresponding spectra after dipolar dephasing, which retain signals of nonprotonated C and mobile segments, are also shown (thick full lines).

This large CSA together with the chemical shift that is unusually low for an sp^2-hybridized carbon matches that of the central carbon site in acac, which is mostly an sp^2-hybridized CH, but an sp^3-hybridized CH$_2$ group in some resonance forms. The position of the 26-ppm peak agrees with the chemical shift of the two CH$_3$ groups of acac. [51]

CSA dephasing. The chemical shift anisotropy (CSA) of immobilized sp^2-hybridized carbons is significantly larger than that of mobile species or sp^3-hybridized C, while that of immobilized sp-carbon is even greater. A large CSA results in faster dephasing of magnetization when the CSA is recoupled by a suitable pulse sequence that interferes with CSA averaging by MAS. This CSA dephasing can therefore be used to determine if the 98 ppm peak of the impregnated samples is from the same species as the 98 ppm peak from acac, if the 163 ppm peak was consistent with carbonate, if a resonance is from COO or bound carbon monoxide, and to compare molecular mobility for different sized nanoparticles. The 98 ppm peak assigned to acac dephases very rapidly, which reflects a large CSA, compared to the 98 ppm peak in the impregnated samples (Figure 8). This fast dephasing is characteristic of an sp^2-hybridized carbon, strong evidence in support of the presence of acac on the Al_2O_3 surface.

The dephasing of COO groups is slower in the samples with small particles compared to large particles. This indicates a greater motional amplitude of the COO group of Met adsorbed to the smaller particles, consistent with the slower dipolar dephasing of the protonated-carbon signals reported above. Another question that CSA characteristics can answer conclusively is that the 180-ppm peak that originated from a SCH_3 is associated with a COO, and not a PdCO moiety. A COO has a CSA span of 140 ppm, while a metal-bound CO has >230 ppm. Shown in Figure S1 is the comparison of a slow spinning (4 kHz) CP spectra of glycine, and SCH_3 (180 ppm) and have side band patterns consistent with the correct assignment of COO, and that on the Pd surface the methyl carbon has been oxidized to COO, likely after exposure to air.

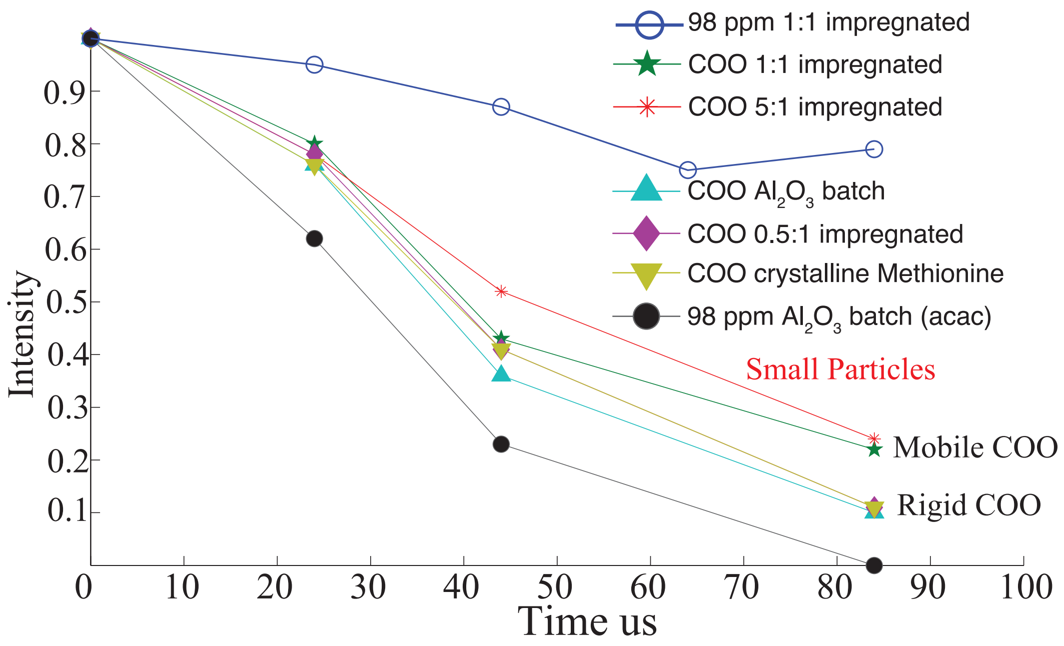

Figure 8. Chemical-shift anisotropy measurements. The assignment of signals between 90 and 120 ppm to sp^2- or sp^3-hybridized C can be decided based on the > 4-fold difference in their chemical-shift anisotropies (CSAs). Similarly, CO (carbon monoxide) with a large, uniaxial CSA of $\Delta\sigma = 230$ ppm or more can be distinguished from carbonate (small $\Delta\sigma = 86$ ppm) and COO (moderate $\Delta\sigma = 140$ ppm).

Discussion

Mobility and binding of Met on Pd and Al_2O_3. ^{13}C ssNMR can be used to probe large-amplitude molecular mobility with rates >10^5/s using dipolar dephasing of CH_2 signals. Peaks of CH_2 groups in a rigid environment will dephase efficiently while those of mobile CH_2 groups will not. The NMR spectra in Figure 1 show that Pd particle size (~10-nm vs. 4-nm diameter particles) had an effect on the dipolar dephasing of CH_2 groups. Met is seen to be immobilized when bound to larger Pd particles, and mobile on small particles. Since the chemical shifts and peak broadening are similar for both samples, an explanation for this mobility in terms of a fraction of Met not bound to the smaller Pd particle seems unlikely. We propose that this motion originates from rotations about the S-Pd bond (depicted in TOC graphic). This suggests that bidentate adsorption of Met (*i.e.*, adsorption at both the SCH_3

and COOH moieties) may be more energetically favorable, but can only occur on extended Pd surfaces. In contrast, adsorption via the SCH_3 group can occur even at under-coordinated Pd sites. The dynamics of Met on Al_2O_3 without and with Pd are distinct. Without Pd, the CH_2SCH_3 end group is highly mobile but NCH is not, which indicates that only the COOH/NH_2 end of the molecule interacts strongly with the Al_2O_3 surface. Lastly, it is interesting to compare the mobility of Met on Pd with amino butyric acid or propionic acid on Pd, which shows mobility of CH_2 and CH_3, but not NCH, which indicates that only the COOH/NH_2 end of the molecule is bound to Pd. In both fragments, the CH_2-CH_3 end is mobile, while the NCH group shows limited mobility. This indicates that both 2-amino butyric and propionic acid are bound only via COOH/NH_2. By contrast, Met on Pd was more immobilized, which must be attributed to the interaction of both the SCH_3 group and the COOH/NH_2 with the surface of larger Pd particles, and only the SCH_3 group with smaller particles.

Carbonate formation. All the samples that contain Pd yield spectra with a large carbonate peak, distinguished from formate by dipolar dephasing. [52] Carbonate is formed from Met on the catalyst exposed to air at ambient conditions. For the impregnated samples, a significant fraction (7-13%) of the total peak area is carbonate, while other Met fragmentation products are not prominent. While the integration values might suggest that the COO and S-CH_3 portions of the spectra are conserved and the new peaks are formed from carbon originated as CH_2 and NCH, it seems more likely that COO and SCH_3 only appear to be conserved; formation of acetic acid could produce two carbons whose signals overlap with the SCH_3 and COO peaks. These observations indicate a rapid carbonate formation mechanism that oxidizes most of the Met molecule to carbonate with very little accumulation of products on the path to carbonate, unlike the reactions with hydrogen where many intermediate species were observed. The efficient catalytic oxidation is surprising given that the catalyst is totally deactivated toward C=C bond reduction after exposure to high concentrations of Met. This finding implies that different sites are required for Met oxidation and breakdown than for hydrogenation and can be explained in terms of a model that attributes rapid oxidation to reactive step sites and moderate reduction to terrace sites.

Effect of PVA overcoat. A poly(vinyl alcohol) overcoat of Pd has been shown to reduce the rate of Met induced catalyst deactivation. [11] Surprisingly, the PVA overcoat did not seem to prevent Met from binding to Pd, as the same 19-ppm chemical shift was observed without and with the overcoat. However, the peak intensities showed indications of a weaker affinity for Met to the surface. [11] The spectra showed that carbonate formation is also not affected by the PVA overcoat, but interestingly in the PVA-coated samples formation of methane and carbonate is also observed (Figure S3) after exposure to flowing hydrogen. This suggests that PVA prevents the sites required for reduction reactions from being completely deactivated by methionine, or keeps hydrogen near the catalyst surface for a longer period of time. Interestingly, given that nearly 30% of the PVA is converted to polyacetylene by acid-catalyzed dehydration from the Al_2O_3, [11] some altered interaction with hydrogen may also play a role in the effect of the polymer overlayer, which could be blocking some sites responsible for hydrogen dissociation, suggested by the decrease in CO uptake observed for the PVA-overcoated catalyst. [11][5] A recent publication [53] summarizing work on Al_2O_3 overcoated Pd catalyst provides good evidence to support the hypothesis that the overcoat was beneficial to maintaining activity for reasons beyond reduction of sintering, and that different reactive sites on the Pd nanoparticle may be responsible for reactions that lead to deactivation. Our NMR studies were able to discern Met on Pd from the Al_2O_3 surface, but no conclusive experiments were conducted to see how Pd was affected from the PVA overcoat, which would also be insightful to see if altered reactivity was also an mechanism to improve the catalyst stability, and elucidate the mechanism by which the gold alloying improved catalyst stability.

Conclusions

We have demonstrated the application of a number of NMR techniques on poisoned catalyst materials prepared under “real” and “idealized for NMR” conditions to determine the mechanism by which methionine deactivates Pd particles, and its fate on the catalyst surface. Solid state NMR was shown to be an effective method to characterize a deactivated Pd/γ-Al_2O_3 catalyst using ^{13}C-enriched Met, which is a strong inhibitor of Pd catalysts. NMR is an effective technique to see differences in Met binding and reactions for different Pd loadings. The NMR data show that Met is selectively bound to Pd, and is rapidly fragmented at the carbon-sulfur bond under reducing conditions, leaving a mixture of Pd-SCH_3, and organic acids (aminobutyric, butyric, propionic, etc.). When the Pd catalyst is exposed to oxygen, it oxidizes Met to carbonate without showing significant accumulation of the acids observed under reducing conditions. Observation of the rapid oxidation activity even on a material that is deactivated for reduction reactions indicates that the sites required for reduction and oxidation on Pd particles are different. This demonstrates the potential utility of using solid state ^{13}C NMR to probe heterogeneous Pd nanoparticle catalyst on support surfaces using methionine, a sulfur-containing organic molecule, by observing the chemical shift of $S^{13}CH_3$, which is sensitive to binding onto different surfaces. Future work could be conducted to investigate the effects of catalyst alloying or overcoating.

Acknowledgements

This work was supported by the Center for Biorenewable Chemicals (CBiRC) funded by NSF grant EEC-0813570. T.J.S. acknowledges support from the National Science Foundation Graduate Research Fellowship Program under Grant No. DGE-1256259. Any opinions, findings, and conclusions or recommendations expressed in this material are those of the authors and do not necessarily reflect the views of the National Science Foundation.

References

(1) Nikolau, B.J., et al., *Platform biochemicals for a biorenewable chemical industry.* Plant Journal, 2008. **54**(4): p. 536-545.
(2 Shanks, B.H., *Unleashing biocatalysis/chemical catalysis synergies for efficient biomass conversion.* ACS Chemical Biology, 2007. **2**(Copyright (C) 2013 American Chemical Society (ACS). All Rights Reserved.): p. 533-535.
(3) Schwartz, T.J., et al., *Bridging the chemical and biological catalysis gap: Challenges and outlooks for producing sustainable chemicals.* ACS Catalysis, 2014. **4**: p. 2060-2069.
(4) Chia, M., et al., *Triacetic acid lactone as a potential biorenewable platform chemical.* Green Chem., 2012. **14**(7): p. 1850-1853.
(5) Albers, P., J. Pietsch, and S.F. Parker, *Poisoning and deactivation of palladium catalysts.* J. Mol. Catal. A, 2001. **173**(1–2): p. 275-286.
(6) Albers, P., et al., *Catalyst poisoning by methyl groups.* Chem. Commun., 1999(17): p. 1619-1620.
(7) Shen, J., et al., *Microcalorimetric, Infrared Spectroscopic, and DFT Studies of Ethylene Adsorption on Pt/SiO_2 and Pt-Sn/SiO_2 Catalysts.* Journal of Physical Chemistry B, 1999. **103**: p. 3923-3934.
(8) Hoyos, L.J., M. Primet, and H. Praliaud, *Sulfur Piosoning and Regeneration of Palladium-based Catalysts.* Journal of the Chemical Society, Faraday Transactions, 1992. **88**(1): p. 113-119.
(9) Brands, D.S., et al., *Sulfur Deactivation of Fatty Ester Hydrogenolysis Catalysts.* Journal of Catalysis, 1999. **186**: p. 169-180.
(10) Rodríguez, J.C., J. Santamaría, and A. Monzón, *Hydrogenation of 1,3-butadiene on Pd/SiO_2 in the presence of H_2S Deactivation and reactivation of the catalyst.* Applied Catalysis A, 1997. **165**: p. 147-157.

(11) Schwartz., T.J., et al., *Engineering catalyst microenvironments for metal-catalyzed hydrogenation of biologically-derived platform chemicals.* Angew. Chem. Int. Ed., 2014. **53**(47): p. 12718-12722.

(12) Li, X., et al., *Insights into the Deactivation Mechanism of Heterogeneous Mo/Hβ-Al2O3 Catalysts for Olefin Metathesis.* J. Phys. Chem. C, 2009. **113**(19): p. 8228-8233.

(13) Weitkamp, J. and S. Maixner, *Isobutane/butene alkylation on a LaNaY zeolite. Characterization of carbonaceous deposits by CP/MAS13C n.m.r. spectroscopy.* Zeolites, 1987. **7**(1): p. 6-8.

(14) Gutsze, A., et al., *Carbonization of polyethylene over acidic zeolites.* J. Catal., 1988. **113**(2): p. 525-528.

(15) Somorjai, G.A. and C. Aliaga, *Molecular Studies of Model Surfaces of Metals from Single Crystals to Nanoparticles under Catalytic Reaction Conditions. Evolution from Prenatal and Postmortem Studies of Catalysts†.* Langmuir, 2010. **26**(21): p. 16190-16203.

(16) Weckhuysen, B.M., *Snapshots of a working catalyst: possibilities and limitations of in situ spectroscopy in the field of heterogeneous catalysis.* Chem. Commun., 2002(2): p. 97-110.

(17) Azais, T., et al., *Solution State NMR Techniques Applied to Solid State Samples: Characterization of Benzoic Acid Confined in MCM-41.* J. Phys. Chem. C, 2010. **114**(19): p. 8884-8891.

(18) Kubies, D., R. Jérôme, and J. Grandjean, *Surfactant Molecules Intercalated in Laponite as Studied by 13C and 29Si MAS NMR.* Langmuir, 2002. **18**(16): p. 6159-6163.

(19) Fyfe, C.A. and A.C. Diaz, *Investigation of Slow Molecular Motions and Chemical Exchange in the High Loaded Form of p-Xylene in ZSM-5 by Two-Dimensional 13C Solid-State NMR Exchange Experiments.* J. Phys. Chem. B, 2002. **106**(9): p. 2261-2268.

(20) Azaïs, T., et al., *Solid-State NMR Study of Ibuprofen Confined in MCM-41 Material.* Chem. Mater., 2006. **18**(26): p. 6382-6390.

(21) Aguilar-Parrilla, F., et al., *High-Resolution Solid-State 13C and 15N NMR Spectroscopy of Pyrazole and 3,5-Dimethylpyrazole Adsorbed on Alumina and Silica.* J. Phys. Chem. , 1994. **98**(35): p. 8752-8760.

(22) Zhang, W., et al., *In situ solid-state NMR for heterogeneous catalysis: a joint experimental and theoretical approach.* Chem. Soc. Rev., 2012. **41**(1): p. 192-210.

(23) Slichter, C.P., *Probing phenomena at metal surfaces by NMR.* Annu. Rev. Phys. Chem., 1986. **37**(1): p. 25.

(24) McGrath, P., et al., *Site-Dependent 13C Chemical Shifts of CO Adsorbed on Pt Electrocatalysts.* J. Phys. Chem. C, 2008. **112**(38): p. 14702-14705.

(25) McGrath, P., et al., *Characterizing electrocatalytic surfaces: Electrochemical and NMR studies of methanol and carbon monoxide on Pt/C.* Electrochim. Acta, 2007. **53**(3): p. 1365-1371.

(26) Zelakiewicz, B.S., A.C. de Dios, and Tong, *13C NMR Spectroscopy of 13C1-Labeled Octanethiol-Protected Au Nanoparticles: Shifts, Relaxations, and Particle-Size Effect.* J. Am. Chem. Soc., 2002. **125**(1): p. 18-19.

(27) Tedsree, K., et al., *13C NMR Guides Rational Design of Nanocatalysts via Chemisorption Evaluation in Liquid Phase.* Sci., 2011. **332**(6026): p. 224-228.

(28) Tirendi, C.F., et al., *Platinum-proton coupling in the NMR spectrum of benzene on an alumina-supported platinum catalyst.* J. Phys. Chem., 1992. **96**(12): p. 5045-5048.

(29) Tirendi, C.F., G.A. Mills, and C. Dybowski, *Solid-state nuclear magnetic resonance investigations of benzene and cyclohexane adsorbed on platinum/aluminum oxide.* J. Phys. Chem., 1984. **88**(24): p. 5765-5767.

(30) Tirendi, C.F., G.A. Mills, and C.R. Dybowski, *Solid-state NMR spectroscopy of benzene adsorbed on .eta.-alumina.* J. Phys. Chem., 1989. **93**(8): p. 3282-3286.

(31) Fang, H., et al., *13C Chemical Shift of Adsorbed Acetone for Measuring the Acid Strength of Solid Acids: A Theoretical Calculation Study.* J. Phys. Chem. C, 2010. **114**(29): p. 12711-12718.

(32) Haw, J.F., et al., *NMR and Theoretical Study of Acidity Probes on Sulfated Zirconia Catalysts.* J. Am. Chem. Soc., 2000. **122**(50): p. 12561-12570.

(33) Barich, D.H., et al., *Theoretical and Experimental Study of the 13C Chemical Shift Tensors of Acetone Complexed with Brønsted and Lewis Acids.* J. Am. Chem. Soc., 1998. **120**(47): p. 12342-12350.

(34) Thursfield, A. and M.W. Anderson, *1H, 2H, and 13C Solid-State NMR Studies of Methanol Adsorbed on a Series of Acidic Microporous Zeotype Materials.* J. Phys. Chem., 1996. **100**(16): p. 6698-6707.

(35) Chin, Y.H. and P.D. Ellis, *Solid-state NMR study of acetylene adsorbed to platinum on alumina as followed by direct observation using CP MAS methods. Differentiation between acetylene adsorbed to alumina and platinum.* J. Am. Chem. Soc., 1989. **111**(19): p. 7653-7654.

(36) Gul-E-Noor, F., et al., *Adsorption of Small Molecules on Cu3(btc)2 and Cu3–xZnx(btc)2 Metal–Organic Frameworks (MOF) As Studied by Solid-State NMR.* J. Phys. Chem. C, 2013. **117**(15): p. 7703-7712.

(37) Zelakiewicz, B.S., et al., *13C NMR and Infrared Evidence of a Dioctyl−Disulfide Structure on Octanethiol-Protected Palladium Nanoparticle Surfaces.* J. Am. Chem. Soc., 2004. **126** (32): p. 10053-10058.

(38) Pruski, M., et al., *Solid-state NMR of carbon-13 in ethylene adsorbed on silica-supported ruthenium.* J. Am. Chem. Soc., 1990. **112**(11): p. 4232-4240.

(39) Soederlind, E. and P. Stilbs, *Chain conformation of ionic surfactants adsorbed on solid surfaces from carbon-13 NMR chemical shifts.* Langmuir, 1993. **9**(7): p. 1678-1683.

(40) Piedra, G., et al., *Solid-State 1H and 13C NMR Investigations of Dodecyl Sulfate−Alumina Interfacial Interactions Using High Surface Area Pseudo-Boehmite Solids Containing Adsorbed Surfactants.* Langmuir, 1996. **12**(8): p. 1958-1966.

(41) Wang, L.-Q., et al., *Conformation Heterogeneity and Mobility of Surfactant Molecules in Intercalated Clay Minerals Studied by Solid-State NMR.* J. Phys. Chem. B, 2000. **104**(13): p. 2810-2816.

(42) Yahnke, M.S., et al., *Quantitative Solid-State NMR Spectra of CO Adsorbed from Aqueous Solution onto a Commercial Electrode.* J. Am. Chem. Soc., 1996. **118**(48): p. 12250-12251.

(43) Mao, J.D. and K. Schmidt-Rohr, *Accurate Quantification of Aromaticity and Nonprotonated Aromatic Carbon Fraction in Natural Organic Matter by 13C Solid-State Nuclear Magnetic Resonance.* Environ. Sci. Tech., 2004. **38**(9): p. 2680-2684.

(44) Johnson, R.L., et al., *Spectrally edited 2D 13C13C NMR spectra without diagonal ridge for characterizing 13C-enriched low-temperature carbon materials.* J. Magn. Reson., 2013. **234**(0): p. 112-124.

(45) Armarego, W.L.F. and C.L.L. Chai, *Purification of Laboratory Chemicals*. 6th ed. 2009: Elsevier, Inc.

(46) Johnson, R.L. and K. Schmidt-Rohr, *Quantitative solid-state 13C NMR with signal enhancement by multiple cross polarization.* J. Magn. Reson., 2014. **239**(0): p. 44-49.

(47) Mao, J.D. and K. Schmidt-Rohr, *Separation of aromatic-carbon 13C NMR signals from di-oxygenated alkyl bands by a chemical-shift-anisotropy filter.* Solid State Nucl. Magn. Reson., 2004. **26**(1): p. 36-45.

(48) Fritzsching, K.J., et al., *Practical use of chemical shift databases for protein solid-state NMR: 2D chemical shift maps and amino-acid assignment with secondary-structure information.* J. Biomol. NMR, 2013. **56**(2): p. 155-167.

(49) Chia, M., et al., *Mechanistic Insights into Ring-Opening and Decarboxylation of 2-Pyrones in Liquid Water and Tetrahydrofuran.* Journal of the American Chemical Society, 2013. **135**: p. 5699-5708.

(50) Chia, M., et al., *Triacetic Acid Lactone as a Biorenewable Platform Chemical.* Greem Chemistry, 2012. **14**: p. 1850-1854.

(51) van Wüllen, L. and M. Kalwei, *13C–27Al TRAPDOR and REDOR Experiments for the Detection of 13C–27Al Dipolar Interactions in Solids.* J. Magn. Reson., 1999. **139**(2): p. 250-257.

(52) Lazo, N.D., et al., *In situ carbon-13 solid-state NMR study of the Cu/ZnO/Al2O3 methanol synthesis catalyst.* J. Am. Chem. Soc., 1992. **114**(22): p. 8552-8559.

(53) Lu, J., J.W. Elam, and P.C. Stair, *Synthesis and Stabilization of Supported Metal Catalysts by Atomic Layer Deposition.* Acc. Chem. Res., 2013. **46**(8): p. 1806-1815.

Supporting Information

SOLID-STATE ^{13}C NMR OF METHIONINE-POISONED Pd/γ-Al_2O_3 CATALYSTS

Robert L. Johnson[1], Thomas J. Schwartz[2], James A. Dumesic[2], Klaus Schmidt-Rohr*[,1,3]

[1]Department of Chemistry, Iowa State University, Ames, IA 50011
[2]Department of Chemical and Biological Engineering, University of Wisconsin, Madison, WI 53706
[3]Department of Chemistry, Brandeis University, Waltham, MA 02453

S1. Comparison of side band pattern for COOH identification

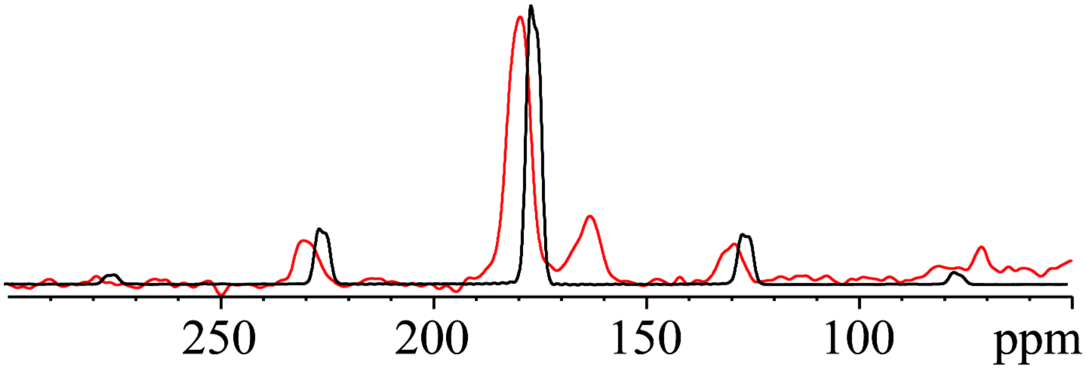

Figure S1. CP/echo experiments run under 4 kHz MAS for ^{13}COO labeled glycine (red) and the 180 ppm peak from SCH_3 labeled met produced from batch conditions. The pattern of spinning sidebands is a match, and proves this assignment.

S2. Time dependence of carbonate formation

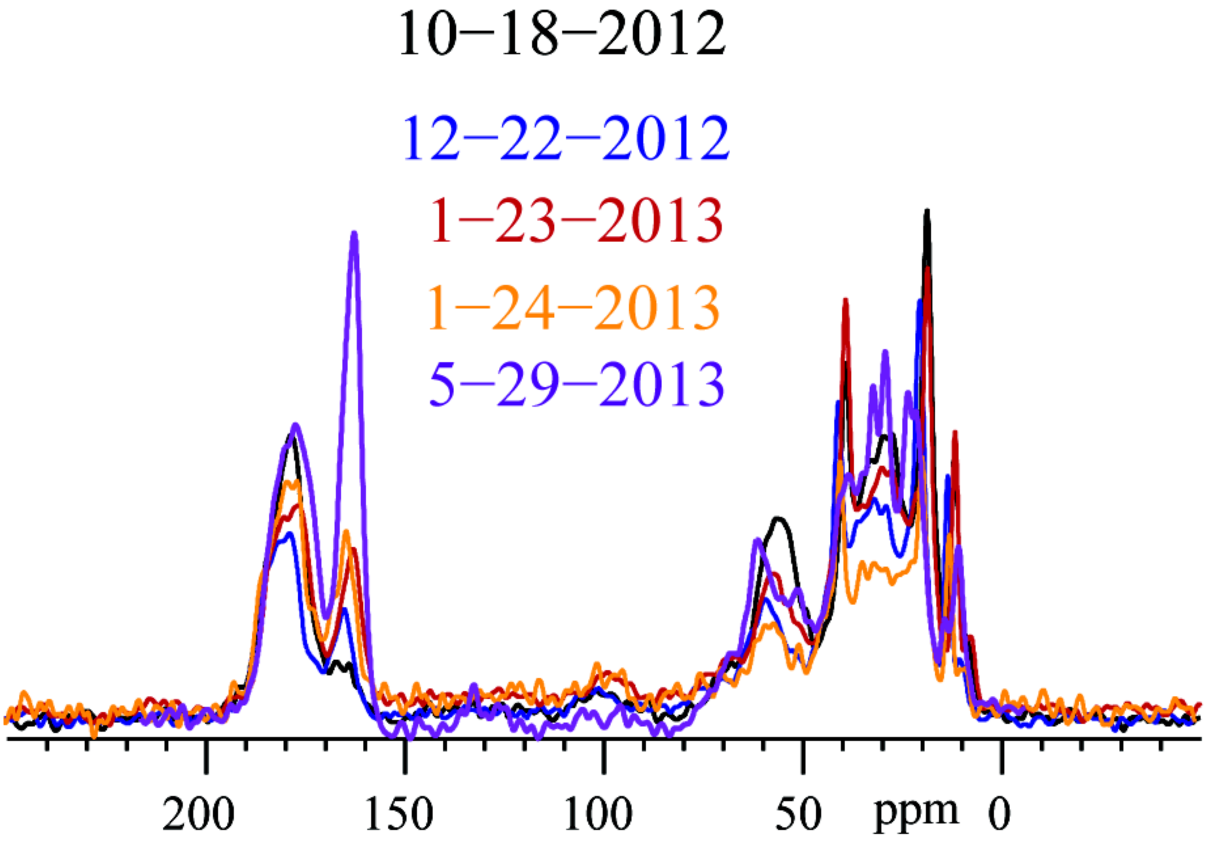

Figure S2. Transformation occurring at room temperature to a sample in the NMR rotor. The carbonate peak at 163 ppm increases dramatically during this 6-month period.

S3. Effect of PVA to produce methane

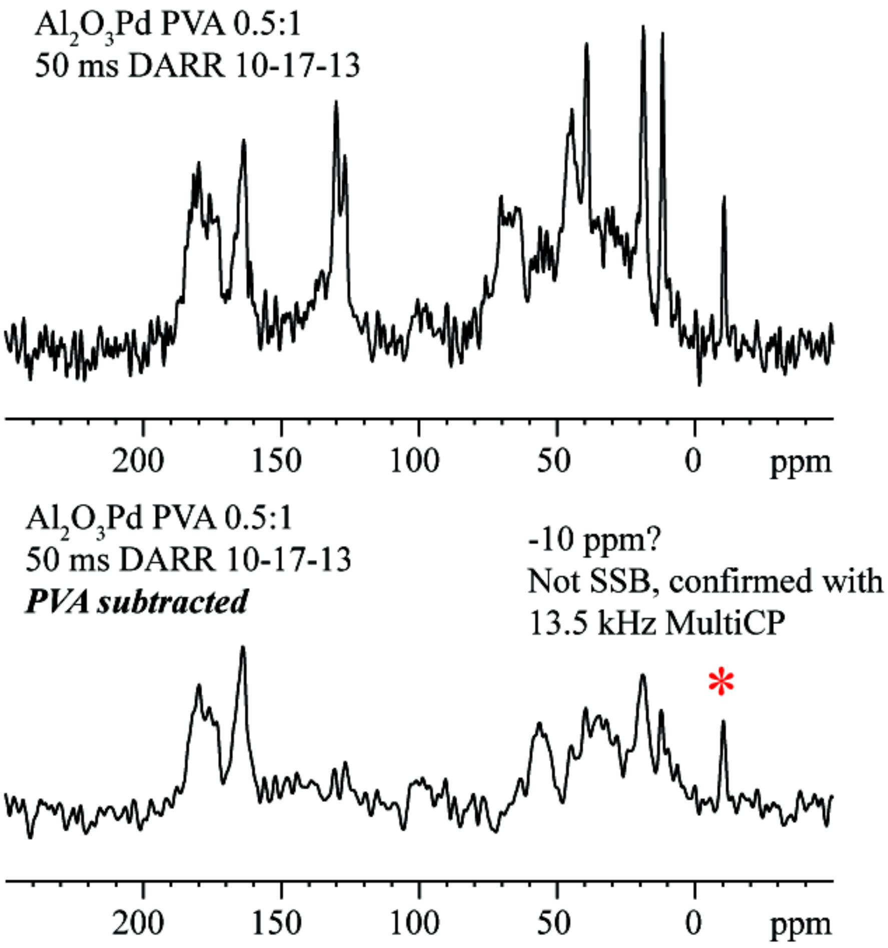

Figure S3. Spectra from Pd catalyst with PVA overcoat impregnated with met in a 0.5:1 molar ratio with Pd CO adsorption sites after reaction in flowing H_2 and stored in the rotor at room temp. The spectrum exhibits a peak at -10 ppm, which we assign to methane. To verify this, we ran another experiment at a different spinning frequency to show ensure it was not a spinning sideband, and observed that the peak was removed after venting the rotor.

CHAPTER 6. QUANTITATIVE SOLID-STATE ^{13}C NMR WITH SIGNAL ENHANCEMENT BY MULTIPLE CROSS POLARIZATION

Journal of Magnetic Resonance, **239** pp 44-49, 2014

Department of Chemistry, Iowa State University, Ames, IA 50011, USA
*Corresponding Author: srohr@iastate.edu, 001-515-294-6105

Keywords. Cross polarization; quantitative CP; ramp CP; aromaticity; complex organic matter

Abstract

A simple new method is presented that yields quantitative solid-state ^{13}C magic-angle spinning (MAS) NMR spectra of organic materials, with good signal-to-noise ratios. It achieves long (>10 ms) cross polarization (CP) from ^{1}H without significant losses due to relaxation and with a moderate duty cycle of the radio-frequency irradiation, by multiple 1-ms CP periods alternating with ^{1}H spin-lattice relaxation periods that restore the ^{1}H magnetization. The new method incorporates previous techniques for less distorted CP/MAS spectra, such as a linear variation ("ramp") of the radio-frequency field strength, and it overcomes their main limitation, which is $T_{1\rho}$ relaxation of the spin-locked ^{1}H magnetization. The ramp of the radio-frequency field strength and the asymptotic limit of cross polarization makes the spectral intensity insensitive to the exact field strengths used. The new multiCP pulse sequence is a "drop-in" replacement for previous CP methods and produces no additional data-processing burden. Compared to the only reliable quantitative ^{13}C NMR

method for unlabeled solids previously available, namely direct-polarization NMR, the measuring time is reduced by nearly two orders of magnitude, enabling higher-throughput quantitative NMR studies. The new multiCP technique is demonstrated with 14-kHz MAS on amino-acid derivatives, plant matter, a highly aromatic humic acid, and carbon materials made by low-temperature pyrolysis.

Introduction

Quantification of composition is a central aspect of solid-state NMR characterization of complex materials and natural organic matter [1-9]. This enables NMR to provide accurate functional-group concentrations and aromatic-carbon fractions (aromaticities), for instance in natural [1] or man-made biochars [5] for carbon sequestration and enhanced soil fertility [1, 2], or for carbon-based hydrothermally stable catalyst supports [8]. NMR is also the best available method for analyzing various forms of organic matter that are present in the environment in megaton quantities, from kerogen in rocks [3] to soil organic matter [7] and dissolved organic matter in the oceans [4]. Measurements of the concentrations of various biomolecules are further of interest for characterizing raw plant materials and process intermediates in biofuels production. Quantification of aromatic C-H and C-O enables estimates of the size of polycondensed aromatic clusters [5], while quantification of crystallinity is important for polymers [6] and pharmaceuticals [9].

If NMR experiments are properly designed and executed, peak areas in the spectrum are proportional to the numbers of spins in the respective chemical sites or phases. This is a great advantage over vibrational spectroscopies, where band intensities also depend on variable factors like transition-matrix elements. The most reliable method for obtaining quantitative NMR spectra is magic-angle spinning (MAS) with direct polarization (DP) and recycle delays that permit essentially complete longitudinal (T_1) relaxation of the magnetization of the observed nuclei.[10, 11] However, this approach is time-consuming when T_1 is long. Acquiring a quantitative DP/MAS spectrum of ^{13}C in natural abundance with acceptable signal-to-noise ratio usually takes overnight for complex organic materials [1, 7, 10, 11]. It is particularly challenging in relatively “clean” and rigid solids, including plant matter, where fluctuating fields driving longitudinal relaxation are weak due to limited segmental motions and low concentrations of unpaired electrons.

Most solid-state ^{13}C and ^{15}N NMR experiments of organic solids rely not on direct polarization, but on cross polarization from ^{1}H using simultaneous radio-frequency irradiation on ^{1}H and the observed nucleus [12], with specific conditions for the field strengths (“Hartmann-Hahn match”) [13]. This enhances the signal intensity by about an order of magnitude through several factors, including the larger magnetic dipole moment of ^{1}H and the faster recovery of ^{1}H magnetization. However, CP/MAS spectra are usually not quantitative, since the magnetization transfer from ^{1}H is faster for carbons bonded to ^{1}H than for nonprotonated C or mobile segments with their weaker H-C dipolar couplings [14]. In particular in materials with ^{13}C far from ^{1}H (e.g. in the fused aromatic rings of chars) and with MAS frequencies >10 kHz, standard cross polarization underrepresents significant parts of the spectrum [5, 7, 11].

Methods for obtaining quantitative ^{13}C spectra after cross polarization have been demonstrated for homogeneous, uniformly ^{13}C-enriched materials [15, 16], but they rely on equilibration by ^{13}C spin diffusion, which is too slow without isotope enrichment. One of the best available cross polarization methods for ^{13}C in natural abundance (1.1%) is ramp

CP,[14] where the radio-frequency (rf) field strength of ^{1}H or ^{13}C is varied linearly so that a Hartmann-Hahn match is achieved at some time in all parts of the samples and for all functional groups, and in the presence of some fluctuations in radio-frequency field strengths. Ramp CP has been shown to be quantitative in ^{1}H-rich crystalline model compounds with nonprotonated carbons separated by two bonds from the nearest H, but only with CP times of ca. 10 ms [14]. These long times are required because most sites experience the necessary Hartmann-Hahn match only during a fraction of the CP period. However, for most "real" materials, signal loss due to $T_{1\rho}$ relaxation during 10 ms of cross polarization is substantial, and differential $T_{1\rho}$ relaxation, as shown schematically in Fig. 1a, would result in nonquantitative spectra. Rf-induced heating is another problem of the long irradiation required for quantitative ramp CP, in particular for low-γ nuclei or conducting samples. Thus, ramp CP cannot reliably provide quantitative spectra in most complex organic materials.

Results and Discussion

Multiple CP with ^{1}H repolarization.

The new multiple-CP (multiCP) pulse sequence, shown in Fig. 1b, eliminates the problems described above for the most part and enables long CP providing quantitative spectra even for materials with $T_{1\rho} < 10$ ms. The crucial innovation of the multiCP approach is repeated blocks of CP separated by periods of duration t_z (~0.5 s), during which the ^{1}H magnetization can recover to a near-equilibrium value (Fig. 1b). Both ^{1}H and ^{13}C magnetization are stored along the z-direction (i.e., along the B_0 field) by 90^{o} pulses at the start of t_z. During t_z, the ^{1}H magnetization undergoes $T_{1,H}$ relaxation towards its thermal-equilibrium value, which reverses most of the ^{1}H magnetization loss by $T_{1\rho H}$ during the preceding CP period. In addition, the local magnetization loss of ^{1}H spins near ^{13}C due to the polarization transfer to ^{13}C will be canceled by ^{1}H spin diffusion from the surrounding spins; these constitute a large reservoir of ^{1}H magnetization in samples with ^{13}C in natural abundance, where the ^{1}H:^{13}C ratio usually exceeds 50:1.

The ^{1}H repolarization by $T_{1,H}$ relaxation during t_z and the resulting converging high levels of ^{13}C magnetization are seen in the magnetization traces shown in Figure 1, which were generated using a simple simulation model with $T_{1\rho H}$, $T_{1,H}$, T_{CH}, and $T_{1,C}$ time constants as well as pulse flip-angle errors. During CP, ^{1}H magnetization was reduced by exponential $T_{1\rho H}$ relaxation of towards zero, while it increased during t_z, due to $T_{1,H}$ relaxation toward equilibrium. During CP, the ^{13}C magnetization was generated with time constants T_{CH} = 0.2 ms and 1 ms, and an exponential dependence approaching the instantaneous ^{1}H magnetization; during t_z, it was slightly decreased by $T_{1,C}$ relaxation toward equilibrium. A small fraction of ^{1}H and ^{13}C magnetization (2%, corresponding to a 12° root-mean-square flip-angle error) was lost after each 90° pulse. Loss of ^{1}H magnetization due to transfer to ^{13}C, and replenishment by ^{1}H spin diffusion was not included in the simulations.

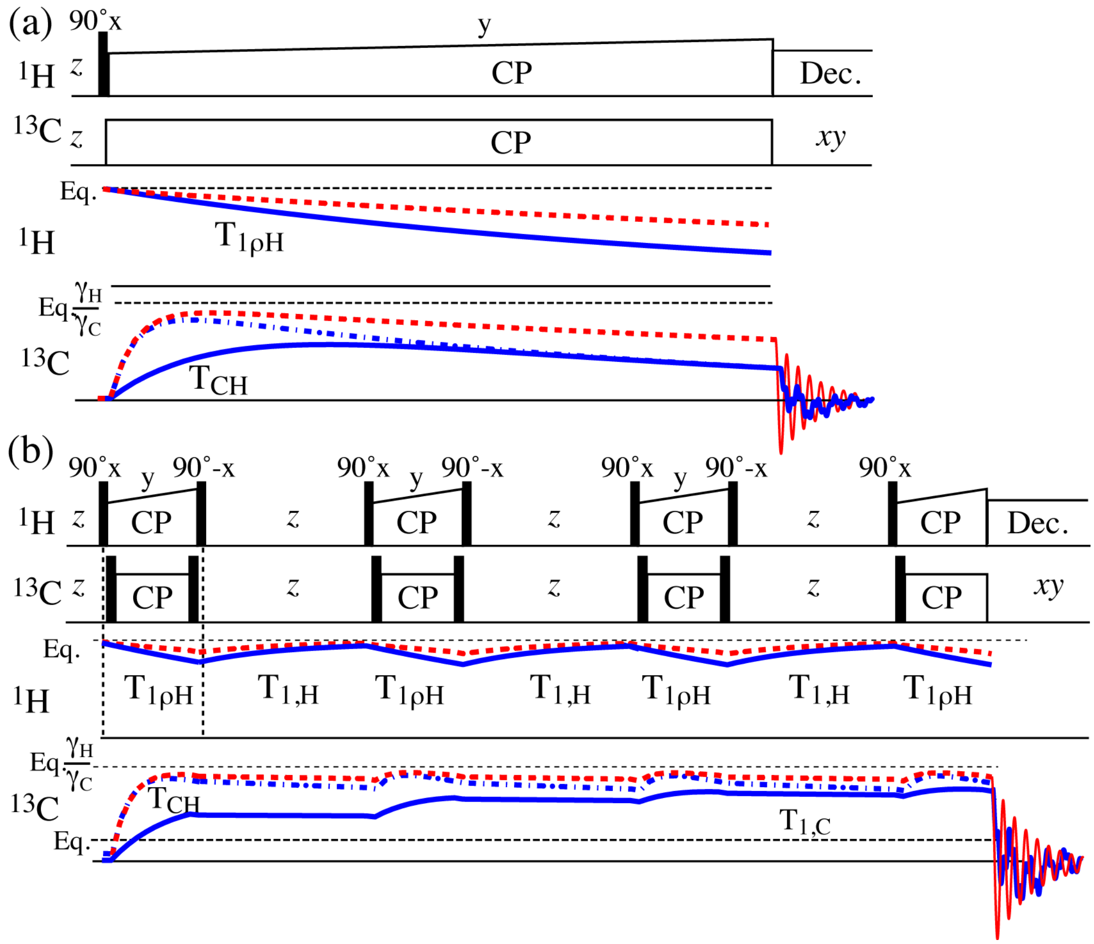

Fig. 1. (Color online) Cross-polarization pulse sequences (two top traces in a and b), and time courses from numerical simulations (two bottom traces, in color) of ^{1}H and ^{13}C magnetizations for three types of segments: CH with T_{CH} = 0.2 ms, T_{1rH} = 12 ms, and $T_{1,C}$ = 10 s (dashed red line); CH with shorter T_{1rH} = 5 ms and $T_{1,C}$ = 3 s (dash-dotted blue line), and nonprotonated C with T_{CH} = 1 ms, T_{1rH} = 5 ms, and $T_{1,C}$ = 10 s (continuous blue line). Filled black rectangles: 90^o pulses. (a) Standard ramp CP. The ^{13}C magnetizations of the three components never achieve similar values, which means that a quantitative spectrum cannot be obtained. (b) Multiple CP. During each period with only z-magnetization, of duration $t_z \approx$ 2 $T_{1,H}$, ^{1}H spin-lattice relaxation mostly reverses the loss of ^{1}H magnetization that has resulted from T_{1rH} relaxation during the preceding CP period. Thus, the total CP time can be long enough to fully polarize nonprotonated carbons without significant magnetization loss by T_{1rH}. The durations of the CP and z periods are not drawn on the same scale, with time steps of 0.1 ms during CP, and of 10 ms during t_z. In the experiments, we used a CP ramp on the ^{1}H channel with 11 steps of 0.05 or 0.1 ms duration and a 1% amplitude increment. A Hahn echo of 2 t_r = 0.14 ms duration (not shown) with high-power decoupling was used after the last CP period to achieve dead-time-free signal detection. The original pulse sequence code is shown in the Supporting Information and at http://www.public.iastate.edu/~nmrksr/.

The simulations show that $t_z \approx 2\ T_{1,H}$ is sufficient for repolarization to >95% of equilibrium ^{1}H magnetization, if $T_{1\rho,H}/t_{CP} > 4$. Thus, for natural organic matter and low-temperature carbon materials with unpaired electrons driving fast $T_{1,H}$ relaxation, t_z between 0.2 and 0.5 s gives good results, while for plant materials with their longer relaxation times, $t_z \approx 1$ s should be used. For two reasons, t_z should not be chosen too long. First, it increases the time per scan and thus the measuring time. Secondly, during t_z, $T_{1,C}$ relaxation of the ^{13}C magnetization will also occur and can reduce the magnetization when the carbons are polarized beyond their equilibrium magnetization. Fortunately, $T_{1,C}$ of most carbons is much longer than $T_{1,H}$ [10, 11]. In addition, the signal of short-$T_{1,C}$ carbons that cross polarize quickly, such as CH_3 and CH_2, is not significantly affected by $T_{1,C}$ relaxation, since their magnetization recovers during each cross polarization period (dash-dotted line in Fig. 1); indeed, in our spectra, we did not see CH_3 signal reduction. In ^{13}C-enriched materials, ^{13}C spin diffusion during t_z will contribute to equilibrating the magnetization of protonated and nonprotonated C, and an additional t_z period optimized for ^{13}C spin diffusion [15, 16] should be added before detection.

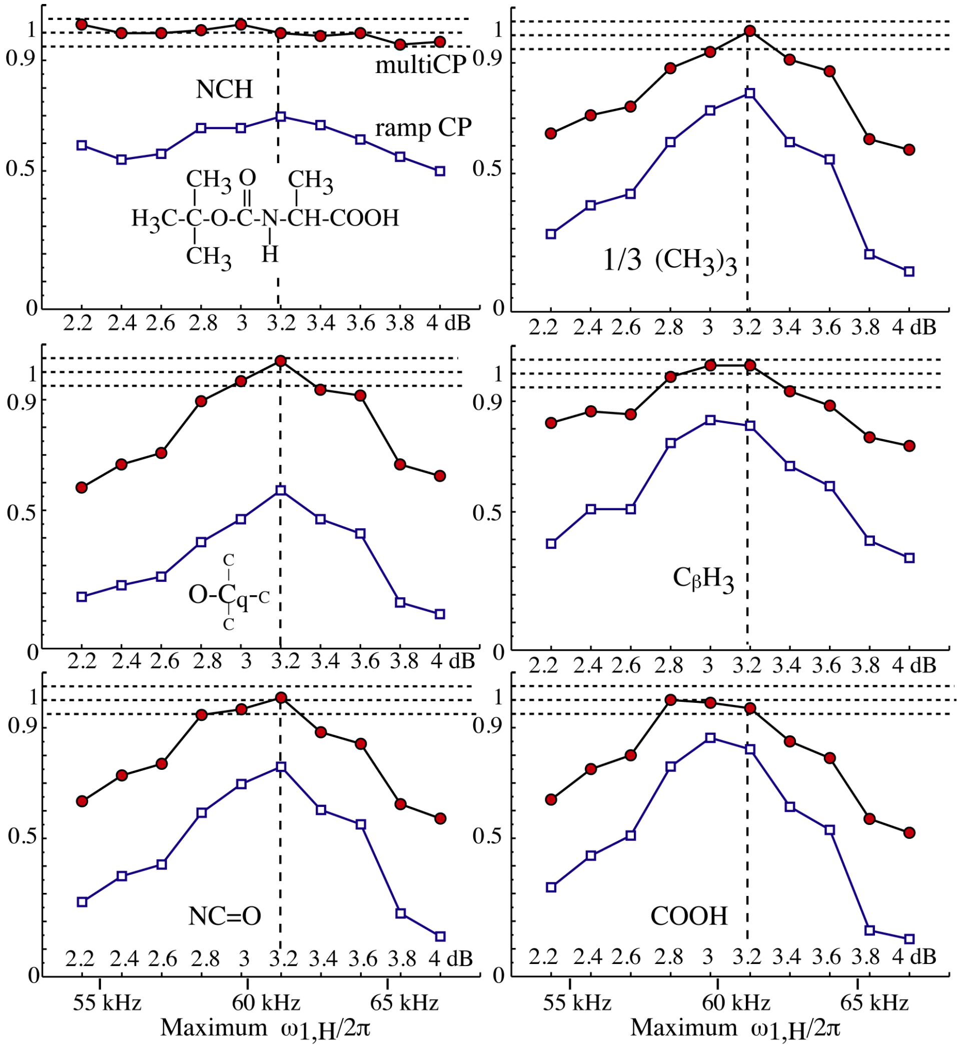

Fig. 2. (Color online) Integral peak intensities for the six carbon sites in N-t-BOC alanine (structure shown in the top left panel) as a function of the maximum ^{1}H radio-frequency strength in 12-ms multiCP (red circles) and regular 1.1-ms ramp CP (open blue squares) experiments, at 14-kHz MAS with fixed ^{13}C irradiation at ca. $\gamma_C B_{1C} = 2\pi$ 43 kHz, and ^{1}H irradiation with an amplitude ramp from 90 – 100%. Maxima are observed when the ^{1}H ramp is centered near $\gamma_C B_{1C} = 2\pi$ 57 kHz (corresponding to a maximum of ca. 2π 60 kHz). All integrals are on the same scale. The 95-105% intensity range is marked by dashed lines. The value of $20 \log(\omega_{1,H,max}/\omega_{1C})$, in dB, is also shown on the horizontal axis.

Due to $T_{1,C}$ relaxation during t_z, one cannot simply increase the number of CP periods to very large values with the goal of polarizing species with very weak couplings to ^{1}H. When the duration of all t_z periods taken together exceeds $T_{1,C}$ of the slowly cross-polarizing species, loss by $T_{1,C}$ cancels the gain by T_{CH} for these species, and a further increase in the number of CP steps will not increase the signal. This means that t_z should be chosen as short as possible while still permitting recovery of the ^{1}H magnetization and keeping the rf duty cycle moderate. Since typically $t_z \approx 2\ T_{1,H,max}$, no further gain in intensity will be observed when the number of repeats is approximately ½ $T_{1,C}/T_{1,H}$.

The individual CP periods are typically around 1 ms in duration. If very short (< 3 ms) $T_{1\rho,H}$ components are present, one should use shorter (< 1 ms) individual CP times, in particular directly before detection, to avoid residual effects of differential $T_{1\rho,H}$ relaxation. Instead of the simple amplitude ramps shown in Fig. 1 and used in the experiments, more complex schemes providing superior CP dynamics can also be used.

MultiCP of model compounds.

In crystalline model compounds, multiCP performs well, as expected from analogous ramp-CP studies.[14] Relative signal intensities are within ±5%, see Table 1, which compiles peak integrals for N-t-BOC-alanine and N-acetyl valine (without ^{13}C enrichment) measured with 12-ms multiCP at 14-kHz MAS, with ramps from 90-100% on the ^{1}H spin-lock field. The intensities with conventional ramp CP of 1.1-ms duration were lower and varied much more, by ±20%. The dependence of the peak intensities on the rf field strength is shown in Fig. 2 for N-t-BOC alanine. As expected, the signal intensity for protonated carbons with their strong C-H couplings is not sensitive to the radio-frequency field strength, while the curves for the nonprotonated carbons show a pronounced maximum. Matched intensities of 1 ± 0.05 are found after multiCP over a sufficiently broad range of rf-field strengths, broader and higher than for the corresponding 1.1-ms ramp CP. The match between different groups is best near the intensity maxima, which provides a clear criterion for the best CP matching condition to use in multiCP experiments. The corresponding data for N-acetyl-L-valine are shown in Fig. S1.

Table 1. Integrated peak intensities in 12-ms multiCP (90-100% ramp) and corresponding 1.1-ms ramp-CP spectra of ^{15}N-t-BOC alanine (two top rows) and ^{15}N-acetyl valine (two bottom rows), recorded at 14-kHz MAS.

Sample	COO	NC=O	OCq	NCH	CH	CH_3	CH_3	CH_3
N-t-BOC Ala multiCP	**1.01**	**1.00**	**1.04**	**1.00**[1]	**--**	**3 x 1.02**		**1.03**
N-t-BOC Ala ramp CP	0.82	0.76	0.58	0.69	--	3 x 0.80		0.82
NAV multiCP	**2 x 1.01**		**--**	**1.00**[1]	**1.01**	**0.98**	**0.98**	**0.97**
NAV ramp CP	2 x 0.94		--	0.73	0.78	0.92	0.97	0.96

[1]: The multiCP NCH signal intensity for each sample has been set to 1.00.

The dependence of the peak intensities of N-tBOC alanine on the total CP time in multiCP experiments is displayed in Figure 3. Within 6 - 9 ms, the asymptotic intensity has been reached to within ±5%. The slowest increase is observed for the nonprotonated quaternary sp^3-hybridized C-O carbon ("C_qO"), consistent with a literature study of ramp CP on the same compound. [14] However, the initial increase of the NCH intensity is slower than expected (while at 10.3-kHz MAS, the time dependence is more normal, similar to that reported in the literature [14]). The observed high final intensity shows that this effect is unrelated to potential effects of insufficient decoupling before detection of the Hahn echo, which would be independent of the duration of cross polarization. Instead, we attribute the unusual behavior to the disruption of the ^{1}H dipolar coupling network (weakened by a factor of ½ due to the spin lock during CP) by 14-kHz MAS. A CH group then becomes a ^{13}C-^{1}H spin pair, and its strong coupling truncates weaker long-range ^{13}C-^{1}H couplings during CP.

Within the spin pair, the ^{13}C magnetization equilibrates quickly at only 50%, and transfer of magnetization from other protons occurs only on a slower time scale.

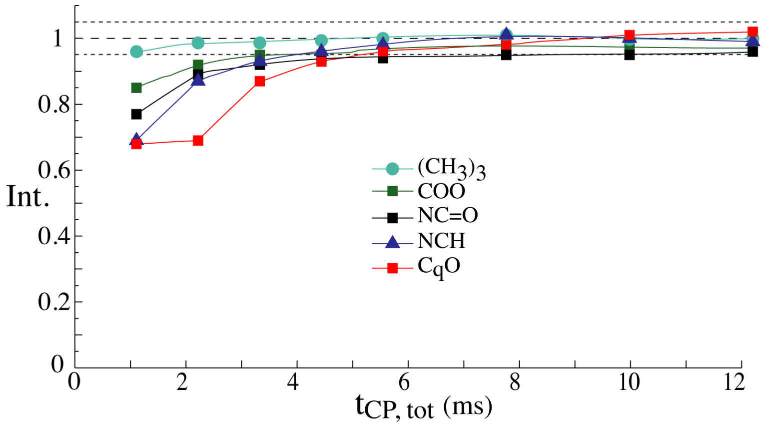

Figure 3. Integral peak intensities for N-t-BOC alanine as a function of the total cross-polarization time in multiCP experiments with an increasing number of 1.1-ms ramp CP periods. The 95-105% intensity range is marked by dashed lines. The initial intensity (after 1.1 ms) is higher in than for 1.1-ms ramp CP in Figure S2 due to the additional ^{13}C direct-polarization pulse used in multiCP.

MultiCP of complex organic matter.

Figure 4 shows multiCP spectra of two low-temperature carbon materials with significant aromaticities (signal fraction between 100 and 165 ppm). As a high-quality reference for the spectra of the unenriched materials, quantitative direct-polarization spectra of corresponding ^{13}C-enriched materials are also shown (dashed red lines). The agreement is seen to be excellent. Much noisier quantitative DP spectra of the unenriched chars taken within the same measuring time and scaled up to compensate for the smaller number of scans resulting from the much longer recycle delays are also shown for comparison (bottom of Fig. 4). The higher noise level in the DP spectra precludes analysis of smaller peaks clearly seen in the corresponding multiCP spectra.

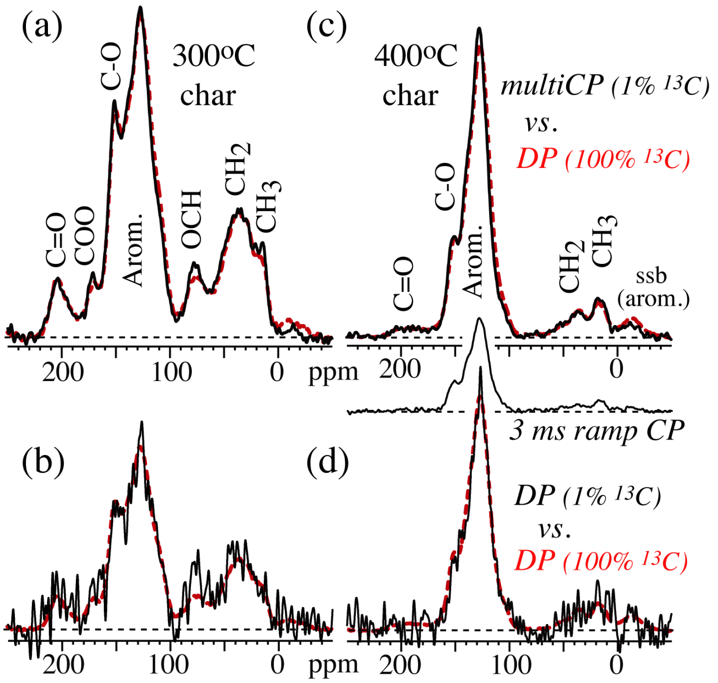

Figure 4. (Color online) ^{13}C NMR spectra of chars, measured at 14-kHz MAS in a 9.4-T field within 3 hr each. (a, b) Char made from regular glucose by pyrolysis at 300°C. (a) The signal from 11 x 1.1 ms = 12-ms multiCP (full line) is matched with a quantitative direct-polarization spectrum of the corresponding ^{13}C-enriched material (red dashed line). (b) DP spectrum (bottom row) taken with recycle delays of 280 s within the same measuring time and scaled up to compensate for the smaller number of scans. (c) Same as in (a) for 400°C pyrolysis char (with a shorter multiCP time of 11 x 0.55 ms = 6 ms). A regular 3-ms ramp-CP spectrum (middle row) is also shown; its intensity is reduced by $T_{1\rho}$ relaxation. (d) Same as in (b) for 400°C pyrolysis char. The experimental conditions were the same as for the optimum in Fig. 2. “ssb”: Spinning sideband.

Fig. 5a compares the multiCP spectrum (full black line) of unlabeled plant matter (switchgrass, a promising raw material for cellulosic ethanol) with the quantitative direct-polarization spectra of ^{13}C-enriched switchgrass (dashed red line). Again, the agreement is very good. The multiCP spectrum in Fig. 5a shows a signal enhancement by ~2 relative to the DP spectrum of the same material in Fig. 5b, which is equivalent to a $2^2 \approx$ 4-fold shorter measuring time. Combined with a ~30-times shorter recycle delay in multiCP, this yields a ~100-fold reduction in measuring time of multiCP compared to DP. The aromatic (lignin) signals of switchgrass are barely above the noise level in the DP NMR spectrum of Fig. 5b, while they are well defined in the multiCP spectrum, Fig. 5a. Quantitative analysis of plant materials with fairly high throughput can be expected to represent a particularly useful application of multiCP ^{13}C NMR.

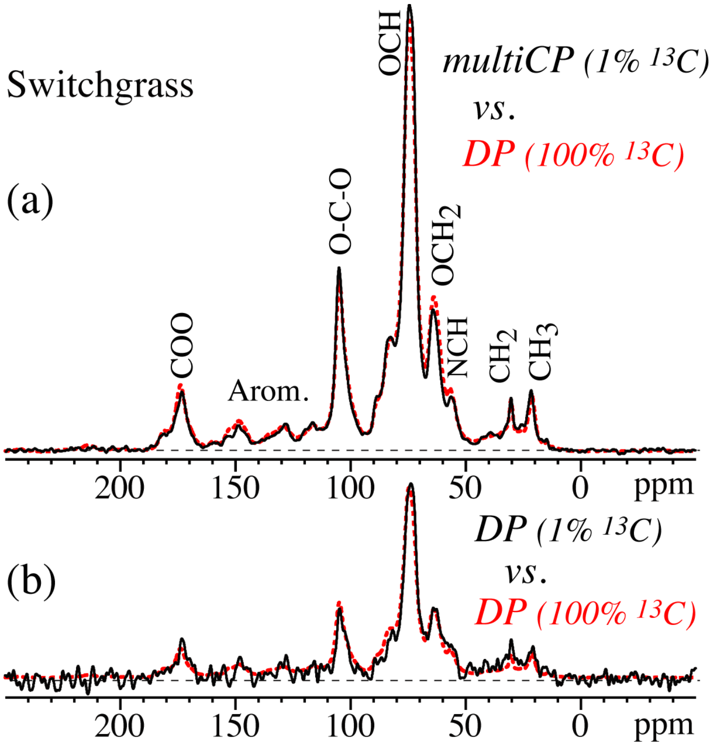

Fig. 5. (Color online) Quantitative ^{13}C NMR spectra of switchgrass, measured at 14-kHz MAS within 5 hr each. (a) Spectrum after 7 x 1.1 ms multiCP, with t_z = 0.9 s (full line); it is matched with a quantitative DP spectrum of the corresponding ^{13}C-enriched material (red dashed line). (b) For comparison: DP spectrum taken within the same measuring time with 120-s recycle delays. Red dashed line: Intensity-matched DP spectrum of the ^{13}C-enriched material.

The multiCP of a standard prairie-soil humic acid, shown in Fig. 6, also agrees well with its – again much noisier – direct-polarization counterpart obtained within the same measuring time. Fig. 6 also demonstrates that multiCP can be combined with recoupled dipolar dephasing in order to determine the fraction of nonprotonated carbons [17]. This is particularly useful for estimating the size of clusters of polycondensed aromatic rings [5] in carbon materials.

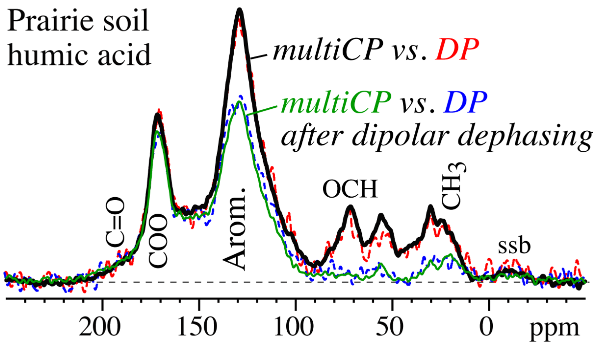

Figure 6. Quantitative ^{13}C NMR spectra of a standard prairie soil humic acid, measured at 14-kHz MAS within 5 hr each, after 11.5-ms (10 x 1.1 ms + 0.5 ms) multiCP with t_z = 0.4 s (thick full line), and after DP with 30-s recycle delays (red dashed line), scaled to match peak intensities. Thin full (green) and dashed (blue) lines: Corresponding multiCP and DP spectra, respectively, of nonprotonated C and mobile segments selected by recoupled dipolar dephasing.

Parameters for multiCP NMR.

The new multiCP pulse sequence is a “drop-in” replacement for conventional, less quantitative CP methods. Beyond standard CP optimization and accurate 90^o-pulse length determination, it requires only one additional delay: the spacing t_z between CP periods, typically chosen as ~ 2 $T_{1,H}$, which corresponds to about half the normal minimum recycle delay. Thus, for most soil organic matter samples and chars, $t_z \approx 0.25$ s, while in cleaner plant materials, $t_z \approx 1$ s should be used. The relevant relaxation times $T_{1,H}$, $T_{1,C}$, and $T_{1\rho H}$ need to be known only approximately. $T_{1,H}$ should be estimated just as for regular optimized CP experiments, for instance by comparing the signal intensities obtained in simple CP experiments with a few different recycle delays (e.g. 0.5 s, 2 s, and 6 s). $T_{1,C}$ needs to be known less accurately than for quantitative DP NMR, since one only needs to establish that it exceeds 10 t_z for the nonprotonated carbons or liquid-like components. This can be achieved, for instance, using a 5- or 10-s $T_{1,C}$ filter after CP. [10] $T_{1\rho}$ can be estimated easily from a two-point measurement, with a 0.01 ms and a ~5 ms ^{1}H spin lock before simple CP. If after the 5-ms spin lock no significant peak is decreased to less than 40%, or if no differential relaxation is observed and >20% of the signal is left, the regular 1.1-ms CP periods can be used. Otherwise, the CP periods should be shortened to ~ 0.5 ms.

The data and theory show that if the results from ramp CP are quite good, those of multiCP will be excellent, since the last step of the multiCP pulse sequence is ramp CP, and the preceding CP periods boost the challenging signals. The multiCP approach can be used not only with ramp CP at 14 kHz MAS as shown here, but with any CP method that provides quantitative spectra in model compounds with long $T_{1\rho}$. Finally, the quantitative peak areas in a multiCP spectrum can be determined by simple integration, without complicated data processing. Among other information, the carbon aromaticity can be obtained, in particular when quantitative ^{13}C NMR is complemented with separation of overlapping aromatic and alkyl O-C-O signals by CSA-filtering [17]. The application of multiCP to ^{15}N, ^{31}P, and ^{29}Si NMR are currently being explored.

Conclusions

MultiCP is a simple, robust method that can provide quantitative ^{13}C NMR spectra with much better signal-to-noise ratios than previously achievable in quantitative direct-polarization NMR. It has been validated successfully with ramp CP at 14 kHz MAS not only on amino acid-derivatives, but also on plant matter, chars from low-temperature pyrolysis, and a humic acid.

Experimental

Materials.

^{15}N-t-BOC-alanine and ^{15}N-acetyl-L-valine, purchased from Cambridge Isotopes, were used because of their availability in our laboratory, already packed in rotors; the corresponding unlabeled samples should produce equivalent ^{13}C NMR results. A standard humic acid (from Elliot prairie soil) was purchased from the International Humic Substances Society.

^{13}C-enriched and regular switchgrass stems were purchased from Isolife (Wageningen, The Netherlands), where plants were grown exposed to $^{13}CO_2$ and regular CO_2, respectively, under otherwise identical conditions. Each sample arrived as a 1-inch section of stem, which was then ground into a fine powder using a cryomill, with identical grinding programs for both the ^{13}C-enriched and the regular material.

Low-temperature carbon materials were prepared by pyrolysis of regular or ^{13}C-enriched glucose in a tube furnace with flowing Argon (20 ml/min) with a heating rate of 1°C/min. Samples were reacted at 300^{o}C or 400^{o}C for 10 hrs, at which point the heating was turned off. ^{13}C-enriched glucose was purchased from Cambridge Isotopes.

NMR parameters.

The NMR experiments were performed on a Bruker Avance 400 spectrometer at a 100 MHz ^{13}C resonance frequency, using a double-resonance magic-angles spinning probehead for 4-mm rotors. Samples filled the radio-frequency coil from end to end; a cylindrical glass plug of 2-mm height at the bottom of the rotor prevented sample material from being placed outside the coil. All spectra were measured at a spinning frequency of 14 kHz, where spinning sidebands are fairly small (< 3%) and have little overlap with centerbands. The 90° pulse lengths were 4.3 μs for ^{1}H and 4 μs for ^{13}C. To achieve dead-time-free detection, which is indispensable for spectra with broad lines, all spectra were recorded with a Hahn echo generated by an EXORCYCLEd 180° pulse [18] applied one rotation period (t_r) after the end of cross polarization or the direct-excitation pulse. The ^{1}H decoupling field strength was $\gamma B_1/(2\pi) = 65$ kHz during the period of $2 t_r = 0.14$ ms duration before the Hahn echo, and ca. 55 kHz during signal detection. The ramp for CP was implemented with 11 steps of 0.05 or 0.1 ms duration and a 1% amplitude increment (90 to 100%). The recycle delays for the CP experiments ranged between 0.5 s for the humic acid to 2 s for the 300°C char and the plant material, while those in the DP experiments ranged from 30 s for the humic to 120 s for the plant material (which is probably too short for complete equilibration) and 280 s for the chars. The duration of the repolarization period t_z in multiCP ranged from 0.4 s for the humic acid to 0.9 s for the 300°C char and the plant material.

Acknowledgment

This work was supported by the Center for Biorenewable Chemicals (CBiRC) funded by NSF grant EEC-0813570.

References

(1) J.-D. Mao, R.L. Johnson, J. Lehmann, D.C. Olk, E.G. Neves, M.L. Thompson, K. Schmidt-Rohr, , Abundant and Stable Char Residues in Soils: Implications for Soil Fertility and Carbon Sequestration, Environ. Sci. Technol., 46 (2012) 9571-9576.

(2) D.A. Laird, The charcoal vision: A win-win-win scenario for simultaneously producing bioenergy, permanently sequestering carbon, while improving soil and water quality, Agronomy J., 100 (2008) 178-181.

(3) S.R. Kelemen, M. Afeworki, M.L. Gorbaty, M. Sansone, P.J. Kwiatek, C.C. Walters, H. Freund, M. Siskin, Direct Characterization of Kerogen by X-ray and Solid-State 13C Nuclear Magnetic Resonance Methods, Energy and Fuels, 21 (2007) 1548-1561.

(4) L.I. Aluwihare, D.J. Repeta, S. Pantoja, C.G. Johnson, Two chemically distinct pools of organic nitrogen accumulate in the ocean, Science, 308 (2005) 1007-1010.

(5) C.E. Brewer, K. Schmidt-Rohr, J.A. Satrio, R.C. Brown, Characterization of biochar from fast pyrolysis and gasification systems, Environ. Progress Sustain. Energy, 28 (2009) 386-396.

(6) W.-G. Hu, K. Schmidt-Rohr, Characterization of Ultradrawn UHMWPE Fibers by NMR: Crystallinity, Domain Size and a Highly Mobile Second Amorphous Phase, Polymer, 41 (1999) 2979-2987.

(7) X. Fang, T. Chua, K. Schmidt-Rohr, M.L. Thompson, Quantitative ^{13}C NMR of whole and fractionated Iowa Mollisols for assessment of organic matter composition, Geochim. Cosmochim. Acta, 74 (2010) 584-598.

(8) H. Pham, A.E. Anderson, R.L. Johnson, K. Schmidt-Rohr, A.K. Datye, Improved Hydrothermal Stability of Mesoporous Oxides for Reactions in Aqueous Phase, Angewandte Chemie, 51 (2012) 1-6.

(9) T.J. Offerdahl, J.S. Salsbury, Z.D. Dong, D.J.W. Grant, S.A. Schroeder, I. Prakash, E.M. Gorman, D.H. Barcih, E.J. Munson, Quantitation of crystalline and amorphous forms of anhydrous neotame using C-13 CPMAS NMR spectroscopy, J. Pharmaceut. Sci., 94 (2005) 2591-2605.

(10) J.-D. Mao, W.-G. Hu, K. Schmidt-Rohr, G. Davies, E.A. Ghabbour, B. Xing, Quantitative Characterization of Humic Substances by Solid-State ^{13}C NMR, Soil Sci. Soc. Am. J., 64 (2000) 873-884.

(11) R.J. Smernik, J.M. Oades, The use of spin counting for determining quantitation in solid state ^{13}C NMR spectra of natural organic matter 2. HF-treated soil fractions, Geoderma, 96 (2000) 159-171.

(12) A. Pines, M.G. Gibby, J.S. Waugh, Proton-enhanced NMR of dilute spins in solids, J. Chem. Phys., 59 (1973) 569-590.

(13) S.R. Hartmann, E.L. Hahn, Nuclear double resonance in the rotating frame, Phys. Rev., 128 (1962) 2042 - 2053.

(14) G. Metz, M. Ziliox, S.O. Smith, Towards Quantitative CP-MAS NMR, Solid State Nucl. Magn. Reson., 7 (1996) 155-160.

(15) G. Hou, F. Deng, S. Ding, R. Fu, J. Yang, C. Ye, Quantitative cross-polarization NMR spectroscopy in uniformly ^{13}C-labeled solids, Chem. Phys. Lett., 421 (2006) 356-360.

(16) K. Takeda, Y. Noda, K. Takegoshi, O. Lafon, J. Trebosc, J.P. Amoureux, Quantitative cross-polarization at magic-angle spinning frequency of about 20 kHz, J. Magn. Reson., 214 (2012) 340-345.

(17) J.-D. Mao, K. Schmidt-Rohr, Accurate Quantification of Aromaticity and Nonprotonated Aromatic Carbon Fraction in Natural Organic Matter by ^{13}C Solid State NMR, Environ. Sci. Technol., 38 (2004) 2680-2684.

(18) G. Bodenhausen, R. Freeman, D.L. Turner, Suppression of Artifacts in 2-Dimensional J Spectroscopy, J. Magn. Reson., 27 (1977) 511-514.

Acknowledgements

I would like to express my deepest appreciation to advisors, Professor Klaus Schmidt-Rohr, who have guided me through my Ph.D. studies.

I sincerely appreciate my Program of Study committee members; Dr. Patrica Thiel, Dr. Marek Pruski, Dr. Keith Woo, and Dr. Brent Shanks for their valuable time and support during my studies at Iowa State University.

I want to thank my many colleagues in Dr. Schmidt-Rohr’s group I have enjoyed working with all of you.

APPENDIX A. ABUNDANT AND STABLE CHAR RESIDUES IN SOILS: IMPLICATIONS FOR SOIL FERTILITY AND CARBON SEQUESTRATION

Environmental Science and Technology **46,** pp 9571-9576, 2012

J-D. Mao[1], R. L. Johnson[2], J. Lehmann[3], D. C. Olk[4], E. G. Neves[5], M. L. Thompson[6]*, K. Schmidt-Rohr[2]*

[1] Department of Chemistry and Biochemistry, Old Dominion University, Norfolk, VA 23529, USA.
[2] Department of Chemistry, Iowa State University, Ames IA 50011, USA.
[3] Department of Crop and Soil Sciences, Cornell University, Ithaca, New York 14853, USA.
[4] USDA-ARS, National Laboratory for Agriculture and the Environment, Ames IA 50011, USA.
[5] Museu de Arqueologia e Etnologia, Universidade de Sao Paulo, Sao Paulo, SP, 05508-900 Brazil.
[6] Department of Agronomy, Iowa State University, Ames IA 50011, USA.

Abstract

Large-scale soil application of biochar may enhance soil fertility, increasing crop production for the growing human population, while also sequestering atmospheric carbon. But reaching these beneficial outcomes requires an understanding of the relationships among biochar's structure, stability, and contribution to soil fertility. Using quantitative ^{13}C nuclear magnetic resonance (NMR) spectroscopy, we show that Terra Preta soils (fertile anthropogenic dark earths in Amazonia that were enriched with char >800 years ago) consist predominantly of char residues composed of ~5 fused aromatic rings substituted by COO^- groups that significantly increase the soils' cation-exchange capacity and thus the retention of plant

nutrients. We also show that highly productive, grassland-derived soils in the U.S. (Mollisols) contain char (generated by pre-settlement fires) that is structurally comparable to char in the Terra Preta soils and that is much more abundant than previously thought (~40-50% of organic C). Our findings indicate that these oxidized char residues represent a particularly stable, abundant, and fertility-enhancing form of soil organic matter.

Introduction

Feeding the ~9 billion people expected on Earth by 2050 will require a number of coordinated agricultural, economic, and social strategies, including changes in the nutrient management of cultivated soils to increase crop production (1, 2). Application of biochar to soils on a large scale has been proposed as a method to increase food security by enhancing soil fertility, while at the same time sequestering carbon from the atmosphere (3-6). Bringing this approach to fruition requires an understanding of the relations among the structure of biochars, their stability, and their contribution to soil fertility. Although a global soil survey using mid-infrared analysis has shown evidence of black carbon in soils of all climate zones (7), apart from their high aromaticity, relatively little is known about the chemical structure of char residues (8, 9) in soils.

Amazonian Terra Preta soils are anthropogenic dark earths that were enriched with char >800 years ago; they are more fertile than surrounding soils that received little char input (10-12). Other, more common, fertile and char-containing soils are Mollisols. These grassland-derived soils are extensive in central North America, Ukraine, the Russian Federation, Argentina, and Uruguay, and they contribute a significant fraction of global grain production. In the World Reference Base for Soil Resources, these soils are typically classified as Phaeozems, Chernozems, and Kastanozems (13). Char in these soils has been widely attributed to grassland fires (14); in North America, such pre-settlement fires are well documented (15).

In both Terra Preta soils and North American Mollisols, NMR studies have confirmed the presence of char residues (16-19). For example, aromaticity values estimated by extended X-ray absorption fine structure (EXAFS) and nonquantitative cross-polarization NMR previously suggested that char accounts for ~25 - 50% of organic carbon in Terra Preta soils (19). Here, using quantitative ^{13}C NMR and NMR size measurements (20, 21), we show that a much larger fraction of the organic carbon in both kinds of soils consists of oxidized char residues that are composed of fused aromatic rings substituted by COO^{-} groups. Despite contrasting soil environments, the chemical structures of the char residues are similar. Our findings suggest that oxidized char residues containing ~5 fused aromatic rings and 5 carboxylate groups are particularly stable in soil environments and contribute to soil fertility by accounting for a significant fraction of the cation-exchange capacity. These insights have implications for both carbon sequestration in soils and large-scale production of biochars for soil application.

Materials and Methods

Soil samples. Terra Preta soil samples were collected from archeological sites in the central Amazon near Manaus, Brazil, as described previously (19). Samples from horizons at depths of 43-69 and 43-67 cm at the Hatahara and Lago Grande sites, respectively, were studied by NMR after demineralization by treatment with 2% HF solution (w/v) for NMR analysis (19). As a result of the acid treatment, most of the COO groups in the samples studied by NMR were protonated. The observed COO chemical shift of 170.5 ppm and the COOH proton signal in the ^{1}H-^{13}C correlation spectrum of Figure S1 (Supporting Information) support this conclusion (16). Combustion analysis showed that the (partially) demineralized Hatahara Terra Preta sample consisted of 86.7% ash, 12.3 ± 0.1% C, 0.6 ± 0.2% H, and 0.4 ± 0.05 % N by weight. The Maxfield soil sample (5 – 15 cm sampling depth) was collected in Greene County, Iowa, and was demineralized by HF with heating (16). The Zook sample (0 – 20 cm sampling depth) was collected in Story County, Iowa, and humic acid was extracted by standard procedures (22).

Solid-state ^{13}C NMR spectroscopy was performed at 100 MHz using a Bruker DSX400 spectrometer and a Bruker 4-mm ^{1}H-^{13}C double-resonance MAS probe head. Samples were packed into 4-mm diameter zirconia rotors with 5-mm long glass inserts at the bottom to constrain the samples to the space within the radio-frequency coil. The mass of each sample was recorded for quantification of ^{13}C observability. The ^{13}C chemical shifts were referenced to tetramethylsilane using the COO$^-$ resonance of glycine at 176.49 ppm as a secondary reference. The 90^o pulse length was 4 μs. The recycle delay was 40 s for Hatahara and 26 s for Lago Grande, which is > 4 times the measured spin-lattice relaxation time (23, 24) (see also Figure S2 in the Supporting Information). A spectrum with 100-s recycle delay experiments confirmed complete relaxation, as did >95% observability in spin counting analysis. The fully relaxed ^{13}C spectrum of Zook soil humic acid extract was measured with a 100-s and that of the Maxfield organic matter with a 50-s recycle delay.

The quantitative direct-polarization ^{13}C NMR spectra were recorded at 14 kHz MAS, which avoids the overlap of aromatic spinning sidebands with alkyl peaks that has plagued several previous NMR studies of chars and highly aromatic soil organic matter. A Hahn spin echo was generated before detection to avoid baseline distortions due to pulse dead time (25).

^{1}H decoupling of sufficiently high-power ($|\gamma B_1| = 2\pi$ 70 kHz) with two-pulse phase modulation (TPPM) (26) was applied during detection. Carbon observability was determined to be >95% by comparison of the total ^{13}C NMR signal with that of a polystyrene standard, per scan and mg C. In addition, for each sample, a corresponding quantitative spectrum of nonprotonated and methyl carbons, obtained after 68 μs of recoupled dipolar dephasing (25) was also recorded. By combining dipolar dephasing with direct polarization experiments, we obtained separate quantitative spectra of nonprotonated aromatic carbon, and those of protonated aromatics by difference.

To estimate the size of fused aromatic rings, recoupled ^{1}H-^{13}C dipolar dephasing (21) was applied, with two ^{1}H 180^o pulses per rotation period that prevent magic angle spinning from averaging out weak ^{1}H-^{13}C dipolar couplings. In order to detect nonprotonated carbons with good relative efficiency, direct polarization/total sideband suppression (DP/TOSS) was used at a spinning speed of 7 kHz. The signal of nonprotonated C, selected by 40 μs of regular gated decoupling, between 107 and 142 ppm was considered in the analysis. The dipolar dephasing times varied from 0.29 ms to 1.7 ms.

Results

NMR Spectroscopy and Biochar Structural Analysis

Our findings are enabled by the analysis of whole soil organic matter using quantitative direct polarization (DP) ^{13}C NMR. With sufficiently long recycle delays and fast magic-angle spinning (MAS), DP ^{13}C NMR provides the aromatic peaks of char at full intensity. This avoids the reduction of signals from larger aromatic clusters that has affected previous NMR studies that relied on cross polarization (CP) from ^{1}H (19, 27), which inefficiently detects carbon atoms in the core of fused aromatic rings in char (28). In addition, we have applied advanced NMR techniques for estimating the size of the clusters of fused aromatic rings (20).

Figure 1a, b shows the quantitative DP solid-state ^{13}C NMR spectra of the organic carbon from the ca. 0.4 to 0.7 m deep horizons of two Brazilian Terra Preta soils (19, 27). (To isolate char-rich materials, we avoided surface horizons that were enriched with younger organic matter.) The spectra are dominated by aromatic-carbon peaks around 130 ppm and signals of COO groups near 170 ppm. The spectra of carbons not bonded to hydrogen (thin lines in Figure 1) show that most of the aromatic carbons are not protonated and resonate near 130 ppm, which is characteristic of fused aromatic rings as found in char (20), while nonprotonated carbons of substituted single benzene rings give signals around 150 ppm (aromatic C-O), 133 ppm (aromatic C-C), and <125 ppm (aromatic C two bonds from O or N) (25, 29). The signals of all types of alkyl carbons, between 97 and 7 ppm, are quite negligible (~9% of the total spectral area, see Table 1). This indicates that carbon not derived from char represents only a small fraction of the organic carbon in these horizons, and it is consistent with the low H:C ratios (ca. 0.6:1) in these samples. In fact, the H:C ratio can be calculated from the data in Table 1,(23) if we assume that 80±20% of the COO groups are protonated (due to the HF treatment; this is consistent with the strong COOH signal in ^{1}H-^{13}C heteronuclear correlation NMR, see Figure S1) and that half of the aromatic C-O are phenols (C-OH). This analysis yields an H:C ratio of 0.51 ± 0.05, consistent with the experimental value of 0.58 ± 0.19.

Table 1 shows that ~20% of all Terra Preta carbon is in COO or C=O groups, while alkyl C accounts for only 10%. No compound of high molecular weight exists that consists predominantly of COO groups. (This would be different for CH_2 groups (*n*-alkanes and polyethylene are all CH_2), HCOH (polysaccharides), and aromatic C (graphite and char)). Therefore, the COO groups must be bonded to alkyl or aromatic carbons.

The amount of alkyl C is too small (~10%) to support all of the COO (17%) groups. For HCOH carbons (polysaccharides) and for NCH (peptides), which account for half of the alkyl C (see Table 1), there are usually at least two alkyl carbons per COO group. It is interesting to note that CH_2 and CH_3 groups, which necessarily have several bonds saturated by H, cannot support many COO groups in a structure of significant molecular weight. In this context, it is relevant that we have previously shown, by NMR, that esters are rare in Mollisol organic matter (16). So most COO groups are end groups.

Thus, the maximum number of COO groups that can be supported by the alkyl residues is 10%/2, which is less than 1/3 of the total (16.5%). Even this is probably too high; the COO peak in humic substances rarely reaches more than 1/4 of the total spectral area. Some COO groups bonded to alkyl carbons, attributed to organic matter not derived from char, do exist in Terra Preta. In our decomposition (see Table 1, third row), we propose that this is 2% out of 17%.

Substantial bonding of the COO^- groups, resonating at 170 ppm, to aromatic rings is confirmed by ^1H-^{13}C heteronuclear correlation NMR (see Figure S1), which shows that the COO^- groups are close to aromatic protons. The conclusion that COO^- groups are associated with aromatic rings has also been drawn from multivariate curve resolution analysis of (non-quantitative) ^{13}C NMR spectra of Terra Preta humic acid extracts (30). The C=O groups, with their chemical shifts <200 ppm, must also be bonded to aromatic rings, since alkyl-bonded C=O resonates at >200 ppm.(31)

Table 1 shows that ≥90% of all carbons in our Terra Preta samples are found in aromatic rings or in COO^- and C=O groups mostly bonded to aromatic rings. While a small fraction (~6%) of the aromatic C will be from soil organic carbon not derived from char, some of the alkyl segments probably do belong to the char, given that 3-6% of synthetic pyrolysis chars are alkyl moieties (20). Table 1 shows the distribution of carbon in the Terra Preta samples into 88% char residues and 12% other organic matter of moderate aromaticity. These results are particularly meaningful since they were obtained from whole organic matter rather than merely humic extracts (19, 27, 30) that represent only a fraction of all soil carbon. The abundant COO^- groups are probably the remnants of aromatic rings that have been oxidized, similar to the COO groups attached to aromatic rings that are formed by chemical oxidation of char in controlled laboratory experiments (32).

The spectral pattern of COO^- and C=O substituted aromatic rings revealed in ^{13}C NMR of Terra Preta organic carbon can also be recognized in the spectra of organic matter of temperate-region grassland soils, though with a larger background of non-char organic carbon (16, 22, 33, 34). This is exemplified in Figure 1c, which shows the ^{13}C NMR spectrum of a humic acid extract from the surface horizon of an Iowa Mollisol (Zook, a Cumulic Vertic Endoaquoll) (22). Counting the non-protonated cores and the substituted or protonated edges of the aromatic clusters, as well as the COO and C=O groups bonded to them, oxidized char residues represent 67 ± 9 % of all carbon in the Mollisol humic acid (see Table S1, Supporting Information). The selective extraction makes the humic acid not fully representative of the parent organic matter. On the other hand, by concentrating the char-derived carboxylic acids and associated fused aromatic rings, it allows the spectra of these char-derived structures to be detected with less background from other soil organic matter.

Quantitative char contents can be estimated from the ^{13}C NMR spectra of the organic carbon of an unfractionated, poorly drained Mollisol (Maxfield, a Typic Endoaquoll) in Iowa (16), see Figure 1d, which are also dominated by COO and aromatic-carbon peaks. Again, the low chemical shifts of the C=O groups indicate their bonding to aromatic rings. The quantitative distribution of functional groups shows that 52 ± 11 % of carbon occurs in oxidized char residues (Table 1); the corresponding estimate for two better drained Argiudolls in the same Iowa landscape is 44 ± 12 % (16).

These values exceed those of other studies that have used less quantitative methods. For example, using a benzene polycarboxylic acid method, one international study reported that char residues accounted for a minimum of 4 – 30% of soil organic carbon in 27 studied Mollisols (14). They are considerably greater than values (4 – 18%) estimated in a climosequence of North American primarily short-grass prairie soils using the benzene polycarboxylic acid approach, which provides only a relative measure of the pyrogenic carbon content of a soil (35). Our values are also generally higher than the values of 4 - 45% (average for 11 horizons: 19%) estimated for German chernozemic soils from nonquantitative CP NMR (with an unspecified "empirically determined correction") (17). Finally, they are greater than the char content of 26% estimated for an Australian Mollisol using UV photooxidation and DP NMR with relatively slow magic-angle spinning, where aromatic spinning sidebands overlap with alkyl resonances (18). The previous NMR estimates are lower in part because the aromatic carbons resonating at <110 ppm and the COO and C=O groups bonded to the fused aromatic rings were not included in the char fraction, even though it was recognized that the spectra of the char residues after photooxidation showed pronounced COO resonances (18).

Our observations are very consistent with the conclusions of radiocarbon dating studies that about one-half of the near-surface soil organic carbon of North American grassland soils consists of a stable pool with a mean residence time on the order of 1000 – 2000 years BP (36). In the older literature, that stable pool was associated with the (empirically defined) humic acid fraction (37) and indeed the extracted humic acid in our study was found to be enriched in oxidized char residues.

Significant condensation of the aromatic rings, a hallmark of char-derived material (20), is indicated by the large signal fraction (81% for the Terra Preta soils) of nonprotonated aromatic C remaining after ^{1}H-^{13}C dipolar dephasing (thin lines in Figure 1). By tallying up all the aromatic C that must be at the edge of aromatic rings (20) (aromatic C-H, aromatic C-O, aromatic C-(C=O or COO), and aromatic C-alkyl, assuming the average alkyl substituent to contain two carbons), we can estimate the aromatic edge fraction, χ_{edge} (20). This value provides a stringent lower limit, $n_{min} = 6/\chi_{edge}^2$, to the number of carbons in an aromatic cluster (20). For the Terra Preta char residues (last row in Table 1), the aromaticity (including aromatic C-O) is 75 ± 3%, and $\chi_{edge} = 0.58 \pm 0.04$. From $\chi_{edge} \leq 0.62$, we calculate that at least $n_{min} = 16$ carbons are in the typical aromatic cluster derived from char. Adding one C=O / COO substituent per every four aromatic carbons (from Table 1: (3.5+14.5)%/0.655 = 26%) results in a total of at least 20 carbons in the typical cluster.

The size of the aromatic clusters can also be estimated based on NMR experiments probing the ^{1}H-^{13}C dipolar couplings, which depend strongly ($\sim 1/r^3$) on the ^{1}H-^{13}C internuclear distance r. Figure 2 shows recoupled ^{1}H-^{13}C dipolar dephasing (21) of the nonprotonated nonpolar aromatic signals of Terra Preta soil organic carbon, of the humic acid extract from the Zook Iowa prairie soil, and of whole organic matter from the Maxfield

Iowa prairie soil. These are compared with published reference data from several types of fresh char as well as lignin (20). Slower dephasing reflects weaker dipolar fields of the ^{1}H nuclear magnets experienced by the ^{13}C spins, which is the hallmark of larger aromatic clusters. The dephasing of the Terra Preta signal intensity is rather slow, which excludes linear condensation of the aromatic rings (21). The data for the Terra Preta organic carbon, the Iowa prairie soil organic carbon, and the Iowa soil humic acid extract are strikingly similar, which underlines the similarity between the oxidized char residues in these relatively fertile tropical and temperate-region soils.

Discussion

Based on the NMR composition and H-C distance data, a structural model for a typical aromatic ring system in the Terra Preta and temperate grassland soils can be proposed (Figure 3). A typical cluster consists of about 5 aromatic rings heavily substituted with COO^{-} groups, which impart to the char residue a large cation exchange capacity (27, 38) and make it hydrophilic, both favorable features for soil fertility. Soil fertility is a composite of many soil properties, but cation exchange capacity is surely one of the most important.

Impact of char residues on cation exchange capacity.

We estimate that char COO^{-} groups can account for essentially the entire contribution of organic matter to the pH-7 cation exchange capacity (CEC) of the Iowa Mollisols. The CEC of soil is derived from both permanent charges associated with clay-size layer silicates and the pH-dependent charges of organic matter. Unfortunately, the unique contribution of organic matter to CEC is difficult to determine since clay and organic matter are typically aggregated. Methods to measure one in the absence of the other inevitably must destroy the aggregates, creating artifact surfaces and exchange sites. Moreover, standard multiple regression approaches must account for the usual positive correlation between clay and organic matter concentrations in soil – a correlation that limits the confidence with which the organic matter contribution can be strictly assessed. To overcome these problems, Thompson et al. (39) used principal components analysis to estimate the unique contribution of soil organic carbon (SOC) to the CEC of silt and clay fractions of a suite of central-Iowa soil horizons. The contribution of SOC to CEC at pH 7 was determined to be 559 cmol(–) kg^{-1} SOC. In the present investigation, we have concluded that the functional units of char in Iowa Mollisols are comprised of about 5 moles of COO^- per 30 moles of C (Figure 3), which would account for 1390 cmol(–) kg^{-1} char C. Thus, if just 40% of a soil's organic carbon were composed of char (a low estimate for the Mollisols we have investigated – see Tables 1 and S1), essentially the entire contribution of organic matter to the soil's CEC could be attributed to the CEC of the char component [(0.40 kg char C kg^{-1} SOC) x (1390 cmol(–) kg^{-1} char C) = 556 cmol(–) kg^{-1} SOC].

While other studies have shown that synthetic biochars may have considerable cation exchange capacity (40) and that natural char can be gradually oxidized in the soil environment (41, 42), our work serves as an independent, direct, structural confirmation of the hypothesis that the large cation exchange capacity in Terra Preta soils and Iowa Mollisols is related to the high density of oxidized functional groups on the char aromatic core (10, 38). The cluster size is similar to that of synthetic pyrolysis chars, but the fresh chars have far fewer COO^- substituents (20, 43) and therefore a lower cation exchange capacity. The similarity of the structure of the char residues in both fertile tropical Terra Preta and highly fertile, temperate-region, prairie-derived soils suggests that aromatic clusters of this size and level of oxidation are stable in the soil environment and likely to enhance soil fertility.

Analyses of our NMR data reveal that the organic carbon from deeper horizons of two well-characterized Terra Preta soils consists almost completely of oxidized char residues in the form of small clusters of aromatic rings substituted by COO groups. Similarly oxidized char accounts for about half of the organic carbon in surface horizons of the investigated fertile, prairie-derived soils of Iowa, USA. These results suggest that substantial amounts of char could be incorporated into many soils with positive long-term effects on soil fertility. The proposed structure of soil char residues, together with their high abundance in the temperate-region prairie soils investigated, implies that most of the organic-matter-derived cation exchange capacity in these fertile soils is directly attributable to the abundant COO^- groups in the char residues. Extensive application of locally produced or industrial biochar to soils has been proposed for its impact on Earth’s carbon budget. The net agronomic impacts of such soil amendments are not yet consistently predictable across all soils or with all biochars (44). Still, our results support the potential for biochar amendments to improve soil fertility and thereby raise agricultural productivity. Our findings also suggest that the fertility of char-amended soils could be enhanced in the short term by partially oxidizing fresh, pyrolysis char to simulate the oxidative aging processes deduced in this and other studies (41, 42).

Acknowledgments.

KSR and MLT thank D. A. Laird, R. C. Brown, and C. E. Brewer for insightful discussions on biochar. JDM thanks the NSF (EAR-0843996 and CBET-0853950) for financial support.

References

(1) Godfray, H. C. J.; Beddington, J. R.; Crute, I. R.; Haddad, L.; Lawrence, D.; Muir, J. F.; Pretty, J.; Robinson, S.; Thomas, S. M.; Toulmin, C., Food security: The challenge of feeding 9 billion people. *Science* **2010,** *327*, (5967), 812-818.

(2) Power, A. G., Ecosystem services and agriculture: tradeoffs and synergies. *Philosophical Transactions of the Royal Society B: Biological Sciences* **2010,** *365*, (1554), 2959-2971.

(3) Glaser, B.; Lehmann, J.; Zech, W., Ameliorating physical and chemical properties of highly weathered soils in the tropics with charcoal - a review. *Biol. Fert. Soils* **2002,** *35*, (4), 219-230.

(4) Lehmann, J., A handful of carbon. *Nature* **2007,** *447*, (7141), 143-144.

(5) Laird, D. A., The charcoal vision: A win-win-win scenario for simultaneously producing bioenergy, permanently sequestering carbon, while improving soil and water quality. *Agronomy J.* **2008,** *100*, (1), 178-181.

(6) Woolf, D.; Amonette, J. E.; Street-Perrott, F. A.; Lehmann, J.; Joseph, S., Sustainable biochar to mitigate global climate change. *Nat Commun* **2010,** *1*, (5), 56.

(7) Krull, E.; Lehmann, J.; Skjemstad, J.; Baldock, J.; Spouncer, L., The global extent of black C in soils: Is it everywhere? In *Grasslands: Ecology, Management and Restoration* Schröder, H. G., Ed. Nova Science Publishers: 2008; pp 13-17.

(8) Glaser, B.; Haumaier, L.; Guggenberger, G.; Zech, W., The 'Terra Preta' phenomenon: A model for sustainable agriculture in the humid tropics. *Naturwissenschaften* **2001,** *88*, (1), 37-41.

(9) Lehmann, J.; Pereira da Silva, J.; Steiner, C.; Nehls, T.; Zech, W.; Glaser, B., Nutrient availability and leaching in an archaeological Anthrosol and a Ferralsol of the Central Amazon basin: fertilizer, manure and charcoal amendments. *Plant and Soil* **2003,** *249*, (2), 343-357.

(10) Glaser, B., Prehistorically modified soils of central Amazonia: a model for sustainable agriculture in the twenty-first century. *Phil. Transact. Royal Soc. B* **2007,** *362*, 187-196.

(11) *International Union of Soil Science Working Group WRB. World Reference Base for Soil Resources 2006*. FAO: Rome, 2006.

(12) Rodionov, A.; Amelung, W.; Peinemann, N.; Haumaier, L.; Zhang, X.; Kleber, M.; Glaser, B.; Urusevskaya, I.; Zech, W., Black carbon in grassland ecosystems of the world. *Global Biogeochem. Cycles* **2010,** *24*, GB3013.

(13) Krug, E. C.; Hollinger, S. E. *Identification of Factors That Aid Carbon Sequestration in Illinois Agricultural Systems*; ISWS CR 2003-02; Illinois Council on Food and Agricultural Research: Champaign, IL, 2003; p 90.

(14) Fang, X.; Chua, T.; Schmidt-Rohr, K.; Thompson, M. L., Quantitative ^{13}C NMR of whole and fractionated Iowa Mollisols for assessment of organic matter composition. *Geochim. Cosmochim. Acta* **2010,** *74*, (2), 584-598.

(15) Schmidt, M. W. I.; Skjemstad, J. O.; Gehrt, E.; Kögel-Knabner, I., Charred organic carbon in German chernozemic soils. *Europ. J. Soil Sci.* **1999,** *50*, 351-365.

(16) Skjemstad, J. O.; Taylor, J. A.; Smernik, R. J., Estimation of charcoal (char) in soils. *Comm. Soil Sci. Plan. Anal.* **1999,** *30*, 2283-2298.

(17) Solomon, D.; Lehmann, J.; Thies, J. E.; Schafer, T.; Liang, B.; Kinyangi, J.; Neves, E.; Petersen, J.; Luizao, F.; Skjemstad, J., Molecular signature and sources of biochemical recalcitrance of organic C in Amazonian Dark Earths. *Geochim. Cosmochim. Acta* **2007,** *71*, 2285-2289.

(18) Brewer, C. E.; Schmidt-Rohr, K.; Satrio, J. A.; Brown, R. C., Characterization of biochar from fast pyrolysis and gasification systems. *Environ. Progress Sustain. Energy* **2009,** *28*, (3), 386-396.

(19) Mao, J. D.; Schmidt-Rohr, K., Recoupled long-range C-H dipolar dephasing in solid-state NMR, and its use for spectral selection of fused aromatic rings. *J. Magn. Reson.* **2003,** *162*, (1), 217-227.

(20) Mao, J.; Fang, X.; Schmidt-Rohr, K.; Carmo, A. M.; Hundal, L. S.; Thompson, M. L., Molecular-scale heterogeneity of humic acid in particle-size fractions of two Iowa soils. *Geoderma* **2007,** *140*, (1-2), 17-29.

(21) Mao, J. D.; Hu, W. G.; Schmidt-Rohr, K.; Davies, G.; Ghabbour, E. A.; Xing, B., Quantitative characterization of humic substances by solid-state carbon-13 nuclear magnetic resonance. *Soil Sci. Soc. Am. J.* **2000,** *64*, (3), 873-884.

(22) Torchia, D. A., The measurement of proton-enhanced carbon-13 T1 values by a method which suppresses artifacts. *J. Magn. Reson.* **1978,** *30*, 613-616.

(23) Mao, J.-D.; Schmidt-Rohr, K., Accurate quantification of aromaticity and nonprotonated aromatic carbon fraction in natural organic matter by ^{13}C solid state NMR. *Environ. Sci. Technol.* **2004,** *38*, 2680-2684.

(24) Bennett, A. E.; Rienstra, C. M.; Auger, M.; Lakshmi, K. V.; Griffin, R. G., Heteronuclear decoupling in rotating solids. *J. Chem. Phys.* **1995,** *103*, (16), 6951-6958.

(25) Novotny, E. H.; deAzevedo, E. R.; Bonagamba, T. J.; Cunha, T. J.; Madari, B. E.; Benites, V. D. M.; Hayes, M. H. B., Studies of the compositions of humic acids from Amazonian Dark Earth soils. *Environ. Sci. Technol.* **2007,** *41*, 400-4005.

(26) Smernik, R. J.; Baldock, J. A.; Oades, J. M., Impact of remote protonation on 13C CPMAS NMR quantitation of charred and uncharred wood. *Solid State Nucl. Magn. Reson.* **2002,** *22*, (1), 71-82.

(27) Mao, J.-D.; Holtman, K. M.; Scott, J. T.; Kadla, J. F.; Schmidt-Rohr, K., Differences between Lignin in Unprocessed Wood, Milled Wood, Mutant Wood, and Extracted Lignin Detected by 13C Solid-State NMR. *J. Agri. Food Chem.* **2006,** *54*, 9677-9686.

(28) Novotny, E. H.; Hayes, M.; Madari, B. E.; Bonagamba, T.; deAzevedo, E.; de Souza, A. A.; Song, G.; Nogueira, C. M.; Mangrich, A. S., Lessons from the Terra Preta de Indios of the Amazon Region for the Utilisation of Charcoal for Soil Amendment. *J. Braz. Chem. Soc.* **2009,** *20*, (6), 1003-1010.

(29) Hammes, K.; Schmidt, M. W. I.; Smernik, R.; Currie, L. A.; Ball, W. P.; Nguyen, T. H.; Louchouran, P.; Houel, S.; Gustafsson, O.; Elmquist, M.; Cornellisen, G.; Skjemstad, J. O.; Masiello, C. A.; Song, J.; Peng, P. a.; Mitra, S.; Dunn, J. C.; Hatcher, P. G.; Hockaday, W. C.; Smith, D. M.; Hartkopf-Froder, C.; Bohmer, A.; Luer, B.; Huebert, B. J.; Amelung, W.; Brodowski, S.; Huang, L.; Zhang, W.; Gschwend, P. M.; Flores-Cervantes, D. X.; Largeau, C.; Rouzand, J.-N.; Rumpel, C.; Guggenberger, G.; Kaiser, K.; Rodionov, A.; Gonzalez-Perez, F. J.; Gonzalez-Perez, J. A.; De la Rosa, J. M.; Manning, D. A. C.; Lopez-Capel, E.; Ding, L., Comparison of quantification methods to measure fire-derived (black/elemental) carbon in soils

and sediments using reference materials from soil, water, sediment and the atmosphere. *Glob. Biogeochem. Cyc.* **2007,** *21*.

(30) Skjemstad, J. O.; Reicosky, D. C.; Wilts, A. R.; McGowan, J. A., Charcoal carbon in U.S. agricultural soils. *Soil Sci. Soc. Am. J.* **2002,** *66*, (4), 1249-1255.

(31) Mao, J. D.; Olk, D. C.; Fang, X. W.; He, Z.; Schmidt-Rohr, K., Influence of animal manure application on the chemical structures of soil organic matter as investigated by advanced solid-state NMR and FT-IR spectroscopy. *Geoderma* **2008,** *146*, 353-362.

(32) Paul, E. A.; Follett, R. F.; Leavitt, S. W.; Halvorson, A.; Peterson, G. A.; Lyon, D. J., Radiocarbon dating for determination of soil organic matter pool sizes and dynamics. *Soil Science Society of America Journal* **1997,** *61*, 1058-1067.

(33) Liang, B.; Lehmann, J.; Solomon, D.; Kinyangi, J.; Grossman, J.; O'Neill, B.; Skjemstad, J. O.; Thies, J.; Luizao, F. J.; Petersen, J.; Neves, E. G., Black carbon increases cation exchange capacity in soils. *Soil Sci. Soc. Am. J.* **2006,** *70*, (5), 1719-1730.

(34) Thompson, M. L.; Zhang, H.; Kazemi, M.; Sandor, J. A., Contribution of organic matter to cation exchange capacity and specific surface area of fractionated soil materials. *Soil Science* **1989,** *148*, (4), 250-257.

(35) Nguyen, B. T.; Lehmann, J.; Hockaday, W. C.; Joseph, S.; Masiello, C. A., Temperature sensitivity of black carbon decomposition and oxidation. *Environ. Sci. Technol.* **2010,** *44*, (9), 3324-3331.

Table 1. Quantitative ^{13}C NMR spectral analysis of (top) organic C in two Terra Preta soils (averaged, since the data differ by ≤ 1%), followed by a possible decomposition into contributions from low-alkyl char residues and from typical soil organic carbon not derived from char (with an aromaticity of 25%). Bottom rows: Same for Iowa Endoaquolls (based on averaged data of Maxfield Mollisol and Webster soil organic matter from ref. (16)). Intensities have been corrected for residual spinning sidebands. Error margins: ± 2%.

	Carbonyls		Aromatics			Alkyls			
Moieties	C=O	COOH	C-O-H/C	$C_{non-pro}$	C-H	HCOH(a)	CH_2/CH	CH_3	**Total**
ppm	210 - 183	183 - 160	160 - 145	145 - 97		97-50	50-25	25 - 7	
					%				
Terra Preta	4	17	8	48	13	5	3	2	**100%**
Terra Preta char residue	3.5	15	7	47	12	1	1	1	**88%**
Terra Preta soil org. C	0.5	2	1	1	1	4	2	1	**12%**
Endoaquoll	2	16	7	34	11	18	8	4	**100%**
Endoaquoll char residue	1	7	3.5	31	7	1	1	0.5	**52%**
Endoaquoll soil org. C	1	9	3.5	3	4	17	7	3.5	**48%**

(a) Anomeric (O-C-O alkyl) carbons have been included here (1/6 of this intensity). This chemical-shift range also includes HCNH of peptides.

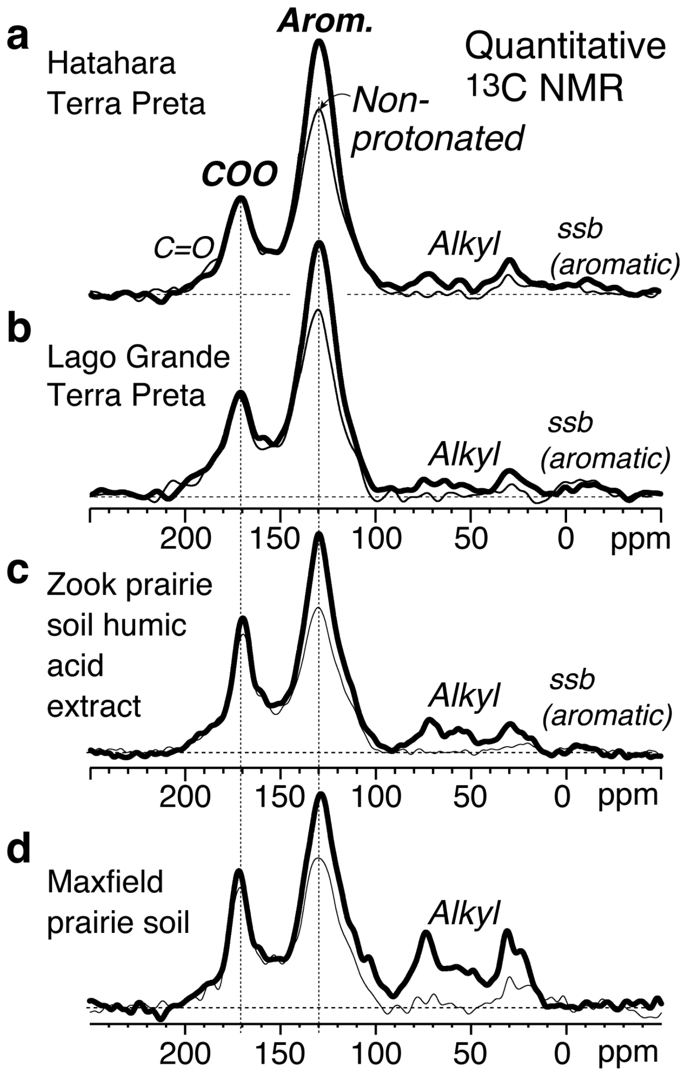

Figure 1. Quantitative, direct polarization ^{13}C NMR spectra of Terra Preta soil organic matter (HF-treated) from two sites (**a**) Hatahara and (**b**) Lago Grande. Thick line: spectrum of all carbons; thin line: spectrum of nonprotonated C and of CH_3. (**c**, **d**) Corresponding spectra of Iowa prairie soil organic matter: (**c**) humic acid extract of Zook soil and (**d**) unfractionated organic matter of Maxfield soil. The spectra were obtained at a resonance frequency of 100 MHz with 14-kHz magic-angle spinning. Spinning sidebands of the aromatic peaks are labeled "ssb (aromatic)" and were included in the tally of the total aromatic signal.

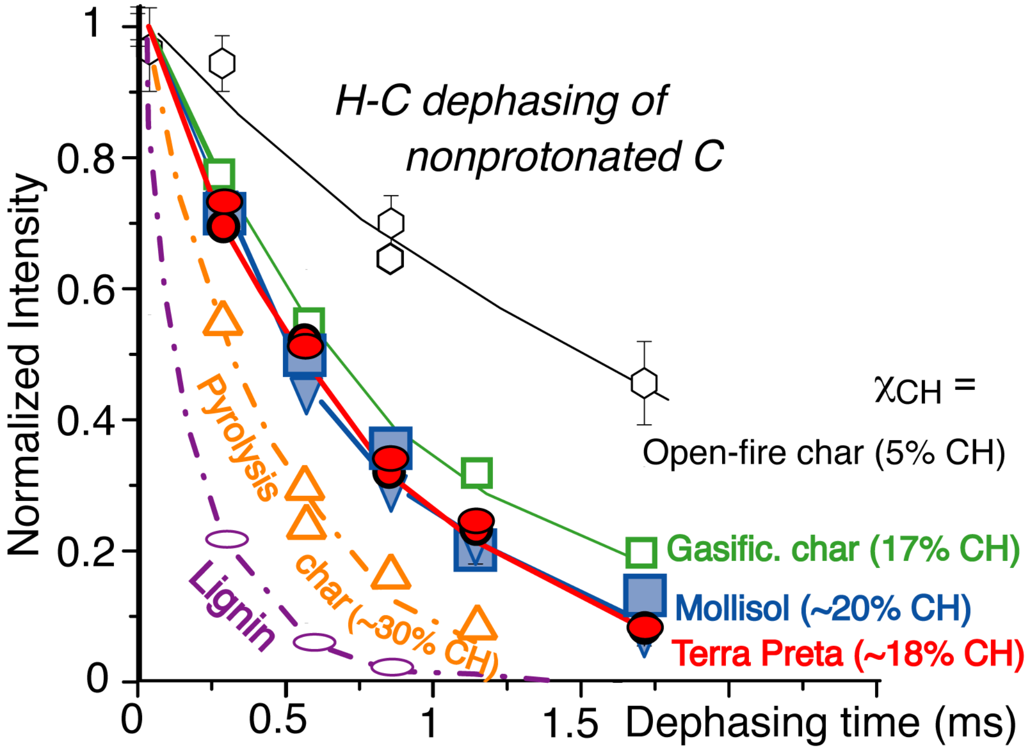

Figure 2. Size determination of aromatic clusters in Terra Preta soil organic matter (red filled ovals: Hatahara site; filled circles: Lago Grande site) as well as prairie-soil (Mollisol) humic acid extract (Zook HA, blue filled inverted triangles) and whole organic matter (Maxfield soil, blue filled squares) by long-range ^{1}H-^{13}C dipolar dephasing NMR. The normalized integral intensity of the nonprotonated aromatic carbon signal between 107 and 142 ppm is plotted as a function of the recoupled H-C dipolar dephasing time. For reference, data are also shown for open-fire grass char (open hexagons), gasification char (open squares), pyrolysis char (open triangles), and lignin (open ellipses) (from ref. (20)). The fraction of aromatic char carbons that are protonated is listed for each sample.

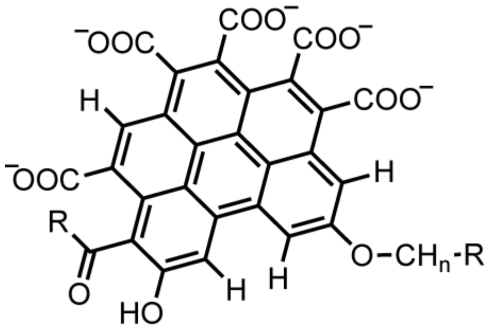

Figure 3. Model of a typical stable and fertile aromatic cluster in Terra Preta and temperate grassland soils, derived from NMR spectroscopy and H-C distance measurements.

Supporting Information

ABUNDANT AND STABLE CHAR RESIDUES IN SOILS:
IMPLICATIONS FOR SOIL FERTILITY AND CARBON SEQUESTRATION

J-D. Mao, R. L. Johnson, J. Lehmann, D. C. Olk, E. G. Neves, M. L. Thompson*, K. Schmidt-Rohr*

Proof of COO bonding to aromatic rings.

We have seen positive evidence that a large fraction of COO groups is bonded to the aromatic rings in the Zook soil HA extract, in terms of cross peaks between aromatic H and COO carbons in two-dimensional ^{1}H-^{13}C (HetCor) spectra (1). Figure S1a shows a two-dimensional ^{1}H-^{13}C heteronuclear correlation spectrum of Hatahara Terra Preta organic carbon. Relevant ^{1}H NMR spectra obtained as partial projections are shown in Figures S1b-e. The spectrum of ^{1}H near the COO groups resonating at 170 ppm, see Figure S1b, shows a dominant aromatic-H peak near 7 ppm (60% of the total area) and a broad shoulder from COOH protons extending to 15 ppm (23%). This confirms that most COO groups substitute aromatic rings, and that many are protonated as a result of HF treatment of the samples.

A shoulder associated with alkyl ^{1}H accounts for 17% of the spectral area in Figure S1b. This component, which according to the spectral pattern in Fig. S1a is mostly associated with COO/NC=O groups resonating around 173 ppm, is enhanced due to the greater proton density of alkyl residues; this is evidenced by a shift of the COO peak from 170 ppm in the DP/MAS spectrum to 172 ppm in the CP/MAS spectrum. According to our decomposition in of Table 1, we expect a fraction of 2/17 = 0.12 COO or NC=O groups bonded to alkyl groups in soil organic matter not derived from char, in good agreement with the HetCor results taking CP enhancement into account.

Whether the COO groups are bonded to single aromatic rings rather than fused rings can be assessed by H-C dipolar dephasing. Our data show relatively slow dephasing of the COO signals, indicating clustering of aromatic rings and heavy substitution of the rings by COO and O, as in a typical char oxidation product.

^{13}C longitudinal relaxation time in Terra Preta soil organic matter.

Figure S2 shows a series of ^{13}C CP NMR spectra of Hatahara Terra Preta soil organic matter after ^{13}C spin-lattice (T_1) relaxation that proves that longitudinal relaxation is essentially complete within the 40-s recycle delay used in the DP spectra of Figure 1, making those spectra quantitative.

Quantitative analysis of Zook soil humic acid.

Table S1 shows the fractions of functional groups in a humic acid extract from the surface horizon of an Iowa Mollisol (Zook, a Cumulic Vertic Endoaquoll) and their decomposition into 67% char residues and 33% other organic matter of moderate aromaticity.

Table S1. Quantitative NMR spectral analysis of Zook Mollisol humic acid extract (based on data from ref. (2)) followed by a possible decomposition into contributions from low-alkyl char residues (of composition similar to those in Terra Preta soils) and from typical soil organic carbon not derived from char (with an aromaticity of 25%). Error margins: ± 2%.

	Carbonyls		Aromatics		Alkyls			
Moieties: ppm:	C=O 210-185	COO / NC=O 185-160	C-OH / C-O-R 160-145	$C_{non\text{-}pro}$ C-H 145 - 100	HCOH / O-C-O 110-50	CH_2 / CH 50-25	CH_3 25-7	**Total**
Zook HA extract	3%	19%	8%	39% 12%	13%	4%	2%	**100%**
Zook HA char residues	2.5%	11%	5%	37% 9%	1%	1%	0.5%	**67%**
Zook HA extract soil org. C	0.5%	8%	3%	2% 3%	12%	3%	1.5%	**33%**

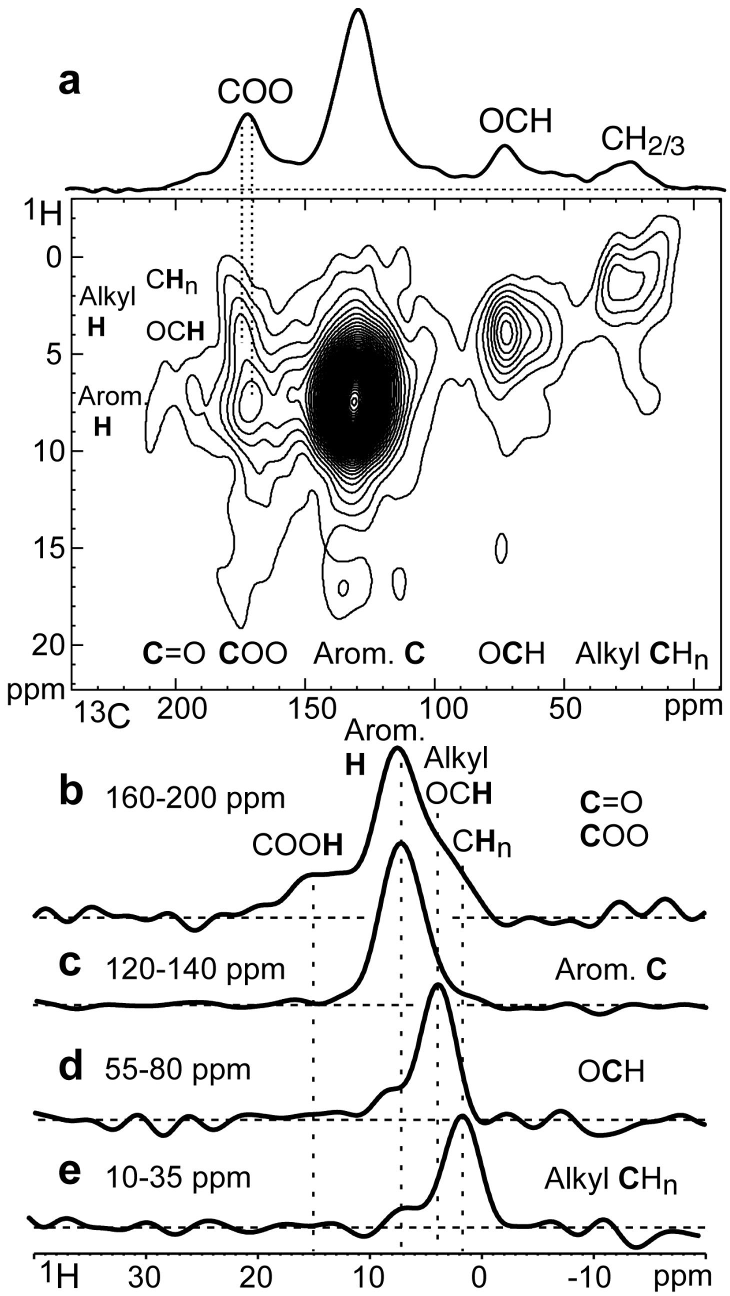

Figure S1. (a) Two-dimensional ^{1}H-^{13}C heteronuclear correlation spectrum of Hatahara Terra Preta soil organic matter with homonuclear (FSLG) decoupling during ^{1}H evolution and 0.5-ms cross polarization. Spinning frequency: 8 kHz. (b-e) Partial projections showing the ^{1}H spectrum associated with the carbons observed at (b) 160-200 ppm (COO, C=O, and NC=O), (c) 120-140 ppm (aromatic C), (d) 55-80 ppm (alkyl OCH), and (e) 10-35 ppm (alkyl CH_n). Total measuring time: 42 hours.

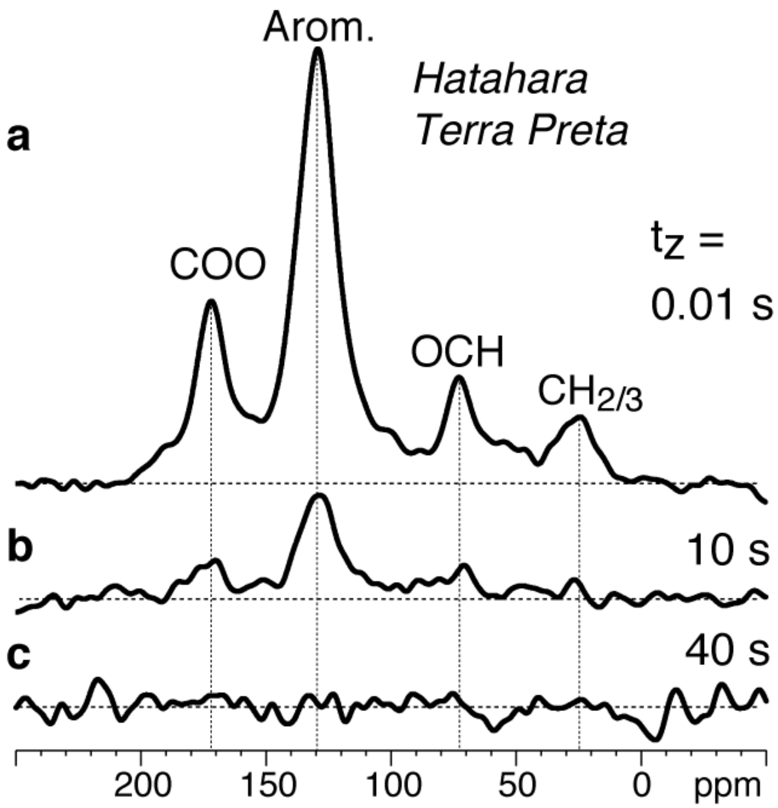

Figure S2. Series of ^{13}C CP NMR spectra of Hatahara Terra Preta soil organic matter after ^{13}C spin-lattice (T_1) relaxation during a period t_z of (a) 0.01 s; (b) 10 s; and (c) 40 s, with Torchia's pulse phase cycle (3) that results in zero magnetization for $t_z >> T_1$ ("CP/T_1/TOSS" method (4)). The comparison of the spectra in (a) and (b) shows that most spectral components relax with similar time constants. The absence of detectable signal in (c) proves that the 40-s recycle delay used in the DP spectra of Figure 1 is long enough for essentially complete relaxation of all types of ^{13}C in the sample.

References

(1) Fang, X.; Chua, T.; Schmidt-Rohr, K.; Thompson, M. L., Quantitative ^{13}C NMR of whole and fractionated Iowa Mollisols for assessment of organic matter composition. *Geochim. Cosmochim. Acta* **2010,** *74*, (2), 584-598.

(2) Mao, J.; Fang, X.; Schmidt-Rohr, K.; Carmo, A. M.; Hundal, L. S.; Thompson, M. L., Molecular-scale heterogeneity of humic acid in particle-size fractions of two Iowa soils. *Geoderma* **2007,** *140*, (1-2), 17-29.

(3) Torchia, D. A., The measurement of proton-enhanced carbon-13 T_1 values by a method which suppresses artifacts. *J. Magn. Reson.* **1978,** *30*, 613-616.

(4) Mao, J. D.; Hu, W. G.; Schmidt-Rohr, K.; Davies, G.; Ghabbour, E. A.; Xing, B., Quantitative characterization of humic substances by solid-state carbon-13 nuclear magnetic resonance. *Soil Sci. Soc. Am. J.* **2000,** *64*, (3), 873-884.

APPENDIX B. SOLID STATE NMR STUDY OF CHEMICAL STRUCTURE AND HYDROTHERMAL DEACTIVATION OF MODERATE-TEMPERATURE CARBON MATERIALS WITH ACIDIC SO_3H SITES

Carbon, **74,** pp 333-345, 2014

Jason M. Anderson[a], Robert L. Johnson[b], Klaus Schmidt-Rohr[b], and Brent H. Shanks[a]*

[a] Chemical and Biological Engineering Department, Iowa State University, 1140 Biorenewables Research Laboratory, Ames, Iowa 50011
Corresponding Author. E-mail: bshanks@iastate.edu (Brent Shanks)
[b] Chemistry Department, Iowa State University, 0205 Hach Hall, Ames, Iowa 50011

Abstract

Hydrothermal stability of carbon based acid catalysts synthesized by sulfonating carbohydrates pyrolyzed at moderate temperatures (300-600°C) has been reported previously. To test the effect of carbon structure on hydrothermal stability, we produced catalysts by dry pyrolysis at 350ºC and 450ºC or by hydrothermal carbonization, followed by sulfonation with fuming sulfuric acid, as well as by direct sulfonation of glucose. The catalysts were characterized by BET, titration, Raman spectroscopy, TGA, XPS, reaction testing, and ^{13}C solid state NMR. Catalysts were hydrothermally treated and then analyzed for sulfur retention and catalytic activity. The lower temperature carbon catalysts showed the best stability, however all showed significant activity loss. Solid state NMR of materials made from ^{13}C-glucose was used to characterize the structural details in an attempt to correlate functional groups to hydrothermal stability of catalyst active sites. Structural

models generated from NMR data showed that the most stable catalysts contained a significant fraction of furan rings and hardly any polycondensed aromatic rings.

Introduction

Acid catalysts promote a variety of important reactions: esterification-/transesterification [1-5], dehydration/hydration [6, 7], hydrolysis [4, 8, 9], etherification [2], alkylation, acylation, condensation, oligomerization, etc. [7]. These reactions generally proceed through a carbocation intermediate, generated either by protonation of a Brønsted acid or through abstraction of electrons by a Lewis acid. Brønsted acids are ubiquitous in the chemical industry in homogeneously and heterogeneously catalyzed systems. Industry uses sulfuric acid for a myriad of reactions [10] and while it is inexpensive and highly active, it requires separation, recycling, and waste treatment, which are energy inefficient [11, 12]. Therefore, significant incentive exists for the development of heterogeneous acid catalysts to replace sulfuric acid thereby reducing costs and minimizing environmental impacts [13].

In general, industry would prefer to utilize solid acid catalysts, and for predominantly gas phase or non-aqueous processing, heterogeneous Brønsted acid catalysts with alumina, silica, zeolites, or resins supports have proven effective. However, the development of heterogeneous acid catalysts functional and stable in aqueous systems, which is a research target for utilization of bio-based feedstocks, has been significantly more challenging. Many common support materials including alumina, silica, and zeolites degrade readily in subcritical water [7, 14, 15]. Recently, promising sulfonated carbon catalysts with improved hydrothermal stability have been reported [16, 17]. While these materials are quite interesting, no systematic experimental testing for the hydrothermal stability of the solid acid catalysts and importantly little correlation of stability to the structure and chemistry of the carbon support has been reported.

The deactivation of sulfonated carbon catalysts may occur in several ways, but is primarily explored through changes in the catalyst activity [1, 18]. Several researchers have explained the decrease in catalyst activity in terms of hydrolysis of the carbon-sulfur bond and then loss of a sulfate group (SO_4) [18, 19] although no definitive experimental evidence was shown of sulfur leaching as the primary deactivation pathway. Yamaguchi and Hara suggested that adjacent electron-withdrawing groups on the arene sheets composing the carbon support improved the strength of the sulfur-carbon bond [20, 21] and thereby reduced hydrolysis of the active site. The current work seeks to explore this hypothesis by producing supports with varying degrees of aromaticity and oxygen-containing functional groups. The sulfonated carbon materials examined include alteration of the balance between the arene and furan aromatic rings as well as the number of carboxylate and phenolic functional groups.

A number of strategies have been used to produce carbons, which are subsequently sulfonated for use as catalyst to transform fatty acids into biodiesel [22]. While there is general agreement that processing temperature is a critical parameter governing the amount of hetero atoms remaining in the final carbon materials, understanding of the transformation from the carbohydrate starting material to carbon remains limited [23, 24]. To provide a more direct basis for comparison, the sulfonated carbon materials examined were similar to those reported previously including pyrolyzed carbons [11], hydrothermal carbon [10, 25, 26], direct sulfonation of a carbohydrate [27], and sulfonation via electrophilically substituting benzene sulfonic acid as shown for carbon nanotubes [28, 29]. Since increasing carbonization temperature decreases the amount of oxygen present in the carbon material, the oxygen functionality should be the most extensive for low synthesis temperature. The expected order from high to low oxygen content of the materials synthesized would be the directly sulfonated carbon (150°C), the hydrothermal carbon (200°C), and the pyrolyzed carbons (350°C and 450°C synthesis temperatures). The structure and chemical composition of the different materials were determined using solid-state NMR. By using uniformly ^{13}C-enriched glucose in the synthesis of the materials, we achieve a 90-fold signal enhancement, which results in truly quantitative spectra with excellent signal-to-noise ratio. With an NMR-active ^{13}C isotope in every carbon site, it also becomes possible to obtain spectrally edited two-dimensional ^{13}C-^{13}C exchange spectra that delineate the bonding between aromatic rings and functional groups, and reveal distinctive signals of arene versus furan rings. [30] Based on the detailed structural information from these spectra, we can propose structural models that are validated through comparing simulated NMR spectra and elemental composition with the experimental data. These models summarize the structural insights from NMR and enable direct assessment of the effect of the carbon structure on hydrothermal stability.

To measure the stability of the sulfonate groups under hydrothermal conditions, the various sulfonated carbon materials were subjected to extended hydrothermal conditions and the retained sulfur content was measured using elemental analysis. Furthermore, the catalytic activity of the materials both freshly produced and after having been subjected to successive hydrothermal treatments was tested via the esterification of acetic acid and methanol, which is quite sensitive to both the number and pK_a of the acid sites present [31].

Experimental

Materials and Synthesis

Glucose, sodium chloride, sodium hydroxide, glacial acetic acid, dimethylsulfoxide (DMSO), sodium hydroxide, and methanol were purchased from Fisher Scientific and methyl acetate, 1,4-dioxane, isoamyl nitrite, and sulfur trioxide were purchased from Sigma-Aldrich. Glucose enriched with ^{13}C was purchased from Cambridge Isotopes. All chemicals were used without further purification. Nitrogen (99.995%) was obtained from Airgas. The fuming sulfuric acid (~20-30 mol% excess SO_3) used for sulfonation was created using a mixture of sulfuric acid with sulfur trioxide.

Pyrolyzed Carbon Preparation

Glucose (~15g) was pyrolyzed at either 350°C or 450 °C in a horizontal tube furnace, for one hour after a temperature ramp (10°C min^{-1}) from room temperature in flowing nitrogen (about 1L min^{-1}) and then cooled and homogenized through grinding with a mortar and pestle. Next, the char was subjected to additional reaction time of 9 hours at the same pyrolysis temperature in nitrogen after the temperature ramp to ensure uniform composition (verified by NMR - data not shown). The ramp rate in the tube furnace was 10°C min^{-1}.

Hydrothermal Carbon Preparation

In a stainless steel Parr reactor, glucose (5 g) was dissolved in deionized (DI) water (50 mL) and then nitrogen flushed three times. The vessel was then pressurized to 500 psi and heated to 200 °C with a ramp rate of 10ºC min^{-1} and then held for ~18.5 hours. The resulting insoluble carbon material was filtered (4.5-5 µm Buchner funnel) and washed with DI water and dried overnight at 100 °C within an air atmosphere in an oven.

Sulfonation of the Carbon by Fuming Sulfuric Acid

The pyrolytic carbons (350°C and 450 °C), and hydrothermal ("Hydro") carbons were individually sulfonated with fuming sulfuric acid. In an Erlenmeyer flask, carbon (~5 g) was placed in 150 mL of fuming sulfuric acid and then heated to 150 °C. The carbon material was allowed to react for 2 hours at 150 °C and then was cooled to room temperature. The resulting solid material was filtered and washed with ~2-3 L of DI water until the effluent was clear and colorless. Measurement of sulfate ions in the filtrate was accomplished by precipitation with barium chloride. The catalyst was dried overnight in an oven at 100ºC.

Preparation of "Direct" Sulfonated Carbon

Glucose will also dehydrate in concentrated sulfuric acid to a char similar in appearance to the pyrolytic carbons. This direct dehydration provided the highest sulfur incorporation seen in the literature for these catalysts [32]. In an Erlenmeyer flask, glucose (~5 g) was placed in 150 mL of fuming sulfuric acid. It was heated to 150ºC and allowed to react for 2 hours. The resulting solid was washed and filtered with DI water (~2-3 L) until the solution was clear and colorless and no sulfate ions were detected with barium chloride. The final material was dried overnight at 100ºC.

Preparation of "Chem" Sample Using Sulfanilic Acid

For comparison, hydrothermal carbon was also sulfonated using an alternative method with sulfanilic acid that was adapted from the literature [28]. Briefly, sulfanilic acid (6 g), isoamyl nitrite (15 mL), and hydrothermal carbon (2 g) were added to DMSO solvent (30 mL) in a stainless steel Parr reactor. The reactor headspace was flushed with nitrogen (pressurized to 750 psi, vented to 100 psi) three times before heating the reactor to 70°C for 2 hours. The resulting slurry was first filtered with toluene to remove any residual organics, with NaOH (1M) to remove remaining sulfanilic acid, with HCl (0.05M) to reacidify the catalyst for storage, and lastly with DI (2-3 L) water to remove as many ions as possible. The final material was dried overnight at 100ºC.

A summary of the materials produced for the study with their synthesis conditions are given in Table 1. The synthesized materials were labeled either with the pyrolysis temperature (350°C or 450°C) or the unique synthesis step: Hydro, Direct, or Chem. Each sample preparation was duplicated to demonstrate reproducibility, so the sample names were annotated with #1 or #2 such as Chem#1 or 350°C#2.

Table 1. Carbon Samples Synthesis Parameters.

Pyrolysis		Direct	Hydro	Chem	350°C	450°C
Temp	°C	N/A	200	200	350	450
Media		N/A	Water	water	nitrogen	nitrogen
Time	hr	N/A	18.5	18.5	1+9.33	1+9.33
Sulfonation						
Temp	°C	150	150	70	150	150
Media		fuming H_2SO_4	fuming H_2SO_4	DMSO	fuming H_2SO_4	fuming H_2SO_4
Time	hr	2	2	2	2	2

Catalyst Characterization

The carbon materials were imaged with scanning electron microscopy (FEI Quanta-250 SEM), to compare their morphologies with carbons generated by similar synthesis methods in the literature. Surface area characterization was performed by physisorption using Kr as the adsorbing gas in a Micromeritics ASAP 2020. Kr was used as the physisorption gas due to the low surface areas of the samples. Analysis of the materials with a Perkin Elmer STA 6000 Simultaneous Thermal Analyzer (TGA), using a ramp rate of 10°C in flowing air was performed. Elemental analysis results for the carbon, hydrogen, nitrogen, and sulfur (CHNS) were acquired using a PE 2100 Series II combustion analyzer (Perkin Elmer Inc., Waltham, MA). The chemical state of sulfur was analyzed using a Physical Electronics 550 Multitechnique XPS system employing a standard Al electron source. The samples were run at 10^{-9} Torr and mounted on double-sided tape. Charging was corrected for by adjusting the carbon peak to 284 eV. Ion exchange titrations were run to measure the number of acidic groups present on the sulfonated carbons. The number of sulfonic acid (R-SO_3H), carboxylic acid, and phenolic hydroxyl groups were measured using the titration method reported by Suganuma et al. [33]. One back titration measured all the acidic functionalities. It used a known amount of NaOH (~0.1g) dissolved in water with the catalytic material using sufficient time (~2 hours) to exchange the sodium ions with all the hydrogen ions from the acid groups on the material. Then, a simple acid titration using sodium hydroxide was used to exchange the acidic protons from the sulfonic acid and carboxylic acid groups. It was assumed that the sulfonic acid, carboxylic acid, and hydroxyl groups were measured. The sulfonic acid groups were determined based on the sulfur content from elemental analysis, assuming that most sulfur was in the SO_3H form, and the other acidic groups were determined by subtraction of these measurements. Following Suganuma [8], Raman spectra of the sulfonated carbon materials were recorded, using a Renishaw InVia Raman spectrometer using a 488 nm laser and wave numbers from 500 to 2500 and measured at two different locations with three scans each.

Solid State NMR and Structure Simulations

The ^{13}C NMR experiments were performed at a resonance frequency of 100 MHz on ^{13}C-enriched samples using a Bruker DSX400 spectrometer, magic angle spinning (MAS) at 14 kHz in 4-mm rotors, and high power ^{1}H decoupling. The 90° ^{13}C pulse-length was 4.5 μs. Quantitative ^{13}C NMR spectra were measured using direct polarization (DP) magic-angle spinning with high-power decoupling for 5 ms, [34, 35] after recycle delays of 30 s (> 5 T_1); due to efficient ^{13}C-^{13}C spin exchange between fast- and slowly-relaxing sites during the recycle delay, T_1 relaxation is accelerated and homogeneous across each spectrum. A Hahn echo ($2\tau = 0.14$ ms) was generated before detection to avoid baseline distortions arising from the deadtime after the excitation pulse [34]. Corresponding spectra of nonprotonated carbons (and mobile segments) were obtained similarly after recoupled ^{13}C-^{1}H dipolar dephasing of 68 μs duration [34]. Due to the isotope enrichment, a small number of scans (64) was sufficient to provide spectra with excellent signal-to-noise rations. Sufficiently strong ^{1}H decoupling at $\gamma B_1/ 2\pi = 72$ kHz with the two-pulse phase-modulated (TPPM) scheme was applied during an acquisition time of 3 ms. Chemical shifts were referenced to neat TMS using the resonance of ^{13}C1-labeled glycine with a chemical shift of 176.46 ppm as a secondary reference.

Two-dimensional (2D) NMR spectra to identify nonprotonated C near CH in the Hydro sample were measured by 2D exchange NMR after short (0.07 ms) cross-polarization, with 1-s recycle delays, dipolar dephasing before detection (exchange with protonated and nonprotonated spectral editing, EXPANSE NMR), and t_1 increments of $t_r/2 = 35.7$ μs up to 0.9 ms. Dipolar assisted rotary recoupling (DARR) [36] was applied during the mixing time of 10 ms. Details of this new combination of spectral editing with 2D ^{13}C-^{13}C NMR are described in ref. [30]. 2D NMR correlation spectra showing selectively peaks from pairs of nonprotonated carbons in the Hydro sample were obtained by dipolar dephasing of double-quantum coherence in a double-quantum/single-quantum (DQ/SQ) correlation experiment, with a total of 0.57 ms of supercycled post-C5 (SPC5) double quantum excitation [37] homonuclear dipolar recoupling [30] and t_1 increments of $t_r/4 = 14.28$ μs up to 1 ms. The initial magnetization was generated by a combination of cross polarization and direct polarization, followed by 100 ms of spin diffusion [30]. The DQ/SQ spectrum was sheared for direct comparison with the EXPANSE spectrum [30]. The 2D spectra were recorded at a MAS frequency of $\nu_r = 14$ kHz within 10 h each. Other experimental parameters were similar to those given in ref. [30].

To convert the COOH to COOLi groups, which have a characteristic ^{13}C NMR chemical shift difference of +7 ppm, [38] the Hydro and 350^{o}C materials were treated with 0.1 M LiOH, which was titrated to a pH of 9.0 to ensure exchange of H on COO groups but not phenols. The materials (~100 mg) were washed three times with 1 mL of the LiOH solution and pelleted by centrifugation. After washing with DI water the materials were freeze dried.

Structural models were generated for each of the sulfonated carbon materials based on the quantitative 1D and spectrally edited 2D ^{13}C NMR spectra as well as elemental analysis (C, H, N, S, and then O by difference), which provide relative amounts of key structural fragments and atomic compositions and thus greatly constrain the possible structures. Integration of the one-dimensional ^{13}C NMR spectra (also taking into account the small spinning sidebands of the aromatic peaks) directly provided quantitative amounts of major functional groups present, including alkyls, ketones, carboxylic acids, aromatic carbons bonded to O or two bonds from oxygen, protonated and nonprotonated aromatic C, and alkyl C, see Table 2. The spectrally edited two-dimensional NMR experiments [30] were used to identify the predominant linkage patterns of the aromatic subunits and the ketones.

Table 2. Carbon fractions (in atomic %) in functional groups for four ^{13}C-enriched sulfonated carbon materials from quantitative ^{13}C NMR and spectral editing. Error margins: ±1% for large, ±0.5% for small (<10%) signals. For the 350°C and 450°C samples, the C=O/COO and $C_{nonp}O/C_{nonp}$ boundaries were shifted to 175 and 147 ppm, respectively. The percentages can be changed into mmol g^{-1} by multiplication with a factor of 0.67 (1 g ≙ [1/15] mol = 68 mmol; 1 mmol g^{-1} ≙ 1/68 = 1.5%; so 1% ≙ 0.67 mmol g^{-1}) for the low-T and by a factor of 0.77 for the ≥ 350°C materials.

Functional Group	C=O	COO	Aromatic			OCH_n	CH_2+CH	CH_3
			$C_{nonp}O$	C_{nonp}	CH			
Chemical Shift	224-180	180-162	162-142	142-90	162-90	90-52	52-28	28-6
Sample								
Direct	6.6	11.4	24	34	17	2.1	2.9	1.2
Hydro	5.8	11.4	23	44	12	1.7	0.9	0.6
350°C	7.4	10.3	15	51	13	1.7	0.9	0.6
450°C	2.5	1.3	8	65	21	1.0	0.9	0.4

The models were refined by calculating 1D ^{13}C NMR spectra, both for all C and for C not bonded to H, using chemical shifts from the empirical chemical-shift prediction program Advanced Chemistry Devolopment, Inc. (ACD) [39]. These data were input to a MatLab program that converted them into spectra with a Gaussian line broadening of ca. 14 ppm full width at half maximum applied to all peaks. The structural model was optimized iteratively by small modifications of the structures until the simulated and experimental spectra were in good agreement. The structural models presented should be thought of as average structures containing all of the key chemical features of these materials. The inhomogeneous broadening of all resonance lines indicates the presence of many slightly different structures.

Reaction and Stability Testing

Esterification of acetic acid with methanol was used as the test reaction since it is sensitive to the number of acid sites and their pK_a [31]. The reactions were performed at 40 °C in an Alltech 10 mL reactor vial loaded (total volume 7 mL) with methanol (6 M) and acetic acid (3 M) in dioxane with the respective sulfonated carbon (10 mg). The reactions were run at low conversions (<5%) to allow comparison of initial rates. The reaction testing was performed at a range of stir rates so that it was determined that no mass transfer effects occurred as long as the stirring rate was above 200 rpm. The reaction product samples were analyzed on an Agilent 7890A GC equipped with a flame ionization detector. The sulfonated carbons were compared in terms of activity per mass of catalyst, with units of mmol acetate formed min^{-1} (g catalyst)$^{-1}$.

After full characterization of the fresh materials, the catalysts were subjected to hydrothermal treatment. The treatment involved the catalyst material (0.5 g) stirred in DI water (7 mL) at 160°C in the Alltech reactors under autogenous pressure for 24 hours. The solid material was separated from the water with the water subsequently measured for sulfur content using ICP analysis. After the initial separation, the samples were washed copiously (generally about 0.5 L of DI water) until the filtrate was clear and colorless. The hydrothermally treated sulfonated carbon was then characterized and subjected to two more hydrothermal treatments following the same protocol as the first treatment.

Results and Discussion

Characterization results of the samples produced in the current study provide good evidence that the materials were representative of the carbon-based materials studied in previous publications. The SEM images of the hydrothermal carbon, Figure 1, showed the same clusters of nearly uniform spheres of about 0.5-1 µm diameter that have been reported by other groups [40, 41]. The sulfonation of the hydrothermal carbon via fuming sulfuric acid did not affect the spherical morphology. However, the morphology of the spheres changed significantly when modified with sulfanilic acid as they changed from well-defined spheres to pitted amorphous shapes only vaguely reminiscent of the original spherical morphology (Figure 1(B)). The other materials (Direct, 350°C, and 450°C) exhibited shapes resembling shards of glass of ca. 10-150 µm in size with amorphous characteristics (Figure 1(C)), also consistent with previous literature [42, 43]. The samples all had low BET surface areas of 0.22 ± 0.11 m^2 g^{-1}, except for the Hydro samples, which had 1.6 m^2 g^{-1}, in agreement with standard values found in literature [40, 43]. After sulfonation, the materials retained the same BET surface areas. The results can be found in the supplemental information (Table S1).

The TGA results demonstrated that all of the materials were thermally stable in air up to 300°C and with the 450°C material up to 400°C. The sulfonated carbons lost about 10% of their mass, presumably water, before reaching their highest stable temperature. After the noted stable temperature, the materials quickly decomposed, presumably due to oxidation.

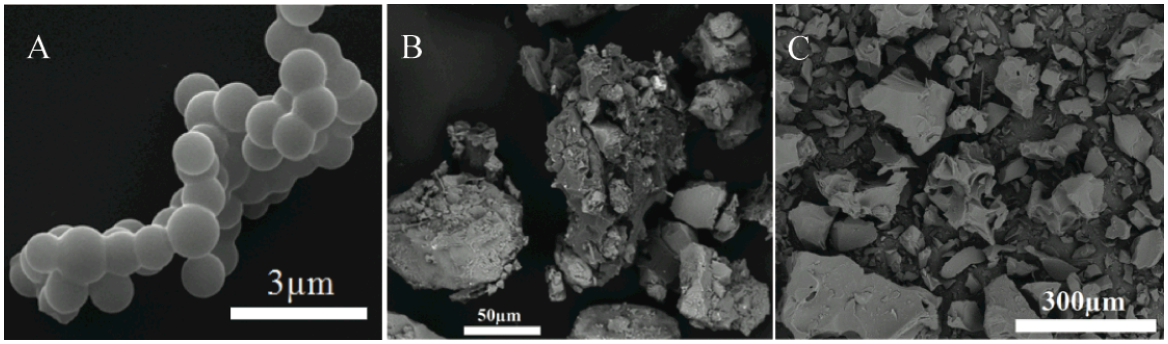

Figure 1. Scanning electron micrograph of (A) hydrothermal carbon before sulfonation, (B) after reaction with sulfonilic acid, and (C) 450 ^oC carbon before sulfonation.

The Raman spectra in Figure 2 show two partially resolved D and G bands [44] [45] for all the carbon materials tested. The D:G area ratio, commonly used to characterize carbon materials [44] [45], failed to provide any differentiation of structure. It was 0.7 ± 0.15 for all the materials, similar to literature values [44]. It has been shown that these two peaks in lower-temperature chars cannot be delineated simply as graphene core and defect/edge carbons, respectively [46]. NMR (see below) shows no graphene cores for the Hydro and Direct materials, and this is supported by their low C : (O+H) atomic ratios of about 0.8 : 1. Even in this range of synthesis temperatures, the materials fail to show significant differences with Raman spectroscopy.

Literature reports show examples of using IR for these types of materials generated from pyrolysis [8] or hydrothermal synthesis [47]. The IR spectra show peaks relating to OH stretching, C=O bending, OH bending, O=S=O bending, and SO_3 stretching. Unlike the NMR peak areas, the area under the IR bands are not quantitative, i.e., their area fractions do not quantitatively correspond to the fraction of the individual functional groups, since IR band intensities are distorted by variable transition-matrix elements [48]. As a result, the quantitative amount of the functional groups cannot be determined from IR spectra without extensive calibrations using reference materials. In addition, the complexity of the fingerprint region between 1500 and 500 cm^{-1} makes it difficult even to unambiguously identify oxygen-bonded aromatic C (especially when it is not protonated) or oxygen-bonded alkyl CH, OCH_3, or $C\text{-}CH_3$ groups, while this can be done based on ^{13}C NMR spectra, particularly when using spectra editing. Furthermore, clusters of fused aromatic rings, which are particularly relevant in carbon materials, do not show specific IR bands, whereas 1D and 2D ^{13}C NMR spectra exhibit a characteristic narrow band of nonprotonated interior aromatic carbons near 130 ppm. In a previous spectroscopic study of chars [35], IR spectra suggested that some of the materials retained a significant fraction of lignocellulosic functional groups, while quantitative ^{13}C NMR spectra, validated by large C:O ratios from elemental analysis, showed that none of the chars contained more than a few percent of carbohydrates [35]. Therefore, the use of solid-state NMR for characterization allowed more in-depth analysis of the quantitative amounts of the functional groups than could be achieved with IR.

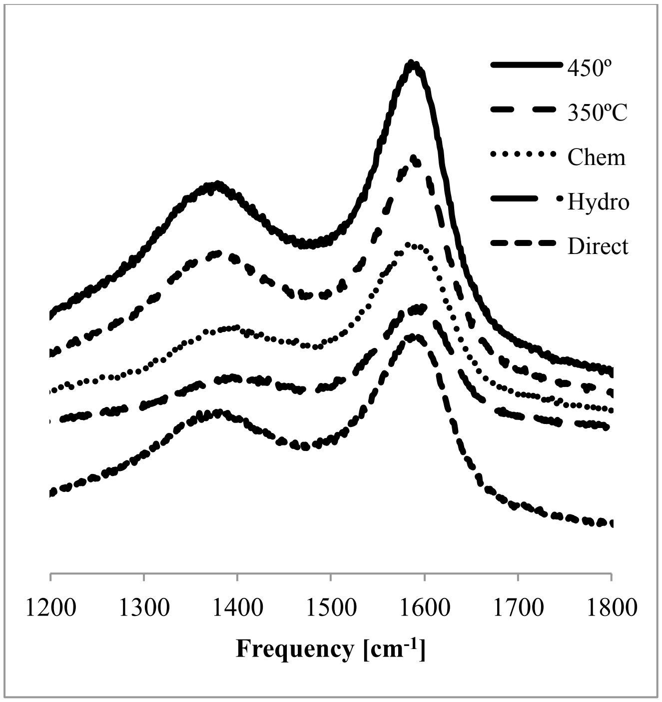

Figure 2. Stacked Raman spectra of the sulfonated carbon materials. The ratio of the peak areas of the D band (1375 cm^{-1}) relative to that of the G peak (1575 cm^{-1}) for all materials was 0.7 ± 0.15.

The initial elemental analysis of the materials, Figure 3, resembled the reported results for both the pyrolyzed carbon material [13] and the hydrothermal carbon [41]. The sulfonated carbons only contained C, H, N, S, and O, with the oxygen determined by difference, and carbon was the most abundant element in all samples. Figure 3 shows a general trend of decreasing oxygen content with increasing treatment temperature; in particular, the 450°C material clearly had the least oxygen. However, the Hydro materials contained slightly more oxygen than the Direct material. The synthesis used for the Chem materials resulted in significant incorporation of oxygen-free aromatic rings, which gave an overall decrease in the weight fraction of oxygen in the resulting material. This hypothesis was confirmed by NMR spectra, which showed a substantial increase in the intensity of the 127 ppm resonance, typical of fused benzene rings. The Chem samples were the only ones with significant amounts of nitrogen, as expected from the synthesis technique. The XPS data showed the sulfur groups on all the materials to be in the reduced chemical state corresponding to the sulfonic acid group, at ca. 168 eV [49]. This value agreed satisfactorily with the sulfur peak of sulfanilic acid.

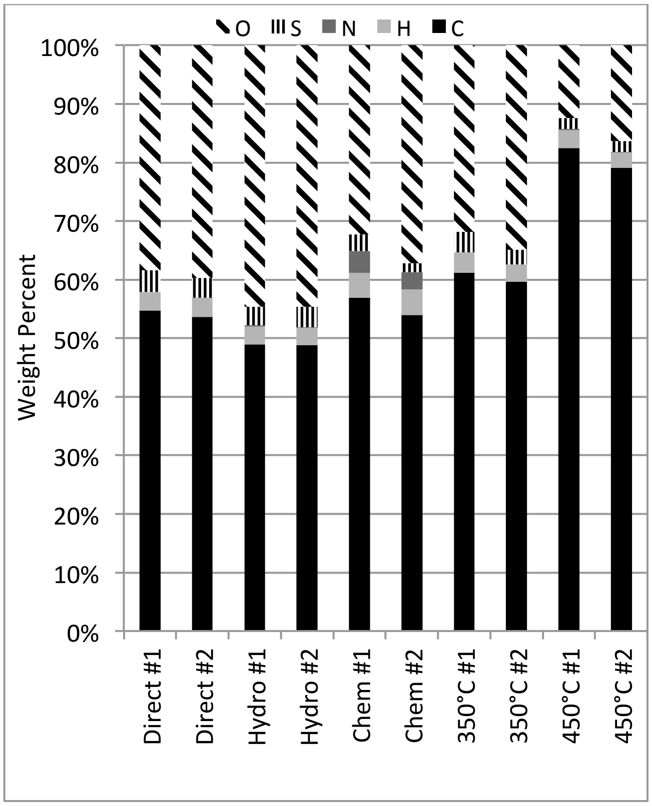

Figure 3. Initial elemental analysis of the sulfonated carbon materials.

Figure 4 shows the sulfonated carbons exhibited different amounts of acidic functional groups. Duplicate syntheses showed good reproducibility, with the amount of sulfonic acid groups per gram remaining consistent. The temperature of synthesis roughly correlated with the amount of carboxylic acids on the carbons: Direct < Chem ≈ Hydro ≈ 350°C < 450°C. Consistent with the elemental analysis, the 450°C samples possessed less oxygen than the lower-temperature materials. However, comparison of the oxygen atoms in the acidic functional groups with the elemental analysis, showed that oxygen bound in acidic groups comprised only 30-50% of the total oxygen in the 450°C carbon. The Direct samples were the most similar in oxygen balance with >67% of the total oxygen accounted for by the acidic functionalities. The numbers of SO_3H groups and the COOH groups agree with other literature for the sulfonated pyrolyzed carbons [4, 33], while the number of OH groups reported in the literature was more than three times larger [4, 33] than the number of phenolic OH groups measured here. Overall, the preliminary characterization of the carbons suggested they share similarities with materials described in the recent literature.

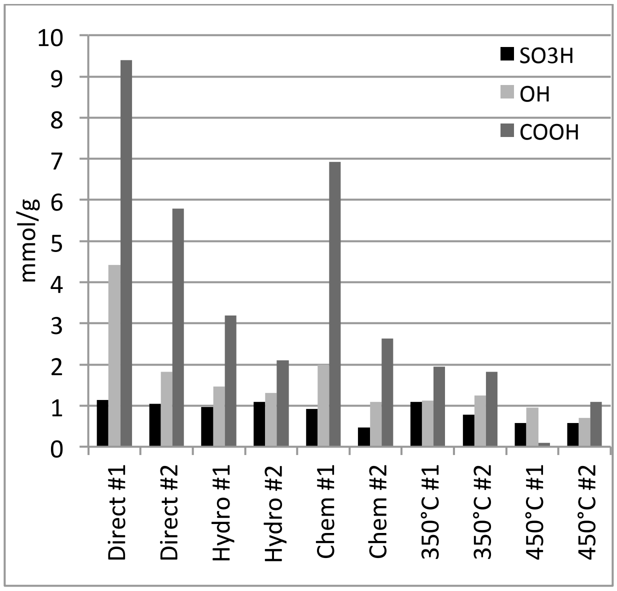

Figure 4. The acidic groups on the sulfonated carbon materials, determined by back titration.

Solid-State NMR

One-dimensional ^{13}C NMR spectra of the four sulfonated carbon materials are presented in Figure 5 and 6 (the Chem samples were not characterized with NMR since their activity in reaction testing was extremely poor). Shown are quantitative (direct-polarization) ^{13}C NMR spectra of all carbons (thick line) and selective spectra of only nonprotonated carbons and CH_3 groups (thin line) in each of the sulfonated materials. In all samples, the dominant signals, observed between 100 and 155 ppm, are from aromatic carbons. Peaks of alkyl OCH groups, which resonate near 70 ppm, are not observed, indicating that complete transformation of the precursor sugar molecules has occurred as a result of both heat treatment and sulfonation. The materials show only minor signals (< 8%) from other alkyl carbons, which demonstrates that sulfonation has effectively removed any small molecules resulting from fragmentation of furan rings, such as levulinic acid [50]. The large fraction of nonprotonated aromatic carbons (~85% of all aromatic C) revealed by the small difference between the spectra without and with dipolar dephasing indicates ample substitutions of, and linkages between, the aromatic rings. The substituents include ketones (C=O), which can resonate between 210 and 165 ppm, and COO groups (180-162 ppm). The relatively low chemical shifts of both ketones and carboxylic acids in the Direct and Hydro samples confirm that these groups are linkers and substituents on aromatic rings [50].

The lower temperature materials show a broad range of chemical shifts in the aromatic region characteristic of oxygen bonded to aromatic carbons, e.g. in phenols or furans. Oxygen not only induces a significant increase in chemical shift of the directly bonded aromatic carbon, to 140-162 ppm, but also shifts the signal of the next carbon (i.e., separated from O by two bonds) down to 95-130 ppm [40, 51]. Since all the carbons in furan rings are bonded to O (α-carbons) or two bonds from O (β-carbons), furans show only two main resonances, near 150 ppm and near 120 ppm, in 1:1 ratios. This has been nicely demonstrated on polyfurans, where the two peaks are baseline-resolved [51]. It is also confirmed in the simulated spectra of the furan components in our low-temperature samples, bottom half of Figure 5(c) and (d); here, even with a multitude of different substituents on the furan rings, whose effects on chemical shifts can be complicated, the two peaks are clearly resolved. The absence of a deep intensity minimum near 135 ppm in the measured spectra of our materials must be attributed to the presence of six-membered aromatic rings (termed arenes in the following), which resonate between 120 and 145 ppm.

Spectrally edited two-dimensional ^{13}C-^{13}C NMR spectra [30] shown in Figure 7 provide proof of arene rings and characterize the linkages between the aromatic rings in the Hydro sample. Figure 7(a) is a spectrum correlating signals of CH in the vertical dimensional with signals of nearby nonprotonated-C in the horizontal dimension, while Figure 7(b) shows the spectrum of directly bonded nonprotonated carbons [30]. Several characteristic peaks, in particular those of arene rings in Figure 7(a), are labeled in the spectra. Cross sections from the spectrum in Figure 7(a) are shown in Figure 8.

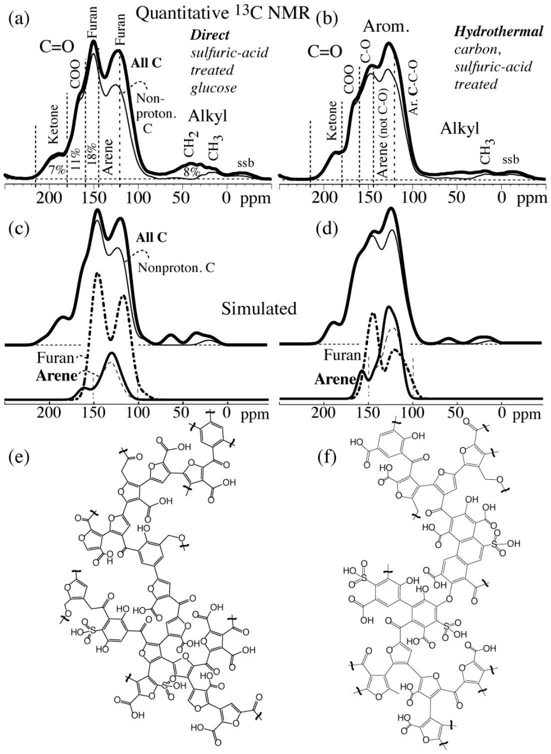

Figure 5. Quantitative ^{13}C NMR spectra of sulfonated carbon materials made from ^{13}C-enriched glucose at low temperatures. Thick line: all C; thin line: nonprotonated C as well as CH_3. "ssb": spinning sideband (14-kHz MAS). (a) Direct, (b) hydrothermal synthesis. (c, d) Corresponding simulated spectra from the structural models shown in (e, f). In (c) and (d), below the full spectra, the contributions from furan carbons (dash-dotted line), arene carbons (thick black line), and nonprotonated arene carbons (dashed lines) are also shown separately. Furan rings exhibit two peaks of similar integrated intensity at 145 and 120 ppm, while arenes display a main peak near 130 ppm; also, the average chemical shifts of C-O in furan (147 ppm) and phenol (158 ppm) are distinctly different.

The selective 2D spectrum of nonprotonated carbons shown in Figure 7(b) exhibits the signals of linkages between aromatic rings, which must show up here since they always involve directly bonded nonprotonated carbons. The intensity distribution shows evidence for many different inter-aromatic linkages, including furan Cα-Cβ and Cβ-Cβ, and of some substitution by C=O and COO groups. The most pronounced peak is from substituted furan Cα connected to substituted furan Cα, which highlights that both sites are heavily substituted. This is also required by the large fraction of nonprotonated Cα (145-155 ppm) and Cβ (in the region < 125 ppm) detected in the quantitative spectra of Figure 5(b). These signals support the presence of the multiple types of linkages seen in the model of Figure 5(f).

Figure 7(c) shows a DQ/SQ NMR spectrum of the nonprotonated carbons in the 450°C material. By far the most intense peak is observed at 130 ppm on the diagonal. It must be assigned to pairs of nonprotonated carbons (the C-CH signals have been suppressed by ^{1}H-^{13}C dipolar dephasing of ^{13}C-^{13}C double-quantum coherence [30]) in the interior of clusters of fused aromatic rings, while pairs of nonprotonated aromatic carbons connected by a single bond would resonate near 140 ppm [52]. The characteristic 130-ppm diagonal signal of polycondensed aromatic rings is barely discernible in the corresponding spectra of the lower-temperature materials [30], for instance in Figure 7(b).

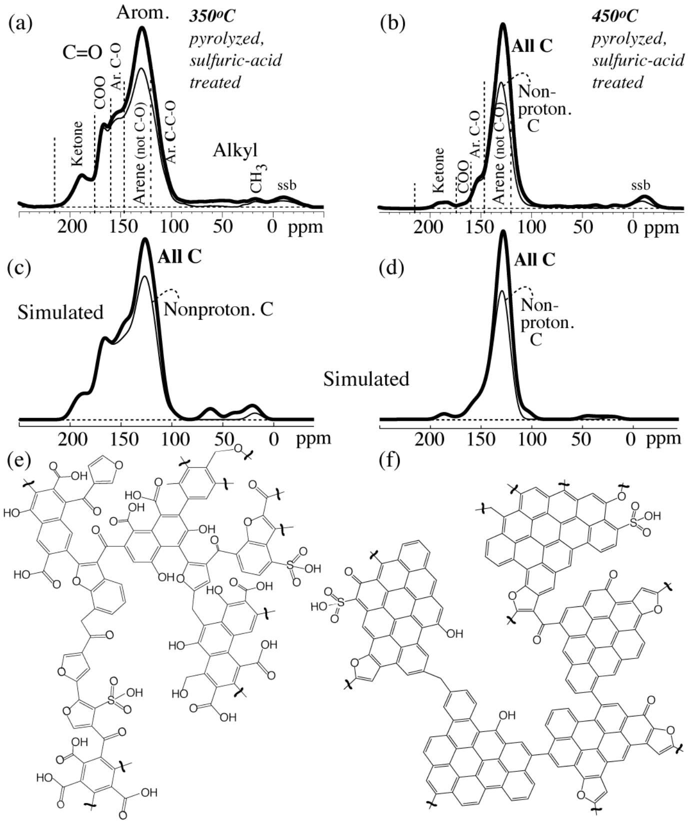

Figure 6. Quantitative ^{13}C NMR spectra of sulfonated carbon materials made from ^{13}C-enriched glucose at higher temperatures. Thick line: all C; thin line: nonprotonated C as well as CH_3. "ssb": spinning sideband (14-kHz MAS). (a) 350°C, (b) 450°C synthesis temperature. (c, d) Corresponding simulated spectra from the structural models shown in (e, f).

The carbon materials pyrolyzed above 300°C exhibit a main maximum near 130 ppm in their ^{13}C NMR spectra, Figure 6, indicative of arene rings. In the material pyrolyzed at 450°C, this is by far the most intense peak. The low chemical shift of the nonprotonated carbons, near 130 ppm, indicates polycondensation, which is confirmed by the strong diagonal peak at 130 ppm from pairs of nonprotonated carbons in fused aromatic rings seen in the dipolar dephased DQ/SQ spectrum of Figure 7(c). Due to its higher degree of polycondensation, the 450°C material contains only a low concentration of edge sites that can easily undergo oxidation, resulting in only relatively minor changes in the backbone structure resulting from the sulfonation procedure.

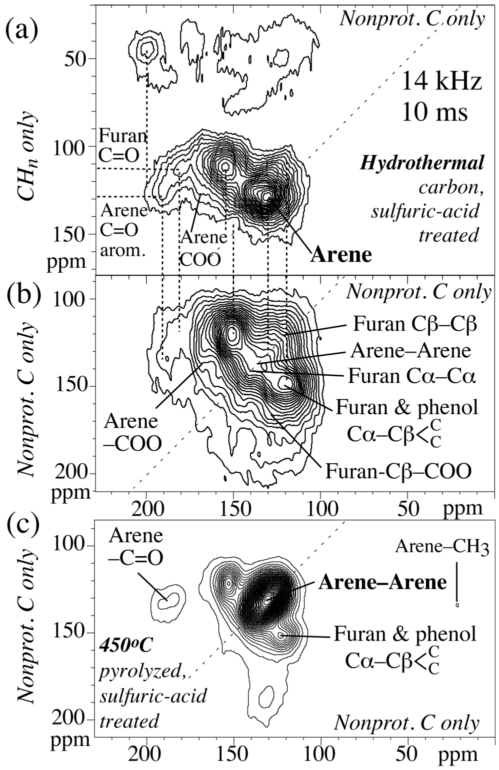

Figure 7. Two-dimensional ^{13}C-^{13}C NMR spectra with spectral editing, of (a, b) the ^{13}C-enriched Hydro material, used to identify structural units and establish their connectivities. (a) Exchange with protonated and nonprotonated spectral editing (EXPANSE) spectrum with a spin-diffusion time of 10 ms, correlating signals of CH (vertical axis) and nonprotonated C (horizontal axis). (b) Sheared dipolar-dephased double-quantum/single-quantum NMR spectrum, showing cross peaks exclusively from pairs of directly bonded nonprotonated carbons. The diagonal in the spectra (at $\omega_2 = \omega_1$) is marked by a dashed line. (c) Same as (b) for the ^{13}C-enriched sulfonated 450°C material, with a dominant peak characteristic of nonprotonated carbons in polycondensed aromatic rings.

In the quantitative ^{13}C NMR spectra of Figures 5 and 6, many peaks are merged into broad spectral bands. In order to prove that our interpretation of the various shoulders and components of these broad bands is correct, selective spectra of the four materials obtained by spectral editing and 2D NMR are displayed in Figures 8, 9, S1, and S2 (Supporting Information). For each sample, these show half a dozen peaks that are only visible as shoulders in the unselective spectrum. Peaks resolved in this way include signals from: aromatic C-H; COO (shifted by +7 ppm after Li binding); furan-bonded vs. arene-bonded vs. alkyl-bonded C=O (from EXPANSE or DQ/SQ ^{13}C-^{13}C spectra); aromatic C-O (from EXPANSE or DQ/SQ spectra); nonprotonated arene C (bonded to protonated arene C, from EXPANSE spectrum); and CH$_2$-bonded arene (from EXPANSE spectrum).

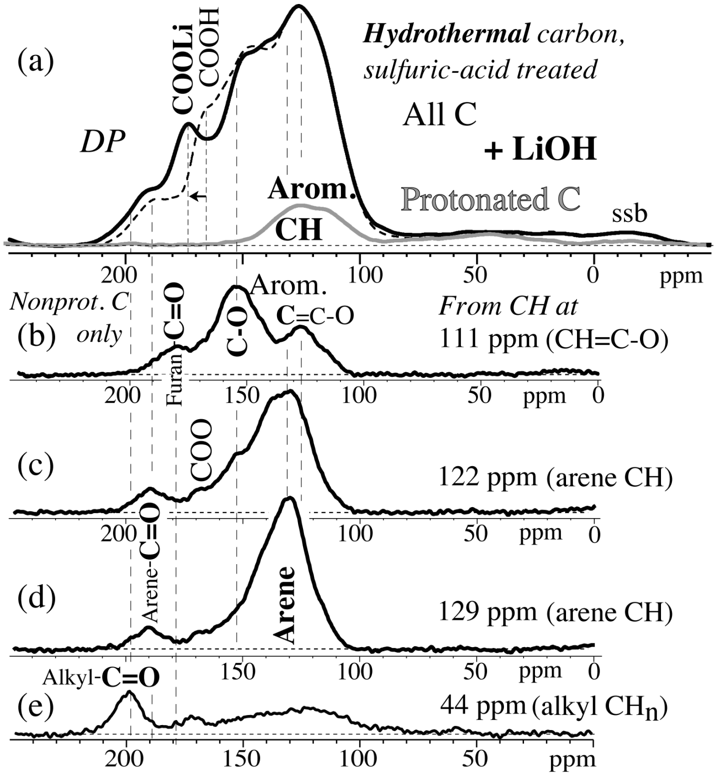

Figure 8. Selective ^{13}C NMR spectra of the ^{13}C-enriched Hydro material. (a) Full quantitative spectrum (dashed line, for reference) with corresponding selective quantitative spectrum of protonated C (gray line), obtained by dipolar-dephasing difference, and (full line) spectrum after treatment of the material with LiOH; the signal of COOLi groups is shifted by +7 ppm from that of COOH and is thus better resolved. "ssb": spinning side band. (b-e) Horizontal cross section from the 2D ^{13}C-^{13}C EXPANSE spectrum in Figure 7(a), with signals of (b) aromatic C-O bonded to aromatic CH and C=O bonded to a furan ring; (c, d) nonprotonated arene C bonded to arene CH; a peak of C=O bonded to an arene ring is also detected; and (e) C=O and other sp^2-hybridized C bonded to alkyl C.

The spectra in Figure 8(c, d), obtained as cross sections from EXPANSE ^{13}C-^{13}C spectra, show a particularly distinct peak of arene rings: CH carbons with a maximum near

127 ppm exhibit a strong correlation with nonprotonated C resonating around 131 ppm. These chemical shifts are very rare in furans, where CH usually resonates near 115 or 145 ppm and nonprotonated C near 120 or 147 ppm, but they are typical of arene rings, in particular with COO substitution. The corresponding spectra of the other materials, Figures S1(c, d) and S2(c, d), also exhibit this arene peak, while it is completely overlapped by the furan signals in the unselective ^{13}C NMR spectra of 5(a, b). In addition, the spectra show cross peaks of C=O near 190 ppm with aromatic C near 130 ppm; both chemical shifts are characteristic of arene-bonded C=O [30], confirming the presence of arene rings.

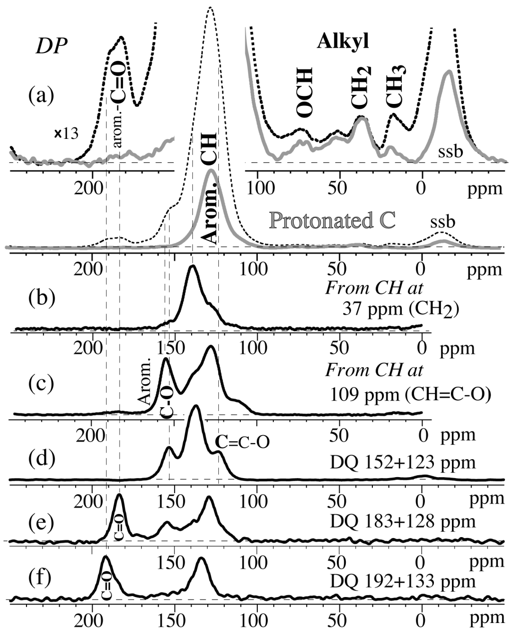

Figure 9. Selective ^{13}C NMR spectra of the ^{13}C-enriched sulfonated 450°C material. (a) Full quantitative spectrum (dashed line, for reference) with corresponding selective quantitative spectrum of protonated C (gray line), obtained by dipolar-dephasing difference; the top traces show the spectra vertically expanded by a factor of 13. "ssb": spinning side band. (b, c) Horizontal cross sections from 2D ^{13}C-^{13}C EXPANSE spectrum, with signals of (b) 140-ppm arene C bonded to CH$_2$ resonating at 37 ppm, and (c) aromatic C-O bonded to aromatic CH. (d-f) Horizontal cross sections from a dipolar-dephased DQ/SQ ^{13}C-^{13}C correlation spectrum (not sheared), with signals of (d) aromatic C-O and neighboring nonprotonated aromatic C; (e) C=O at 183 ppm and its bonded aromatic C at 128 ppm; and (f) C=O at 192 ppm and its bonded aromatic C at 133 ppm.

The NMR-derived percentages of the carbons in the various functional groups obtained by integration of the respective spectral ranges are compiled in Table 2. Based on these data, and also taking into account the elemental composition as well as linkages established by 2D NMR, structural models have been generated, Figure 5(e, f) and Figure 6(e, f). The structures have been adjusted such that the corresponding simulated spectra, Figure 5(c, d) and Figure 6(c, d), match the main features of the quantitative ^{13}C NMR spectra. As expected given the pronounced differences between the experimental spectra in Figure 5 and 6, the models show significant differences in the molecular structures comprising this suite of materials. The arene:furan ratios and degree of condensation (aromatization) increase with processing temperature, and functional group substitutions also change.

The sulfonated glucose (Direct sample) contains predominantly furan rings, as proved by (i) strong cross peaks between protonated alkyl carbon and aromatic C-O, [30] which are impossible in phenols or arene ethers; (ii) the similar intensity of the pair of peaks at 150 and 123 ppm in Figure 5a, while the intensity at 150 ppm would be lower in phenols; and (iii) the low chemical shifts of C=O (<195 ppm) and COO (<165 ppm) groups, which are characteristic of bonding to furan [30]. The furan rings are linked via direct C_α-C_β, C_α-C_α, and C_β-C_β bonds, as well as ketones and a few alkyls. The furan rings are also heavily substituted with carboxylic acids. Some arene formation has also occurred but to a rather limited extent. The characteristic signal of interior carbons in polycondensed arene rings is not observed in the selective 2D spectrum of nonprotonated C [30].

The structure in Figure 5(e), with large fractions of ketone and acid groups linked directly to furan rings, has not been often reported in the literature and seems to be characteristic of a carbohydrate subjected to oxidation by hot, concentrated fuming sulfuric acid. Without NMR, this highly aromatic material might appear as consisting of polycondensed aromatic rings substituted with SO_3H groups [32] as well as many electron-withdrawing OH, –O–, COOH, and C=O moieties. This model can be directly refuted, even without detailed chemical-shift and cross-peak analysis, based on the large fractions of edge carbons that are aromatic and bonded to H, O, COO, C=O, SO_3, or to alkyl C, which account for 17, 24, >10, >5, >3, and >2%, respectively (Table 2 and S content). The total of these carbons that cannot be in the interior of a polycondensed aromatic cluster is >61%, to be compared with <17% of other aromatic carbons that could be in the interior of a cluster (or linked to another aromatic C through a single bond). Such a small fraction of interior carbons does not permit construction of polycondensed clusters of significant size.

Sulfonation of hydrothermal carbon produces a material with a larger arene:furan ratio, which is nearly 1:1 on a carbon-atom basis. The arene groups, proved by the spectra in Figures 7(a) and 8(c, d), are linked individual rings and have not polycondensed to a significant degree. This is proved by the absence of a strong peak at 130 ppm near the diagonal in the 2D spectrum of nonprotonated carbons, Figure 7b. Our model incorporates the arene with the furan rings, which is contrary to models proposed in a previous publication for hydrothermal char without sulfonation [50]. This conclusion is further supported by 2D exchange NMR spectra with long mixing times that show no domain separation (data not shown). Similarly as in the Direct sample, numerous ketone linkers, with characteristic NMR signals, connect arene and furan aromatic rings, and these rings are heavily substituted with carboxylic acid groups. While the fuming sulfuric acid treatments result in nearly complete conversion of carbohydrates to aromatic carbons, it does not catalyze the polycondensation of the aromatic rings, which is only achieved by higher-temperature treatment.

Our sulfonated 350°C carbon model in Figure 6(e), although more condensed than that of the Hydro material, does not contain large polycondensed aromatic sheets, again supported by the absence of a strong peak at 130 ppm near the diagonal in the spectrum of nonprotonated carbons (Figure 6 of [30]). Instead, it is mainly composed of naphthalene units, benzofurans, arenes, and a small fraction of individual furan rings. The abundance of ketone linkers and carboxylic acid groups, directly based on NMR peak areas, is reduced compared to either the Direct or the Hydro material, which can be attributed to a lower amount of sites that are susceptible to oxidation in the precursor material. Our analysis shows that polycondensation does not occur to a significant extent until above 350°C.

Models containing large (>5 rings) polycondensed aromatic units, as proposed in the literature even for materials heated to only 350°C [53], are plausible only for carbohydrate materials heated to significantly higher temperatures. For instance, the model in reference [53] with more than a dozen fused aromatic rings corresponds to elemental ratios of C:H:O:S = 1 : 0.32 : 0.12 : 0.02, completely inconsistent with the measured elemental compositions [53] of C:H:O:S = 1 : 0.71 : 0.58 : 0.011 at 300°C and 1 : 0.45 : 0.39 : 0.014 at 400°C.

At higher temperatures, the structures of the materials begin to appear like those postulated in literature. In the sulfonated 450°C carbon, the aromatic rings have undergone polycondensation reactions to a significant extent, nearly all furan rings have been removed, and virtually no carboxylic acid groups have been introduced from the sulfonation procedure. These data show that the suite of materials produced here contain substantially different structures, and they indicate that while fuming sulfuric acid treatment produces five- and six-membered aromatic rings, thermal treatment at > 350^{o}C is required to induce significant polycondensation of aromatic rings. These results complement the existing knowledge about carbons and their structure, especially filling in details about the structures resulting from lower temperature pyrolysis.

Additionally, we were able to use the NMR-based structural analysis to test the utility of less involved methods such as Raman spectroscopy. Our structural analysis shows that the Raman methods used to indicate the graphitic character and defect sites of high temperature carbons are not reliable for low temperature materials. Raman analysis would lead to grossly incorrect conclusions about the material structure. The Direct sample shows a strong peak at 1575 cm^{-1}, Figure 2, which is usually taken to indicate a highly graphitic character [46, 54, 55]. In contrast, NMR clearly shows that this material is predominantly furanic with only minor fraction of arene rings, which is supported by the relatively low C:(O+H) atomic ratio. On the other hand, the NMR spectra clearly identify polycondensed aromatic rings in the 450^{o}C sample. Advanced solid-state NMR techniques can achieve a level of detail unmatched by conventional characterization methods.

Hydrothermal Treatment and Reaction Testing

The sulfonated carbons were tested for their hydrothermal stability using the protocol given in the Experimental section. Shown in Figure 10 is the elemental analysis for the sulfonated carbons through the progression of stability testing. As demonstrated by the NMR characterization, the overall chemical structures for these materials were quite different. Despite the range of structures, the differences in hydrothermal stability for the range of sulfonated materials were relatively small. The first hydrothermal treatment (24 hr at 160°C) significantly reduced the sulfur content for all of the sulfonated carbons. As clearly demonstrated from elemental analysis, the sulfur-containing functional groups could not withstand extended exposure to condensed-phase water at 160°C. With subsequent treatments, the sulfur content continued to diminish significantly in all the materials never asymptoting to a stable value. The least stable material, the 450°C carbon, lost >90% of its original sulfur content. The other catalysts, Hydro, Direct, 350°C, and Chem, retained similar percentages of original sulfur 50% ±20%. Most of the sulfur was lost in the first hydrothermal treatment and less was generally lost in subsequent treatments. The carbon structures with more furan rings (Direct and Hydro) retained slightly more sulfur than the carbon structures with more arene rings (350º and 450 ºC). The well-known equilibrium incorporating sulfate groups on the aromatic rings, which was strongly favored by the excess sulfur acid present during the synthesis worked in reverse under the harsh hydrothermal conditions. The ICP results for the water phase after hydrothermal treatment (data not shown) validated the considerable leaching seen with all of the sulfonated carbons. While literature reports have suggested enhanced stability based on less severe hydrothermal treatments, [17, 44, 56] the carbon sulfur bond produced from electrophilic substitution on a double bond undoubtedly hydrolyzes in 160ºC condensed-phase water to release the sulfur independently of the overall amount of substitution on the arene carbons.

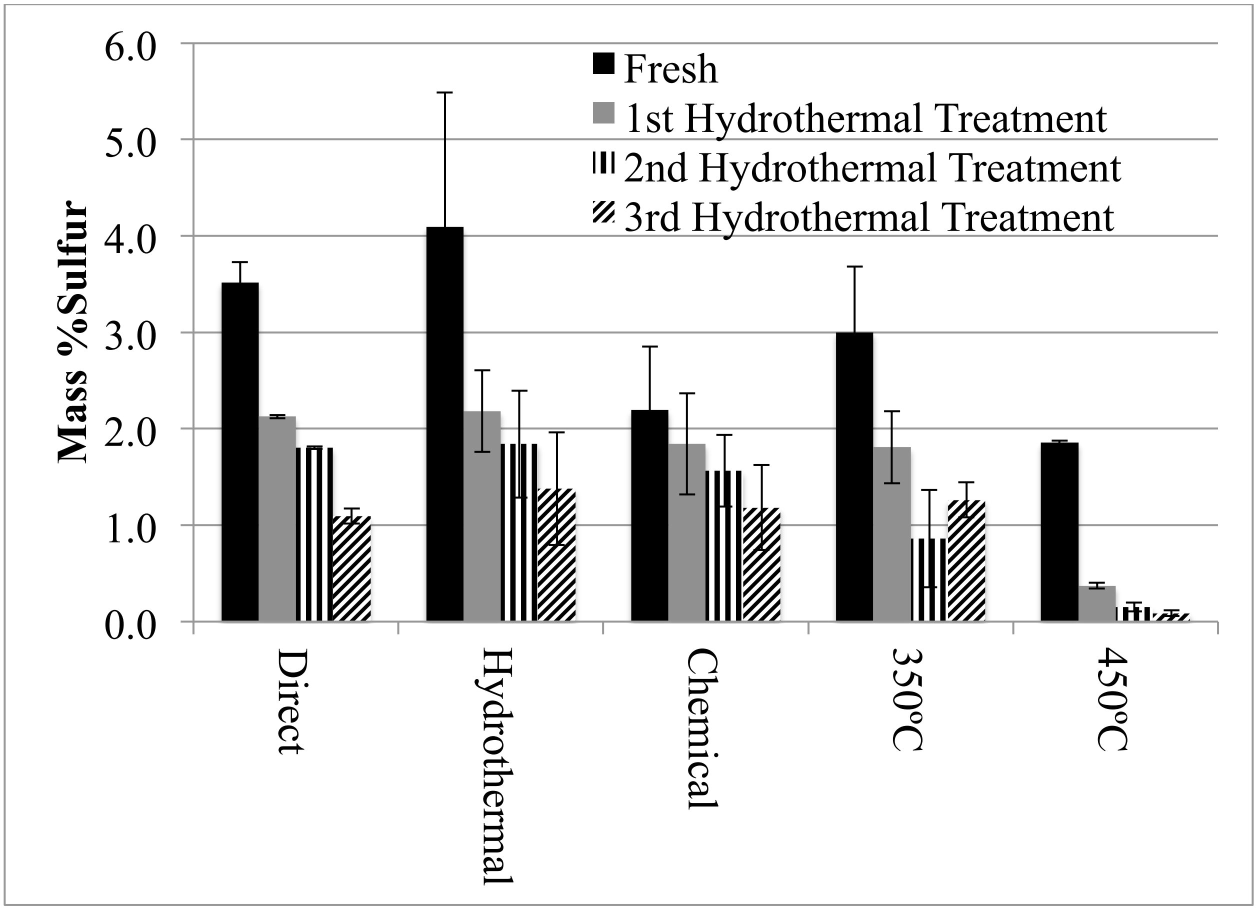

Figure 10. Sulfur elemental analysis of the sulfonated carbons throughout the hydrothermal testing. Hydrothermal testing was 160ºC in liquid water (autogenous pressure) for 24 hours.

Results for reaction testing of the sulfonated carbons are summarized in Figure 11. A preferred carbonization temperature, which has been a phenomenon reported in the literature,[23] was observed for the lower synthesis temperatures in this work as the 350°C, Hydro, and Direct (200°C and 150°C synthesis) materials had much better reaction rates than the 450°C or Chem samples. After hydrothermal treatment, however, even these catalysts did not retain significant activity nor did they plateau to a consistent value after three treatments. The Chem catalysts, while synthesized from the hydrothermally created carbon, did not share the same reaction rates as the Hydro catalysts even though the Chem catalysts retained sulfur reasonably well. In the supplemental information (Figure S3), the calculated turnover frequency based on the number of acid sites is shown. The trend for the materials was consistent with the overall reaction rates given in Figure 10. As can be seen from the data, the sulfonated carbons performed poorly after hydrothermal treatment, which further validated the poor stability of all these materials under aggressive hydrothermal conditions.

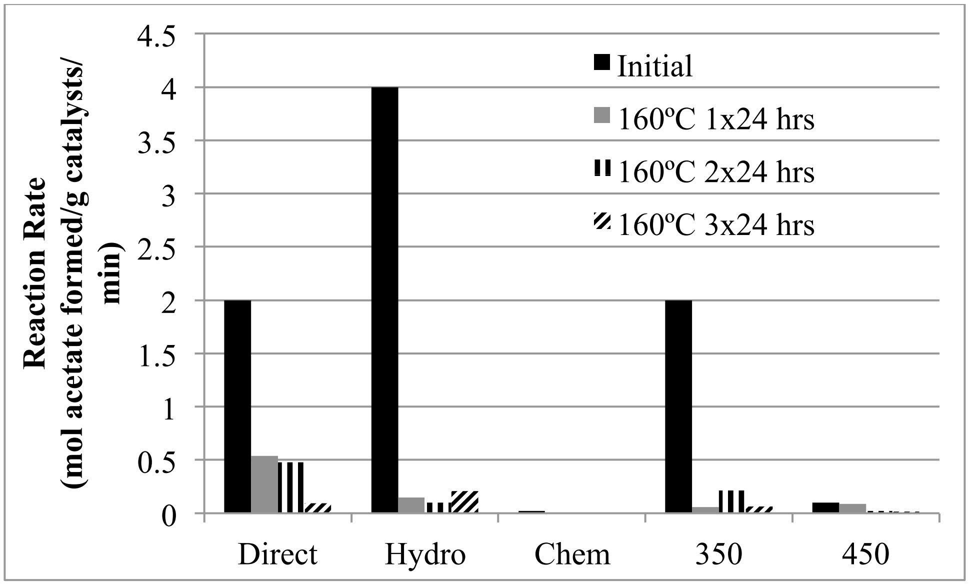

Figure 11. Reaction rate data throughout the hydrothermal treatments.

Conclusions

Several sulfonated carbon catalysts made from glucose, synthesized analogously to materials reported recently, were characterized by NMR and other techniques, and subjected to rigorous hydrothermal-stability testing. By analyzing a suite of different materials, we tested how their structure, characterized in detail by quantitative ^{13}C NMR with spectral simulations, affects the hydrothermal stability. In materials produced from ^{13}C enriched glucose, NMR was able to identify contributions from many different functional groups, quantify their proportions, and identify connections between these groups by means of spectrally edited 2D NMR experiments. Structures ranged from tightly linked individual furan and arene rings, to fused aromatic clusters of about 1 nm diameter. The rate of sulfur loss for the sulfonated carbons was considerable during the initial water exposure and then generally slowed with successive treatments, but it showed no sign of reaching a stable plateau. The lower temperature chars (Direct and Hydro), which have relatively high C=O and furan concentrations, retained a slightly higher percentage of sulfur than the higher temperature chars (350º and 450 ºC), suggesting that furan-carbon bonds to sulfur are slightly less susceptible to hydrolysis than are arene–sulfur bonds. Nevertheless, all the catalysts lost significant amounts of their sulfur (>90%), making their utilization ultimately problematic and suggesting that they are not industrially viable at or above 160°C. While the sulfur loss itself could be expected from the reversible reaction, its extent was not known before this study. Subsequent research is needed to determine if a different chemical attachment of the sulfonic acid groups can lead to a truly hydrothermally stable sulfonated carbon catalyst.

Acknowledgements

The authors would like to acknowledge NSF Award number EEC-0813570 for generously supporting this work. Purchase of the Perkin Elmer 2100 Series II CHN/S analyzer used to obtain results included in this publication was supported in part by the National Science Foundation under Grant No. DBI 9413969. We wish to thank ISU Chemical Instrumentation Facility staff members Stephen Veysey for training and assistance pertaining to the PE 2100 CHN/S elemental analysis. Keith Fritzsching developed the coding for transferring ACD NMR chemical shifts into MatLab. The authors would like to acknowledge undergraduates that worked on the project: Molly Lohry, Cherita Young, Ashley Leitner, and Scott Nauert. Jim Anderegg graciously ran and expertly helped interpret the XPS results. Any opinions, findings, and conclusions, or recommendations expressed herein are those of the authors and do not necessarily reflect the views of the National Science Foundation.

References

(1) Peng L, Philippaerts A, Ke X, Van Noyen J, De Clippel F, Van Tendeloo G, et al. Preparation of sulfonated ordered mesoporous carbon and its use for the esterification of fatty acids. Catalysis Today. 2010;150(1-2):140-6.

(2) Luque R, Budarin V, Clark JH, Macquarrie DJ. Microwave-assisted preparation of amides using a stable and reusable mesoporous carbonaceous solid acid. Green Chemistry. 2009;11(4):459-61.

(3) Luque R, Budarin V, Clark JH, Macquarrie DJ. Glycerol transformations on polysaccharide derived mesoporous materials. Applied Catalysis, B: Environmental. 2008;82(3-4):157-62.

(4) Kitano M, Yamaguchi D, Suganuma S, Nakajima K, Kato H, Hayashi S, et al. Adsorption-Enhanced Hydrolysis of β-1,4-Glucan on Graphene-Based Amorphous Carbon Bearing SO3H, COOH, and OH Groups. Langmuir. 2009;25(9):5068-75.

(5) Hara M. Biodiesel Production by Amorphous Carbon Bearing SO3H, COOH and Phenolic OH Groups, a Solid Bronsted Acid Catalyst. Topics in Catalysis. 2010;53(11-12):805-10.

(6) Luque R, Clark JH. Water-tolerant Ru-Starbon materials for the hydrogenation of organic acids in aqueous ethanol. Catalysis Communications. 2010;11(10):928-31.

(7) Xing R, Liu Y, Wang Y, Chen L, Wu H, Jiang Y, et al. Active solid acid catalysts prepared by sulfonation of carbonization-controlled mesoporous carbon materials. Microporous and Mesoporous Materials. 2007;105(1-2):41-8.

(8) Suganuma S, Nakajima K, Kitano M, Yamaguchi D, Kato H, Hayashi S, et al. Hydrolysis of cellulose by amorphous carbon bearing SO3H, COOH, and OH groups. Journal of the American Chemical Society. 2008;130(38):12787-93.

(9) Dutta S. Catalytic materials that improve selectivity of biomass conversions. RSC Advances. 2012;2(33):12575-93.

(10) Liang X, Yang J. Synthesis of a Novel Carbon Based Strong Acid Catalyst Through Hydrothermal Carbonization. Catalysis Letters. 2009;132(3-4):460-3.

(11) Kitano M, Arai K, Kodama A, Kousaka T, Nakajima K, Hayashi S, et al. Preparation of a Sulfonated Porous Carbon Catalyst with High Specific Surface Area. Catalysis Letters. 2009;131(1-2):242-9.

(12) Tian X, Su F, Zhao XS. Sulfonated polypyrrole nanospheres as a solid acid catalyst. Green Chemistry. 2008;10(9):951-6.

(13) Hara M, Yoshida T, Takagaki A, Takata T, Kondo JN, Hayashi S, et al. A Carbon Material as a Strong Protonic Acid. Angewandte Chemie International Edition. 2004;43(22):2955-8.

(14) Budarin VL, Clark JH, Luque R, Macquarrie DJ, Koutinas A, Webb C. Tunable mesoporous materials optimized for aqueous phase esterifications. Green Chemistry. 2007;9(9):992-5.

(15) Petrus L, Stamhuis EJ, Joosten GEH. Thermal deactivation of strong-acid ion-exchange resins in water. Industrial & Engineering Chemistry Product Research and Development. 1981;20(2):366-71.

(16) Zaiku Xie, Xie, Xie Z. An overview of recent development in composite catalysts from porous materials for various reactions and processes. International journal of molecular sciences. 2010;11(5):2152.

(17) Onda A, Ochi T, Yanagisawa K. Hydrolysis of Cellulose Selectively into Glucose Over Sulfonated Activated-Carbon Catalyst Under Hydrothermal Conditions. Top Catal. 2009;52(6-7):801-7.

(18) Mo X, Lotero E, Lu C, Liu Y, Goodwin JG. A Novel Sulfonated Carbon Composite Solid Acid Catalyst for Biodiesel Synthesis. Catalysis Letters. 2008;123(1-2):1-6.

(19) Mo X, Lopez DE, Suwannakarn K, Liu Y, Lotero E, Goodwin JG, Jr., et al. Activation and deactivation characteristics of sulfonated carbon catalysts. Journal of Catalysis. 2008;254(2):332-8.

(20) Yamaguchi D, Hara M. Starch saccharification by carbon-based solid acid catalyst. Solid State Sciences. 2010;12(6):1018-23.

(21) Shuit SH, Yee KF, Lee KT, Subhash B, Tan SH. Evolution towards the utilisation of functionalised carbon nanotubes as a new generation catalyst support in biodiesel production: an overview. RSC Advances. 2013;3(24):9070-94.

(22) Lou W-Y, Guo Q, Chen W-J, Zong M-H, Wu H, Smith TJ. A Highly Active Bagasse-Derived Solid Acid Catalyst with Properties Suitable for Production of Biodiesel. ChemSusChem. 2012;5(8):1533-41.

(23) Hara M, Okamura M, Toda M, Kondo JN, Takagaki A, Domen K, et al. Sulfonated incompletely carbonized glucose as strong Bronsted acid catalyst. Studies in Surface Science and Catalysis. 2007;172(Science and Technology in Catalysis 2006):405-8.

(24) Franklin RE. Homogeneous and heterogeneous graphitization of carbon. Nature (London, United Kingdom). 1956;177:239.

(25) Zhang B, Ren J, Liu X, Guo Y, Guo Y, Lu G, et al. Novel sulfonated carbonaceous materials from p-toluenesulfonic acid/glucose as a high-performance solid-acid catalyst. Catalysis Communications. 2010;11(7):629-32.

(26) Xiao H, Guo Y, Liang X, Qi C. One-step synthesis of novel biacidic carbon via hydrothermal carbonization. J Solid State Chem. 2010;183(7):1721-5.

(27) Boonoun P, Laosiripojana N, Muangnapoh C, Jongsomjit B, Panpranot J, Mekasuwandumrong O, et al. Application of Sulfonated Carbon-Based Catalyst for Reactive Extraction of 1,3-Propanediol from Model Fermentation Mixture. Ind Eng Chem Res. 2010;49(24):12352-7.

(28) Bahr JL, Yang J, Kosynkin DV, Bronikowski MJ, Smalley RE, Tour JM. Functionalization of Carbon Nanotubes by Electrochemical Reduction of Aryl Diazonium Salts: A Bucky Paper Electrode. Journal of the American Chemical Society. 2001;123(27):6536-42.

(29) Kang S, Ye J, Chang J. Recent advances in carbon-based sulfonated catalyst: preparation and application. Int Rev Chem Eng. 2013;5:133-44.

(30) Johnson RL, Anderson JM, Shanks BH, Fang X, Hong M, Schmidt-Rohr K. Spectrally edited 2D 13C13C NMR spectra without diagonal ridge for characterizing 13C-enriched low-temperature carbon materials. J Magn Reson. 2013;234:112-24.

(31) Miao S, Shanks BH. Esterification of biomass pyrolysis model acids over sulfonic acid-functionalized mesoporous silicas. Applied Catalysis A: General. 2009;359(1-2):113-20.

(32) Mirkhani V, Moghadam M, Tangestaninejad S, Mohammadpoor-Baltork I, Mahdavi M. Preparation of an improved sulfonated carbon-based solid acid as a novel, efficient, and reusable catalyst for chemoselective synthesis of 2-oxazolines and bis-oxazolines. Monatshefte fuer Chemie. 2009;140(12):1489-94.

(33) Suganuma S, Nakajima K, Kitano M, Yamaguchi D, Kato H, Hayashi S, et al. Synthesis and acid catalysis of cellulose-derived carbon-based solid acid. Solid State Sciences. 2010;12(6):1029-34.

(34) Mao JD, Schmidt-Rohr K. Accurate Quantification of Aromaticity and Nonprotonated Aromatic Carbon Fraction in Natural Organic Matter by 13C Solid-State Nuclear Magnetic Resonance. Environmental Science & Technology. 2004;38(9):2680-4.

(35) Brewer CE, Schmidt-Rohr K, Satrio JA, Brown RC. Characterization of biochar from fast pyrolysis and gasification systems. Environ Prog Sustainable Energy. 2009;28(3):386-96.

(36) Takegoshi K, Nakamura S, Terao T. C13-H1 dipolar-assisted rotational resonance in magic-angle spinning NMR. Chem Phys Lett. 2001;344:631-7.

(37) Hohwy M, Rienstra CM, Jaroniec CP, Griffin RG. Fivefold symmetric homonuclear dipolar recoupling in rotating solids: Application to double quantum spectroscopy. J Chem Phys. 1999;110:7983-92.

(38) http://www.chem.wisc.edu/areas/reich/handouts/nmr-c13/cdata.htm.

(39) ACD/Structure Elucidator, version 12.01, Advanced Chemistry Development, Inc., Toronto, ON, Canada, http://www.acdlabs.com, 2014.

(40) Demir-Cakan R, Baccile N, Antonietti M, Titirici M-M. Carboxylate-Rich Carbonaceous Materials via One-Step Hydrothermal Carbonization of Glucose in the Presence of Acrylic Acid. Chemistry of Materials. 2009;21(3):484-90.

(41) Sevilla M, Fuertes AB. The production of carbon materials by hydrothermal carbonization of cellulose. Carbon. 2009;47(9):2281-9.

(42) Torri C, Samorì C, Adamiano A, Fabbri D, Faraloni C, Torzillo G. Preliminary investigation on the production of fuels and bio-char from Chlamydomonas reinhardtii biomass residue after bio-hydrogen production. Bioresource Technology. 2011;102(18):8707-13.

(43) Takagaki A, Toda M, Okamura M, Kondo JN, Hayashi S, Domen K, et al. Esterification of higher fatty acids by a novel strong solid acid. Catalysis Today. 2006;116(2):157-61.

(44) Nakajima K, Okamura M, Kondo JN, Domen K, Tatsumi T, Hayashi S, et al. Amorphous Carbon Bearing Sulfonic Acid Groups in Mesoporous Silica as a Selective Catalyst. Chemistry of Materials. 2008;21(1):186-93.

(45) Yun S, Heo Y, Im H, Kim J. Sulfonated multiwalled carbon nanotube/sulfonated poly(ether sulfone) composite membrane with low methanol permeability for direct methanol fuel cells. Journal of Applied Polymer Science. 2012;126(S2):E513-E21.

(46) Knauer M, Schuster ME, Su D, Schlögl R, Niessner R, Ivleva NP. Soot Structure and

Reactivity Analysis by Raman Microspectroscopy, Temperature-Programmed Oxidation, and High-Resolution Transmission Electron Microscopy. The Journal of Physical Chemistry A. 2009;113(50):13871-80.

(47) Kang S, Ye J, Zhang Y, Chang J. Preparation of biomass hydrochar derived sulfonated catalysts and their catalytic effects for 5-hydroxymethylfurfural production. RSC Advances. 2013;3(20):7360-6.

(48) Levine IN. Molecular Spectroscopy: Wiley-Interscience; 1975.

(49) Shu Q, Gao J, Nawaz Z, Liao Y, Wang D, Wang J. Synthesis of biodiesel from waste vegetable oil with large amounts of free fatty acids using a carbon-based solid acid catalyst. Applied Energy. 2010;87(8):2589-96.

(50) Baccile N, Laurent G, Babonneau F, Fayon F, Titirici M-M, Antonietti M. Structural Characterization of Hydrothermal Carbon Spheres by Advanced Solid-State MAS 13C NMR Investigations. The Journal of Physical Chemistry C. 2009;113(22):9644-54.

(51) Burket CL, Rajagopalan R, Marencic AP, Dronvajjala K, Foley HC. Genesis of porosity in polyfurfuryl alcohol derived nanoporous carbon. Carbon. 2006;44(14):2957-63.

(52) Ewing DF. Carbon-13 substituent effects in monosubstituted benzenes. Org Magn Reson. 1979;12(9):499-524.

(53) Okamura M, Takagaki A, Toda M, Kondo JN, Domen K, Tatsumi T, et al. Acid-Catalyzed Reactions on Flexible Polycyclic Aromatic Carbon in Amorphous Carbon. Chemistry of Materials. 2006;18(13):3039-45.

(54) Nakamizo M, Kammereck R, Walker Jr PL. Laser raman studies on carbons. Carbon. 1974;12(3):259-67.

(55) Wang Y, Alsmeyer DC, McCreery RL. Raman spectroscopy of carbon materials: structural basis of observed spectra. Chemistry of Materials. 1990;2(5):557-63.

(56) Clark JH, Budarin V, Dugmore T, Luque R, Macquarrie DJ, Strelko V. Catalytic performance of carbonaceous materials in the esterification of succinic acid. Catalysis Communications. 2008;9(8):1709-14.

Supporting Information

SOLID STATE NMR STUDY OF CHEMICAL STRUCTURE AND HYDROTHERMAL DEACTIVATION OF MODERATE-TEMPERATURE CARBON MATERIALS WITH ACIDIC SO_3H SITES

Jason M. Anderson, Robert L. Johnson, Klaus Schmidt-Rohr, and Brent H. Shanks*

Table S1. Initial surface area of the catalyst

Sample Name	Surface Area (m^2/g)
Direct	0.21
Hydro	1.55
Chemical	0.32
350ºC	0.15
450ºC	0.11

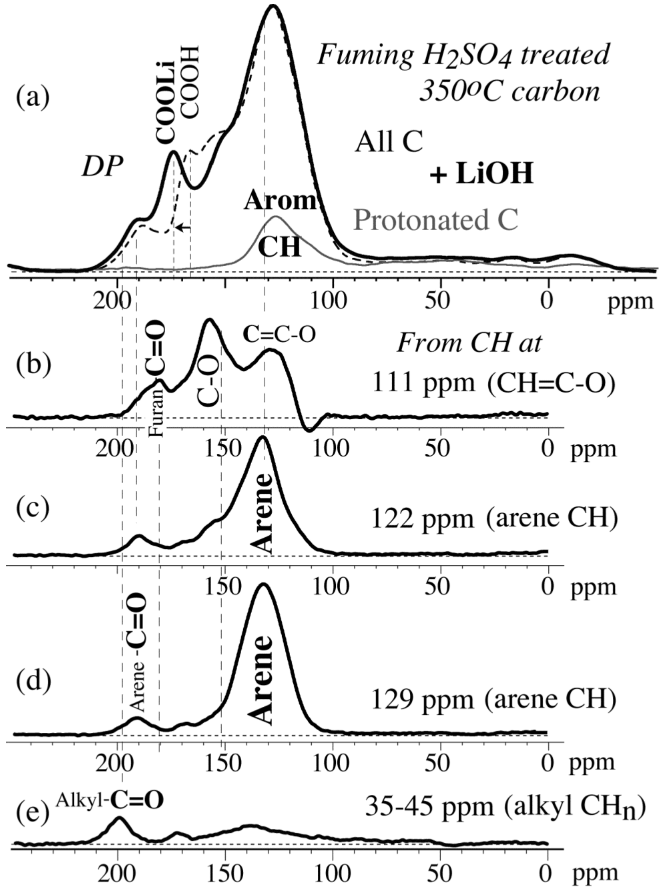

Figure S1. Selective ^{13}C NMR spectra of the ^{13}C-enriched sulfonated 350°C sample. (a) Full quantitative spectrum (dashed line, for reference) with corresponding selective quantitative spectrum of protonated C (gray line), obtained by dipolar-dephasing difference, and (full line) spectrum after treatment of the material with LiOH; the signal of COOLi groups is shifted by +7 ppm from that of COOH and is thus better resolved. “ssb”: spinning side band. (b-e) Horizontal cross section from a 2D ^{13}C-^{13}C EXPANSE spectrum, with signals of (b) aromatic C-O bonded to aromatic CH and C=O bonded to a furan ring; (c, d) nonprotonated arene C bonded to arene CH; a peak of C=O bonded to an arene ring is also detected; and (e) C=O and other sp^2-hybridized C bonded to alkyl C. Most of the slices from the EXPANSE spectrum have previously been shown in our paper on the EXPANSE technique [25] and are reproduced here for the convenience of the reader.

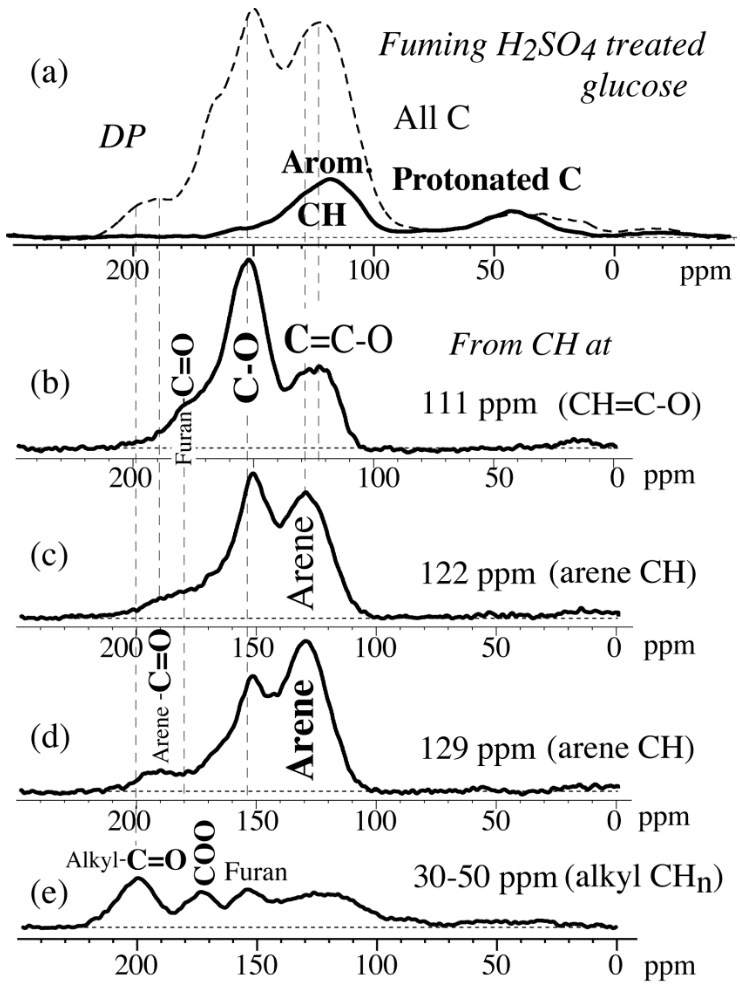

Figure S2. Selective ^{13}C NMR spectra of the ^{13}C-enriched Direct sample. (a) Full quantitative spectrum (dashed line, for reference) with corresponding selective quantitative spectrum of protonated C (gray line), obtained by dipolar-dephasing difference. "ssb": spinning side band. (b-e) Horizontal cross section from a 2D ^{13}C-^{13}C EXPANSE spectrum, with signals of (b) aromatic C-O bonded to aromatic CH and C=O bonded to a furan ring; (c, d) nonprotonated arene C bonded to arene CH; a peak of C=O bonded to an arene ring is also detected; and (e) C=O and other sp^2-hybridized C bonded to alkyl C. Most of the slices from the EXPANSE spectrum have previously been shown in our paper on the EXPANSE technique [25] and are reproduced here for the convenience of the reader.

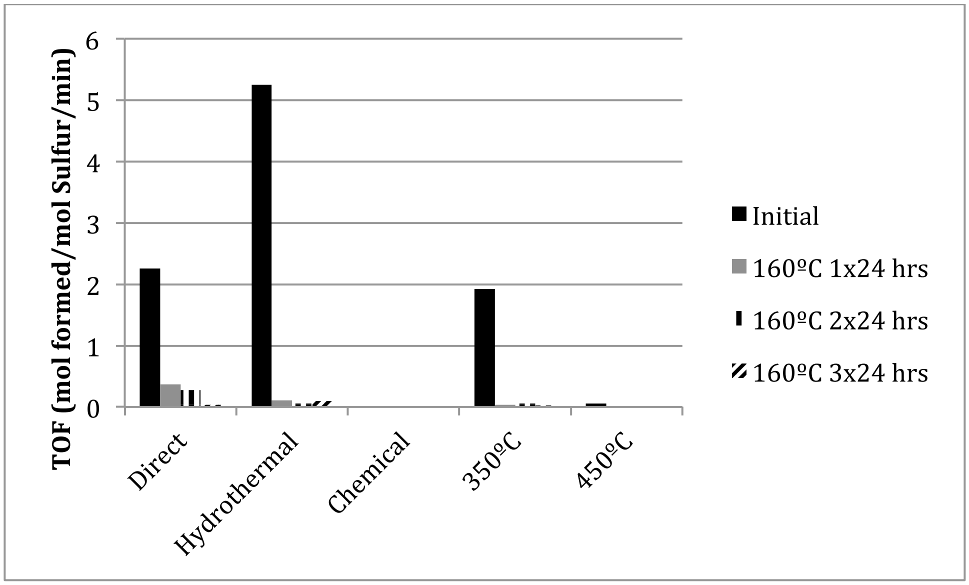

Figure S3. Turnover Frequency data in mols formed/mol sulfur/min. The turnover frequency values were consistent with the overall reaction rate data. These TOF's were calculated based on the number of acid sites as determined by ttitration.

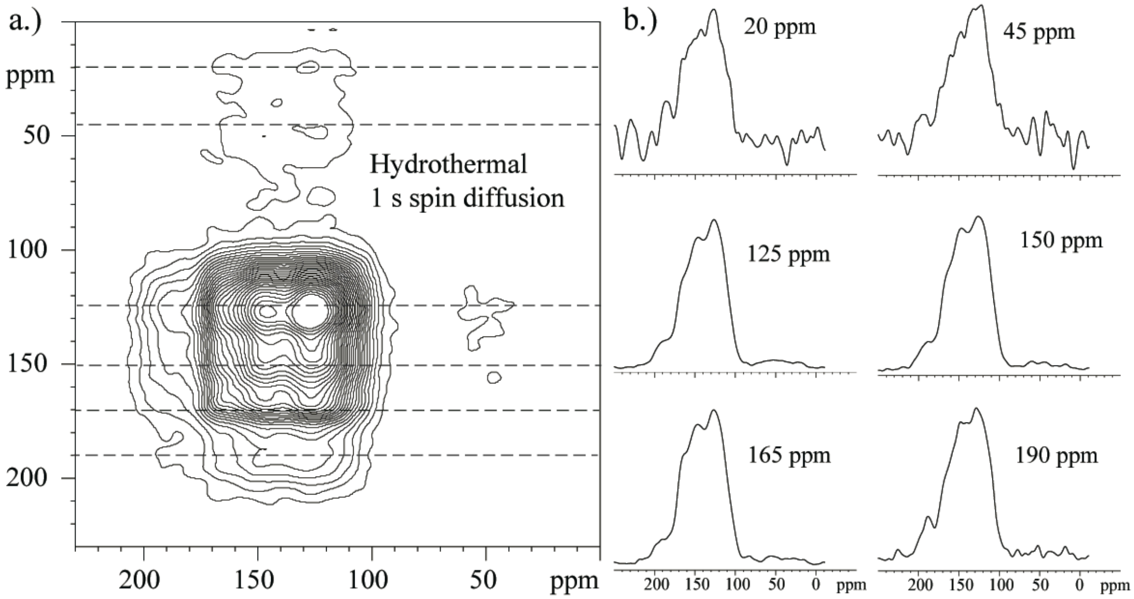

Figure S4. ^{13}C-^{13}C 2D exchange spectrum a) and horizontal cross sections b) with long exchange period (1 s). We see the cross-sections all have the same general shape, meaning that they the spin exchange is homogeneous on the 10's of nm scale. Without domain seperation with U13C enriched materials ^{13}C-^{13}C dipolar coupling, and spin diffusion are strong and will drive T_1 equilibration to an average value for all chemical environments.

450 °C

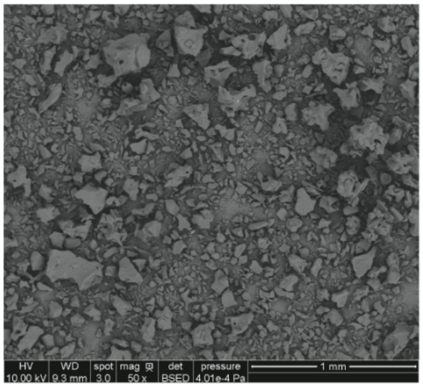
HV 10.00 kV
WD 9.3 mm
spot 3.0
mag 50 x
det BSED
pressure 4.01e-4 Pa
1 mm

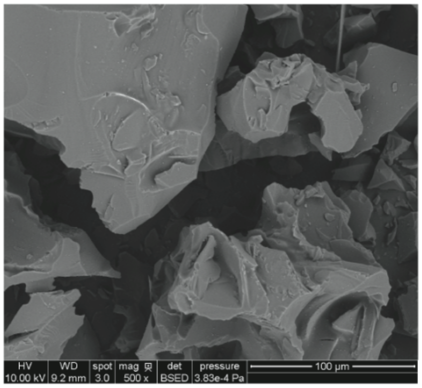
HV 10.00 kV
WD 9.2 mm
spot 3.0
mag 500 x
det BSED
pressure 3.83e-4 Pa
100 µm

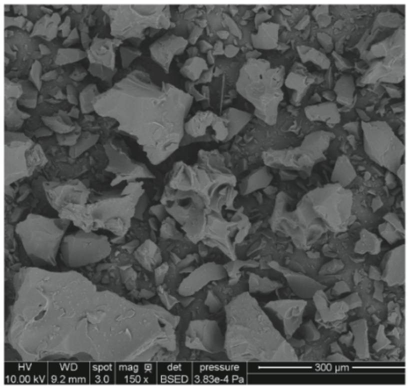
HV 10.00 kV
WD 9.2 mm
spot 3.0
mag 150 x
det BSED
pressure 3.83e-4 Pa
300 µm

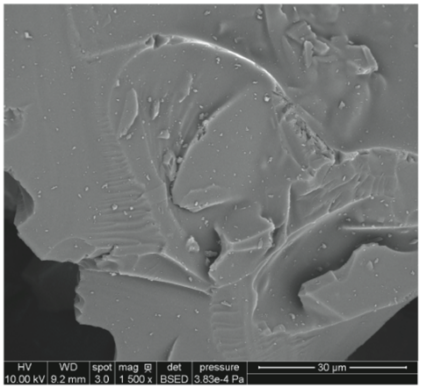
HV 10.00 kV
WD 9.2 mm
spot 3.0
mag 1 500 x
det BSED
pressure 3.83e-4 Pa
30 µm

Direct

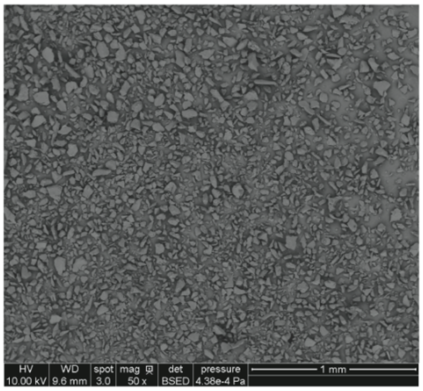
HV 10.00 kV
WD 9.6 mm
spot 3.0
mag 50 x
det BSED
pressure 4.38e-4 Pa
1 mm

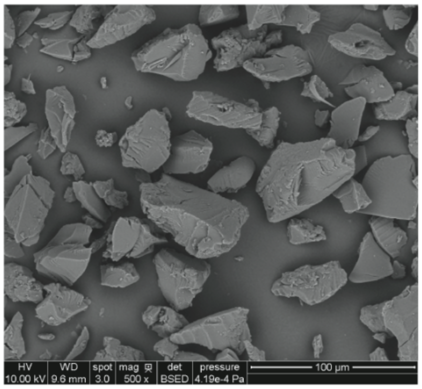
HV 10.00 kV
WD 9.6 mm
spot 3.0
mag 500 x
det BSED
pressure 4.19e-4 Pa
100 µm

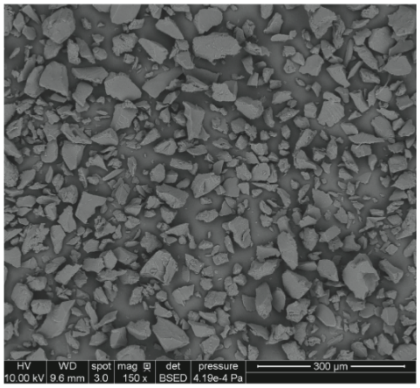
HV 10.00 kV
WD 9.6 mm
spot 3.0
mag 150 x
det BSED
pressure 4.19e-4 Pa
300 µm

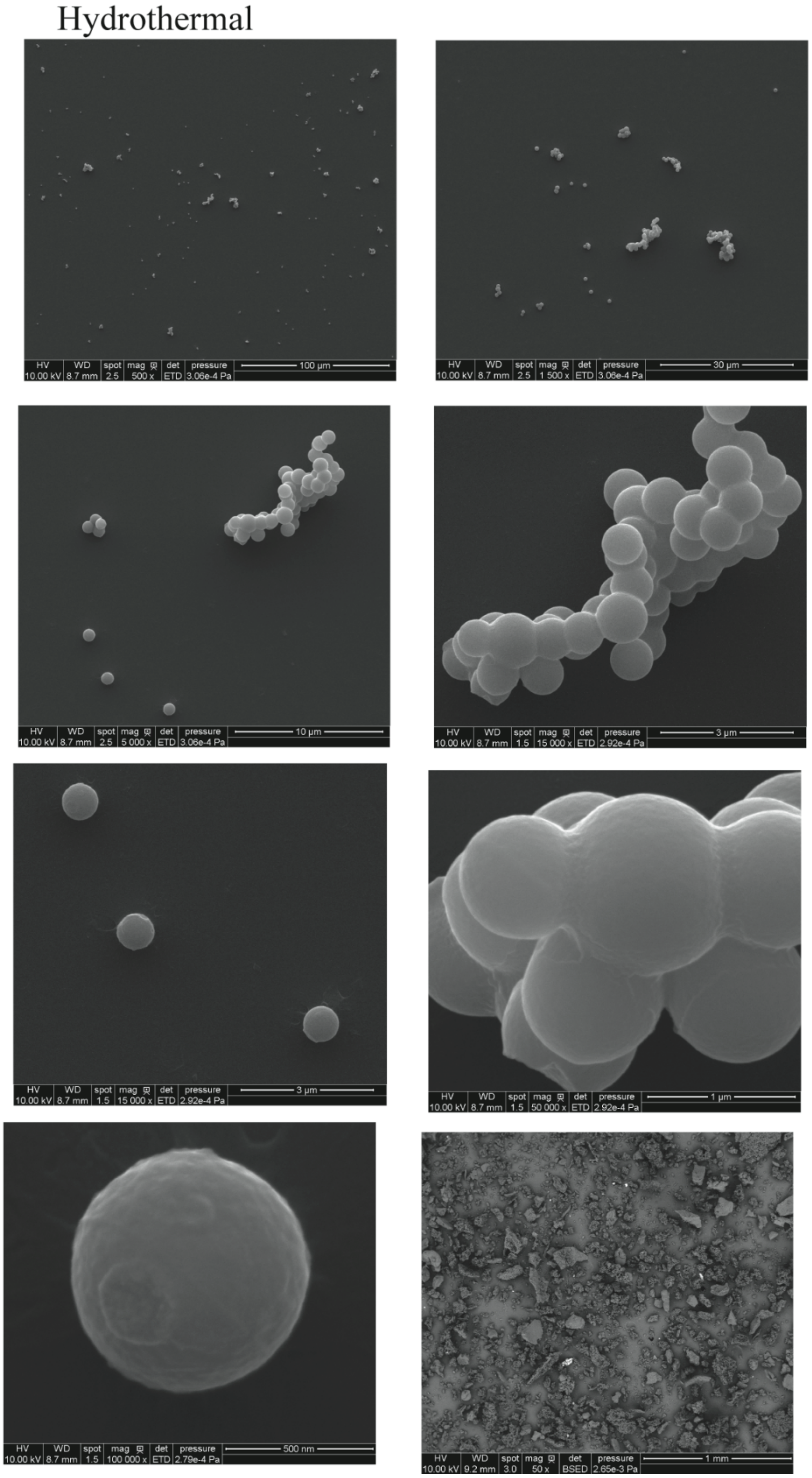

Figure S5: SEM images of the 450°C, Direct and Hydrothermal carbons.

a.)

S2p

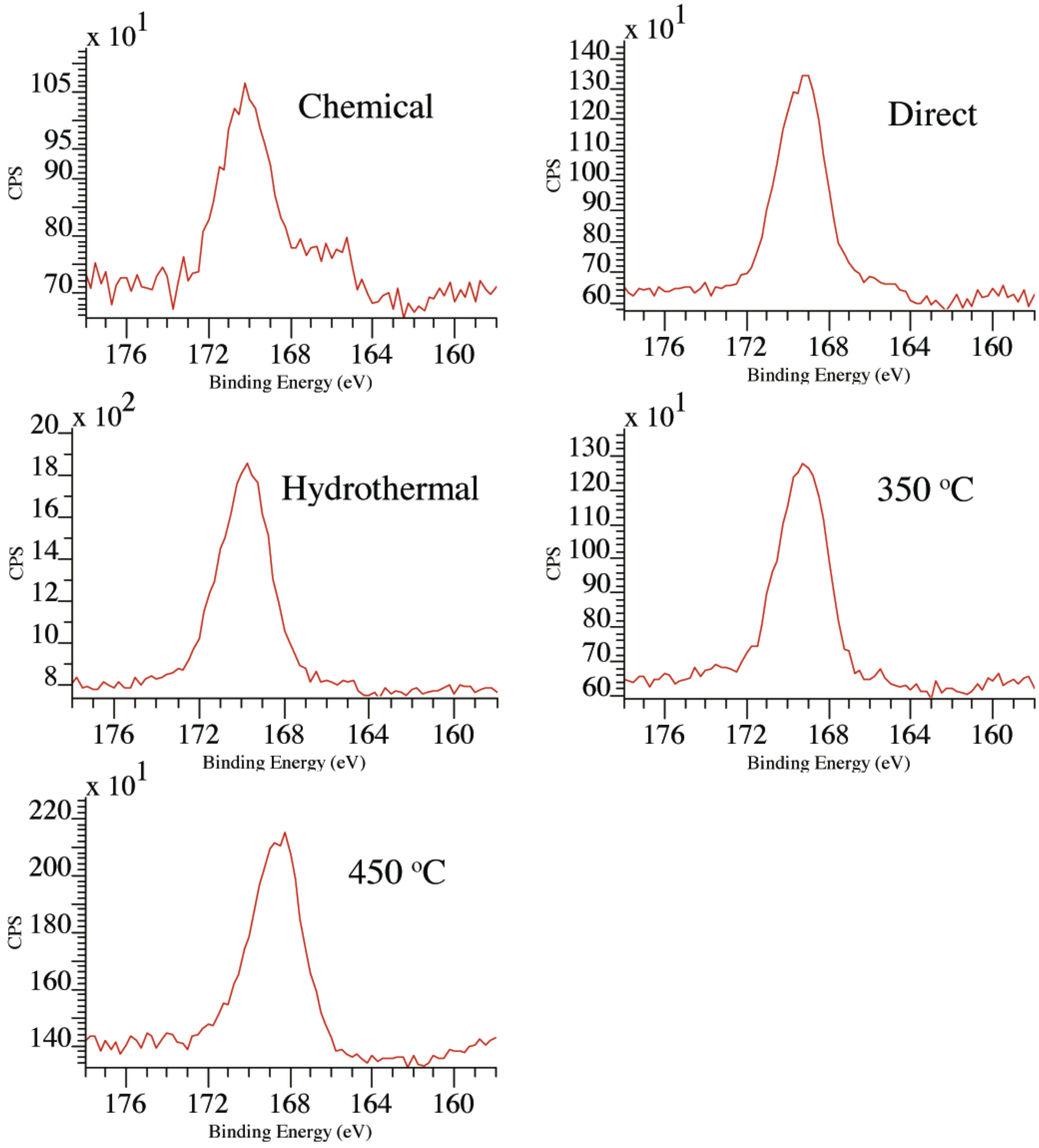
x 10^1
105
95
90
80
70
CPS
Chemical
176
172
168
164
160
Binding Energy (eV)
x 10^1
140
130
120
110
100
90
80
70
60
CPS
Direct
176
172
168
164
160
Binding Energy (eV)
x 10^2
20
18
16
14
12
10
8
CPS
Hydrothermal
176
172
168
164
160
Binding Energy (eV)
x 10^1
130
120
110
100
90
80
70
60
CPS
350 °C
176
172
168
164
160
Binding Energy (eV)
x 10^1
220
200
180
160
140
CPS
450 °C
176
172
168
164
160
Binding Energy (eV)

b)

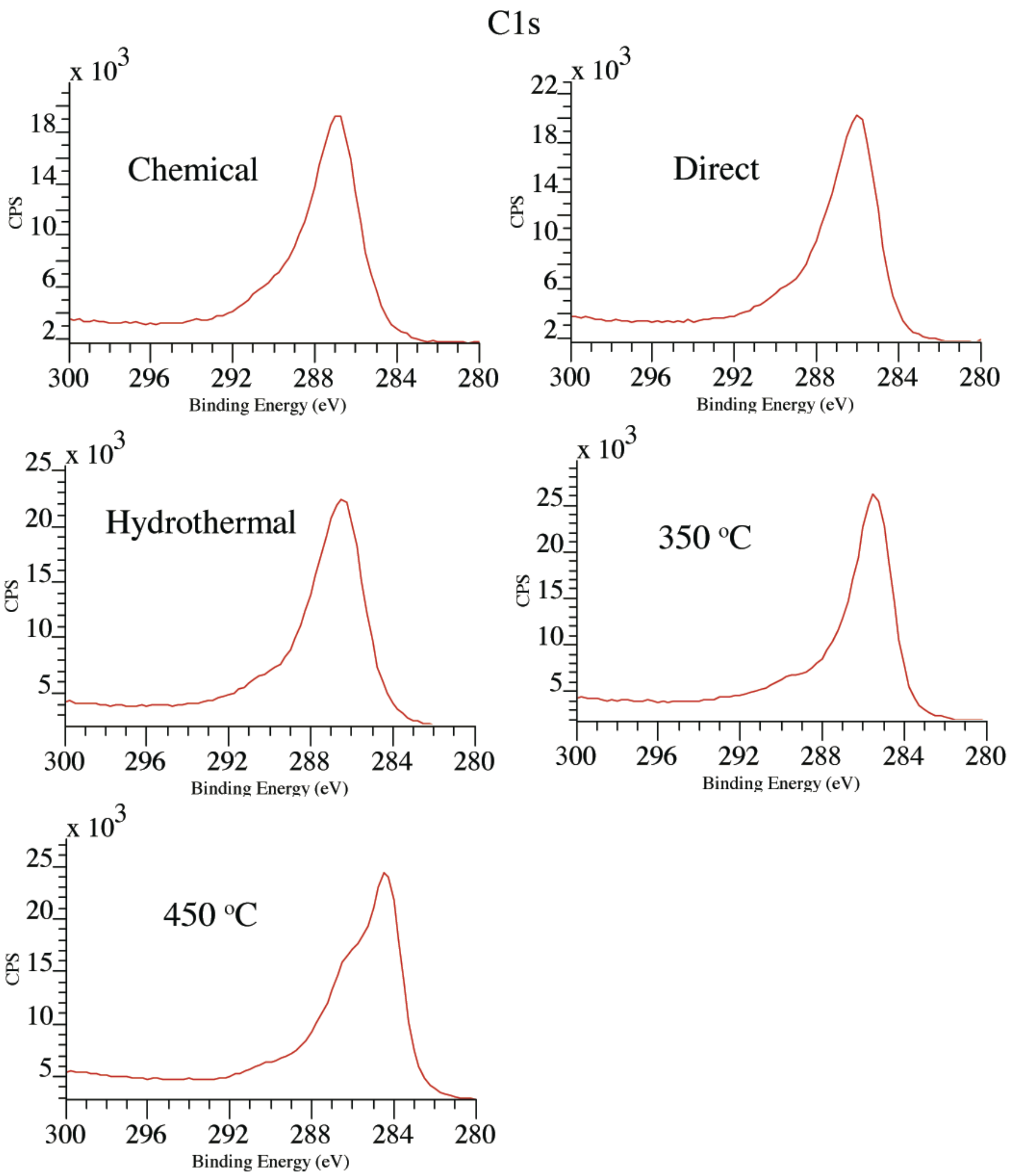
C1s
x 10^3
CPS
Chemical
18
14
10
6
2
300
296
292
288
284
280
Binding Energy (eV)
x 10^3
CPS
Direct
22
18
14
10
6
2
300
296
292
288
284
280
Binding Energy (eV)
x 10^3
CPS
Hydrothermal
25
20
15
10
5
300
296
292
288
284
280
Binding Energy (eV)
x 10^3
CPS
350 °C
25
20
15
10
5
300
296
292
288
284
280
Binding Energy (eV)
x 10^3
CPS
450 °C
25
20
15
10
5
300
296
292
288
284
280
Binding Energy (eV)

c)

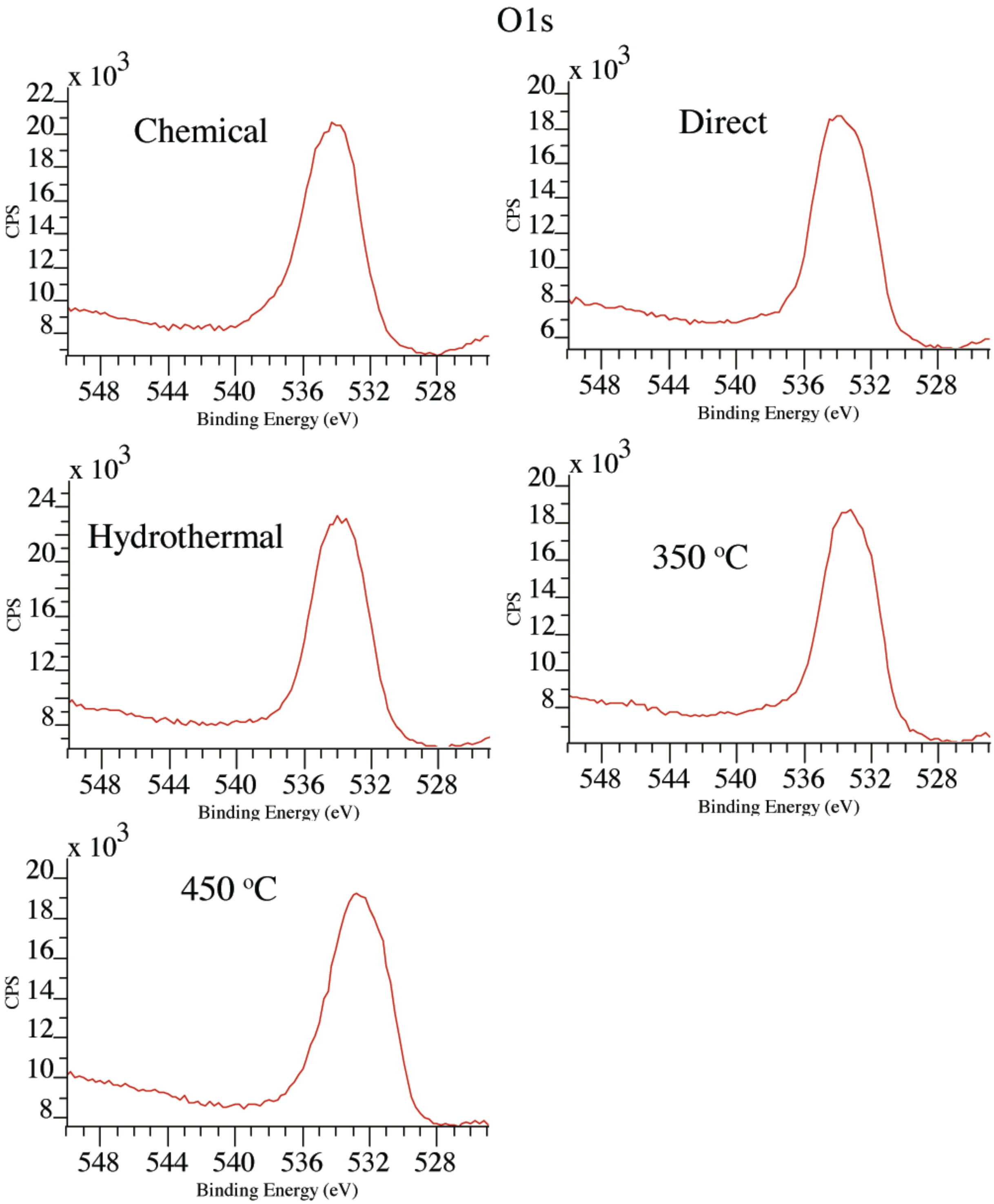

Figure S6: XPS spectra for the sulfonated carbons; a) S2p, b) C1s, and c) O1s.

APPENDIX C. HYDROTHERMAL DEGRADATION OF MODEL SULFONIC ACID COMPOUNDS: PROBING THE RELATIVE SULFUR–CARBON BOND STRENGTH IN WATER.

Catalysis Communications, **51,** pp 33-36, 2014

Jason M Anderson[1], Robert L Johnson[2], Klaus Schmidt-Rohr[2], Brent H Shanks[1]*

[1]Chemical and Biological Engineering Department, Iowa State University Ames, IA 50011 USA
[2]Department of Chemistry Iowa State University, Ames, IA 50011 USA
[*] Corresponding Author E-mail: bshanks@iastate.edu

Keywords: Sulfonated carbon, hydrothermal stability, NMR characterization

Abstract

Development of heterogeneous catalysts for the biorenewables industry requires hydrothermal degradation resistance. However, the relationship between hydrothermal stability and the immediate electronic hybridization of the carbon atoms adjacent to the sulfonic acid active group is not fully known. We systematically tested model compounds containing sulfonic acid groups linked to aromatic, alkane, or cycloalkane carbon atoms. We subjected them to hydrothermal conditions. The compounds' structural integrity was monitored with solution NMR. The aromatic-sulfonic acid compounds degraded readily, while the hydrolysis of the alkyl sulfonic acid linkages was negligible. Therefore, hydrothermally stable sulfonic-acid catalysts need sulfonic acid attached via alkyl linkers.

Introduction

Development of heterogeneous catalysts for transforming carbohydrate and other biomass-derived feedstocks into higher-value chemicals will require catalyst materials that are stable in the condensed phase. Carbohydrates are quite reactive or non-volatile relative to hydrocarbons, and even when catalysts can be used in gas phase reactors results the resulting conversions can have poor selectivity and rapid coke formation [1, 2]. Even more challenging are aqueous-phase reactions since water under hydrothermal conditions (typically pressurized at 120-250°C) [3, 4] is physically destructive to a large number of materials, including silica, metal oxides such as gamma alumina, zeolites and numerous functionalized polymers [5-7]. Metal oxides are by far the most widely used support materials in the petroleum industry, while carbon and polymer resins have found only limited applications. Carbon is quite resistant to hydrothermal breakdown and shows promise to be a viable support material and catalyst for hydrothermal reactions. It can also be produced at relatively low cost from a wide variety of feedstocks including lignocellulosic materials and carbohydrates.

The use of solid carbon-based acid catalysts with sulfonic acid functionality is a promising approach to replace sulfuric acid used in numerous applications including cellulose hydrolysis, sugar dehydration, and transesterification of biodiesel. These materials can be produced in a simple two-step process using glucose or carbohydrate pyrolysis at temperatures ranging from 350-550°C followed by sulfonation [8, 9] with fuming sulfuric acid or sulfur trioxide. Electrophilic aromatic substitution has been the predominant mechanism forming the $C\text{-}SO_3$ bond and these treatments result in nearly complete removal of alkyl carbons, and minor additional polycondensation [10]. Sulfonated carbon materials produced using this method have sulfonic-acid groups linked to aromatic carbons and are highly acidic due to the electronegativity of the aromatic system [10]. While these materials have been demonstrated to have excellent activity, their hydrothermal stability is less certain. In recent studies, a spectrum of carbon materials, produced at a range of temperatures, were sulfonated, and tested for hydrothermal stability [10, 11]. All readily lost activity through hydrolysis and leaching of sulfur, which clearly indicated that these materials are not sufficiently stable for long term use in a reaction system. Given the difficulty of characterizing the location of sulfur in the chemical structures that were synthesized, it was not possible to draw conclusions about the effects of the local structure on sulfonate stability, including the influence of adjacent groups and carbon hybridization, and temperature at which degradation occurred [11, 12]. The literature suggests that bonding of S to aliphatic C would be more stable [13], but a systematic comparison of hydrothermal stability has not been published. The current work sought to investigate these effects by using model compounds that simulate various bonding environments that could exist on a carbon surface.

The molecule types chosen for stability analysis included sulfonic acid groups bonded to aromatic, saturated cyclic, and straight chain aliphatic structures. It has been proposed in the literature that an increase in electron-withdrawing functional groups near an aromatic-bound sulfonic acid would lead to increased stability of the carbon–sulfur bond [14]. To test this hypothesis, we compared trimethylbenzene sulfonic acid, trinitrosulfonic acid, and benzenesulfonic acid, which represent electron donation, withdrawal, and the control case, respectively. To compare alicyclic versus aromatic rings, cyclohexane and benzene sulfonic acid were included in the study. Linear aliphatic compounds were also investigated. The chain length dependence, important for silica attachments [15, 16], was explored with butane sulfonic acid and octane sulfonic acid. The study of the degradation behavior of all these sulfonic acids enabled us to make specific comparisons about stability of the carbon-sulfur bond and its dependence on its immediate chemical environment.

Experimental

Materials

The trimethylbenzene sulfonic acid, trinitrosulfonic acid, benzenesulfonic acid, cyclohexane sulfonic acid, sodium butane sulfonate, sodium octane sulfonate, and deuterium oxide were purchased from Sigma Aldrich. Hydrochloric acid was purchased from Fisher Scientific. All chemicals were used without further purification. The starting compounds were acidified if they were in the salt form by adding an equivalent molar amount of HCl to the salt.

Each sulfonic acid was placed into a Parr reactor at 160ºC at a 100 mmol/g concentration in D_2O for initial hydrothermal treatment and it also was used to verify safety of the chemical (some compounds created significant pressures when heated). The trinitrobenezensulfonic acid caused the greatest safety concerns as it needed to be vented during the hydrothermal testing to ensure safe operating conditions. If the compound did not generate pressure, it was subsequently placed in Altech glass vials for testing at 130ºC and 100ºC. In this way, all the compounds were tested at the three different temperatures. Samples were taken at time points of 0 (when the Parr reactor reached the desired temperature, ramp rate of 10ºC/min), 1, 6, 12, 18, and 24 hours. Solution NMR was used for species identification.

Since the sulfonic acids with a benzene backbone generated a solid via carbonization, elemental analysis was done on both the liquid filtrate and the solid to determine the amount of sulfur in each. To prevent the solids from interfering with solution NMR, the resulting sample was filtered with a 0.2 μm filter before analysis. The filtrate and solids were analyzed via elemental analysis, ICP-AES, and XPS to determine the amount and oxidation number of sulfur left in each phase.

Characterization

^{1}H and ^{13}C solution NMR spectroscopy was used to monitor the structures of the various sulfonic acids resulting from hydrothermal treatment, using a Bruker Biospin spectrometer with a 14.1 T magnet and TopSpin processing software. For both ^{1}H and ^{13}C, spectra were acquired with excitation pulses of 30^o flip angle (with durations of 3.3 and 4 μs, respectively) to reduce the time required for relaxation between scans. Proton spectra were acquired at 600 MHz with 16 scans and a 1-s recycle delay. Carbon spectra were acquired at 150 MHz with a power gated decoupling scheme during acquisition (WALTZ16), 1024 scans, and a 2-second recycle delay. The compound stability was evident from the loss or retention of signals after subsequent hydrothermal treatments.

The chemical state of sulfur in the remaining solids was analyzed using a Physical Electronics 550 Multitechnique XPS system employing a standard Al electron source. The samples were run at 10^{-9} Torr and mounted on double-sided tape. Charging was corrected by adjusting the carbon peak to 284 eV. The solids underwent elemental analysis for carbon, hydrogen, nitrogen, and sulfur (CHNS) using a PE 2100 Series II combustion analyzer (Perkin Elmer Inc., Waltham, MA). Atomic emission spectra were obtained using an ICP-

AES Spectro CCD. Argon was used as a monitor line and 1 ppm scandium for reference line (internal standard).

Results and Discussion

Hydrolysis and NMR characterization.

The ^{13}C NMR of the materials, see Fig. 1, showed that sulfonated aliphatic molecules remained intact in the solution phase to a far greater extent than sulfonated aromatic rings (Fig. 1 d-f). The most unstable molecules were the substituted aromatics. Both the tri-nitro (electron-withdrawing), and trimethyl (electron-donating) sulfonated benzene had lost signal at the mild 130ºC condition, and formed a solid precipitate (not visible in solution NMR) (Fig. 1 a,b). Benzenesulfonic acid was the most stable of the aromatic molecules, but did form a solid after 24 h at 160°C (Fig. 1 c). It was surprising that no significant degradation was observed prior to 18 h, given that the literature has described facile desulfonation of aromatic sulfonic acids [17, 18]. The data showed that substitution of the aromatic systems only served to weaken the carbon sulfur linkage. The stability of the model compounds decreased from aliphatic to unsubstituted aromatic to substituted aromatic compounds.

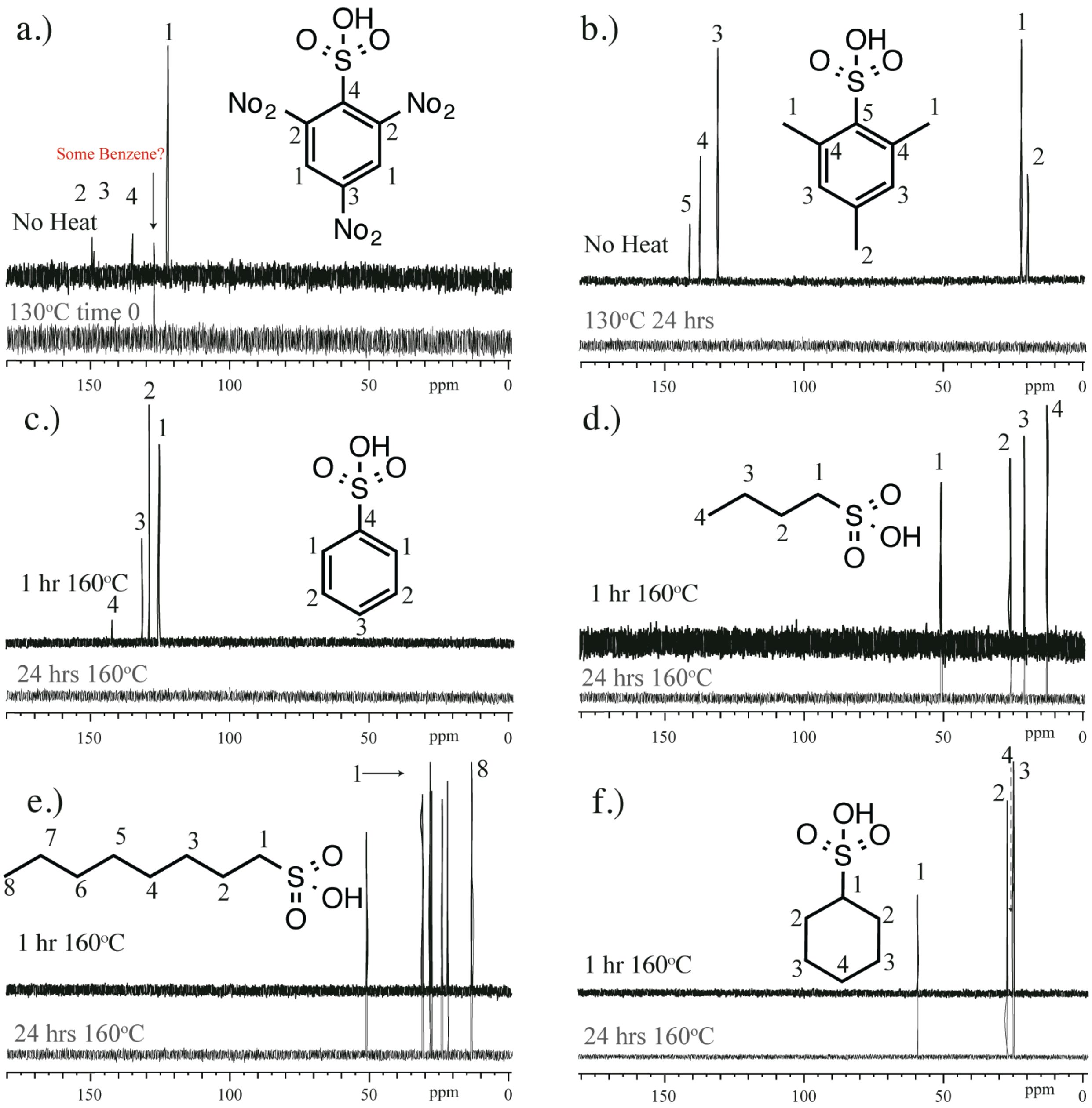

Figure 1. Solution ^{13}C NMR spectra of (a-c) aromatic sulfonic acid compounds and alkyl sulfonic acid molecules (d-f). The black spectrum (top) is from the un-transformed molecule and the red (bottom) is the spectrum showing breakdown at the mildest condition (if any).

Chemical transformations of the sulfonic-acid groups.

The loss of ^{13}C NMR signal from the aromatic sulfonic acids during hydrothermal treatment was accompanied by formation of a solid precipitate. Since solution NMR was not able to characterize this solid material, it was unclear if the condensation process involved the cleavage of the carbon–sulfur bond. To probe the fate of sulfur, the resulting solid and filtrate was analyzed using elemental analysis, XPS, and ICP-AES.

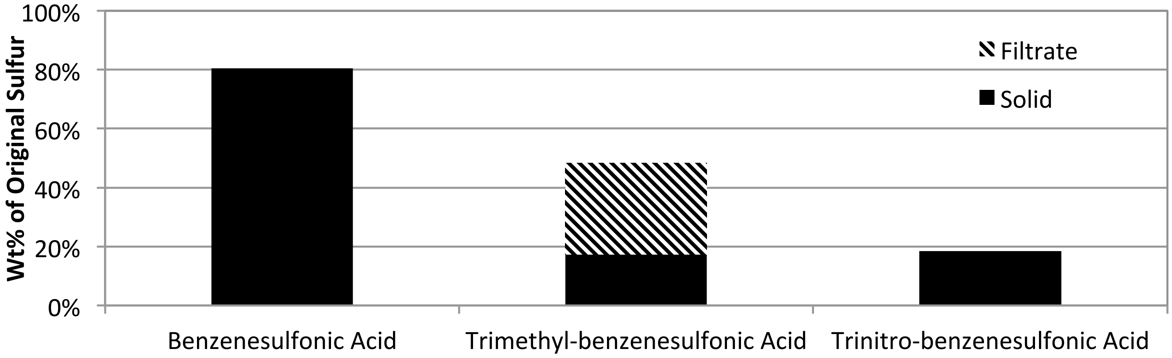

Figure 2. Mass balance, from elemental analysis, after 24-hour hydrothermal treatment for the aromatic sulfonic acids (benzenesulfonic acid, trimethylsulfonic acid, and trinitrosulfonic acid), relative to the initial sulfur content. These materials tended to carbonize and separate into a solid and liquid phase. The two phases were dried and analyzed via CHNS.

Figure 2 shows the sulfur weight fractions, determined by elemental analysis, after hydrothermal treatment for 24 h, in both the solution phase and the solid precipitate formed. In all cases, the total sulfur balance never reached 100%, so it was presumed that the missing sulfur went into the gas phase. The solid phase from the unsubstituted benzenesulfonic acid preserved the most sulfur (80%), whereas the trinitrobenzenesulfonic acid and the trimethylbenzenesulfonic acid has the least (18% each) sulfur retained in the solid. This confirmed that the relative strength of the carbon–sulfur bond for the unsubstituted benzene ring was greater than for the substituted rings. In addition, since the mass balance was not 100% and some was detected in the liquid phase, it was a good indication that cleavage of the carbon sulfur bond occurred to a certain extent for all the aromatic molecules examined.

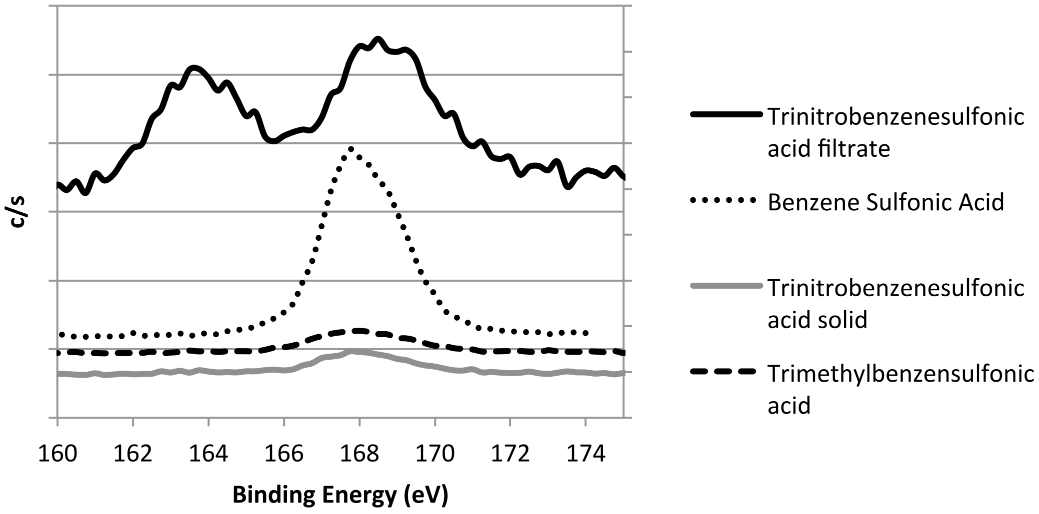

Figure 3. Sulfur XPS data of the solids recovered after filtration and the dissolved material in the dried filtrate. The other samples recovered from drying the respective filtrates were qualitatively the same.

The recovered precipitated solids were also subjected to XPS analysis, to give an indication about what happened to the sulfur as a result of the hydrothermal treatment. The qualitative XPS data of the solids recovered from the aromatics showed they all retained the expected S2p peak at 168 eV (see Figure 3) corresponding to sulfonic acid. Interestingly, the S2p peak from the dried filtrate of the trimethylbenzenesulfonic acid after 24 hours at 160°C was split into two peaks (see Figure 3), one around 168 and another at 164 eV, indicating the presence of both sulfonic acid [19, 20] and a reduced sulfur form, respectively. The latter was possibly a thiophene or a similar molecule containing organic sulfur [13]. Since XPS is qualitative, it was not possible to determine relative amounts of the sulfur species present. Regardless of the specific molecular form, the sulfur peak shift dictated that some of the initial surrounding oxygen atoms bonded to the sulfur atom must have been lost. This would subsequently reduce the acidity on any attached proton(s). In other words, the hydrothermal treatment not only removed sulfur from the trimethylbenzenesulfonic acid, but transformed some of the sulfur into a form that would be catalytically inactive. Since this occurred in the liquid phase, it suggested that carbon-sulfur bond breakage occurred. These results further supported our finding that aromatic sulfonic acids, in particular the substituted ones, were unable to fully retain their sulfur during a single 24 h hydrothermal treatment. Especially when compared to their alkyl counterparts, the aromatic sulfonic acids were significantly less hydrothermally stable (see Figure 4).

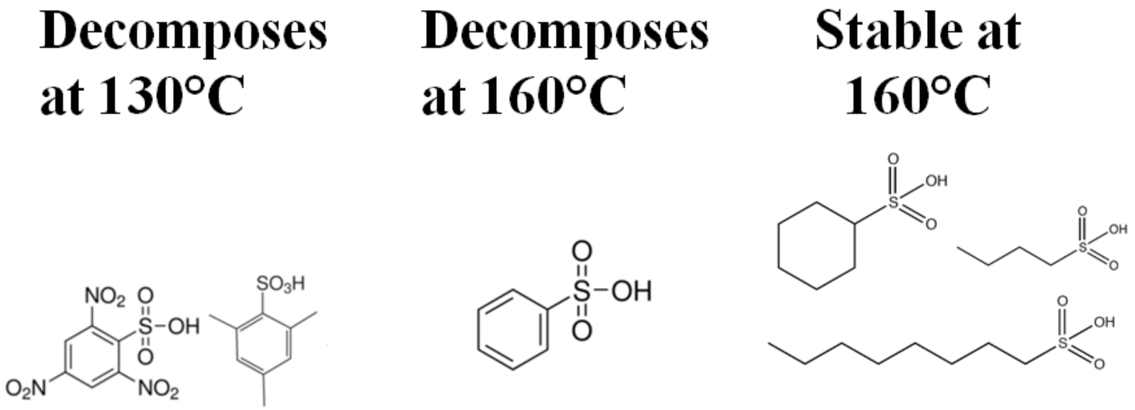

Figure 4. Summary of the results with the least stable sulfonic-acid model compounds on the left and the most stable ones on the right.

Conclusions

Six sulfonic-acid model compounds were tested for hydrothermal stability and characterized by solution NMR, ICP-AES, XPS, and elemental analysis to determine their hydrothermal stability over 24 h exposure to condensed water. The aromatic compounds tended to carbonize and form an insoluble solid, which were subsequently analyzed by CHNS elemental analysis, XPS of the solid, and ICP-AES of the dried liquid filtrate to determine the fate of the sulfur. The least stable compounds were the trisubstituted benzenesulfonic acids, which condensed into insoluble materials even when treated at mild temperature (130°C). The solids from these materials retained only about 18% of the original sulfur. The benzenesulfonic acid remained intact as detected via NMR until about 16 h but degraded after 24 h at 160°C. When the benzensulfonic acid degraded, only about 80% of the sulfur could be accounted for. The alkanes and the saturated cyclic compounds did not degrade even after 24 h at 160° C. From this, the relative carbon-sulfur bond strength in the hydrothermal environment could be inferred to be substituted aromatic < non-substituted aromatic < alkanes. Therefore, in sulfonated acid catalysts designed to withstand hydrothermal conditions, sulfonic acid groups should be attached to sp^3-hybridized carbons to remain stable for extended periods of time. This could be accomplished with the use of aliphatic linkers that connect sulfonic acid groups to an aromatic carbon scaffold. Materials designed according to this principle may provide a path to greater hydrothermal stability than achieved previously using aromatic substitution reactions. As the pK_a values of benzene- and methanesulfonic acid are -2.8 and -1.9, respectively [21], there would only be a minor trade-off between hydrothermal stability and acid strength of the solid acid material.

Acknowledgements

The authors would like to acknowledge NSF Award number EEC-0813570 for generously supporting this work through the NSF Engineering Research Center for Biorenewable Chemicals (CBiRC). We wish to thank ISU Chemical Instrumentation Facility staff members Sarah Cady for the solution NMR and Stephen Veysey for the PE 2100 CHN/S elemental analysis training and assistance. Purchase of the Perkin Elmer 2100 Series II CHN/S analyzer used to obtain results included in this publication was supported in part by the National Science Foundation under Grant No. DBI 9413969. We would also like to thank two undergraduate students, Karl Alderks and Ashley Leitner, who worked on this project. Jim Anderegg graciously ran and helped interpret the XPS results. Any opinions, findings, and conclusions, or recommendations expressed herein are those of the authors and do not necessarily reflect the views of the National Science Foundation.

References

(1) J. Akbar, M.S. Iqbal, S. Massey, R. Masih, Carbohydr. Polym., 90 (2012) 1386-1393.
(2) F. Zamora, K. Hakkou, S. Muñoz-Guerra, J.A. Galbis, Polym. Degrad. Stab., 91 (2006) 2654-2659.
(3) A. Funke, F. Ziegler, Biofuels, Bioprod. Biorefin., 4 (2010) 160-177.
(4) B. Hickel, K. Sehested, Radiat. Phys. Chem., 39 (1992) 355-357.
(5) H. Xiong, H.N. Pham, A.K. Datye, J. Catal., 302 (2013) 93-100.
(6) H.N. Pham, A.E. Anderson, R.L. Johnson, K. Schmidt-Rohr, A.K. Datye, Angew. Chem., Int. Ed., 51 (2012) 13163-13167.
(7) A.T. DeLaRiva, T.W. Hansen, S.R. Challa, A.K. Datye, J. Catal., 308 (2013) 291-305.
(8) X. Zaiku, X. Z, Int. J. Mol. Sci., 11 (2010).
(9) A. Onda, T. Ochi, K. Yanagisawa, Top. Catal., 52 (2009) 801-807.
(10) R.L. Johnson, J.M. Anderson, B.H. Shanks, X. Fang, M. Hong, K. Schmidt-Rohr, J. Magn. Reson., 234 (2013) 112-124.
(11) H. Cerfontain, Mechanistic Aspects in Aromatic Sulfonation and Desulfonation, John Wiley & Sons, Inc., 1968.
(12) E.N. Krylov, Russ. J. Gen. Chem., 67 (1997) 1624-1627.
(13) F.C. Wagner, E.E. Reid, J. Am. Chem. Soc., 53 (1931) 3407-3413.
(14) D. Yamaguchi, M. Hara, Solid State Sci., 12 (2010) 1018-1023.
(15) M.L. Jenkins, R.H. Dauskardt, J.C. Bravman, J. Adhes. Sci. Technol., 18 (2004) 1497-1516.
(16) H. Staub, F. Kleitz, F.-G. Fontaine, Microporous Mesoporous Mater., 175 (2013) 170-177.
(17) B.M. Graybill, J. Org. Chem., 32 (1967) 2931-2933.
(18) E.A. Setzkorn, A.B. Carel, J. Am. Oil Chem. Soc., 40 (1963) 57-59.
(19) A. Takagaki, M. Toda, M. Okamura, J.N. Kondo, S. Hayashi, K. Domen, M. Hara, Catal. Today, 116 (2006) 157-161.
(20) Q. Shu, J. Gao, Z. Nawaz, Y. Liao, D. Wang, J. Wang, Appl. Energy, 87 (2010) 2589-2596.
(21) J.P. Guthrie, Can. J. Chem., 56 (1978) 2342-2354.

APPENDIX D. IMPROVED HYDROTHERMAL STABILITY OF MESOPOROUS OXIDES FOR AQUEOUS PHASE REACTIONS

Angewwandte Chemi, **51,** pp 13163-13167, 2012

Hien N. Pham, Amanda E. Anderson, Robert L. Johnson+, Klaus Schmidt-Rohr+, and Abhaya K. Datye

Abstract

A simple and inexpensive approach for coating of a metal oxide surfaces with thin films of carbon is described. These carbon films provide improved hydrothermal stability to oxides such as silica and alumina which are not otherwise stable at elevated temperatures in the presence of liquid water. Carbon maps are acquired via EFTEM to image the location of carbon in the composites. The carbon changes the surface chemistry of the support, as evident from the improved selectivity of Pd for acetylene hydrogenation. This work provides a route for improved catalyst supports for aqueous phase reactions of biorenewable feedstocks.

Introduction

Catalysts for the production of biorenewable chemicals must operate under aqueous phase conditions, generally at temperatures in excess of 473 K [1-2]. Conventional oxide supports designed for gas-phase reactions are not suitable for aqueous-phase reactions at these elevated temperatures. For example, alumina undergoes a phase change from γ-Al_2O_3 to boehmite at 473 K with a consequent loss of surface area[3-5]. Likewise, mesoporous silica SBA-15 suffers from collapse of the well-ordered mesoporous structure when heated to 473

K in liquid water, resulting in loss of its surface area and structural integrity[6]. In this work, we present a simple and inexpensive approach for modifying the surfaces of oxide supports so as to make them hydrothermally stable in liquid water at 473 K. This general approach can be applied to other oxides, but we report here the improvement in the hydrothermal stability of silica and alumina supports.

Our approach involves the deposition of a thin film of carbon, generally around 10 wt% carbon, derived from simple sugars such as sucrose. We demonstrate the utility of this approach through improved hydrothermal stability of SBA-15 mesoporous silica, commercial silica gel (Aldrich) as well as commercial fumed alumina (Degussa). Detailed catalyst synthesis procedures are given in the experimental section. Hydrothermal treatment of each sample was carried out by heating the sample to 473 K at autogenous pressure (22 bar) and held at this temperature for 12 hr.

Both alumina and silica gel have an open pore structure, but SBA-15 has well-ordered cylindrical pores having a hexagonal structure. As we show here, the carbon coating can be successfully applied even to cylindrical pores having aspect ratios (length/diameter) exceeding 200. To confirm the presence of carbon on the pore walls of SBA-15, we acquired elemental carbon maps via energy filtered transmission electron microscopy (EFTEM). Elemental carbon maps of the SBA-15-based samples are shown in Figure 1, where bright red regions indicate the location of carbon in the EFTEM image at the Carbon K edge. The uncoated SBA-15 particle is dark in the map (b), indicating that carbon is not present. For reference, the underlying carbon support film is visible in the EFTEM map in Figure 1(b). The HRTEM image of carbon-coated SBA-15 (c) is similar to that of uncoated SBA-15 (a) since carbon does not produce any additional contrast in this image. However, the EFTEM image of coated SBA-15 (d) shows bright red regions showing the location of the carbon within the pores, and the dark regions within SBA-15 correspond to the silica walls.

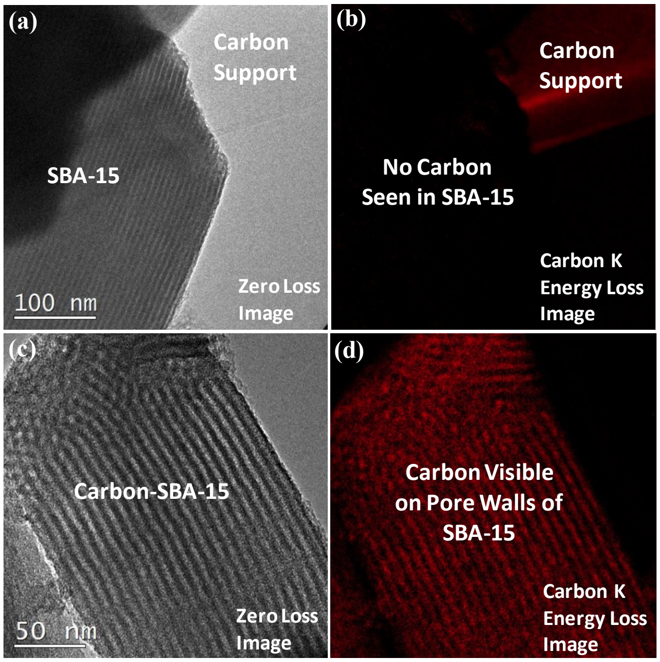

Figure 1. HRTEM images of calcined (a) SBA-15 and (c) 10 wt% carbon-SBA-15; elemental carbon maps of (b) SBA-15 and (d) 10 wt% carbon-SBA-15.

These images confirm that the carbon is able to coat the internal surfaces of the mesoporous silica SBA-15. From the EFTEM image of coated SBA-15, it might appear that carbon has filled the pores of SBA-15. However, N_2 sorption isotherms obtained from the coated samples are very similar to the uncoated SBA-15, indicating a narrow pore size distribution (see Figure S1). Due to the coating, the pore diameter decreases from 4.8 nm in SBA-15 to 3.8 nm for carbon-coated SBA-15 (see Table S2). The major difference is the loss of microporosity and a decrease in total pore volume due to a narrowing of the pores. These are the major factors causing a decrease in the total BET surface area of the carbon-coated sample.

HAADF-STEM images of the SBA-15-based samples (Figure 2) show the retained hexagonal arrangement of pores (inset) after coating the pore walls of SBA-15 (a) with carbon (c). After treatment in liquid water at 473 K for 12 hr, uncoated SBA-15 loses 96% of its surface area due to a complete collapse of the ordered mesopores, and loss of its structural integrity (Figure 2 (b)). In contrast, hydrothermal stability is significantly improved after coating SBA-15 with carbon, with a surface area loss of only 55% and a partially retained ordered mesoporous structure (d). If we increase the carbon loadings (e.g., 25 wt%), we can further retain the well-ordered structure of SBA-15 and minimize the loss of surface area after hydrothermal treatment (see Figure S2). For the silica gel-based samples (Figure 3), uncoated silica gel (a) loses 75% of its surface area after hydrothermal treatment due to grain growth and sintering (b), whereas carbon-coated silica gel (c) neither loses surface area nor its structural integrity after hydrothermal treatment (d). For the alumina-based samples (Figure 4), uncoated alumina (a) loses 70% of its surface area after hydrothermal treatment (b), whereas both the morphology and surface area of carbon-coated alumina (c) are retained after hydrothermal treatment (d).

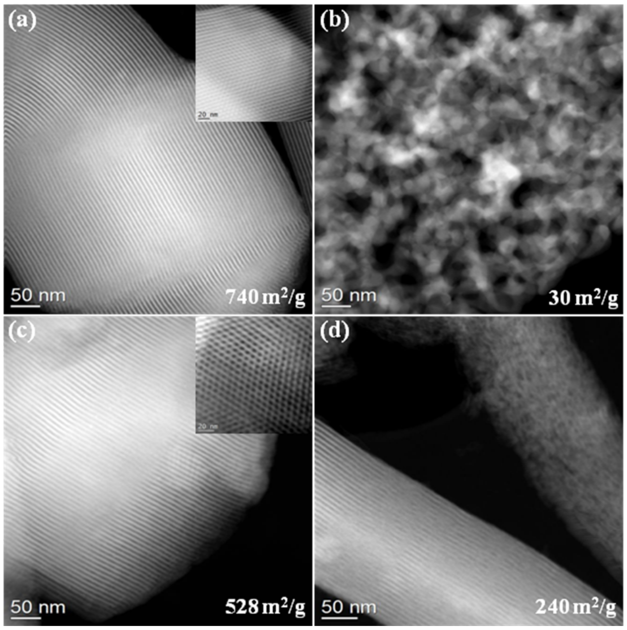

Figure 2. STEM images of calcined (a) SBA-15 and (c) 10 wt% carbon-SBA-15 with well-ordered hexagonal pores (insets), and after treatment in liquid water at 473 K for 12 hr (b) SBA-15 and (d) 10 wt% carbon-SBA-15.

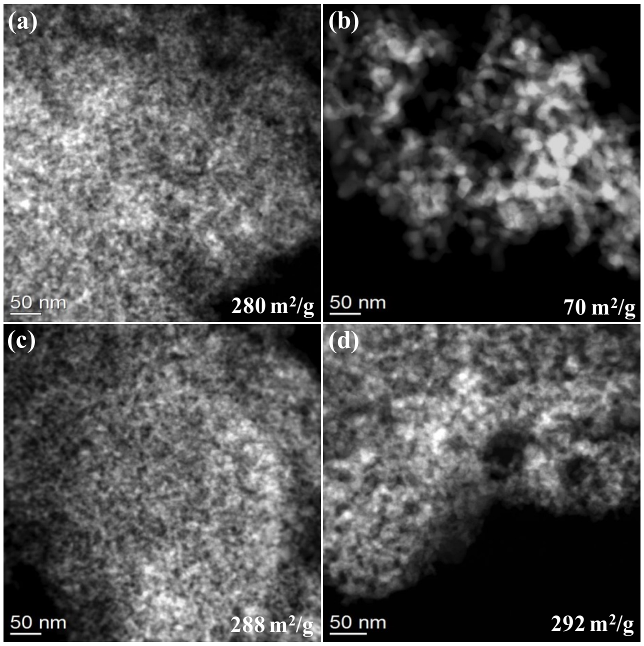

Figure 3. STEM images of (a) silica gel and (c) 10 wt% carbon-silica gel, and after treatment in liquid water at 473 K for 12 hr (b) silica gel and (d) 10 wt% carbon-silica gel.

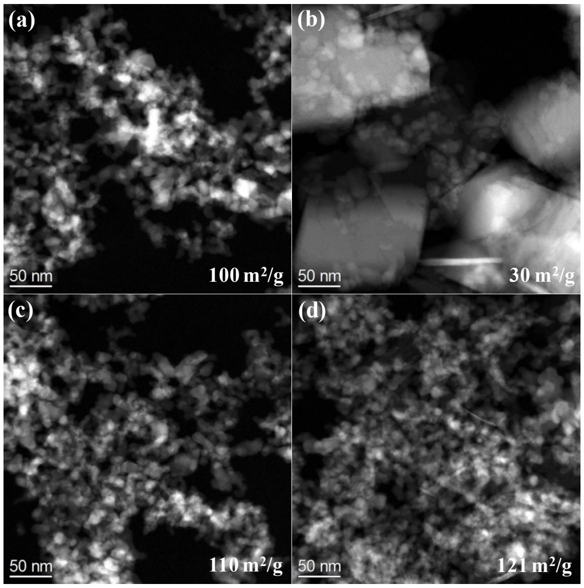

Figure 4. STEM images of (a) fumed alumina and (c) 10 wt% carbon-alumina, and after treatment in liquid water at 473 K for 12 hr (b) fumed alumina and (d) 10 wt% carbon-alumina.

The chemical composition of the carbon layer was probed by solid-state NMR. Figure 5 shows the ^{13}C NMR spectrum of carbon-SBA-15 produced using ^{13}C-enriched glucose, with the corresponding spectrum of the nonprotonated carbons (and mobile segments) superimposed. The spectra are dominated by aromatic-carbon signals between 100 and 160 ppm (75% aromaticity). Nevertheless, CH_3 (3.5%), alkyl CH/CH_2 (5%), OCH_n (10%), COOH (3.5%), and C=O (3.5%) are also observed; ^{13}C-^{13}C correlation NMR (see supporting information) shows that the C=O and alkyl CH_n groups are attached to the aromatic rings, while many of the OCH_n carbons are not. From the fractions of aromatic C-O (14%) and C-H (32%), as well as C=O, COO and alkyl-C bonded to aromatic rings, one finds that aromatic C bonded only to other aromatic C, as found in polycondensed rings, accounts for ~1/5 of all C. Aromatic H-C-O intensity (see supporting information) indicates that $\geq$ 6% of

C is in furan rings. A structural model reproducing the measured spectra (see Figure S6) is shown in Figure 5(b).

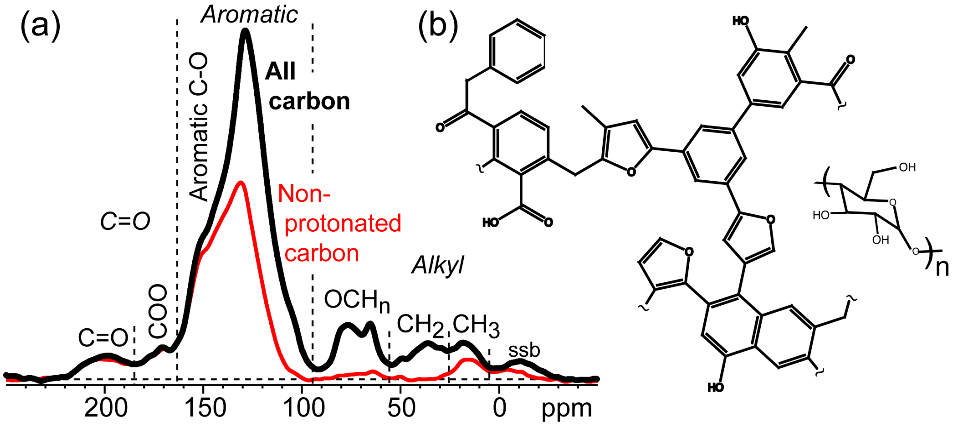

Figure 5. (a) Quantitative ^{13}C NMR spectra of all carbons (thick line), and of nonprotonated carbons and CH_3 groups (thin red line) in ^{13}C-enriched carbon-SBA-15. "ssb": Spinning sideband (14-kHz MAS). (b) Structural model reproducing the experimental spectra.

In addition to depositing a thin film of carbon on a concave surface, such as on the pore walls of SBA-15, we can improve the hydrothermal stability of oxides which have a convex surface such as Stöber spheres, a non-porous silica with a BET surface area of 10 m^2/g (see Figure S7). After hydrothermal treatment, uncoated Stöber spheres show pronounced neck formation due to sintering of the spheres, as well as formation of large pores in the spheres. In contrast, hydrothermal stability is improved after coating Stöber spheres with carbon, with retention of the individual coated spheres and no pronounced sintering or formation of large pores after hydrothermal treatment. Furthermore, there is no delamination and formation of defects which are generally more pronounced when thin films are deposited on convex than on concave surfaces.

The FTIR spectra of the SBA-15-based samples (see Figure S8) show a broad absorption band at ~3200-3400 cm^{-1} assigned to the O-H stretching vibration and an absorption band at ~1640 cm^{-1} assigned to the bending vibrations of molecular water. Both the absorption bands at ~3200-3400 cm^{-1} and at ~1640 cm^{-1} are initially small for SBA-15, which is expected since FTIR was performed on SBA-15 just after calcination to remove the surfactant, minimizing exposure of SBA-15 to moisture. These two absorption bands slightly increased for carbon-coated SBA-15 after SBA-15 was mixed with the aqueous sucrose solution followed by carbonization. We then re-hydrated each sample by re-suspending it in water at room temperature overnight in order to determine the extent of re-adsorbed water on the pore walls of SBA-15. SBA-15 shows a significant increase in the absorption bands at ~3200-3400 cm^{-1} and at ~1640 cm^{-1} after re-hydration, which indicates that water has re-adsorbed on the pore walls of SBA-15. In contrast, re-adsorption occurs to a much lesser extent for carbon-coated SBA-15. The results suggest that SBA-15 changes from a hydrophilic to a more hydrophobic state after coating the pore walls with 10 wt% carbon. The FTIR results are in agreement with improved hydrothermal stability for carbon-coated SBA-15. For the uncoated silica samples used in this study, the surface consists of siloxane bridges and silanol groups. When silica was exposed to water at elevated temperatures, silicate hydrolysis occurs. The hydrolytic cleavage of the siloxane bonds leads to a dissolution and re-precipitation of silica resulting in loss of both high surface area and structural integrity. By coating the surface of silica with carbon, we make the surface resistant to hydrolytic attack. With increased carbon loading, we are able to further improve the stability of the SBA-15 sample.

Figure 6 shows the XRD patterns of the alumina-based samples. Before hydrothermal treatment, the patterns for both uncoated (a) and carbon-coated alumina (b) are characteristic of the γ-Al_2O_3 phase. After hydrothermal treatment, the XRD pattern for uncoated alumina is characteristic of boehmite (d). The transformation from γ-Al_2O_3 to boehmite is due to hydration of alumina when it is subjected to liquid water at 473 K for several hours. In contrast, carbon-coated alumina remains as γ- Al_2O_3 after hydrothermal treatment (c). Similar changes in phase transformations were recently reported by Ravenelle et al[3-5]. In their work, they also found that the transformation of alumina to boehmite was inhibited when it was subjected to water in the presence of polyols, such as glycerol and sorbitol, at 498 K for several hours[4]. The increase in the hydrothermal stability of alumina was caused by the formation of carbonaceous layers which partially coat the surface of alumina, and therefore, prevent the transformation of γ-Al_2O_3 into boehmite. The extent of boehmite formation, however, depends on how well the carbonaceous species protect the alumina. In our work, we are able to modify the surface of alumina with carbon before subjecting it to hydrothermal conditions, thereby achieving improved stability. The extent of carbon coating, and the carbon loading, can be varied to achieve different degrees of surface modification of the γ-Al_2O_3 surface.

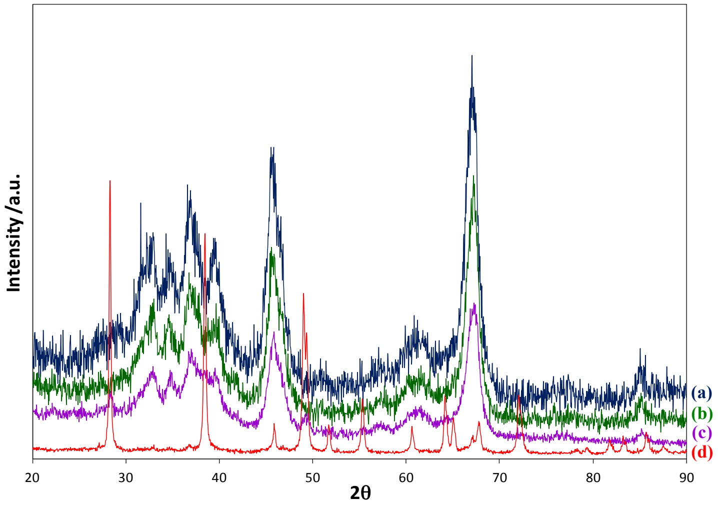

Figure 6. XRD patterns of (a) fumed alumina and (b) 10 wt% carbon-alumina, and after treatment in liquid water at 473 K for 12 hr (c) 10 wt% carbon-alumina and (d) fumed alumina.

We have also explored the catalytic performance of carbon-coated oxides. The reaction we chose was selective hydrogenation of acetylene in the presence of excess ethylene. In previous work[7], we found that Pd on carbon black was very selective towards ethylene while Pd on alumina was not very selective. For this work, we compared the performance of 0.5 wt% Pd on the uncoated oxide with the corresponding oxide pre-coated with 10 wt% carbon. The catalysts contained similar sized (1-1.5 nm) Pd nanoparticles (see Figure S9) prepared by using a room temperature direct alcohol reduction route. A selective catalyst will convert all of the acetylene to ethylene with no ethane formation. However, as the acetylene is converted, all catalysts lose selectivity and start to show formation of excess ethane due to loss of ethylene in the feed. The amount of ethane formed is therefore a good measure of the selectivity of the catalyst, since selectivity at high acetylene conversion is desired. Ethane formation is presented as the ratio of moles of ethane in the effluent to moles of ethylene in the feed, which allows comparison with other feed compositions in the literature. Figure 7 shows that the amount of ethane formed at the same acetylene conversion is high on the silica and alumina supports and lower on the carbon-coated supports which are comparable in selectivity to Pd/Vulcan XC carbon black. These catalysts prevent over hydrogenation of ethylene even at near 100% conversion of acetylene. Addition of promoters such as Ag will further improve selectivity; here we use this test reaction to show changes in the surface chemistry at the metal-oxide interface. It is clear that coating these oxides with carbon changes the surface chemistry, making the surface more hydrophobic (fewer surface hydroxyls by FTIR), and the oxide surface chemistry is reflected in the improved selectivity for the acetylene hydrogenation. A hydrothermally stable support is a necessary condition for achieving improved reactivity for metal catalyzed reactions, as shown in our previous work[6, 8] on aqueous phase reactions. Future work will explore the application of carbon coated oxides for these reactions.

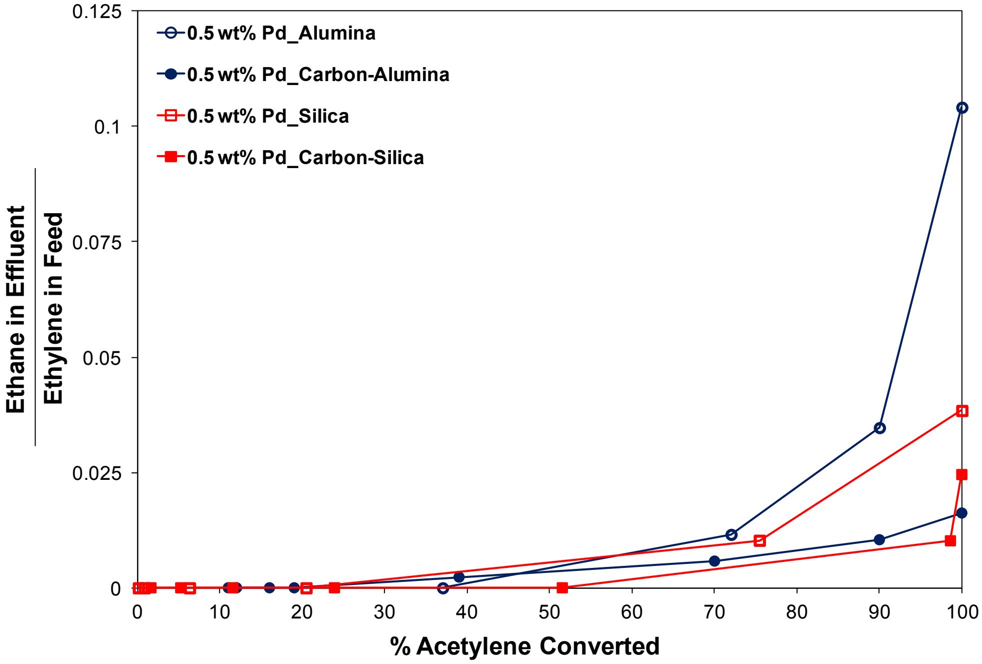

Figure 7. Selective acetylene hydrogenation to ethylene for 0.5 wt% Pd on alumina (open circles) and on 10 wt% carbon-alumina (closed circles); 0.5 wt% Pd on silica gel (open squares) and on 10 wt% carbon-silica gel (closed squares). Feed ratio of acetylene to ethylene is 1:70.

In conclusion, our results show that carbon coatings can impart improved hydrothermal stability to silica and alumina which are otherwise not stable for aqueous-phase reactions. Thin film coatings of carbon change the surface chemistry of the oxides, making them less susceptible to hydrolytic attack at elevated temperatures. We demonstrated that high dispersions of metal particles can also be achieved on these supports, opening up the possibility of novel catalyst designs that could be applied to demanding aqueous-phase reactions. The carbon coatings provide a simple route to create supports for biomass conversion having properties that conventional carbon supports may lack, such as mesoporosity and mechanical strength.

Experimental

To prepare mesoporous silica SBA-15, Pluronic P123 surfactant (4.0 g) was dissolved in deionized water (30 g) while stirring at 308 K. Once dissolved, 2M HCl (120 g) and TEOS (8.6 g) were added to the solution. The solution was then transferred to a Nalgene bottle and placed in a water bath at 308 K without stirring for 20 hr. The solid product was filtered, washed with deionized water, and air dried at room temperature. The dried product was calcined in air at 773 K (5 K/min ramp) for 12 hr to remove the P123 template.

To coat the surface of oxides with 10 wt% carbon, an aqueous solution of sucrose (^{13}C-glucose for NMR) was added to SBA-15, silica gel or fumed alumina. The mixture was stirred at room temperature overnight until the water evaporated. The dried product was collected and partially pyrolyzed under flowing UHP N_2 gas at 673 K (5 K min^{-1} ramp) for 2 hr.

A solution of Pd acetate in methanol was sonicated for 10 min to completely dissolve the Pd acetate, and the solution was added to the uncoated or 10 wt% carbon-coated oxides to obtain a Pd loading of 0.5 wt%. A Buchi rotary evaporator was used to gently remove methanol from the sample at 313 K, and the dried product was collected. Selective acetylene hydrogenation to ethylene was performed with a reactant mixture (0.5% acetylene, 35% ethylene, balance N_2; 70 cm^3 (STP) min^{-1}), hydrogen (3.5 cm^3 (STP) min^{-1}) and nitrogen (75 cm^3 (STP) min^{-1}), with a hydrogen:acetylene ratio of 7:1. Reactivity measurements for the samples (20 mg) were carried out at temperatures from 308 to 388 K, and the gas effluents were analyzed by GC (Varian CP-3800).

Samples were dispersed in ethanol and mounted on holey carbon grids for examination in a JEOL 2010F 200 kV transmission electron microscope. Images were recorded both in bright field (BF) and high angle annular dark field (HAADF) modes. Elemental carbon maps were acquired using energy filtered transmission electron microscopy (EFTEM) with an exposure time of 8 s for the SBA-15-based samples. Surface area was measured using N_2 adsorption at 77 K in a Micromeritics Gemini 2360 multipoint BET analyzer. N_2 sorption isotherms and pore size distributions were measured at 77 K in a Quantachrome Autosorb-1 analyzer. Infrared spectra of samples were recorded on a Nicolet 7600 FTIR analyzer equipped with an attenuated total reflectance (ATR) attachment. The spectra were acquired between 400-4000 cm^{-1} at 4 cm^{-1} resolution and 128 scans. ^{13}C NMR was performed at 100 MHz on ^{13}C-enriched samples washed with water to remove trapped low-molar mass species, using a Bruker DSX400 spectrometer, magic angle spinning at 14 kHz, and high power ^1H decoupling. Quantitative ^{13}C spectra were measured using direct polarization (DP) and a Hahn echo, with recycle delays of 30 s (> 5 T_1), and spectra of nonprotonated carbons (and mobile segments) were obtained after recoupled ^{13}C-^1H dipolar dephasing[9]. Details of the analysis of the spectra, also using spectral editing, are given in the supporting information. X-ray powder diffraction (XRD) was performed using a Scintag Pad V diffractometer (Cu Kα radiation) with DataScan 4 software (MDI, Inc.).

References

(1) J. N. Chheda, G. H. Huber, James A. Dumesic, Angew. Chem. Int. Ed. 2007 46, 7164-7183.

(2) A. Corma, S. Iborra, A. Velty, Chem. Rev. 2007 107, 2411-2502.

(3) R. M. Ravenelle, J. R. Copeland, W. G. Kim, J. C. Crittenden, C. Sievers, ACS Catal. 2011 1, 552-561.

(4) R. M. Ravenelle, J. R. Copeland, A. H. Van Pelt, J. C. Crittenden, C. Sievers, Top. Catal. 2012 55, 162-174.

(5) R. M. Ravenelle, F. Z. Diallo, J. C. Crittenden, C. Sievers, Chemcatchem 2012 4, 492-494.

(6) Y. J. Pagan-Torres, J. M. R. Gallo, D. Wang, H. N. Pham, J. A. Libera, C. L. Marshall, J. W. Elam, A. K. Datye, J. A. Dumesic, ACS Catal. 2011 1, 1234-1245.

(7) P. D. Burton, T. J. Boyle, A. K. Datye, J. Catal. 2011 280, 145-149.

(8) H. N. Pham, Y. J. Pagan-Torres, J. C. Serrano-Ruiz, D. Wang, J. A. Dumesic, A. K. Datye, Appl. Catal. A 2011 397, 153-162.
(9) J.-D. Mao, K. Schmidt-Rohr, Environ. Sci. Technol. 2004 38, 2680-2684.

Supporting Information

IMPROVED HYDROTHERMAL STABILITY OF MESOPOROUS OXIDES FOR AQUEOUS PHASE REACTIONS

Hien N. Pham, Amanda E. Anderson, Robert L. Johnson, Klaus Schmidt-Rohr, Abhaya K. Datye

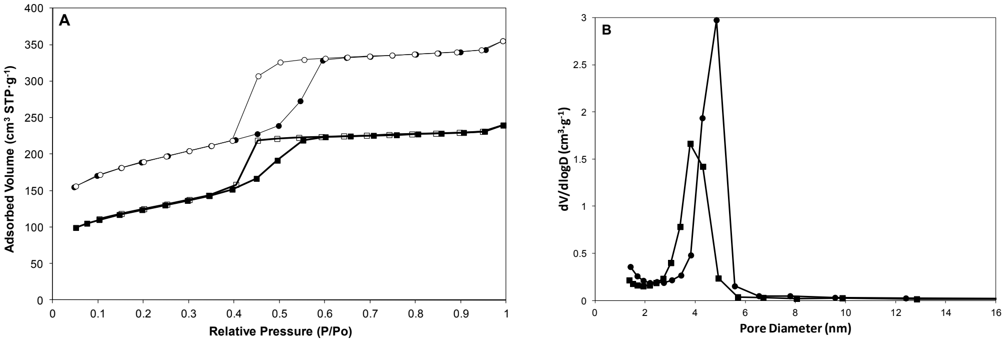

Figure S1. (A) N_2 sorption isotherms and (B) pore size distribution curves of calcined SBA-15 (circles) and 10 wt% carbon-SBA-15 (squares).

Table S2. *Table of structural properties for calcined SBA-15 and carbon-SBA-15*

Sample	S_{BET} [a] ($m^2 g^{-1}$)	S_{Microp} [b] ($m^2 g^{-1}$)	V_P ($cm^3 g^{-1}$)	$V_{P\text{-}Microp}$ [b] ($cm^3 g^{-1}$)	D_P [c] (nm)
SBA-15	740	241	0.46	0.12	4.8
10 wt% Carbon-SBA-15	528	109	0.33	0.056	3.8
25 wt% Carbon-SBA-15	465	91	0.19	0.049	3.1

[a] BET specific surface area. [b] Micropore surface area and volume determined by the t-plot method.
[c] Calculated by BJH method.

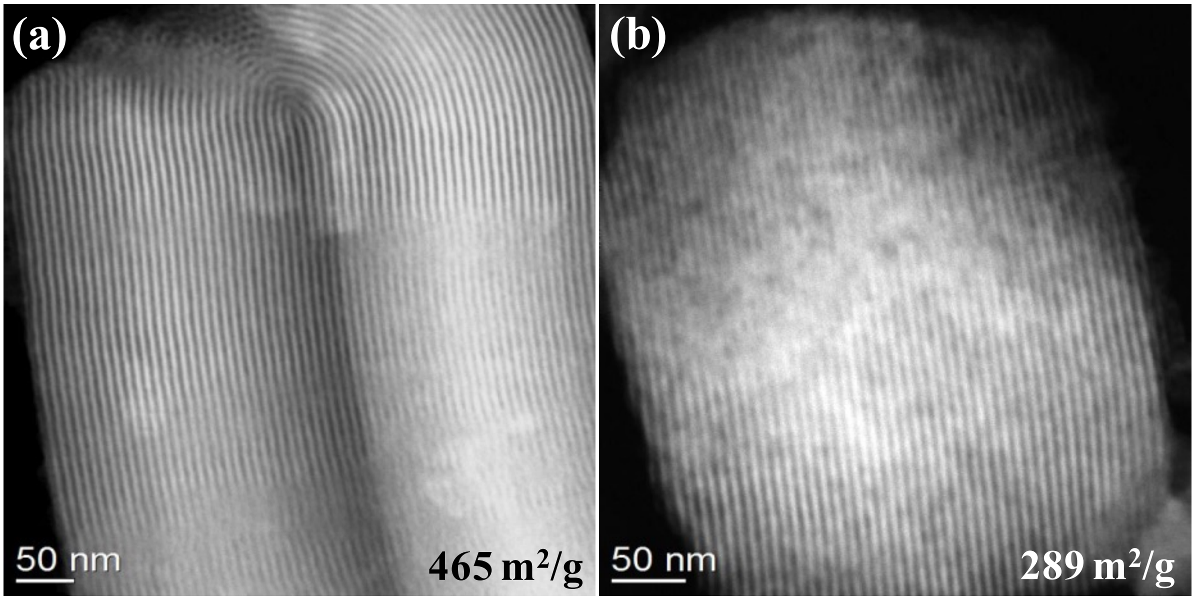

Figure S3. HAADF-STEM images of 25 wt% carbon-SBA-15 (a) as-prepared and (b) after treatment in liquid water at 473 K for 12 hr. Note how the structural integrity is preserved with the higher carbon loading.

Analysis of quantitative ^{13}C NMR spectra, with spectral editing

Various chemical groups were identified in the quantitative ^{13}C NMR spectrum of Figure 4(a) in terms of chemical shifts as follows: CH_3: 10-26 ppm; alkyl CH_2/CH not bonded to O: 26-55 ppm; COO: 163-185 ppm; carbonyl C=O: 185-220 ppm. With spectral editing of nonprotonated vs. protonated C by dipolar dephasing, we obtained: nonprotonated aromatic C-O: 163-143 ppm; and aromatic H-C-O: 140-157 ppm (see Figure S4(a)). With spectral editing of sp^3- vs. sp^2-hybridized C by chemical-shift-anisotropy (CSA) filtering [J-

D. Mao, K. Schmidt-Rohr, *Environ. Sci. Technol*. **38**, 2680-2684 (2004)] (see Figure S4(b)), we determined: OCH_n: 55-95 ppm (8.6% of all C) plus CSA-filtered 95-110 ppm (1.3% of all C); total aromatic: 95-163 ppm (minus CSA-filtered alkyl O-CH-O at 95-110 ppm); and aromatic C-H: 95-158 ppm, see Figure S4(a) (minus CSA-filtered alkyl O-CH-O at 95-110 ppm). The fractions of functional groups given in the main text were obtained from the peak areas in the quantitative ^{13}C NMR spectra, with error margins of ±1%. ^{13}C chemical shifts were referenced to TMS at 0 ppm, using the ^{13}COO resonance of a-glycine at 176.46 ppm as a secondary reference.

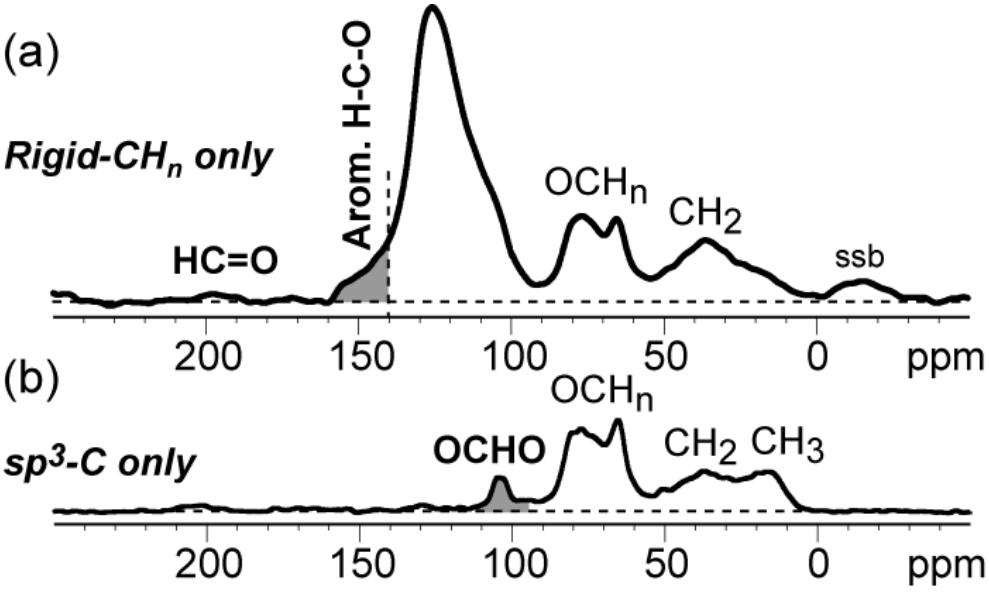

Figure S4. ^{13}C NMR of ^{13}C-enriched carbon-SBA-15 with spectral editing. (a) Quantitative ^{13}C NMR spectrum of immobile protonated carbons, obtained as the dipolar-dephasing difference in DP NMR at 14 kHz MAS (see main text). The small peak of aldehydes near 197 ppm and the signal of aromatic H-C-O near 147 ppm found in furan rings are highlighted. (b) Spectrum of alkyl (sp^3-hybridized) C, selected by chemical-shift anisotropy dephasing. The peak of alkyl O-CH-O (e.g. found in sugar rings) near 105 ppm is highlighted.

Two-dimensional ^{13}C-^{13}C exchange NMR

Figure S5 shows a two-dimensional ^{13}C-^{13}C exchange NMR spectrum of ^{13}C-enriched carbon-SBA-15. Spectral editing was applied to simplify the spectrum, which only shows cross peaks linking the signals of CH_n carbons in the vertical dimension with those of nonprotonated (or mobile) C in the horizontal dimension. The largest peak, at (123 ppm, 130 ppm), is characteristic of CH and nonprotonated C in six-membered aromatic rings; the 130-ppm chemical shift of the nonprotonated carbons is indicative of fused rather than alkyl-substituted C. Near the top center of the spectrum, at (35 ppm, 135 ppm), a cross peak between alkyl CH_2 and six-membered aromatic rings is observed. The corresponding ~5% fraction of aromatic C bonded to alkyl C was included with those of the aromatic C-O and C-H carbons, and of C=O and COO bonded to aromatic rings, to estimate the fraction of aromatic C at the edge of clusters of fused aromatic rings; this yielded the complementary fraction of arene C only bonded to aromatic C (see main text). The absence of a significant cross peak between OCH_n and aromatic-ring signals, near (70 ppm, 135 ppm), indicates that the OCH_n–rich components, apparently from only partially transformed glucose, and the aromatic-rich regions are not bonded to each other.

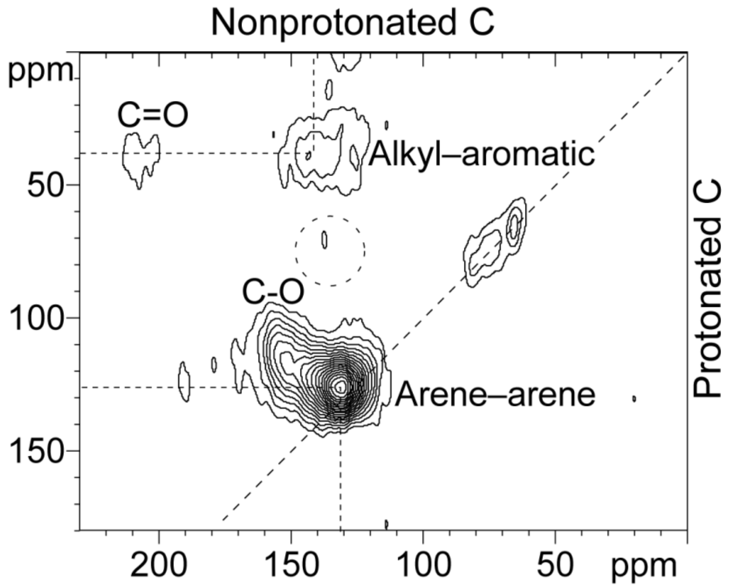

Figure S5. ^{13}C-^{13}C exchange NMR spectrum of ^{13}C-enriched carbon-SBA-15 with spectral editing, correlating the signals of protonated carbons in the vertical dimension with signals of nonprotonated C in the horizontal dimension. Spin-exchange mixing time with ^{1}H rotary-resonance recoupling: 10 ms; spinning frequency: 14 kHz. Cross peaks characteristic of arene (rather than furan) rings, and of alkyl CH_n bonded to arene rings, are labeled. Note the absence of a significant cross peak between OCH_n and aromatic-ring signals (dashed circle).

Figure S6(a) shows the ^{13}C NMR spectra (all C, and nonprotonated C plus CH_3) calculated for the structural model shown in Figure 5(b) of the main text (and also in Figure S6(b)). The fairly good agreement with the spectral intensities in the experimental spectrum of Figure 5(a) indicates that the composition of the model is compatible with the experimental data.

Simulated ^{13}C NMR spectrum

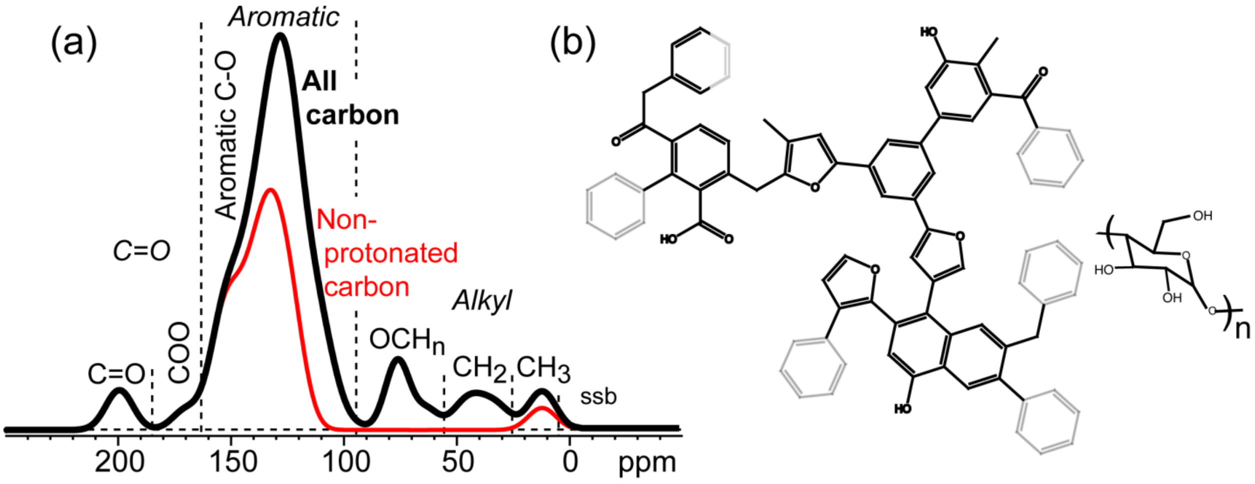

Figure S6. (a) ^{13}C NMR spectra of all carbons (thick line), and of nonprotonated carbons and CH_3 groups (thin red line) calculated for the structural model of carbon-SBA-15 shown in Figure 5(b), to be compared with the experimental spectra of Figure 5(a). The ACD/NMR Predictors software for empirical chemical-shift prediction was used, and a line broadening of ±6 ppm applied. (b) Structural model of Figure 5(b), with aromatic rings outside the "repeat unit" shown in gray.

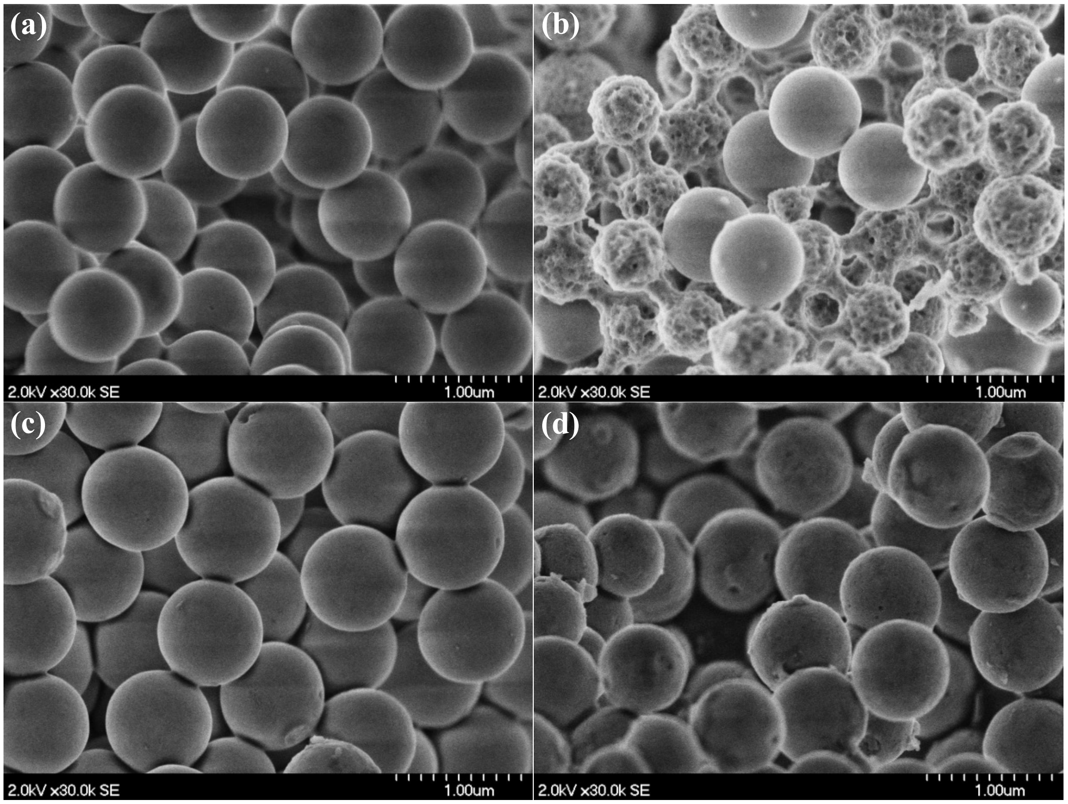

Figure S7. HRSEM images of (a) Stöber spheres and (c) 10 wt% carbon-Stöber spheres, and after treatment in liquid water at 473 K for 12 hr (b) Stöber spheres and (d) 10 wt% carbon-Stöber spheres.

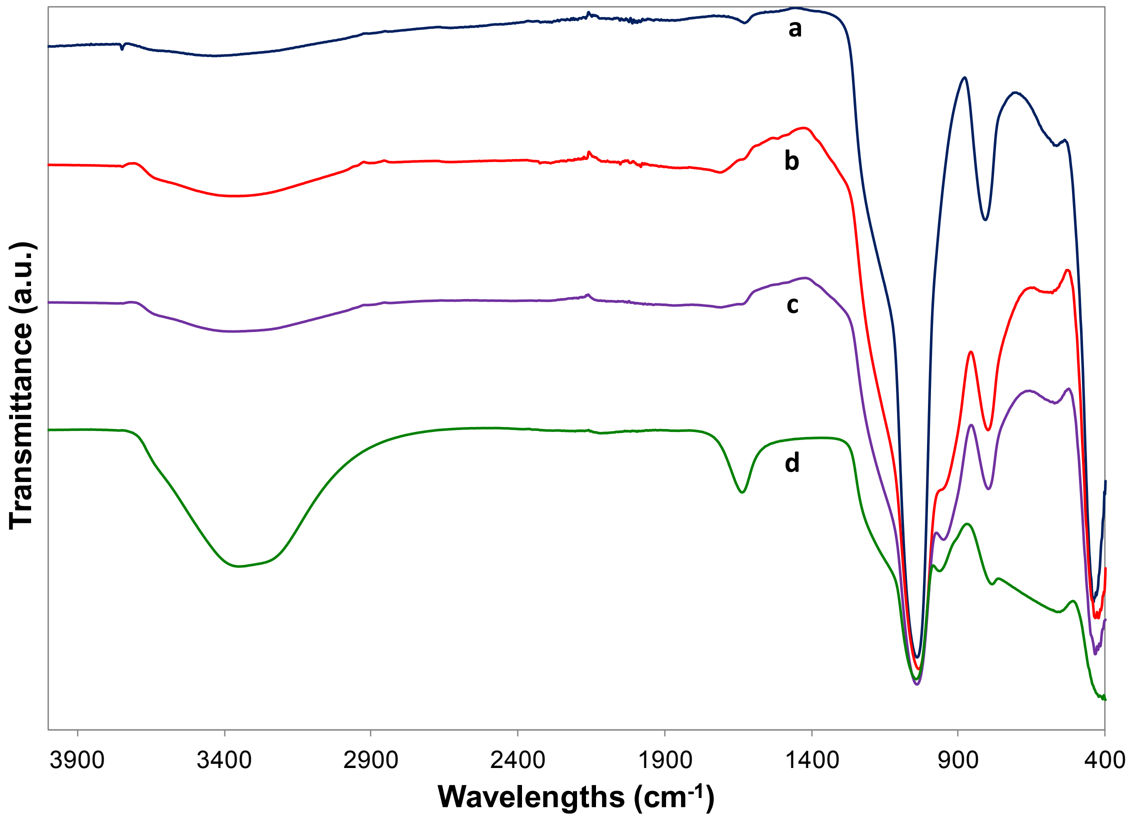

Figure S8. FTIR spectra of calcined (a) SBA-15 and (b) 10 wt% carbon-SBA-15, and after re-hydration at room temperature (c) 10 wt% carbon-SBA-15 and (d) SBA-15.

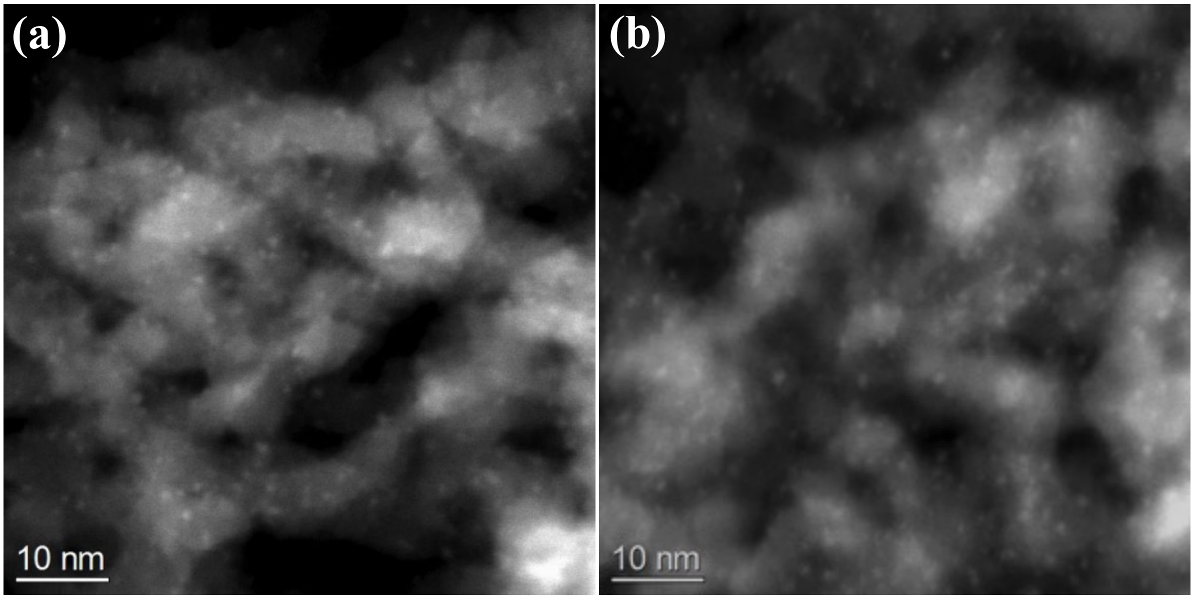

Figure S9. HAADF-STEM images of 1 to 1.5 nm Pd nanoparticles (0.5 wt%) supported on silica gel (a) and on 10 wt% carbon-silica gel (b). Similar results are observed for the alumina-based-supported Pd samples.

APPENDIX E. EFFECT OF PD DISPERSION ON HYDROTHERMALLY STABLE CARBON COATED-BASED MESOPOROUS SILICA FOR AQUEOUS PHASE REACTIONS

Under review, *ACS Catalysis,* October 2014

Hien N. Pham[†], Amanda E. Anderson[†], Robert L. Johnson[‡], Klaus Schmidt-Rohr[‡], and
Abhaya K. Datye[†,*]

[†]Department of Chemical & Nuclear Engineering and Center for Microengineered Materials, University of New Mexico, Albuquerque, NM 87131, United States
[‡]Department of Chemistry, Iowa State University, Ames, IA 50011, United States

Abstract

Commercial mesoporous oxides, such as silica, are not stable under aqueous conditions at elevated temperatures. In contrast, silica is significantly improved by coating the surface with a thin carbon film. We report on the improved dispersion, and therefore better stability, of Pd nanoparticles when deposited on a hydrothermally stable carbon-coated silica support. After hydrothermal treatment, Pd sintering, observed in Pd deposited on uncoated silica, is inhibited and the structural integrity of the carbon-coated silica is preserved. The stability of Pd is also improved by introducing carbon as a thin amorphous overlayer to an uncoated silica-supported Pd catalyst. Hence, a hydrothermally stable catalyst is necessary for achieving high reactivity and stability for metal-catalyzed reactions in the aqueous phase.

The transformation of biomass-derived oxygenated feedstocks to fuels and chemicals occurs in liquid-phase reactions, particularly aqueous-phase reactions in excess of 473 K due to their high solubility and reactivity in water.[1-4] Conventional oxide supports designed for gas-phase reactions are not suitable for aqueous-phase reactions at these elevated temperatures. For example, alumina undergoes a phase change from γ-Al_2O_3 to boehmite at 473 K with a consequent loss of surface area.[5-7] Likewise, mesoporous silica SBA-15 suffers from collapse of the well-ordered mesoporous structure when heated to 473 K in liquid water, resulting in loss of its surface area and structural integrity.[8]

Under aqueous conditions, mesoporous carbons are more stable than mesoporous oxides since carbons are hydrophobic, and therefore not susceptible to hydrolytic attacks at elevated temperature.[9] Yet, there are drawbacks to using carbons as supports. Commercially available carbons with surface areas comparable to highly ordered mesoporous silicas mostly contain micropores. Thus, the current methods used to prepare high surface area mesoporous carbon materials involve the templating approach.[10-12] However, it is challenging to tailor pore size and connectivity for mesoporous carbons since the templating approach may not produce carbon with a replicate of the parent template once the template is removed from carbon, compared to the current methods used to prepare mesoporous silicas.[13-15] The hydrophobic carbons typically need to be functionalized to provide active sites for the anchoring of metal nanoparticles. Additionally, replica carbon materials tend to be amorphous or have a low degree of graphitization, and consequently may have limited mechanical strength compared to oxides. Therefore, a central challenge in the production of biorenewable fuels and chemicals is the development of supports, and subsequently, catalysts that can withstand high-water environments at elevated temperatures with high activity and, most importantly, high stability.

Previously, we reported a simple and inexpensive approach for modifying the surfaces of mesoporous oxide supports, such as silica and alumina, to make them hydrothermally stable in liquid water at 473 K. [16] Our approach is similar to what others have reported,[17-20] and involves the deposition of a thin film of carbon, derived from saccharides, on the surface of oxides from an aqueous solution; it is simpler than other methods used to carbon coat oxides.[21-27] We also compared the catalytic performance between Pd on uncoated oxides and Pd on carbon-coated oxides by selective acetylene hydrogenation to ethylene.

In this work, we show that to improve the dispersion, and therefore the stability, of Pd nanoparticles in catalysts under aqueous conditions, Pd needs to be deposited on hydrothermally stable supports. The support used to demonstrate Pd dispersion in this work is a Davisil-type silica obtained from Sigma-Aldrich. We also introduce the concept of adding a thin amorphous carbon overlayer to a silica-supported Pd catalyst as another approach to improving Pd dispersion and hydrothermal stability of the catalysts at elevated temperatures.

To coat the surface of silica or silica-supported Pd catalyst with 10 wt% carbon, an aqueous solution of sucrose was added to silica. The mixture was stirred at room temperature overnight until the water evaporated. The dried product was collected and partially pyrolyzed under flowing UHP N_2 gas at 673 K (5 K min^{-1} ramp) for 2 hr.

Pd acetate in methanol was sonicated for 10 min to completely dissolve the Pd acetate, and the solution was added to the uncoated or 10 wt% carbon-coated silica to obtain a Pd loading of 0.5 wt%. A Buchi rotary evaporator was used to gently remove methanol from the sample at 313 K, and the dried product was collected. Carbon was then added as a thin carbon overlayer to part of the Pd on uncoated silica sample.

Hydrothermal treatment of each sample was carried out by heating the sample in liquid water to 473 K at 15 bar and holding it at this temperature for 12 hr. Samples were dispersed in ethanol and mounted on holey carbon grids for examination in a JEOL 2010F 200 kV transmission electron microscope. Images were recorded both in bright field (BF) and high-angle annular dark field (HAADF) modes. An elemental carbon map was acquired using energy-filtered transmission electron microscopy (EFTEM) with an exposure time of 6 s. Surface area was measured using N_2 adsorption at 77 K in a Micromeritics Gemini 2360 multipoint BET analyzer. Nitrogen sorption isotherms and pore size distributions were measured at 77 K in a Quantachrome Autosorb-1 analyzer. Infrared spectra of samples were recorded on a Nicolet 7600 FTIR analyzer equipped with an attenuated total reflectance (ATR) attachment. The spectra were acquired between 400-4000 cm^{-1} at 4 cm^{-1} resolution and 128 scans. Thermogravimetic analysis (TGA) was performed under air flow between 25-700°C (5 K min^{-1}) in a TA Instrument SDT Q600 Simultaneous TGA/DSC analyzer. CO oxidation of the hydrothermally treated samples was performed under flowing CO (1.5 cm^3 (STP) min^{-1}), O_2 (1 cm^3 (STP) min^{-1}) and He (75 cm^3 (STP) min^{-1}). Reactivity measurements for the samples (20 mg) were carried out from room temperature to 573 K for 2 hr. The gas effluents were analyzed by GC (Varian CP-4900).

Figures 1a and 1c show HRTEM images of as-prepared mesoporous silica and 10 wt% carbon-silica, respectively, comprising around 10-15 nm primary size particles. At a higher magnification, the image of carbon-silica (Figure 1d) is similar to the image of uncoated silica (Figure 1b). This suggests that the carbon layer on the surface of the amorphous silica is very thin and amorphous. While a thin amorphous carbon layer should be observable on a crystalline oxide,[20] the amorphous substrate blurs the contrast. Conversely, if the thin carbon film on the silica was graphitic, even as thin as a monolayer, we should be able to observe it .[23] To actually confirm the presence of carbon on the surface of silica, we acquired an elemental carbon map via energy filtered transmission electron microscopy (EFTEM) at the carbon K edge, shown in Figure 2, where the bright red regions indicate the presence of carbon. Figure 2a shows the corresponding unselective HRTEM image for reference. The EFTEM image (Figure 2b) clearly shows that carbon is present on the surface of silica and that carbon is uniformly distributed throughout the silica particles. We can prepare uniform carbon coatings on the surface of mesoporous oxides with a 10 wt% carbon loading without having to repeat the coating-pyrolysis step to achieve similar loadings.[17-18] Both the N_2 sorption isotherm (Figure 3a) and pore size distribution (Figure 3b) curves are similar for silica and carbon-silica with BET surface areas of 280 m^2/g and 288 m^2/g, respectively, indicating that thin carbon films do not block the pores of silica. The increase in surface area after carbon coating may be due to pores in the thin carbon films that are formed during pyrolysis of sucrose on silica.

In our previous work, we showed that when uncoated silica is subjected to liquid water at 473 K for 12 hr, silica is not hydrothermally stable and loses surface area because of grain growth and sintering, whereas carbon-coated silica loses neither surface area nor its structural integrity after hydrothermal treatment.[16] Remarkably, the very thin layer of carbon can inhibit silica from hydrolytic attacks at elevated temperatures, and does not need to be a graphitic carbon to improve the hydrothermal stability of mesoporous oxide supports. FTIR spectra of the silica-based samples (see Figure S1, Supporting Information) show a broad absorption band at around 3200-3600 cm^{-1} assigned to the O-H stretching vibration and an absorption band at around 1640 cm^{-1} assigned to the bending vibrations of molecular water. Both absorption bands are initially small for uncoated and carbon-coated silica. We then rehydrated each sample by re-suspending it in water at room temperature overnight and drying the samples at room temperature in order to determine the extent of re-adsorbed water on the surface of the samples. Both uncoated and carbon-coated silica did not show an increase in the two absorption bands after rehydration, indicating that no added water has re-adsorbed on the surface of these samples. We had previously found that on the pore walls of uncoated SBA-15, hydroxyl groups were significantly recovered after rehydration.[16] Compared to commercial silica, SBA-15 has a much higher surface area than silica (740 m^2/g and 280 m^2/g, respectively). Thus, SBA-15 can re-adsorb water more readily and re-populate the pore walls with hydroxyl groups. Although no additional hydroxyl groups occur in uncoated silica after rehydration, silica does initially contain hydroxyl groups, and their presence is reflected in poor hydrothermal stability via hydrolytic attacks at elevated temperatures. In contrast, there are almost no absorption bands at around 3200-3600 cm^{-1} or 1640 cm^{-1} for 10 wt% carbon-silica before and after rehydration, indicating that the surface is more hydrophobic than hydrophilic silica. By changing the surface chemistry of silica with carbon, the silica surface is more resistant to hydrolytic attacks at elevated temperatures; this is demonstrated by the superior hydrothermal stability of carbon-coated silica compared to uncoated silica.

TGA plots of silica and 10 wt% carbon-silica in air (see Figure S2, Supporting Information) show two distinct curves. The first curve from 25-100°C shows loss of 1.7 wt% water from the carbon-silica sample, in agreement with the FTIR results in which the initial absorption band due to molecular water is very small for this sample. The corresponding loss of water in silica is 3.4 wt%, in agreement with a slightly more noticeable FTIR absorption band at around 1640 cm^{-1}. The second curve from 100-700°C for silica results from loss of hydroxyl groups (2.6 wt%) from the surface, whereas for carbon-silica it is mostly due to combustion of carbon from the surface of silica, which is complete at around 500-600°C. The wt% loss of carbon at this stage is 9.2 wt%, close to the nominal carbon loading of 10 wt%. The thin carbon films at this loading cover the silica surface sufficiently to significantly improve the stability of silica under aqueous conditions at elevated temperatures.

HAADF-STEM images of the 0.5 wt% Pd on uncoated silica (see Figure 4a,b) show that the sample contains highly dispersed 1-1.5 nm sized Pd nanoparticles prepared by the direct alcohol reduction route. After treatment in liquid water at 473 K, the Pd loading was < 0.1 wt%, as measured by EDS, presumably because of leaching of Pd from the uncoated silica support. The remaining Pd on silica is poorly dispersed and has sintered to form larger particles (2-20 nm), and this Pd sintering is accompanied by the grain growth and sintering of silica particles (c,d). Highly dispersed, similar sized Pd nanoparticles (1-1.5 nm) are also observed for 0.5 wt% Pd on 10 wt% carbon-silica (Figure 5a,b). There is, however, little to no change both in the Pd loading and in the structural integrity of the support after hydrothermal treatment (Figure 5c,d). The Pd has sintered to form 2-5 nm sized particle, but the extent of Pd sintering is significantly less than Pd sintering on uncoated silica after hydrothermal treatment, and the Pd is still highly dispersed on carbon-silica. For 0.5 wt% Pd on silica with a thin amorphous carbon overlayer of 10 wt% carbon (Figure 6a,b), the Pd nanoparticles are slightly larger (1-3 nm) than for the other two samples. This indicates a slight sintering of Pd during the pyrolysis step, although Pd is still highly dispersed on silica. After hydrothermal treatment, there is also little to no change both in the Pd loading and in the structural integrity of silica. The Pd has sintered to form 1.5-4 nm sized particles, which is also significantly less than Pd sintering on uncoated silica. Therefore, Pd is more stable under aqueous conditions at elevated temperatures when supported on hydrothermally stable carbon-silica or when Pd is deposited on uncoated silica followed by the addition of a thin carbon overlayer.

To show the effects of Pd dispersion and stability after hydrothermal treatment for the three Pd catalysts, we performed CO oxidation measurements; results are shown in Figure 7. Two replicate runs were performed for each catalyst. Both hydrothermally treated Pd/silica and Pd/carbon-silica catalysts showed similar CO conversions and light-off temperatures (T_{50}; see Table S1, Supporting Information) after the first run. After the second run, reactivities for Pd/silica were similar to the first run suggesting that Pd, after sintering during hydrothermal treatment, did not further sinter during the first CO oxidation run. Otherwise, the catalyst would have been less active after the second run. In contrast, hydrothermally treated Pd/carbon-silica was more active for CO oxidation after the second run, which was reflected by a shift in the curve towards a lower light-off temperature. Hydrothermally treated Pd/carbon-silica showed similar reactivities as hydrothermally treated Pd/silica after the first run even though Pd on carbon-coated silica was much smaller than Pd on uncoated silica after hydrothermal treatment. A possible reason is that Pd was covered by an amorphous carbon overlayer during hydrothermal treatment, suggesting partial mobility of the thin carbon film from the surface of silica. Reactivity increases after the second CO oxidation run due to Pd becoming accessible through partial removal of the carbon overlayer under the oxidizing conditions (carbon will completely burn off above 773 K). The coverage of Pd nanoparticles with an amorphous overlayer after hydrothermal treatment is similar to what we previously observed for Pd on commercial HY-340 niobia[28] after undergoing an aqueous-phase reaction of an important biomass-derivative, γ-valerolactone (GVL), to pentanoic acid, a platform chemical that can be further upgraded to fuel components.[29-32]

For hydrothermally treated carbon-coated Pd/silica, the catalyst was more active for CO oxidation after the first run than Pd/silica and Pd/carbon-silica. After the second run, reactivity increased for this catalyst also due to partial removal of the carbon overlayer. Hydrothermally treated carbon-coated Pd/silica was more active than hydrothermally treated Pd/carbon-silica after the first CO oxidation run, even though both catalysts had similar Pd particle sizes and a carbon overlayer was likely formed from Pd/carbon-silica during hydrothermal treatment. A potential explanation for the difference in CO oxidation reactivities between these catalysts is that carbon-coated Pd/silica contained smaller Pd nanoparticles than Pd/carbon-silica after hydrothermal treatment, resulting in the former catalyst being more active for CO oxidation than the latter catalyst. Nevertheless, some of the carbon overlayers in these catalysts were removed under the oxidizing conditions. This made the Pd sites more accessible for CO oxidation during the second run, while the remaining carbon overlayer could further inhibit Pd sintering since formation of larger Pd particles decreases CO oxidation reactivity. Both hydrothermally treated Pd catalysts were significantly more active than hydrothermally treated Pd/silica after two CO oxidation runs. Hence, the presence of thin carbon films in Pd catalysts could be beneficial for improving activity and stability both in gas-phase and aqueous-phase reactions by retaining both high

Pd dispersion and Pd stability in the catalysts, which might not be achieved without the thin carbon films.

The molecular structure of the carbon overlayer was investigated by solid-state NMR. Figure 8(a) presents quantitative ^{13}C NMR spectra of all carbons (full line) and of nonprotonated carbons plus methyl C (dashed line). The largest peaks in the spectra are from aromatic carbons, which resonate between 90 and 165 ppm (79% aromaticity), but CH_3 (5%), alkyl CH/CH_2 (5%), OCH_n (6%), COOH (3%), and C=O (3%) signals are observed as well. The measured peak intensities are well matched by corresponding simulated spectra, see Figure 8(b), obtained from the molecular model shown in Figure 8(c), which summarizes the composition in terms of functional groups and represents a typical, average structure. The NMR analysis demonstrates that the overlayer retains oxygen-containing groups and has developed only moderately polycondensed aromatic structures. These conclusions are validated by both the relatively small fraction of nonprotonated aromatic carbons, see Figure 8(a), and the spectrally edited 2D ^{13}C NMR spectrum [R. L. Johnson, J. M. Anderson, B. H. Shanks, X-W. Fang, M. Hong, K. Schmidt-Rohr "Spectrally Edited 2D ^{13}C-^{13}C NMR Spectra without Diagonal Ridge for Characterizing ^{13}C-Enriched Low-Temperature Carbon Materials", *J. Magn. Reson.* **234**, 112-124 (2013).] in Figure 8(d), which shows cross peaks characteristic of the edge of arene rings and of alkyl–arene linkages. The Pd-impregnated material gave carbon spectra nearly identical to those displayed in Figure 8(a) (data not shown); the main difference is a slight reduction in the intensity near 180 ppm.

In conclusion, our results show that after hydrothermal treatment in liquid water at 473 K, Pd sinters when deposited on non-hydrothermally stable silica. In contrast, the extent of Pd sintering is significantly reduced when deposited on hydrothermally stable carbon-silica or when Pd is deposited on uncoated silica followed by the addition of a thin amorphous carbon overlayer. The presence of a carbon overlayer inhibits the sintering of Pd and retains the dispersion of Pd under hydrothermal conditions, and these effects are measured by CO oxidation. By coating the surface of oxides with a thin carbon film, we can design catalysts with superior hydrothermal stability and improved catalytic performance (in gas-phase or aqueous-phase reactions) that will overcome some of the limitations of carbon or oxide supports alone. Furthermore, by introducing carbon as a thin amorphous overlayer to a catalyst, we may provide unique properties to achieve higher reactivity and stability in aqueous-phase reactions.

Acknowledgment

This work is supported by the Center for Biorenewable Chemicals supported by NSF grant EEC-0813570, and by the Partnership for International Research and Education supported by NSF grant OISE-0730277.

References

(1) Chheda, J. N.; Huber, G. H.; Dumesics, J. A. *Angew. Chem. Int. Ed.* **2007**, *46*, 7164.
(2) Corma, A.; Iborra, S.; Velty, A. *Chem. Rev.* **2007,** *107,* 2411.
(3) Huber, G. W.; Iborra, S.; Corma, A. *Chem. Rev.* **2006,** *106,* 4044.
(4) Alonso, D. M.; Wettstein, S. G.; Dumesic, J. A. *Chem. Soc. Rev.* **2012,** *41,* 8075.
(5) Ravenelle, R. M.; Copeland, J. R.; Kim, W. G.; Crittenden, J. C.; Sievers, C. *ACS Catal.* **2011**, *1*, 552.
(6) Ravenelle, R. M.; Copeland, J. R.; Van Pelt, A. H.; Crittenden, J. C.; Sievers, C. *Top. Catal.* **2012**, *55*, 162.
(7) Ravenelle, R. M.; Diallo, F. Z.; Crittenden, J. C.; Sievers, C. *Chemcatchem* **2012**, *4,* 492.
(8) Pagan-Torres, Y. J.; Gallo, J. M. R.; Wang, D.; Pham, H. N.; Libera, J. A.; Marshall, C. L.; Elam, J. W.; Datye, A. K., Dumesic, J. A. *ACS Catal.* **2011**, *1*, 1234.
(9) Xiong, H.; Pham, H. N.; Datye, A. K. *J. Catal.* **2013**, *302*, 93.
(10) Chang, H.; Joo, S. H.; Pak, C. *J. Mater. Chem.* **2007**, *17*, 3078.
(11) Liang, C. D.; Li, Z. J.; Dai, S. *Angew. Chem. Int. Ed.* **2008**, *47*, 3696.
(12) Ryoo, R.; Joo, S. H.; Kruk, M.; Jaroniec, M. *Adv. Mater.* **2001**, *13*, 677.
(13) Cassiers, K.; Linssen, T.; Mathieu, M.; Benjelloun, M.; Schrijnemakers, K..; Van Der Voort, P.; Cool, P.; Vansant, E. F. *Chem. Mater.* **2002**, *13*, 2317.
(14) Corma, A. *Chem. Rev.* **1997,** *97,* 2373.

(15) Van Der Voort, P.; Vercaemst, C.; Schaubroeck, D.; Verpoort, F. *Phys. Chem. Chem. Phys.* **2008**, *10*, 347.

(16) Pham, H. N.; Anderson, A. E.; Johnson, R. L.; Schmidt-Rohr, K.; Datye, A. K. *Angew. Chem. Int. Ed.* **2012**, *51*, 13163.

(17) Lin, L.; Wei, L.; Pei, W.; Yue-Xiang, Z.; Bi-Ying, Z.; You-Chang, X. *Acta Phys.-Chim. Sin* **2004**, *20*, 1179.

(18) Lin, L.; Lin, W.; Zhu, Y. X.; Zhao, B. Y.; Xie, Y. C.; Jia, G. Q.; Li, C. *Langmuir* **2005**, *21*, 5040.

(19) Yun, S.-M.; Palanivelu, K.; Kim, Y.-H.; Kang, P.-H.; Lee, Y.-S. *J. Ind. Eng. Chem.* **2008**, *14*, 667.

(20) Fu, L. J.; Yang, L. C.; Shi, Y.; Wang, B.; Wu, Y. P. *Micropor. Mesopor. Mat.* **2009**, *117*, 515.

(21) Ribeiro Carrott, M. M. L.; Estevao Candeias, A. J.; Carrott, P. J. M.; Sing, K. S. W.; Unger, K. K. *Langmuir* **2000**, *16*, 9103.

(22) Carrott, P. J. M.; Sing, K. S. W.; Raistrick, J. H. *Colloid Surface* **1986**, *21,* 9.

(23) Mel'gunov, M. S.; Mel'gunova, E. A.; Zaikovskii, V. I.; Fenelonov, V. B.; Bedilo, A. F.; Klabunde, K. J. *Langmuir* **2003**, *19,* 10426.

(24) Vissers, J. P. R.; Mercx, F. P. M.; Bouwens, S. M. A. M.; Debeers, V. H. J.; Prins, R. *J. Catal.* **1988**, *114,* 291.

(25) Adinata, D.; Daud, W. M. A. W.; Aroua, M. K. *J. Nanopart. Res.* **2007**, *9,* 555.

(26) He, C.; Lam, F. L. Y.; Hu, X. J. *Adsorption* **2007**, *13,* 281.

(27) Inagaki, M.; Miura, H.; Konno, H. *J. Eur. Ceram. Soc.* **1998**, *18,* 1011.

(28) Pham, H. N.; Pagan-Torres, Y. J.; Serrano-Ruiz, J. C.; Wang, D.; Dumesic, J. A.; Datye, A. K. *Appl. Catal. A* **2011**, *397*, 153.

(29) Bond, J. Q.; Alonso, D. M.; West, R. M.; Dumesic, J. A. *Langmuir* **2010**, *26*, 16291.

(30) Lange, J. P.; Price, R.; Ayoub, P. M.; Louis, J.; Petrus, L.; Clarke, L.; Gosselink, H. *Angew. Chem. Int. Ed.* **2010**, *49*, 4479.

(31) Bozell, J. J. *Science* **2010**, *329*, 522.

(32) Serrano-Ruiz, J. C.; Wang, D.; Dumesic, J. A. *Green Chem.* **2010**, *12*, 574.

APPENDIX F. ENGINEERING CATALYST MICROENVIRONMENTS FOR METAL-CATALYZED HYDROGENATION OF BIOLOGICALLY DERIVED PLATFORM CHEMICALS

Andewandte Chemie, **53**, pp 12718-12722, 2014

Thomas J. Schwartz[1], Robert L. Johnson[2], Javier Cardenas[3], Adam Okerlund[4], Nancy A. Da Silva[3], Klaus Schmidt-Rohr[2], and James A. Dumesic[1]

[1]Department of Chemical and Biological Engineering University of Wisconsin – Madison, Madison, WI 53706 (USA)
[2]Department of Chemistry, Iowa State University
[3]Department of Chemical Engineering and Materials Science, University of California, Irvine, Irvine, CA 92697 (USA)
[4]Biorenewables Research Laboratory, Iowa State University, Ames, IA 50011 (USA)

Abstract

It is shown that microenvironments formed around catalytically active sites mitigate catalyst deactivation by biogenic impurities that are present during the production of biorenewable chemicals from biologically derived species. Palladium and ruthenium catalysts are inhibited by the presence of sulfur-containing amino acids; however, these supported metal catalysts are stabilized by overcoating with poly(vinyl alcohol) (PVA), which creates a microenvironment unfavorable for biogenic impurities. Moreover, deactivation of Pd catalysts by carbon deposition from the decomposition of highly reactive species is suppressed by the formation of bimetallic PdAu nanoparticles. Thus, a PVA-overcoated PdAu catalyst was an order of magnitude more stable than a simple Pd catalyst in

the hydrogenation of triacetic acid lactone, which is the first step in the production of biobased sorbic acid. A PVA-overcoated Ru catalyst showed a similar improvement in stability during lactic acid hydrogenation to propylene glycol in the presence of methionine.

Introduction

Biomass is an attractive, renewable alternative to petro- leum-derived carbon for producing high-value, low-volume products such as chemicals.[1] A recently suggested[2] approach for biomass conversion uses biocatalysis to selectively retain functionality natively present in biomass, leading to highly functionalized platform species. Subsequent chemical cata- lytic upgrading of these species can then yield drop-in replacements for petroleum.[3] Using this strategy, sorbic acid can be produced from the biologically derived platform molecule triacetic acid lactone (TAL, see Scheme 1).[4] TAL is

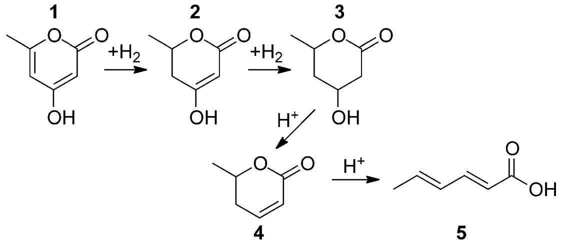

Scheme 1. Conversion of TAL (1) into sorbic acid (5). This work focuses on the hydrogenation of 1 to 5,6-dihydro-4-hydroxy-6-methyl- 2H-pyran-2-one (DHHMP, 2) and 4-hydroxy-6-methyltetrahydro-2- pyrone (HMTHP, 3). 5 is produced over a solid acid catalyst by dehydrating 3 to parasorbic acid (4), which is then ring-opened, produced through polyketide biosynthesis, providing an appealing biochemical platform owing to its potential to yield a wide array of highly functionalized species.[2a]

The first step in the conversion of TAL into sorbic acid is the reduction of the unsaturated carbon–carbon bonds in the pyrone ring. However, metal catalysts for hydrogenation are susceptible to deactivation by biogenic impurities in the cell culture medium. Notably, the Ru catalyst used for lactic acid hydrogenation is deactivated through both pore plugging by proteins and competitive adsorption of amino acids.[5] The sulfur-containing amino acids cysteine and methionine (Met) irreversibly poisoned the catalyst at levels as low as 100– 150 ppm, indicating a need for complex, expensive separation methods to remove trace amounts of biogenic impurities.

We have previously shown that the surface properties of heterogeneous catalysts can be controlled using an organic polymer to create a microenvironment that surrounds the catalytically active sites.[6] In a similar regard, polymer- encapsulated catalysts have also been developed as a means to immobilize metal-based organic synthesis catalysts, allow- ing for their recyclability.[7] Herein, we create a microenviron- ment that surrounds metal nanoparticles by intercalating poly(vinyl alcohol) (PVA) into the pores of the catalyst support. This microenvironment is then used to control which species come into contact with the active sites, thus allowing access of reactants yet mitigating deactivation by suppressing access of biogenic impurities.

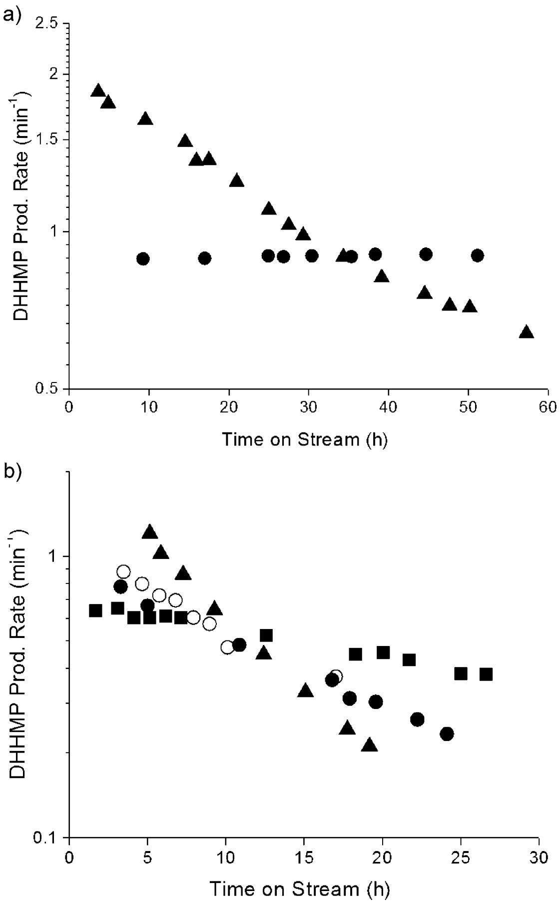

Figure 1. Turnover frequency versus time-on-stream for the hydrogena- tion of TAL to produce DHHMP over Pd/g-Al_2O_3 (~), PdAu/g-Al_2O_3 (Run 1: *, Run 2: *), and PVA/PdAu/g-Al_2O_3 (&). a) DHHMP produc- tion rate for TAL (0.2 %) in 1-butanol. b) DHHMP production rate for TAL (0.2 %) in 1-butanol with Met (0.01 mm). The initial conversion was between 50–70% in all cases.

The unsaturated carbon–carbon bonds in TAL can be reduced using Pd/C, achieving a 96% yield of HMTHP,[4] a key intermediate for sorbic acid production (see Scheme 1). Quantitative selectivity to DHHMP can also be achieved at 24 % conversion using 2 % Pd/g-Al_2O_3. However, as shown in Figure 1 a, this catalyst is ineffective for the sustained conversion of TAL because of catalyst deactivation by carbon deposition, an important consideration when upgrad- ing highly functionalized and reactive species such as TAL. The formation of bimetallic PdAu nanoparticles (1:1 atomic ratio) alleviates this deactivation, achieving a DHHMP production rate of 0.9 min^{-1} for at least 50 hours of time- on-stream, while maintaining quantitative selectivity to DHHMP. However, both catalysts were deactivated rapidly in the presence of Met, which was used as a model biogenic impurity (Figure 1 b).

The effects on the Pd catalyst of alanine (Ala), tryptophan (Trp), and Met, representative amino acids, were decoupled from catalyst deactivation by TAL by pre-equilibrating the catalyst for 14 hours with a feed containing 0.01 mm of the amino acid, after which TAL was added to the feed, and the initial rate of hydrogenation was measured. Low loadings of

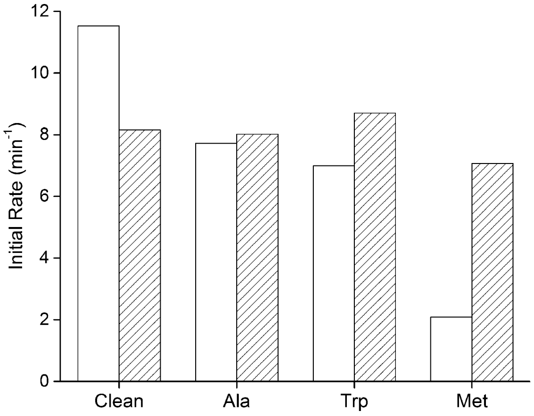

Figure 2. Initial rate of DHHMP production after equilibration for14 hours in in the presence of three different amino acids (0.01 mm) using Pd/g-Al_2O_3 (open bars) and PVA/Pd/g-Al_2O_3 (hashed bars) with TAL (2 %) in 1-butanol. The three amino acids are alanine (Ala), tryptophan (Trp), and methionine (Met). The initial conversion was between 30–50% in all cases.

the amino acids have a strong inhibitory effect on the catalyst (see Figure 2), and this inhibition is governed by the nature of the side chain, in agreement with previous work.[5] Met, with its sulfur group, resulted in 83% deactivation of the Pd catalyst, whereas Trp and

Ala, which do not contain sulfur, resulted in 37% and 30% deactivation, respectively. Interestingly, the PdAu catalyst lost only 65% of its activity after nearly 17 hours on stream. Thus, the addition of gold to the catalyst not only prevents deactivation in the presence of TAL, but it also helps to stabilize the catalyst in the presence of sulfur-containing impurities. Importantly, during the first eight hours of time-on-stream over the PdAu catalyst, the decrease in the rate corresponds to a loss of available surface Pd atoms that is equivalent to the amount of Met fed to the reactor. As discussed below, the support does not bind Met when Pd is present, suggesting that Met binds with a 1:1 stoichiometry to the surface Pd in the PdAu catalyst. This observation is consistent with studies of PdAu catalysts used for hydrodesulfurization and hydrogenation, where the pres- ence of gold was shown to inhibit the formation of bulk palladium sulfide, Pd_4S.[8]

Many biogenic impurities, such as amino acids, organic acid byproducts of fermentation, or vitamins, contain polar functional groups, whereas biologically derived platform molecules such as TAL are often less polar. To take advantage of this disparity, we investigated the use of a polymer coating to act as a pseudo-solvent, thus creating a microenvironment that is unfavorable for polar species. The solubility of TAL and amino acids in various solvents was used to guide the selection of the appropriate polymer. In particular, TAL is highly soluble in alcohols (see the Supporting Information, Table S1), whereas amino acids are not,[9] which led to the selection of PVA.

PVA was intercalated into the pores of both the Pd and PdAu catalysts as previously described.[6] Nitrogen physisorp- tion measurements showed minimal changes in porosity following intercalation, although the pore diameter decreased by approximately 1 nm (see

Table S2), indicating that the polymer coats the pore walls but does not fill the pores of the support. Moreover, the irreversible CO uptake by the metal nanoparticles decreased following intercalation. Inductively coupled plasma atomic emission spectroscopy of the dissolved catalysts showed that the Pd and Au loadings were both unchanged after overcoating (see Table S2). The surface- weighted average particle size, which was determined by scanning transmission electron microscopy, was unchanged at 3.8 - 2.9 nm and 3.9 - 1.3 nm for the parent and overcoated catalysts, respectively. Thus, the decrease in CO uptake is primarily due to site blocking as opposed to sintering or leaching, indicating direct contact between PVA and the metal nanoparticles, as needed to provide a microenvironment in the vicinity of the active sites.

Figure 2 shows that intercalation of the Pd catalyst with PVA decreases the rate of hydrogenation from 11.5 to 8.2 min^{-1}. Importantly, this catalyst shows high activity for TAL hydrogenation after exposure to Met (0.01 mm) for 14 hours. Furthermore, the DHHMP production rate remains essentially unchanged after 14 hours of exposure to Ala (0.01 mm) and Trp as well, demonstrating that the addition of PVA to metal catalysts imparts resistance to inhibitory amounts of polar biogenic impurities. We observed similar effects regardless of polymer chain length, loading, or identity (Table S3). Overcoating the PdAu catalyst with PVA stabil- izes the rate of TAL hydrogenation versus time-on-stream in the presence of Met (see Figure 1 b), with the first-order deactivation rate constant decreasing from 0.12 h^{-1} using Pd/ g-Al_2O_3 to 0.02 h^{-1} using PVA/PdAu/g-Al_2O_3.

Based on the improved impurity tolerance of the PVA- overcoated PdAu catalyst, we examined its stability during the hydrogenation of TAL that was produced by engineered

Saccharomyces cerevisiae, which was expressing a variant of the Gerbera hybrida 2-pyrone synthase (2-PS) gene g2ps1. The 2PS enzyme uses a single acetyl-CoA starter unit and incorporates two additional malonyl-CoA extenders by iterative decarboxylation–condensation reactions, forming TAL when the triketide intermediate undergoes spontaneous cyclization.[10] Using an S. cerevisiae strain engineered for increased precursor availability and an improved 2-PS, we obtained the highest TAL yields described to date, and we have also increased the titer to over 4 g l^{-1}, the highest reported value. Owing to the fact that TAL undergoes decarboxylation at elevated temperature in water,[11] TAL was then recovered from spent culture media prior to hydrogenation (see the Supporting Information, Section 5).

Figure 3 shows that the standard Pd catalyst undergoes rapid deactivation during hydrogenation of recovered and purified TAL, whereas the PVA-overcoated PdAu catalyst is more stable under the same conditions. The first-order deactivation rate constant decreases from 0.31 h^{-1} for Pd to 0.03 h^{-1} for PVA/PdAu. Combined with the observation that the overcoated catalyst is stable in the presence of amino acids, this behavior indicates that the activity loss while upgrading microbially produced TAL is mainly due to the presence of amino acids. Decreasing the amino acid concen- tration by further purifying the feed using an ion-exchange resin does not result in any improvement in the deactivation

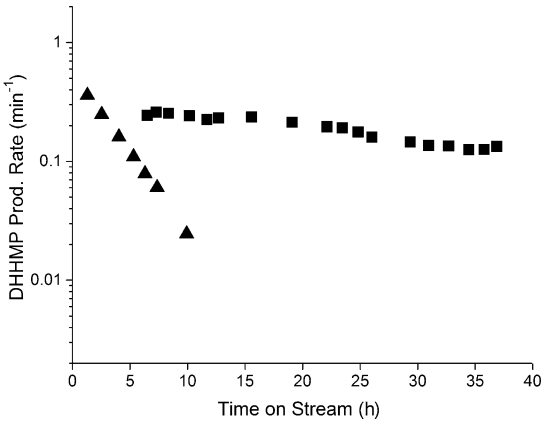

Figure 3. Turnover frequency versus time-on-stream for the hydrogena- tion of microbially synthesized TAL in 1-hexanol (ca. 0.15 %) to produce DHHMP over Pd/g-Al_2O_3 (~) and PVA/PdAu/g-Al_2O_3 (&). The initial conversion was between 50–70% in both cases.

rate constant, demonstrating that the overcoated catalyst allows for a simpler TAL recovery process (see the Support- ing Information, Section 5).

PVA-derived microenvironments can also be used during the hydrogenation of other biologically derived platform species. For example, the supported Ru catalyst that is used for lactic acid (LA) hydrogenation is susceptible to deactiva- tion by Met,[5] and this deactivation was mitigated by over- coatingthecatalystwithPVA.Overcoatinga5%Ru/g-Al_2O_3 catalyst increases the propylene glycol (PG) production rate from 0.36 min^{-1} to 0.55 min^{-1} during batch-mode hydrogena- tion of LA solutions in water (46 % w/w; see Table S4). The PG production rate over the Ru catalyst decreased to 0.07 min^{-1} after 14 hours of equilibration with an amount of Met that is equivalent to half the number of surface Ru sites measured by CO chemisorption (Met concentration between 0.8 and 1.2 mm). In contrast, the PVA-overcoated Ru catalyst was more stable after the same treatment, achieving a rate of 0.25 min^{-1}.

To provide insight into the interaction of Met with metal- based hydrogenation catalysts, we treated the Pd catalyst and the g-Al_2O_3 support with ^{13}C-enriched Met and collected solid-state ^{13}C NMR spectra of these materials. The spectra in Figure 4 a show the SCH_3 resonances of neat Met, Met adsorbed on g-Al_3O_3, and Met adsorbed on Pd/g-Al_2O_3, which were obtained prior to heating the catalyst in hydrogen. The characteristic 13 ppm signal of Met on g-A_2O_3 disappears when Pd is present and is replaced by a broader resonance at 19 ppm. Given that the surface area of Pd is much smaller than that of the support, this observation indicates prefer- ential binding of Met to Pd. The large shift in resonance position indicates that the binding involves the SCH_3 group, likely owing to strong S–Pd interactions. Spectra that were obtained after subjecting the catalysts to the reaction conditions (Figure 4 b) show substantial changes, indicating Met decomposition.

NMR spectra of the PVA overcoated Pd catalyst (Figure S2) reveal that the support dehydrates about one third of the PVA to form unsaturated carbon–carbon bonds. Treating

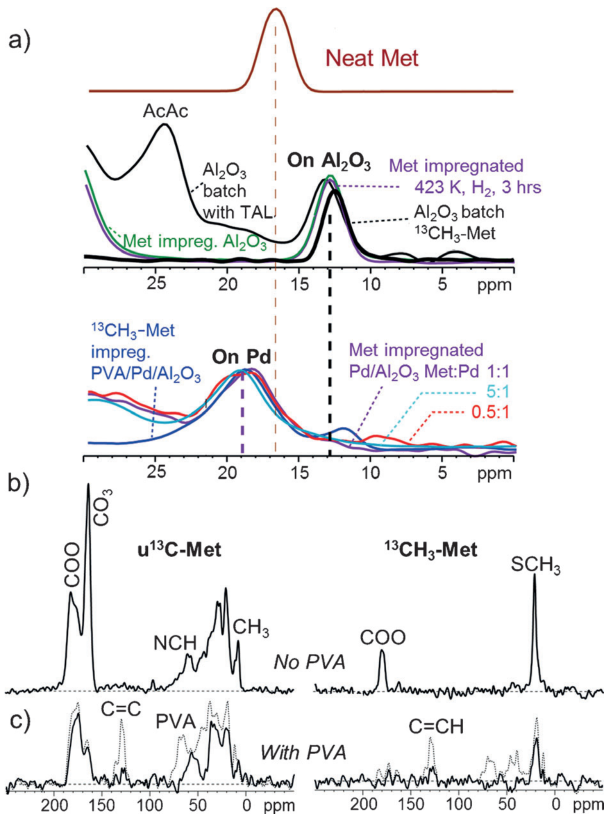

Figure 4. a) ^{13}C NMR resonances from the SCH_3 group of neat Met (top), Met bound to g-Al_2O_3 (middle), and Met bound to Pd/g-Al_2O_3 (bottom). b) ^{13}C NMR spectra of Met on Pd/g-Al_2O_3. c) ^{13}C NMR spectra of Met on PVA/Pd/g-Al_2O_3. The dashed lines in (c) are the unmodified spectra, and the solid lines correspond to the spectra obtained after subtraction of the PVA background. The spectra in (b) and (c) were obtained using uniformly ^{13}C-enriched methionine (u^{13}C-Met) and methionine with a ^{13}C label on the SCH_3 (^{13}C-Met).

both the overcoated and non-overcoated catalysts with ^{13}C- labeled Met (0.5 mm) under the reaction conditions and then recording NMR spectra reveals a substantial decrease in the intensity of the Met signal on the overcoated catalyst, demonstrating that Met adsorption is inhibited by the PVA- derived microenvironment (Figure 4 b and c). Taken together with the overcoating-induced changes in the support pore diameter and the metal surface area, these observations suggest that the PVA-derived microenvironment imitates a “solid solvent” into which species must partition, analogous to liquid–liquid partitioning. Dehydration of the PVA further suggests that this “solid solvent” is similar to a mixture of nonpolar and polar organic solvents, further decreasing the effective partition coefficient of amino acids and explaining the observed stability of the overcoated catalysts. This interpretation also explains the decrease in the DHHMP production rate following PVA overcoating, because the solubility of TAL decreases in nonpolar organic solvents leading to a lower TAL concentration in the vicinity of the metal nanoparticles. The observed increase in the rate of LA hydrogenation using the PVA-overcoated Ru catalyst can be explained in the same way. In particular, it has been shown that LA is the most abundant surface intermediate on Ru catalysts during LA hydrogenation.[12] As the solubility of LA is decreased in the PVA-derived microenvironment, the decreased local concentration of LA leads to a greater fraction of sites available for reaction and the observed increase in reaction rate.

We have shown that a PVA-overcoated PdAu catalyst is stable for the hydrogenation of TAL, a highly functionalized and highly reactive species, in the presence of biogenic impurities. This catalyst also shows improved stability in the hydrogenation of microbially synthesized TAL. Furthermore, we have shown that a PVA-overcoated Ru catalyst mitigates catalyst deactivation during the hydrogenation of LA in the presence of Met. Accordingly, this work demonstrates that successful coupling of heterogeneous chemical catalysis with biocatalysis is possible in the presence of biogenic impurities, and it provides guidance for developing strategies for upgrading biologically derived platform intermediates.

References

(1) J. J. Bozell, Clean Soil Air Water 2008, 36, 641 – 647.

(2) a)B.J.Nikolau,M.Perera,L.Brachova,B.Shanks,PlantJ.2008, 54, 536 – 545 ; b) T. J. Schwartz, B. J. O Neill, B. H. Shanks, J. A. Dumesic, ACS Catal. 2014, 4, 2060 – 2069 ; c) B. H. Shanks, ACS Chem. Biol. 2007, 2, 533 – 535.

(3) a)P.Anbarasan,Z.C.Baer,S.Sreekumar,E.Gross,J.B.Binder, H. W. Blanch, D. S. Clark, F. D. Toste, Nature 2012, 491, 235 – 239; b) R. M. Lennen, D. J. Braden, R. M. West, J. A. Dumesic, B. F. Pfleger, Biotechnol. Bioeng. 2010, 106, 193 – 202 ; c) A. C. Marr, S. Liu, Trends Biotechnol. 2011, 29, 199 – 204 ; d) T. Kieboom, Catal. Renewables 2007, 273 – 297; e) O. Pàmies, J.- E. Baeckvall, Chem. Rev. 2003, 103, 3247 – 3261.

(4) M. Chia, T. J. Schwartz, B. H. Shanks, J. A. Dumesic, Green Chem. 2012, 14, 1850 – 1854.

(5) Z.Zhang,J.E.Jackson,D.J.Miller,Bioresour.Technol.2008,99, 5873 – 5880.

(6) R. Alamillo, A. J. Crisci, J. M. R. Gallo, S. L. Scott, J. A. Dumesic, Angew. Chem. Int. Ed. 2013, 52, 10349 – 10351; Angew. Chem. 2013, 125, 10539 – 10541.

(7) R. Akiyama, S. Kobayashi, Chem. Rev. 2009, 109, 594 – 642.

(8) a) B. Pawelec, A. M. Venezia, V. La Parola, E. Cano-Serrano, J. M. Campos-Martin, J. L. G. Fierro, Appl. Surf. Sci. 2005, 242, 380–391; b)A.M. Venezia, V. LaParola, G. Deganello, B.
Pawelec, J. L. G. Fierro, J. Catal. 2003, 215, 317 – 325.

(9) K. R. Chalcraft, R. Lee, C. Mills, P. Britz-McKibbin, Anal.Chem. 2009, 81, 2506 – 2515.

(10) a) J. M. Jez, M. B. Austin, J.-L. Ferrer, M. E. Bowman, J. Schroder, J. P. Noel, Chem. Biol. 2000, 7, 919 – 930 ; b) M. B. Austin, J. P. Noel, Nat. Prod. Rep. 2003, 20, 79 – 110.

(11) M. Chia, M. A. Haider, G. Pollock III, G. A. Kraus, M. Neurock, J. A. Dumesic, J. Am. Chem. Soc. 2013, 135, 5699 – 5708. [12] a) Z. Zhang, J. E. Jackson, D. J. Miller, Ind. Eng. Chem. Res. 2002, 41, 691 – 696 ; b) Y. Chen, D. J. Miller, J. E. Jackson, Ind. Eng. Chem. Res. 2007, 46, 3334 – 3340.

Supporting Information

ENGINEERING CATALYST MICROENVIRONMENTS FOR METAL-CATALYZED HYDROGENATION OF BIOLOGICALLY DERIVED PLATFORM CHEMICALS

Experimental

Catalyst synthesis

Pd/γ-Al_2O_3 catalysts were prepared by incipient wetness impregnation of γ-Al_2O_3 (Strem, low- soda) with $Pd(NO_3)_2$ (prepared from Aldrich 10% $Pd(NO_3)_2$ solution in 10% HNO_3, 99.999%). The catalysts were subsequently dried at 383 K for 2 hours, calcined in flowing air at 673 K (Medical Grade, USP), reduced at 533 K in flowing hydrogen (Industrial Grade), and passivated with 1% O_2 in Ar (Research Grade). PdAu/γ-Al_2O_3 catalysts were prepared by simultaneous incipient wetness impregnation of aqueous solutions of $PdCl_2$ (Aldrich, 99.5+%) and $HAuCl_4$ (Sigma-Aldrich, 99.999%) on γ-Al_2O_3 following the method outlined by Hutchings, et al.[1] for SiO_2 supported catalysts. The catalyst was dried overnight at 383 K, calcined at 673 K in flowing air, reduced at 773 K in flowing H_2, and passivated in 1% O_2 in Ar. Ru/γ-Al_2O_3 catalysts were prepared by incipient wetness impregnation of γ-Al_2O_3 with $Ru(NO)(NO_3)_3$ (Alfa- Aesar, Ru 31.3% min). The catalysts were subsequently dried at 383 K for 2 hours, and reduced at 673 K in flowing hydrogen, and passivated with 1% O_2 in Ar.

PVA was intercalated into the Pd/γ-Al_2O_3, the PdAu/γ-Al_2O_3, and the Ru/γ-Al_2O_3 catalysts using a procedure previously described.[2] Briefly, PVA (Aldrich, 99+% Hydrolyzed, 89,000- 98,000 or 16,000 amu) and benzoyl peroxide (Luperox A98, ≥98%) in a

50 wt% mixture of THF (Fischer Scientific, Certified) and Milli-Q grade water were added to the Pd/γ-Al_2O_3, PdAu/γ- Al_2O_3, and Ru/γ-Al_2O_3 catalysts via incipient wetness impregnation. To prevent premature cross-linking, the impregnation was performed in the dark. The catalyst was dried under vacuum in the dark at 313 K for 2 hours. The polymer was cross-linked under UV light at 365 nm for 5 minutes, mixed, and cross-linked again at 365 nm for 5 min. Soluble polymer, residual cross- linker, and any other material that would dissolve under reaction conditions were removed via

Soxhlet extraction with 1-butanol for 14 hours. The catalyst was subsequently washed with Milli-Q grade water and dried under vacuum at 313 K for 2 hours. The same procedure was used for impregnation with poly(ethylene glycol) (Aldrich, Ultra, 20,000 amu).

Catalyst characterization

CO uptake (99.99%) was measured using a Micromeritics ASAP 2020 following reduction in flowing hydrogen (UHP) at 373 K for 3 hours. Pd dispersion was determined using a stoichiometry of 0.67 CO per surface metal atom for pure Pd materials and 1 CO per surface Pd atom for PdAu samples. The dispersion of Ru was determined using a stoichiometry of 1 CO per surface metal atom. Surface area, pore volume, and pore diameter were measured via nitrogen physisorption (UHP) using a Micromeritics ASAP 2020. Surface area was determined by the BET method, and pore volume and diameter via the BJH method using the desorption isotherm.

Polymer loading was determined by thermogravimetric analysis (TGA) using a TA Instruments QTGA500 with 20 mg of sample loaded into platinum pans. The temperature was ramped at 20 K/min to 873 K in flowing oxygen (Industrial Grade). Metal loading was determined by inductively coupled plasma atomic emission spectroscopy (ICP-AES) using a Perkin-Elmer Plasma 400 ICP emission spectrometer. For a typical analysis, 5 mg of catalyst were digested in refluxing aqua regia at 413 K for 4 hours. The error reported for metal loading is the standard deviation of the mean. Scanning transmission electron microscopy (STEM) was performed using a high-angle annular dark-field (HAADF) Z-contrast STEM (FEI Titan operated at 200 kV), with HAADF detector angle ranging from 54 to 270 mrad, probe convergence angle of 24.5 mrad, and probe current of ~25 pA. To prepare samples for STEM, the catalysts were first suspended in ethanol, ultrasonicated for 10 min, and then deposited onto

~5 nm thick Si window TEM grids. STEM samples were plasma cleaned for 10 min with 20% O_2 + 80% Ar gas immediately before loading into the microscope. Particles were counted manually using ImageJ software, and the reported average particle size is weighted by surface area for comparison with chemisorption data. The uncertainty is the standard deviation of the mean weighted by surface area. Analysis was performed using 189 and 311 particles for PdAu/γ-Al_2O_3 and PVA/PdAu/γ-Al_2O_3, respectively.

Reaction kinetics measurements

TAL hydrogenation kinetics measurements were carried out using catalyst packed into a quarter inch outside diameter stainless steel tube used as a flow reactor, and the liquid product was separated from non-condensable gasses at room temperature. A fixed-bed, up-flow configuration was achieved by packing the catalyst between two plugs of quartz wool. Temperature in the reactor was maintained using aluminum heat transfer blocks wrapped in heating tape and ceramic insulating blanket. Temperature measurements were made using a type-K thermocouple, and control was provided by a variable transformer connected to a PID controller (Love Controls Series 16A).

Prior to reaction kinetics studies the catalyst was reduced for 30 min at 323 K in 35 cm^3(STP)/min flowing hydrogen (Industrial Grade). Reaction kinetics studies were carried out at 323 K. The flow rate of H_2 was controlled to 35 cm^3(STP)/min using a mass flow controller (Brooks model 5850), and the total gas flow rate of the system was measured using a bubble flow meter. Triacetic acid lactone (TAL, Alfa-Aesar, 98%), methionine (Sigma-Aldrich, ≥98%), tryptophan (Sigma-Aldrich, ≥98%), alanine (Sigma-Aldrich, ≥98%), and 1-hexanol (Sigma- Aldrich, 98%) were used as purchased. Fresh cell culture media was prepared from TAL, yeast extract (BD Biosciences, Bacto), and peptone (BD Biosciences, Bacto). Residual impurities in 1-butanol (Sigma-Aldrich, 99.5%) were observed to affect catalyst stability and were removed by refluxing with $NaBH_4$ overnight under bubbling argon followed by distillation.[3] Liquid was fed to the reactor from a graduated cylinder using a high performance liquid chromatography (HPLC) pump. The total pressure in the reactor was controlled by a backpressure regulator and maintained at 27 bar. Concentrations of species in liquid solutions were determined using HPLC (Waters Alliance 2695) equipped with a photodiode array detector (Waters 996). Separation was achieved using a reversed-phase Zorbax SB-C18 column (4.6 x 300 mm, 5 μm) (Agilent Technologies) using 5 mM H_2SO_4 as the aqueous phase with acetonitrile as the organic modifier.

Hydrogenation of LA was carried out in a 50 mL stainless steel autoclave (Parr Instrument, Model 4792). The catalyst and magnetic stir bar were loaded into the reactor, the vessel was sealed, purged with He, and pressurized with 34 bar of H_2. The catalyst was reduced for 2 hours at 423 K, after which an aqueous solution containing 46% w/w lactic acid (Sigma-Aldrich, 85% solution in water) was pumped into the pressurized vessel using an HPLC pump and the stirring was started. Reaction kinetics measurements were carried out at 403 K with 34 bar of H_2. For experiments where the catalyst was pretreated with Met, aqueous solutions of the appropriate amount of Met to achieve a Met:Ru-site ratio of 0.5 were pumped into the pressurized vessel, the stirring was started, and the reactor heated at 403 K for 14 hours. Following this equilibration step, an aqueous solution of LA was pumped into the pressurized vessel, after which the stirring was started. Concentrations of species in liquid solutions were determined using HPLC (Waters Alliance 2695) equipped with a refractive index detector (Waters 2414). Separation was achieved using an Aminex 87H column (Bio-Rad) using 5 mM H_2SO_4 as the mobile phase.

Biological Synthesis of TAL

Luria-Bertani (LB) media with 150 mg/L ampicillin was used for cultivation of plasmid- containing Escherichia coli XL1-Blue strains.[4] Selective SDC(A) and rich YPD media (1% glucose) were used for cultivation of the Saccharomyces cerevisiae strains producing TAL. The yeast strains were grown for 16 h overnight in 5 mL selective SDC(A) medium in an air shaker (New Brunswick Scientific) at 250 rpm and 303 K, and used to inoculate both small-scale batch and large-scale fed-batch cultures in YPD medium to an initial cell density (OD_{600}) of 0.3 (Shimadzu UV-2450 UV-VIS Spectrophotometer). For fed-batch processes, a New Brunswick BioFloIII bioreactor was used to control aeration (< 0.8 vvm), agitation (400 rpm, baffled), and pH (6.0 using 6M NaOH or HCl) in a 2.5 L working capacity vessel. An ethanol feed was initiated after 24 h of batch cultivation and glucose depletion, ensuring optimal expression of the 2-PS enzyme. Following the 168 h cultivation (V_F ~ 2.1L), cell density was determined and the samples were centrifuged at 3,000 rpm (2,600 g) for 10 min at 298 K to remove the cells (Beckman GS-6R Centrifuge). The TAL-rich cell-free culture broth was collected for subsequent recovery and catalytic stages.

Recovery of TAL from Cell Culture Medium

TAL was recovered from cell culture media by liquid-liquid extraction with an equal volume of 1-hexanol. In order to improve the partitioning of TAL into the organic phase, the pH was decreased to 5 by ion exchange with a sulfonated ion-exchange resin (Amberlyst 15, washed with DI water, dried, and crushed). The resin was then removed by filtration, following which nonpolar organics were removed by extraction into an equal volume of n-hexane (Fisher Scientific, Optima 95%). Amino acid concentrations were decreased to trace levels by adsorption onto silica gel (Macron SilicAR Type 60Å), using 10 mL of silica gel per 15 mL of 1- hexanol. For experiments where the amino acid concentrations were further decreased, additional purification of the hexanol phase was accomplished by treatment with Dowex Marathon C strong cation exchange resin, using 21 g resin per 45 mL of 1-hexanol following treatment with silica gel. The cation exchange resin was first washed with water until the filtrate ran clear, and it was then dried under vacuum at 323 K overnight.

Solid State NMR

^{13}C solid-state NMR spectra were collected using a Bruker DSX400 spectrometer at a resonance frequency of 100 MHz, magic angle spinning at 14 kHz, and high-power proton decoupling at $\gamma B_1/2\pi = 72$ kHz with the two-pulse phase-modulated (TPPM) scheme, applied during an acquisition time of 5 ms. The multiCP sequence[5] was used for generating quantitative signal intensities. The 90° ^{13}C pulse-length was 4.4 μs. Chemical shifts are shown relative to neat TMS, using the resonance of ^{13}COO-labeled glycine in the a-modification as a secondary reference at 176.46 ppm.

2. Solubility of TAL in Various Solvents

Table S1. Solubility of TAL in various solvents.

	TAL Solubility (% w/w)
Water	0.86
THF	2
***n*-pentane**	n.d.[a]
***n*-butanol**	4.9
***n*-hexanol**	4
***n*-octanol**	3.6

a) Not detected

3. Catalyst Characterization Data

Table S2. Characterization of polymer-overcoated materials

	CO Uptake (µmol/g)	BET Area (m^2/g)	BJH Pore Vol (cm^3/g)	BJH Pore Diam (nm)	PVA Loading	Pd Loading (%)	Au Loading (%)
Pure γ- Al_2O_3	--	213	0.55	7.2	--		
PVA/ Al_2O_3	--	208	0.442	6.2	7.3%		
Pd/ Al_2O_3	63	191	0.457	6.9	--		
PVA[a]/Pd/ Al_2O_3	38	185	0.405	5.9	7.4%		
PdAu/Al_2O_3	40	210	0.425	5.9	--	1.7±0.2	4.1±0.4
PVA[a]/PdAu/Al_2O_3	10	188	0.331	5.0	9.5%	1.6±0.2	3.9±0.3
PVA[b]/Pd/Al_2O_3	36	193	0.381	5.9	7.6%		
PVA[a]/Pd/Al_2O_3	33	209	0.419	6.0	3.2%		
PEG[c]/Pd/Al_2O_3	22	183	0.372	5.9	7.5%		
Ru/Al_2O_3	472	199	0.361	5.3	--		
PVA[a]/Ru/Al_2O_3	303	196	0.315	4.8	8.3%		

a) PVA molecular weight range: 89,000-98,000 amu b) PVA molecular weight: 16,000 amu c) PEG molecular weight: 20,000 amu

Influence of Polymer Chain Length, Loading, and Identity

As shown in Table S3, intercalation of the Pd/γ-Al_2O_3 catalyst with 89,000-98,000 molecular weight PVA results in a decrease in rate from 11.5 to 8.2 min^{-1}. Despite the decrease in activity that results from overcoating, the catalyst is stable after exposure to methionine for 14 hours on stream. In contrast, overcoating the catalyst with 7% poly(ethylene glycol) (PEG, 20,000 amu) does not result in a decrease in activity, although the catalyst is more stable in the presence of methionine than the nonovercoated catalyst. Similar behavior is observed when the loading of PVA (measured by thermogravimetric analysis, see Table S2) is decreased from 7% to 3.2%. Similar results were obtained using 16,000 amu molecular weight PVA, indicating that polymer chain lengths at least up to 98,000 amu molecular weight are able to diffuse into the pores of the γ-Al_2O_3 support.

Table S3. Initial rate (min^{-1}) of DHHMP production after 14 hour equilibration in the absence and presence of 0.01 mM methionine for polymer-overcoated materials.

	Initial rate (min^{-1})[a]	
	Clean reaction	**0.01 mM met-exposed**
2% Pd/Al_2O_3	11.5	1.8
7% PVA[b]/2% Pd/Al_2O_3	8.4	7.2
7% PVA[c]/2% Pd/Al_2O_3	9.6	9.6
3.2% PVA[b]/2% Pd/Al_2O_3	12.5	8.6
7% PEG[d]/2% Pd/Al_2O_3	13.1	6.7

a) Reaction conditions: 323 K, 27 bar H_2, 2% TAL/BuOH feed, catalyst treated for 14 hours in amino acid prior to reaction. b) PVA molecular weight range: 89,000-98,000 amu c) PVA molecular weight: 16,000 amu d) PEG molecular weight: 20,000 amu

2% Pd/$Al_2O_3$7% PVA[b]/2% Pd/$Al_2O_3$7% PVA[c]/2% Pd/$Al_2O_3$3.2% PVA[b]/2% Pd/$Al_2O_3$7% PEG[d]/2% Pd/Al_2O_3a) Reaction conditions: 323 K, 27 bar H_2, 2% TAL/BuOH feed, catalyst treated for 14 hours in amino acid prior to reaction. b) PVA molecular weight range: 89,000-98,000 amu c) PVA molecular weight: 16,000 amu d) PEG molecular weight: 20,000 amu

5. Recovery of TAL from Spent Cell Culture Media

Based on the improved performance of the PVA-overcoated PdAu/γ-Al2O3 catalyst for the hydrogenation of TAL in the presence of amino acids, we studied this catalyst for hydrogenation of microbially-produced TAL extracted from cell culture media with 1-hexanol after nonpolar organic species were removed by extraction with n-hexane. The concentrations of amino acids were decreased to trace levels by adsorption onto silica gel.

Figure S1 shows results obtained when hydrogenating TAL recovered from fresh cell culture media, used to simulate biologically-produced TAL. When this material was further purified by treatment with a cation exchange resin (i.e., the concentration of amino acids was decreased almost to zero), the deactivation rate constant remained invariant within experimental error (i.e., 0.05 hr^{-1} vs 0.04 hr^{-1}), demonstrating that the overcoat allows for less stringent purity requirements for recovery processes.

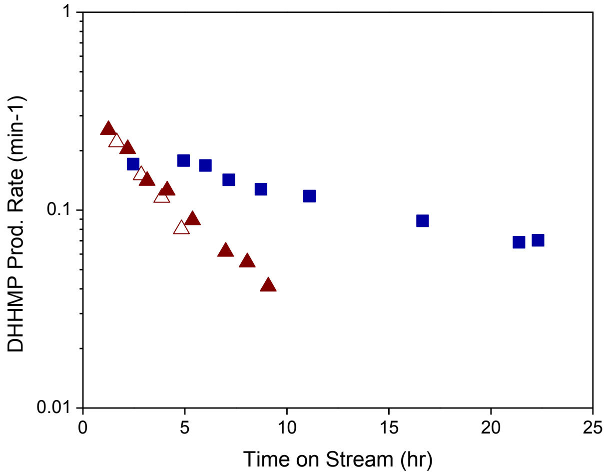

Figure S1. Turnover frequency versus time-on-stream for hydrogenation of TAL recovered from fresh cell culture medium using Pd/γ-Al_2O_3(Run 1 △, Run 2▲)and PVA/PdAu/γ-Al_2O_3(■).

Table S4. Initial rate (min^{-1}) of propylene glycol production after 14 hour equilibration in the absence and presence of 0.8-1.2 mM methionine (equivalent to a Met:Ru-site ratio of 0.5).

	Initial rate (min^{-1})^{a}	
	Clean reaction	**Met-exposed**
5% Ru/Al_2O_3	0.36	0.07
PVA/5% Ru/Al_2O_3	0.55	0.25

a) Reaction conditions: 403 K, 34 bar H_2, 46% lactic acid/water feed, catalyst treated for 14 hours in methionine prior to reaction. Conversion for each run was less than 15%.

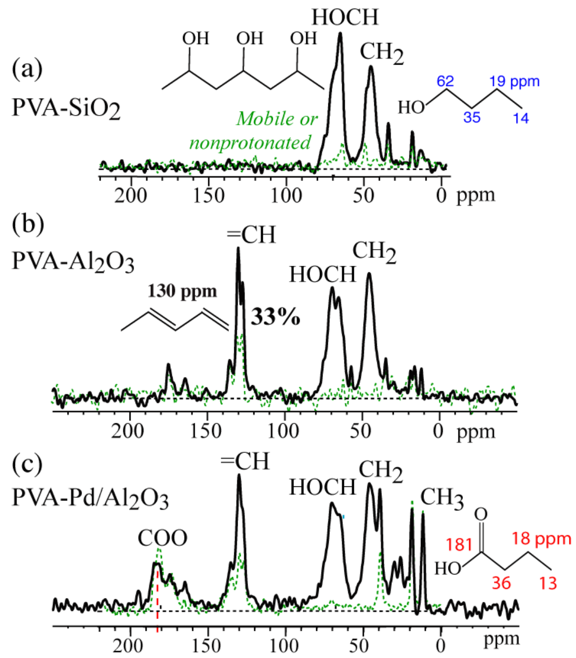

Figure S2. ^{13}C NMR spectra of PVA overcoats on (a) SiO_2, (b) Al_2O_3, and (c) Pd/Al_2O_3. PVA shows peaks near 65 and 45 ppm, from -OCH and $-CH_2$ groups, respectively. In the presence of Al_2O_3, ca. 1/3 of PVA is dehydrated to form -C=C- units (resonance near 130 ppm). The spectra in (a) and (b) show traces of trapped butanol solvent, and the spectrum in (c) shows butyric acid.

References

(1) J. K. Edwards, B. Solsona, N. E. Ntainjua, A. F. Carley, A. A. Herzing, C. J. Kiely, G. J. Hutchings, Science 2009, 323, 1037-1041.
(2) R. Alamillo, A. J. Crisci, J. M. R. Gallo, S. L. Scott, J. A. Dumesic, Angew. Chem. Int. Ed. 2013, 52, 10349-10351.
(3) W. L. F. Armarego, C. L. L. Chai, Purification of Laboratory Chemicals, 6th ed., Elsevier, Inc., 2009.
(4) J. Sambrook, D. Russell, Molecular Cloning: A Laboratory Manual, 3rd ed., Cold Spring Harbour Laboratory Press, Cold Spring Harbour, NY, 2001.
(5) R. L. Johnson, K. Schmidt-Rohr, J. Magn. Reson. 2014, 239, 44-49.